TUNING AND VIBRATIONAL MODULATION OF STRONGLY CORRELATED ORGANIC SALTS

Dissertation

zur Erlangung des Doktorgrades

des Department Physik

der Universität Hamburg

vorgelegt von

GIOVANNI COTUGNO

aus

SAN GIOVANNI ROTONDO (FG) - ITALY

Hamburg

2014

Gutachter der Dissertation	Prof. Dr. Andrea Cavalleri Prof. Dr. Ludwig Mathey
Gutachter der Disputation	Prof. Dr. Andrea Cavalleri Prof. Dr. Andreas Hemmerich
Datum der Disputation	24/09/2014
Vorsitzender des Prüfungsausschusses	Prof. Dr. Peter Schmelcher
Vorsitzender des Promotionsausschusses	Prof. Dr. Daniela Pfannkuche
Dekan der MIN Fakultät	Prof. Dr. Heinrich Graener
Leiter des Fachbereich Physik	Prof. Dr. Peter Hausschildt

Life is one big road with lots of signs.
So when you riding through the ruts, don't complicate your mind.
Flee from hate, mischief and jealousy.
Don't bury your thoughts, put your vision to reality.

Robert Nesta Marley

A mamma,

Abstract

This thesis reports on experiments results and theoretical modeling of ultrafast quantum dynamics in strongly correlated electron materials. Using ultrashort pulses of light, the response of the 1D organic (BEDT-TTF)-F_2TCNQ is probed on its fundamental timescale following different kinds of perturbations. From a theoretical point of view, existing effective model Hamiltonians are extended to encompass the microscopic physics. By comparing theoretical modeling and simulations with experimental data, new physics is exposed and interpreted.

Firstly, we theoretically investigate the change of the Hubbard parameters, and of the binding energy of the excitons, by measuring the optical conductivity while adiabatically compressing the material. Moreover, we develop a model for the relaxation rate of photo-induced holon-doublon pairs. In this manner, we expose the competition between the pairs' tendency to bind, due to the nearest-neighbor Coulomb interaction, and to delocalize because of the electron's kinetic energy.

In a second study, optical pulses at THz frequencies (from 0.3 to 3×10^{12} hertz), and mid-infrared frequencies are tuned to specific vibrational resonances to modulate the lattice along a chosen normal mode coordinate. By using optical pulses we excite localized molecular vibrations and make the electronic interaction time-dependent. We develop a quantum-modulated, dynamic, version of the Hubbard model to explain the response. A third experiment, performed with phase-locked pulses, confirms the validity of our picture. The optical conductivity is shown to undergo oscillation with a frequency predicted by our model when a specific driven mode is used. A central conclusion of both these investigations is that, by combining selective modulation of one degree of freedom while probing the electronic spectrum, it may be possible to experimentally deconstruct the Hubbard Hamiltonian and expose one specific coupling that would otherwise have a vanishingly small contribution to the equilibrium properties.

In the last part of this thesis we propose that vibrational driving can be exploited as a tool to transiently induce magnetic order in an otherwise non-magnetic system away from half-filling. We show that vibrational driving reduces the kinetic energy of the holes, without affecting the exchange interaction strength, and allowing the magnetic exchange coupling to stabilize spin order that would otherwise be disrupted.

Zusammenfassung

Diese Arbeit berichtet über experimentelle Ergebnisse und die theoretische Modellierung von ultraschneller Quantendynamik in stark korrelierten elektronischen Materialien. Unter Anwendung von ultrakurzen Lichtpulsen wird die Reaktion von 1D organischem (BEDT-TTF)-F_2TCNQ auf der fundamentalen Zeitskala unter Einfluss verschiedener Pertubationen untersucht. Unter einem theoretischen Gesichtspunkt werden bereits existierende effektive Model Hamiltonoperatoren erweitert, um Aspekte der mikroskopischen Physik zu umfassen. Durch den Vergleich von theoretischen Modellen und Simulationen mit experimentellen Daten wird neue Physik offenbart und interpretiert.

Als Erstes haben wir die Veränderung des Hubbard Parameters und der Bindungsenergie des Exzitons theoretisch untersucht. Dabei wurde die optische Leitfähigkeit während der adiabatischen Kompression des Materials gemessen. Außerdem haben wir ein Model für die Relaxationsrate der fotoinduzierten Holon-Doublon Paare entwickelt. Auf diese Weise zeigen wir das Gegenspiel von Paarbindung durch die Nächster-Nachbar-Coulomb-Wechselwirkung und Delokalisierung aufgrund der kinetischen Energie des Elektrons.

In einer zweiten Studie wurden optische Pulse im THz Frequenzbereich (von 0.3 bis 3×10^{12} hertz) und infrarot Frequenzen im mittleren Bereich auf spezifische Vibrationsresonanzen eingestellt um das Gitter entlang ausgewählter Normal-Mode-Koordinaten zu modulieren. Mit optischen Pulsen werden lokalisierte molekulare Vibrationen angeregt und elektronische Interaktionen zeitabhängig gemacht. Wir entwickeln eine Quanten modulierte, dynamische Version des Hubbard Models um diese Reaktion zu erklären. Ein drittes Experiment, durchgeführt mit phasensynchronen Pulsen, bestätigt die Gültigkeit unseres Bildes. Die optische Leitfähigkeit erfährt Oszillationen mit einer Frequenz vorhergesagt von unserem Model, wenn eine spezifische Mode getrieben wird. Eine zentrale Schlussfolgerung aus beiden Untersuchungen ist,

dass die Modulation eines ausgewaehlten Freiheitsgrades waehrend der Messung des elektronischen Anregungsspektrums, es ermoeglichen koennte den Hubbard Hamiltonoperator experimentell zu dekonstruieren. Außerdem könnte man eine spezifische Kopplung untersuchen, die andernfalls einen verschwindend kleinen Beitrag zu den Gleichgewichtseigenschaften hat.

Im letzten Teil dieser Arbeit schlagen wir ein Vibrationsverfahren vor, das als Werkzeug genutzt werden kann, um vorübergehend eine magnetische Ordnung zu induzieren in einem ansonsten nicht-magnetischen System entfernt von der Halbfüllung.

Wir zeigen, dass das Vibrationsverfahren die kinetische Energie der Löcher reduziert ohne die Austauschwechselwirkungsstärke zu beeinflussen. Dadurch hemmt es die Lochbewegung, während die Magnetkopplung Spinordnung schafft.

Role of the author

This thesis features work that my colleagues and I undertook collaboratively [1, 2, 3, 4].

The theoretical modeling and numerical simulations, described in detail in Ch. 5, were performed by the author with the helpful support of S. Clark. The resulting physical picture was used to analyze the experimental results and evolved in the publication [1].

The derivation of the Dynamic Hubbard Model in Ch. 6, along with the interpretation, numerical simulation and fitting of the experiments in Ch. 7 and Ch. 8 were carried on by the author, with the help of S. Clark. These results led to publications [2] and [3], respectively.

Among the work performed, but not reported in detail in this thesis, the author with assistance of T. H. Johnson wrote the manuscript of [4] and organized the code for online publication at `http://ccpforge.cse.rl.ac.uk/gf/project/mlgws/`.

Contents

List of Figures

Chapter 1

Introduction

1.1 Ultrafast science with light

In slightly more that fifty years the laser has become one of the most ubiquitous pieces of technology in existence [5], finding a home for itself in environments as diverse as the research laboratory, the hospital, and the living room. Among numerous areas of research, the probing of matter with pulsed laser light has become a field of prominence in physics, biology and chemistry. The ability to sculpt pulses enables the triggering and measurement of dynamical behavior in solids on extremely fast timescales, approaching those of the microscopic dynamics of electrons and phonons in the material itself.

In order to probe a dynamical event we need a method to capture snapshots of the state of the system as it evolves in time. Arranging the snapshots sequentially allows the reconstruction of the behavior of the system at any given time. Each snapshot records the average of the system during the exposure time. If the system is changing during this period, the image gets blurred: to capture a fast dynamical event, snapshots need to be recorded on a timescale comparable or shorter than the event taking place.

In 1878, Eadweard Muybridge performed one of the earliest time-resolved measurements to settle the debate as to whether or not there is a time, while a horse gallops, when all four hooves are off the ground at the same time. The images Muybridge took are reproduced in Fig. 1.1, and were obtained by a series

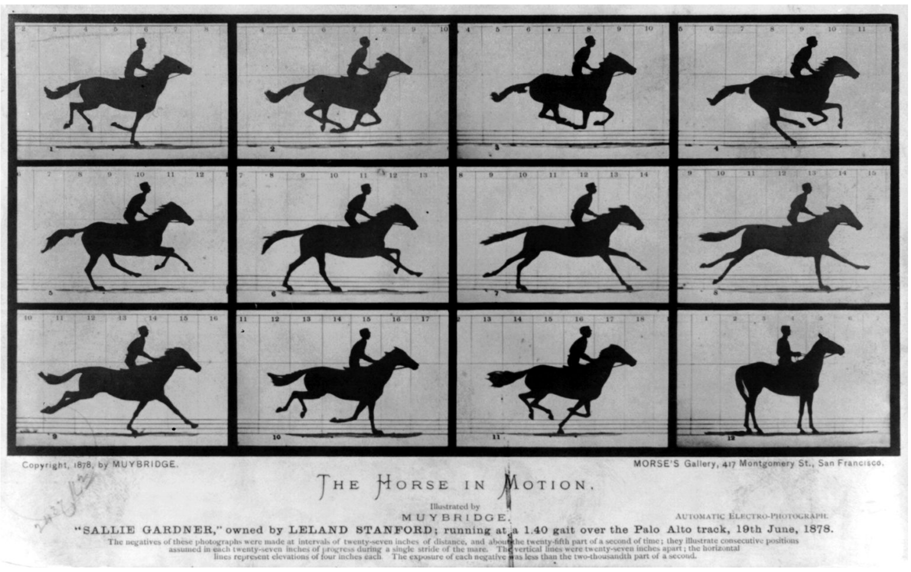

Copyright, 1878, by MUYBRIDGE.

MORSE'S Gallery, 417 Montgomery St., San Francisco.

THE HORSE IN MOTION.

Illustrated by
MUYBRIDGE.

AUTOMATIC ELECTRO-PHOTOGRAPH.

"SALLIE GARDNER," owned by LELAND STANFORD; running at a 1.40 gait over the Palo Alto track, 19th June, 1878.

The negatives of these photographs were made at intervals of twenty-seven inches of distance, and about the twenty-fifth part of a second of time; they illustrate consecutive positions assumed in each twenty-seven inches of progress during a single stride of the mare. The vertical lines were twenty-seven inches apart; the horizontal lines represent elevations of four inches each. The exposure of each negative was less than the two-thousandth part of a second.

Figure 1.1: *The horse in motion* by Eadweard Muybridge. The first time resolved measurement consisting of a series of images of a horse in motion.

of cameras with high shutter speeds, each triggered by a trip wire.

The ultrafast dynamics that occur in solid-state systems can be measured with similar techniques. The cameras are replaced by short laser pulses, that "probe" the state of the system at high-speed. The dynamics is initiated by an intense "pump" pulse, while the temporal evolution is tracked with subsequent probe pulses which encode information about the system properties evaluated at the probe pulse moment of arrival. Much like how Muybridge's images captured the horses motion at consecutive instants of time, measuring the transmitted light as a function of delay between pump and probe pulses encodes information on the evolution of the system.

In order to investigate how a system fundamentally responds to a prompt photo-excitation, pulses with a duration of $\Delta\tau \sim \hbar/2\Delta E$ need to be used, where ΔE is the energy scale of the phenomena responsible for the dynamics. This methodology is founded upon the seminal studies of Zewail *et al.* [6], the importance of which was recognized by the award of the Nobel Prize in Chemistry in 1999. For chemical reactions that occur at room temperature with an energy scale of $\sim k_BT$, the timescale is $\Delta\tau \sim 100$ femtoseconds (fs, 10^{-15} seconds).

Processes occurring on such short timescales are referred to as “ultrafast” processes, and are common in solid state systems, as well as in chemical reactions.

In addition to its use as probe, light can also be used to alter the phase of a material by changing the relative strengths of the couplings and photo-inducing phase transitions [7]. This process is often referred to as photo-doping [8], in analogy to the more traditional chemical doping [9] that affects the material’s carrier concentration by adding or removing electrons from the system.

The first ultrafast phase transition observed was the solid-to-liquid one in semi-conductors [10]. The change in atomic position associated with this phase transition was subsequently tracked with time-resolved diffraction measurement in [11].

In this thesis we are going to apply these methods to explore the physics of strongly correlated systems. These materials have peculiar properties which is worth summarizing in some detail before expanding upon specific methods of control.

1.2 Strongly correlated electron materials

Solid state physics is largely concerned with the description of the macroscopic properties of materials, such as crystal structure, optical, magnetic, conductive properties, all from a microscopic point of view. This is a truly daunting task, since it can involve solving a problem with $N \sim 10^{23}$ particles. As a consequence, we need to resort to approximate theories to reduce the complexity of the microscopic interactions.

In quantum mechanics, the Hamiltonian describes the behavior of a system, and thus governs the electrons’ properties. In the most general form, it contains the kinetic energy of the electron, the potential energy of the nuclei, and the Coulomb interaction among the electrons. The last aspect is by far the hardest to deal with. Imagine the difference between a 100 m and a marathon race. In the former, each runner has his own lane and can be considered as running independently, while in the latter each one of the competitors has to (or try to) avoid the others, or bumps into them. Predicting the behavior of marathon runners is clearly more difficult than for sprinters.

The same is true for electrons in solids: it is no surprise the first successful approximation is the independent electron approximation from Drude and Sommerfeld [12] used to describe simple metals. This technique is based on the observation that the interplay between nuclei and electrons (and the delocalization of the latter) results in very effective screening of Coulomb interactions which also contributes to why electrons (or quasi-particles) in metals are not very strongly interacting. The kinetic energy is assumed to dominate, and the Coulomb interaction is included via perturbation theory. This in turn led to band theory [13] that predicts the conduction properties of a wide variety of condensed matter systems and has driven the electronic revolution, e.g., with the widespread use of transistor based devices.

The pinnacle of this approach is, arguably, Fermi liquid theory [14]. Landau showed that the properties of a system, when taking into account electronic interactions, remain essentially similar to those of free fermionic particles. The key observation is that macroscopic properties involve only excitations on energy scales (e.g. temperature) small compared to the Fermi energy. The state of the system can thus be specified in terms of its ground state (Fermi surface), and of the low-lying elementary excitations that form a rarified gas of "quasi-particles". The latter are still fermions, but their dynamical properties are renormalized by the interactions.

However, there are many materials where the electronic correlations prove to be the dominant dominant energy scale, rather than a simple perturbation. The Coulomb interaction among electrons is then larger than their kinetic energy, meaning an electron remains on a given lattice site long enough to feel the presence of other electrons nearby. In these cases, the independent-electron picture breaks down and the predictions of band theory no longer match the observed behavior [15, 16]. This was first pointed out observing that many transition metals compounds with only partially filled d-levels turn out to be insulators instead of metals [17]. As a result a large number of exotic order states and unusual phase transitions emerge. It was indeed the discovery of high-T_c superconductivity in cuprates [18] that triggered the interest in these compounds, to the extent that the investigation of materials with strongly correlated electronic behavior (also referred to as *complex* materials) has developed into one of the most exciting branches of condensed matter systems.

1.2.1 One dimension

All the effects of interactions mentioned so far are especially strong in low-dimensional systems (e.g. materials with one-dimensional conduction properties), in which the electronic bandwidth is reduced, allowing the Coulomb interaction to dominate the physics [19, 20].

In fact, when an electron propagates, it pushes its neighbors because there is only one pathway of propagation. The strong electron-electron interaction leads to peculiar collective effects. The particle-hole excitations, where an electron is taken from below the Fermi level and promoted above, have well-defined particle-like dispersion in the long-wavelength limit. These collective density fluctuations are bosonic in nature and may be used to construct the low-energy phenomenology. They form the basis of the so-called Luttinger liquid, the properties of which are extensively described in [21, 22].

Another important and singular effect observed in 1D is the so-called spin-charge separation: a single fermionic excitation splits into a collective excitation carrying charge (like a sound wave) and a collective excitation carrying spin (like a spin wave). In general, they have different velocities and propagate independently. Furthermore, filling plays a more important role than in three-dimensional compounds. When the density of carriers is commensurate with the lattice, interactions may cause a system with fractional filling to become a so called Mott-insulator [23].

It is the competition between single electron kinetic energy and the electron-electron Coulomb interaction to dictate the tendency of the electrons to move freely or localize on atomic sites. To complicate matters, also the correlation between the electrons and the lattice may play an important role. All these interactions compete to determine the properties of complex materials, and their understanding is vital to interpret the macroscopic behavior of the compound under investigation.

If several different couplings have similar energy scales, then these properties become very sensitive to subtle perturbations and it is extremely complex to disentangle them. It is crucial to be able to control their relative strength, causing some to become more relevant than others. In the next section, we review some of the experimental methods used for this purpose in the last decade.

1.2.2 Control of materials

The properties of correlated materials can be changed by photo-doping, driving the system into a non-equilibrium yet relatively long-lived conducting state, or by introducing mobile carriers *in situ*. Pioneering experiments in the field include studies into insulator-to-metal transitions [24, 25, 26, 27, 28], melting and recovery of charge density waves [29, 30, 31], and ultrafast dynamics induced in magnetic materials [32, 33].

In one-dimensional materials, of particular interest in this work, photo-induced dynamics have been measured in Refs. [24, 28]. At low photo-doping density, Takahashi *et al.* [34] showed that there is a coexistence of the Mott insulator and free carriers. When photo-doping density exceeds $\sim 10\%$, the Mott gap is destroyed and a metallic state is formed. The time resolution of these experiments was restricted to ≥ 100 fs, which is insufficient to probe the dynamics of the formation of the metallic state. Recently, by using near-IR ultrafast pulses of duration < 10 fs, Wall *et al.* [35] have been able to single out coherent oscillations in the conductivity, occurring at high frequencies and associated with electronic correlations. These oscillations reveal important information on the nature of charge excitations in Mott insulators when both the on-site and inter-site Coulomb interaction is present, as we will discuss in the following.

While photo-doping often puts the system in a highly excited state in which the effect of correlation can be smeared, more recently much lower photon energies (in the THz range) are being used to selectively drive certain optical phonon modes. By strongly driving a selected vibrational mode it is possible to amplify its influence to a macroscopic level, thereby exposing information about the system. Once more, with ultra-fast probes these phenomena can be tracked on their fundamental timescales. This technique has been used, for example, to control metal-to-insulator transitions [36, 37, 38] and to induce superconductivity [39].

1.3 Model Hamiltonians

So far, we have mostly reviewed sophisticated experimental techniques, but very little has been mentioned about theoretical models. An exact description of complex systems is practically impossible, and effective Hamiltonians play a central role in understanding experimental observations.

Hubbard Hamiltonians [15, 40] are believed to capture the essential features of strongly-correlated-electron transport [41]. However, being an effective, low-energy theory, the Hubbard model accounts for coupling of the electrons with other degrees of freedom only through renormalized kinetic and interaction terms. Whilst making the problem manageable, the drawback is that neglecting degrees of freedom obscures the contributions of individual microscopic degrees of freedom.

The main results of this thesis are closely related to the investigation of model Hamiltonians, aimed to bridge the gap between simplified theoretical models and complex pump-probe experiments. From one side, we want to extend existing theoretical descriptions to take into account complex phenomena and make explicit the contributions of individual degrees of freedom; on the other hand, we wish to find a material that allows the maximum possible control, while still showing strongly correlated electron physics. We also wish to expose as much as possible the general physics which is not material specific. We believe the use of accurate effective Hamiltonians is a necessary part of a theory capable of accurately predicting and explaining the behavior of complex materials.

1.3.1 Correlated-electrons physics in optical lattices

A great help in our physical intuition of solid state systems may come by extending concepts used in the study of ultra-cold quantum gases [42, 43]. Most of the non-equilibrium phenomena described so far, in fact, are explained by underlying models showing a striking similarity with the ones that are being realized with cold atomic gases in optical lattices [44, 45, 46, 47]. Amazingly, despite being a completely different class of systems, this similarity provides an ideal realization of many-body lattice models and allows almost perfect control of microscopic parameters, (currently) impossible in electron systems. Cold atoms systems are especially convenient as quantum simulators especially because of the following reasons: (a) the length of their timescales for temporal evolution, which is orders of magnitude longer (s - ms) with respect to that for correlated electron systems (ps - fs); and (b) their almost perfect isolation from the environment on the timescale of typical experiments. In Tab. 1.1 we compare the most relevant time and energy scales for cold-atoms and condensed matter experiments. It is noteworthy to notice that the ratio between the energy of motional excitation of the electronic states, E, and the temperature, $k_B T$, is comparable for cold-atom and condensed matter systems at room temperature, while being order of magnitude apart for a cooled condensed matter systems (CMS). This suggests that the parallel works better in the former case.

Table 1.1: Relevant time and energy scales for experiments performed on cold-atoms and condensed-matter systems.

	Atoms	CMS	CMS cooled
Experiment time	s-ms	ps-fs	ps-fs
Energy $E/\hbar$	Hz - kHz	THz	THz
Temperature T	nK	300 K	mK
Ratio $E/K_B T$	1 - 10	1 - 10	10^4 - 10^6

Among the examples of the usefulness of this approach, it is instructive to mention the dynamics of doubly occupied sites (or doublons). In fact, doublons generated by periodic modulation of an optical lattice [48] show the same behavior, and can be interpreted as, the number of excited carriers in a Mott insulator as a function of time after photo-excitation [24].

It is clear at this point that, to be able to make reliable predictions regarding non-equilibrium phenomena, an accurate knowledge of the microscopic parameters is highly desirable, along with the possibility of modifying the intrinsic properties of the compound one chooses to investigate. For cold atoms, these parameters can be computed from the laser potentials directly [4], while for solid state systems the task is much harder and they can only be inferred indirectly.

1.3.2 Complex organic materials

Organic conductors serve as ideal model compounds because of their versatility and the possibility for easy tuning of electronic properties. The correlation in the organics occurs between the delocalized electrons of the molecular orbitals forming the conduction band [49]. A general feature is the presence of different electronic phases and ground states, tuned by the degree of effective electronic correlation in the system. Moreover, the strong spatial asymmetry in the inter-molecular interactions is such that conduction happens along preferred directions. As a consequence, electron-electron interactions are weakly screened, and combined with electron-lattice coupling are fundamentally important in determining the electronic behavior.

We choose the organic one-dimensional Mott-insulator ET-F_2TCNQ as a prototypical system to investigate. The properties of this material, which are described in more detail in the following chapter, make it an ideal choice to study the ultrafast dynamics in 1D.

The methods developed in this thesis can be extended to address the role of vibrational, magnetic and electronic modes in any material the relevant physics of which is believed to be captured by a Hubbard-like Hamiltonian.

1.4 Thesis overview

The layout of this thesis is divided in two parts: in Part I we review the relevant theoretical models and experimental methods that will be used in Part II to formulate our results.

Part I is broken down as follows.

- In Ch. 2 we expand upon the properties of organic materials in general, and more specifically of ET-F_2TCNQ, in which electronic correlations play a crucial role. Subsequently, we introduce the Hubbard Model, since most of the theoretical original results in this work will have the Hubbard Hamiltonian as the starting point in both analytic and numerical calculations.

- In Ch. 3, we describe the response of a medium when irradiated with light within the framework of linear response theory. We detail the procedure to compute the optical conductivity by using the current-current correlation function for a one-dimensional Hubbard Model.

- In Ch. 4, we follow the work of Gebhard *et al.* [50] to obtain a analytic result for the optical conductivity of a system described by the Extended Hubbard Model, in the limit in which the local Coulomb interactions among the electrons greatly overcomes their kinetic energy.

At this point, we are now in place to present our novel physical contributions to the field in Part II.

- In Ch. 5 we study the ultrafast recombination of photo-excited holon-doublon pairs as a function of external pressure, which is used to tune the electronic structure. The next three chapters contain our theoretical and experimental interpretation of a vibrationally modulated Mott insulator.

- In Ch. 6 we obtain the so-called Dynamic Hubbard Hamiltonian from general consideration about electronic-vibration (vibronic) coupling.

- Then, in Ch. 7, we derive analytic results for the optical conductivity in the atomic limit. We additionally use the appropriate expressions to interpret the ultrafast response of ET-F_2TCNQ to mid-infrared optical pulses.

- To strengthen our claims, we combine the effective model derived in Ch. 5 to fit static optical conductivity measurements, with the time-dependent U-modulation that originates in the Dynamic Hubbard Model of Ch. 6. The ensuing theory is used to describe the results obtained by driving the system with phase-locked (i.e. kept to a fixed value) vibrational excitations.

- Finally, in Ch. 9 we study the effects of vibrational driving on the spin degrees of freedom. To describe the low-energy physics for a system not at half-filling, we start from a strong coupling expansion of the Dynamic Hubbard Model and obtain a version of the $t-J$ model that includes a coupling to local vibrations. We show that the vibrational driving reduces the hopping amplitude but does not change the spin exchange interaction strength. As a consequence, we propose it as a tool to transiently (for as long as the driving is on) induce magnetic ordering in an otherwise non-magnetic complex material.

Part I

Background

Chapter 2

Strongly correlated physics in Organic Materials

Low-dimensional organic compounds are a relatively young class of materials that show a rich variety of properties, such as unconventional superconductivity, charge or spin density waves, and charge or magnetically ordered states.

The first part of this chapter gives an overview on organics in general, with focus on a one-dimensional salt. In the second part, we discuss the fundamental theoretical model in the physics of strongly correlated electrons: the Hubbard model (HM).

2.1 Organic molecular salts

Organic solids are compounds that have carbon, C, as main constitutive element. The free carbon atom has electronic configuration $1s^2 2s 2p^3$, but when bound in a material the electronic configuration is rather $1s^2 2s^2 2p^2$, and thus its valence is four. When two carbons are bound together, they form a double bond ($C = C$), with sp^2 hybridization. Three pairs of valence orbitals, the $2s$ and two $2p$ orbitals, combine into degenerate orbitals lying in the same plane of the two carbon atoms. They are disposed at an angle 120° relative to one another. The chemical bonds formed in this way are called σ bonds and are localized between the two bonding C atoms.

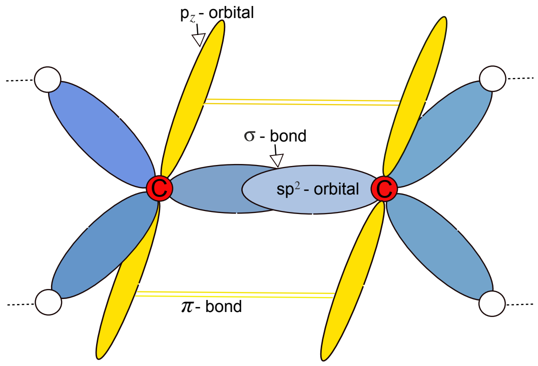

Figure 2.1: Molecular configuration in which each carbon atom is sp^2-hybridized. In this way sp^2-orbitals are generated (three for each carbon atom). One sp^2-orbital of each carbon atom by overlapping forms a sigma bond between carbon atoms. Remaining two sp^2-orbital of each atom overlap with s-orbital of the external atoms (e.g. hydrogen in the case of ethene) to produce four sigma bonds. p_z un-hybrid orbital of each carbon atom by the parallel overlapping form a π-bond between two carbon atoms.

The remaining $2p$ orbital, on the contrary, remains unchanged and is directed perpendicular to the plane of the sp^2 orbitals (and thus to the plane of the carbon atoms). By overlapping with other p orbitals of neighboring atoms, an additional π bond is created. As a consequence, we have a delocalized density of electrons above and below the plane in which the carbons are disposed, as shown in Fig. 2.1.

The π bonds are much weaker then the σ ones, and therefore the lowest electronic excitations are those of π electrons. Moreover, these are exactly the orbitals that determine the intermolecular van der Waals interactions. The Van der Waals force is based on (weak) dipole forces between neutral molecules with fully occupied molecular orbitals. It has a very short range and it is mainly responsible for the cohesion within molecular solids. This has important consequences that make the organics peculiar and different from other solids. First of all, the molecular dimensions and the characteristic intra-molecular frequencies of the free molecules are only slightly modified when they are held together to form a material. Secondly, it is relatively simple to produce materials

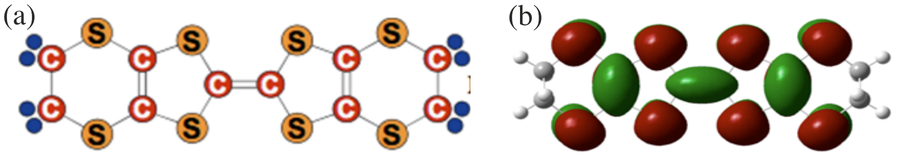

Figure 2.2: (a): BEDT-TTF (ET) molecule. (b): a depiction of the charge density in the valence orbital for BEDT-TTF, calculated with the Gaussian03 code [52].

with low impurity and defect concentration, as well as to modify their properties with minor chemical changes [49].

Over the past decades, a large variety of organic compounds have been synthesized, with very different properties. A comprehensive review of their characteristics goes beyond the objectives of this thesis, and we refer the reader to the excellent books of Schwoerer [49], or Barford [51]. We are rather going to focus on one specific variety, namely the donor-acceptor class, in which a positively-charged ion transfers charge to a negatively-charged one. For this reasons they are also called *charge-transfer* (CT) materials. By partially (or completely) transferring the charge, the compounds are stabilized. The fraction of charge transfer is measured by the parameter δ, e.g., $\delta = 0.5$ means that one-half charge per molecule is transfered, or alternatively a hole charge every second molecule. Typically, CT crystal are arranged in such a way that donors and acceptors are disposed in separate stacks. Conductions happens along the stacks composed of the donor molecules, that are the basic structural unit. Among these, a special place is undoubtedly occupied by the bis(ethylendithyo) - tetrathiafulvalene (BEDT-TTF, or ET) molecule.

Before specializing in Sec. 2.1.2 to the compound on which all the experimental work reported in this thesis was performed, it is worth to mention some of the other materials of which the ET is the fundamental structural unit. This highlights the fact that the results reported in the results' chapters are not specific to the investigated compound.

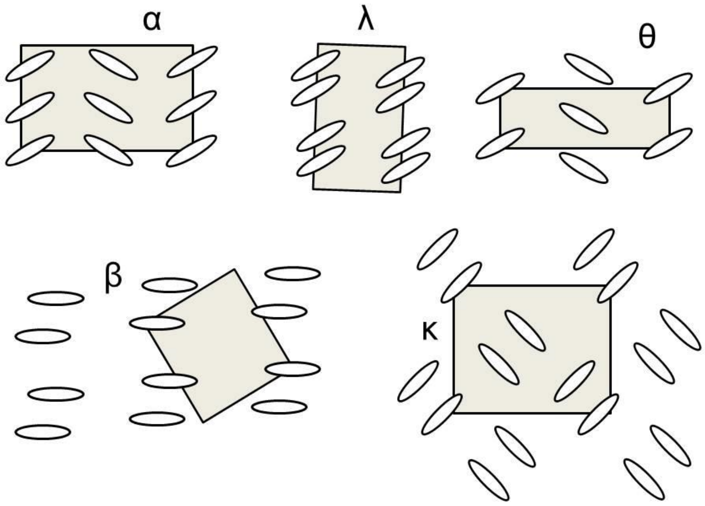

Figure 2.3: Schematic view of the molecular arrangement of ET molecules within the conducting plane for different structures.

2.1.1 The ET

Since the discovery of superconductivity in its iodite salts [53, 54, 55, 56], the ET molecule, shown in Fig. 2.2 along with its charge density in the valence orbital, has been arguably the most important structure in the field of organic superconductors. The ET molecules as cations form salts with a larger number of monovalent anions X of composition $(\mathrm{ET})_m\mathrm{X}_n$. Since the first observation of superconductivity, a lot of work has been performed on these compounds, showing that they exhibit some of the same interesting physics as the cuprates family [57].

Akin to the other famous family of organic superconductors, the Bechgaard salts [58, 59, 60], most of them are prepared by electrocrystallization. In this process, the donor molecules are oxidized at one electrode and then crystallize with the monovalent anions present in the electrolyte. ET is a large planar molecule and the different possible packing patterns are denoted by different Greek letters (e.g. $\alpha, \gamma, \kappa, \ldots$). Some of these are shown in Fig. 2.3. Superconducting and conducting ET donor-acceptor salts have the stoichiometry $(\mathrm{ET})_2\mathrm{X}$, where

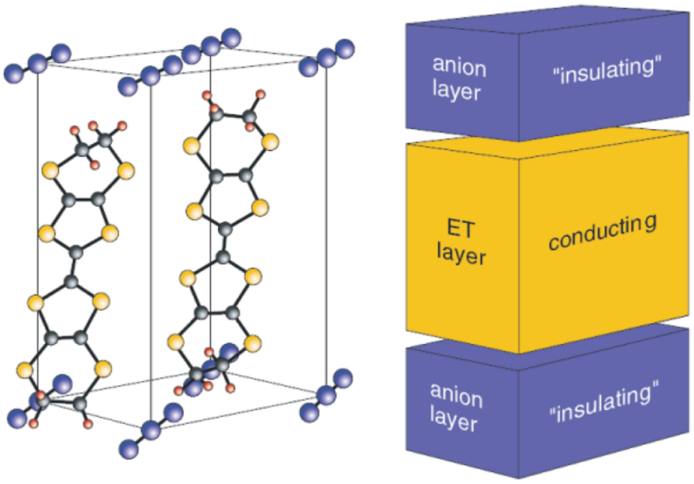

Figure 2.4: Layered structure of the ET charge transfer salts. The quasi two dimensional conducting layers are separated by the insulating anion layers.

X is the monovalent anion (e.g., X=Cu[N(CN)$_2$]). The family κ-(ET)$_2$X is extremely interesting because it has a very rich phase diagram as a function of pressure, temperature, and anion [61, 62, 63]. Moreover, if one replaces pressure with doping, the diagram is quite similar to that of the cuprates.

In general, the anion layer donates electrons to the ET molecules, charging them up to approximately $+0.5e$ per molecule; consequently, the conductance band is partly filled and the material is metallic. The metallic properties are observed only within the layer, in the perpendicular direction the insulating anion layer blocks charge transfer, as shown in Fig. 2.4. For that reason these materials are called two-dimensional conductors.

Despite being by far the most studied, structures with two dimensional electronic character are not the only possible ones. On the contrary, very interesting physics emerges in compounds with one-dimensional conducting properties, such as bis(ethylendithyo) - tetrathiafulvalene - difluorotetracyano - quinodimethane, (ET-F$_2$TCNQ). Its properties are crucial for this work, and are the subject of next section.

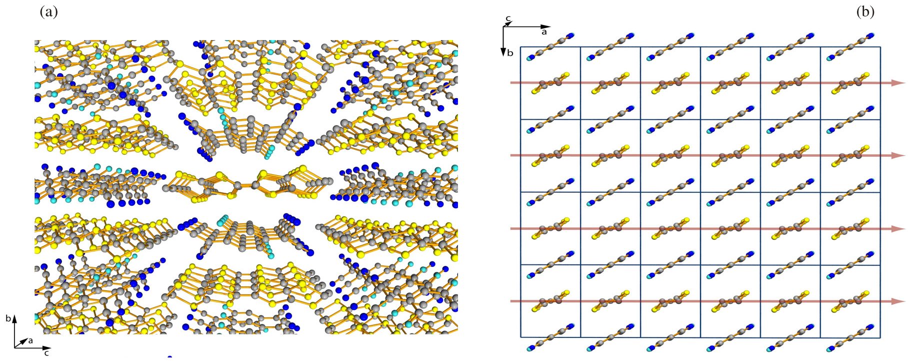

Figure 2.5: View of the crystal structure of ET-F_2TCNQ in (a) 3D along the *a*-axis, and (b) along the *c*-axis. Molecular planes of donors and acceptors stack on top of each other along the *b*-axis while donors are arranged side by side along *a*-axis. Conduction happens along the *a*-axis and is one-dimensional.

2.1.2 ET-F_2TCNQ

ET-F_2TCNQ is a one-dimensional organic Mott insulator (MI). F_2TCNQ is the acceptor ion and ET the donor. Acceptors of F_2TCNQ are isolated and the CT interaction exists only between neighboring donors. The crystal is orthorhombic with P2/m space group symmetry[1], and the dimensions of the unit cell are $a = 5.79$ Å, $b = 8.201$ Å and $c = 1186.34$ Å. The ET and F_2TCNQ molecules are alternatively stacked on top of each other along the *b*-axis, and are arranged side-by-side along the *c*-axis (see Fig. 2.5). They have a greater inter-molecular separation than most other charge transfer solids [64] and along the *a*-axis, the donors and acceptors lie in single chains with the distances between ET molecules being shorter than twice their van der Waals radius.

By analyzing the carbon double bond length in the ET molecules, one finds that the charge transfer between ET and F_2TCNQ is complete, i.e., the donor charge is completely localized on the acceptor molecule ($\delta = 1$). As a consequence, the ET chain has one valence π electron per molecular site: this is usually referred to as a half-filled system. The conduction happens along the ET molecules (the structure and the charge density of which are shown in Fig. 2.2(a)

---

[1] 2/m indicates the monoclinic-prismatic class of the crystal shape, and P stands for primitive lattice in opposition to C, the face centered lattice.

and (b), respectively), and is completely one-dimensional (Fig. 2.5).

Generally speaking, electron-lattice (e-l) interaction plays a significant role on the charge dynamics in one-dimensional MI [24]. In a one-dimensional chain, if an electron-phonon interaction is introduced and the chain is distorted to shift every other atom, the unit cell doubles in size, halving the Brillouin zone. The previously metallic chain turns into a band insulator, and a gap opens at the new Brillouin zone boundaries, $k = \pi/2a$. The reduction in energy at the Fermi surface turns out to be greater than the elastic energy required for the lattice distortion [65, 66]. However, ET-F_2TCNQ is special in this respect. The Spin Peierls (SP) instability is suppressed by the two-dimensionality of the ET sheet and the compound shows no SP transition even at low temperature. However, an antiferromagnetic state perpendicular to the mixed stack of ET molecules forms below the Neél temperature $T_N = 30$ K [67].

Even though the electrons are only weakly coupled to collective modes of the lattice (phonons), intra-molecular vibrations are likely to play an important role. The vibration frequencies associated with molecular vibrations are usually at high-frequencies ($\sim 10^3$ cm^{-1}) with respect to the ones of the phonon modes [49] (typically $<10^2$ cm^{-1}). In [68], a complete analysis of the vibrational dynamics of the ET molecule has been performed through first-principle calculations. It has also been shown that some modes are sensitive to the ionicity of the specific molecule.

This is indeed a crucial point that has to be taken into account in the description of molecular MI, and that can help to shed light on some features of the underlying microscopic model describing them.

2.1.3 Selective vibrational excitation

As suggested above, we expect the vibrational modes to play an important role in explaining the electronic properties of complex solids. In the introduction, we listed a number of methods that have been used to control specific properties of complex materials.

In this section we specialize on a novel way of controlling a phase of matter, involving coherent excitation of a specific vibrational mode of the lattice. Mode-selective modulation spectroscopy allows us to strongly drive a selected

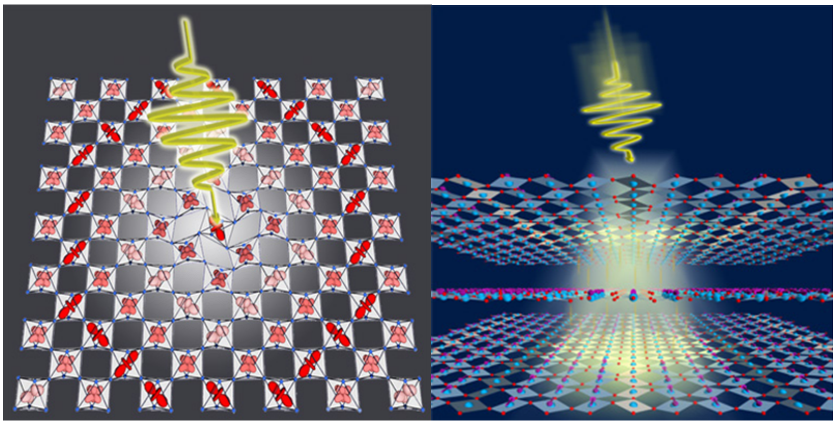

Figure 2.6: Schematic view of vibrational excitation of a manganite by angle distortion.

vibrational mode and amplify its influence to a macroscopic level.

This technique is used in the experiments reported in Ch. 7 and Ch. 8 to investigate the role of Coulomb interaction parameters in the Hubbard Model. It is a powerful and versatile tool, that allowed, for example, Tobey *et al.* [38] to succeed in inducing an insulator-to-metal transition in a manganite. As shown in Fig. 2.6, the bandwidth may be controlled through the creation of a Mn-O bonding angle distortion. Another more recent example is the experiment performed by Fausti *et al.* [39], that showed that the same phonon-pumping technique applied to a copper oxide can induce a superconducting phase.

As we are going to demonstrate in detail in Ch. 7, when applied to the organic salt ET-F_2TCNQ, mode selective driving elevates the chosen modes' contribution, and "deconstructs" the HM by requiring that the vibrations quantum mechanical degree of freedom is explicitly accounted for in the Hamiltonian. Even if we are going to extensively discuss the details in the following, it is instructive to use it as an example here and provide some details on how this approach is implemented. We are going to selectively drive two vibrational modes with different symmetry: an infrared (IR) active asymmetric mode at $\sim 10\ \mu$m wavelength, and a Raman active symmetric mode at $\sim 6\ \mu$m. The situation is represented in Fig. 2.7.

The chain of ET molecules is strongly driven causing the individual molecules

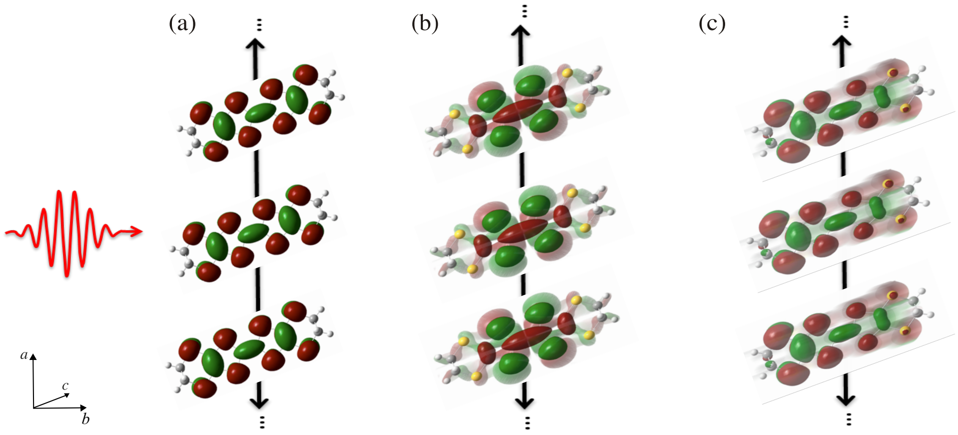

Figure 2.7: The chain of ET molecules are shown individually aligned along the b-axis forming a chain in the a-axis. Light polarized along the a-axis probes the reflectivity of the system as a function of the frequency [2]. The charge density in the valence orbital calculated with Gaussian03 code is shown in (a) non vibrationally excited chain; (b) chain excited with a Raman active vibrational mode; (c) chain excited with IR active vibrational mode.

to oscillate in tandem. The effect on the charge density of the valence orbital is depicted in Fig. 2.7(b) and Fig. 2.7(c) for Raman and IR vibrational modes, respectively. In the pump-probe experiment on ET, the pump has been tuned resonantly on the vibrational modes, and the photo-induced reflectivity changes have been probed at several time delays in a wide frequency range from the near-infrared (NIR) to the Terahertz (THz), as shown in Fig. 2.8. The experiment then examined the reflectivity response on ultrashort timescales, the results of which will be discussed extensively in Ch. 7.

So far, the Hubbard Hamiltonian has been mentioned several times as one of the key theoretical models to study complex materials. Nevertheless, it hasn't been introduced formally yet. The remaining of this chapter is dedicated to this purpose.

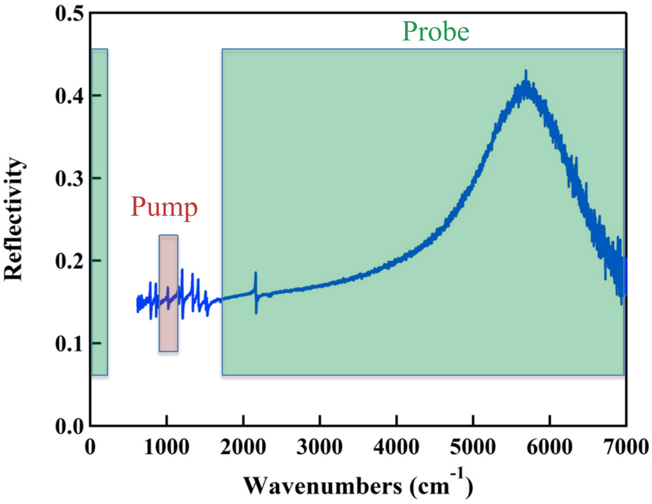

Figure 2.8: Pump probe experiment. The mid-infrared (MIR) (i.e. electromagnetic radiation with frequency range between 37 – 100 THz) pump has been tuned resonantly on the vibrational modes, and the photoinduced reflectivity changes have been probed at several time delays in a wide frequency range from the NIR (frequency range between 214 – 400 THz) to the THz.

2.2 The Hubbard Model

The physics of the HM is of interest here for two reason. Firstly, the Mott insulating behavior underpins the physics of one-dimensional MI, realized in ET-F_2TCNQ. The Mott insulating phase is only obtained if one allows strong interactions, as described by the Hubbard model. Secondly, within this model it is possible to investigate metallic or insulating behavior, the metal-insulator transition, and superconductivity depending on the electronic kinetic energy, band filling, dimension, and obviously, on the parameters that quantify the electronic correlations. As a consequence, all the results presented in the following have a much broader applicability than the specific compound we set about to study.

The HM was originally introduced to describe transition metals and rare-earth metals, both composed of atoms with very localized valence electrons (d or f shells). Owing to the very high degree of localization, the local value of the Coulomb interaction is considered to be completely dominant with respect to the long range contributions. For this reason Hubbard, in a milestone paper [40], wrote the model Hamiltonian as

$$\hat{H}_{\mathrm{HM}} = -t \sum_{\langle ij \rangle, \sigma} \hat{c}^{\dagger}_{i,\sigma} \hat{c}_{j,\sigma} + U \sum_{j} \hat{n}_{j,\uparrow} \hat{n}_{j,\downarrow} \equiv \hat{H}_t + \hat{H}_U, \tag{2.1}$$

that still today carries his name. The first term alone is the so-called tight-binding model and describes the kinetic energy of the electrons (as explained in more detail in Appendix 2.A.1), $\hat{c}^{(\dagger)}_{i,\sigma}$ is the annihilation (creation) operator for an electron at site i with spin $\sigma = \uparrow, \downarrow$, and $\hat{n}_{i,\sigma} = \hat{c}^{\dagger}_{i,\sigma} \hat{c}_{i,\sigma}$ is the number operator. The symbol $\langle ij \rangle$ indicates that the sum is restricted to nearest-neighbor sites only. In Appendix 2.A, we start from the general many-body Hamiltonian for electrons in a lattice and obtain the HM explaining the various approximation that lead to Eq. (2.1).

The value of the transfer integral t, Eq. (2.13), is given by the overlap of onsite electronic wave functions connected by the potential generated by the lattice, and dictates how 'easy' it is for electrons to tunnel between neighboring sites. The strength of the Coulomb interaction is restricted to electrons on the same lattice sites (see Eq. (2.15) in Appendix 2.A.2). In the Hamiltonian of Eq. (2.1) it is assumed we have only a single, isotropic, atomic orbital.

The two parameters, t and U, express two competing effects. This is seen by considering the two extreme limits of $t \gg U$ and $t \ll U$. In the former case, the electrons are delocalized throughout the crystal with well defined k-vectors which form bands; in the latter, the Coulomb repulsion prevents electrons from moving onto occupied lattice sites leading to charge localization.

While the interaction causes the system to be an insulator when the number of electrons N equals the number of lattice sites M (half-filling), as the filling is either reduced or increased, the system becomes metallic-like, as there are more vacant sites onto which electrons/holes can hop [17]. For transition metal ions with an occupation n of the d-levels, the hopping transition is of the type $d_i^n d_j^n \rightarrow d_i^{n-1} d_j^{n+1}$, thereby creating a double occupancy (doublon) on site j and a hole (holon) on site i. The energy cost of this transition, U, can be measured by comparing the difference between the ionization energy, I, and the electron affinity, E, as

$$U = I - E.$$

The density of states for charge excitations displays two bands separated by the Mott-Hubbard gap E_g, which is defined as the jump in the chemical potential, μ, at half-filling

$$\begin{aligned} E_g &= \mu^+(N = M) - \mu^-(N = M), \\ &= [E(N = M + 1) - E(N = M)] - [E(N = M) - E(N = M - 1)]. \end{aligned}$$

The charge gap separates many-particle states to which electrons can be removed (Lower Hubbard Band, LHB) from states to which electrons can be added (Upper Hubbard Band, UHB). Despite being called in the same way, in this context the word “bands” has a very different meaning from the usual single-particle valence and conduction bands. Hubbard bands also have very different properties from the Bloch bands. For example, as the number of electron changes, the width of both band and gap changes accordingly. For $M \rightarrow \infty$, E_g is also equal to the optical gap, defined as the energy threshold of the lowest band in the optical spectrum.

An exact expression for E_g can be found in 1D using the Bethe Ansatz [69]:

$$E_g = \frac{16t^2}{U} \int_1^\infty \frac{\mathrm{d}y \sqrt{y^2 - 1}}{\sinh(2\pi t y/U)},$$

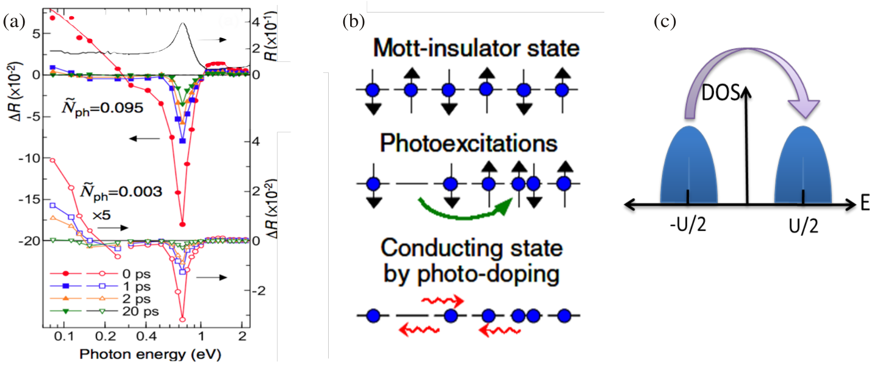

Figure 2.9: (a) Photoinduced reflectivity changes of ET-F_2TCNQ [Taken from [27]]. (b) Schematic explanation of the photoexcitation process and consequent photo-excited state. (c) Excitation effects on the Density of States.

that for strong coupling, $U \gg t$, becomes

$$E_g = U - 4t + \frac{8t^2 \ln 2}{U}.$$

Clearly, optical absorption is only possible if $\omega \geq E_g$, therefore one might expect it to show the signature of a broad band-to-band transition for $U - 4t \leq \omega \leq U + 4t$ [70, 71]. By photo-exciting the system, charges can be moved to neighboring sites, i.e., particles are excited from the LHB to the UHB. This way, a transient conducting state is created. Experimentally, this has been realized in ET-F_2TCNQ by Okamoto *et al.* [27] who have measured the changes in reflectivity obtained by photo-exciting the system with NIR pulses across the Mott gap (Fig. 2.9).

It is important to mention that in some materials the gap energy is found to be significantly lower then expected, suggesting that the electron transfer does not happen between neighboring transition metal ions, but rather between neighboring cations and anions [72]. Such a transition can be represented as $d_i^n \to d^{n+1}\underline{L}$, where $\underline{L}$ corresponds to a hole in the anion valence band, with the transfer process requiring a Δ amount of energy. These systems, referred to as *charge-transfer insulators*, can be regarded as impurity doped semiconductors with the d-band acting as the impurity band and transport is due to holes in the oxygen band.

In Fig. 2.10 we schematically compare the band structures for a Mott and charge-transfer insulators, and indicate the lowest energy transitions for each case. However, charge-transfer insulators have many properties similar to those of MI [73], and very often one also uses for their description the Hubbard model Eq. (2.1).

2.2.1 The Extended Hubbard Model

As detailed in Appendix 2.A, the HM is derived from a series of approximation on the general many-body Hamiltonian describing the behavior of electrons and nuclei in a solid. It is assumed that the on-site Coulomb interaction, parametrized by U, and the kinetic energy, t, are enough to describe the low energy physics. All the other terms are considered the be irrelevant. Sometimes, though, this approximation is too crude, and it results to be necessary to take into account also the inter-site Coulomb repulsion. The matrix element expressing the strength of this term is usually called V. The resulting Hamiltonian is known as Extended Hubbard Model (EHM):

$$\begin{aligned}\hat{H}_{\mathrm{EHM}} &= -t\sum_{\langle ij\rangle}\hat{c}^{\dagger}_{i,\sigma}\hat{c}_{j,\sigma} + U\sum_{j}\hat{n}_{j,\uparrow}\hat{n}_{j,\downarrow} + V\sum_{\langle ij\rangle}\hat{n}_{j}\hat{n}_{j+1}, \\ &\equiv \hat{H}_t + \hat{H}_U + \hat{H}_V.\end{aligned} \tag{2.2}$$

The electronic properties of Eq. (2.2) are substantially different from the ones of the original HM. Arguably, the most interesting effect arising from the V term is the creation of excitonic states. In the context of complex materials, these consist of holon-doublon pairs, bound by an energy V.

In low dimensions, the additional term is needed to interpret the ground state phase diagram of systems like the two-dimensional quarter-filled systems [74, 75], in which the sites are occupied just by half an electron in average. Even more interestingly, Wall *et al.* [76] have shown that a $\hat{H}_V$ term is necessary to explain the nature of charge excitations in MI in 1D. Using NIR pulses, they have measured coherent electronic excitations in ET-F_2TCNQ and singled out coherent oscillations in the conductivity. Time-resolved spectroscopy reveals the quantum interference between two different excitation paths, those between excitons and free holon-doublon states.

Non-local interactions allow us to study general features of doped systems like copper-oxide materials [77, 78, 79], high-temperature superconductors [80,

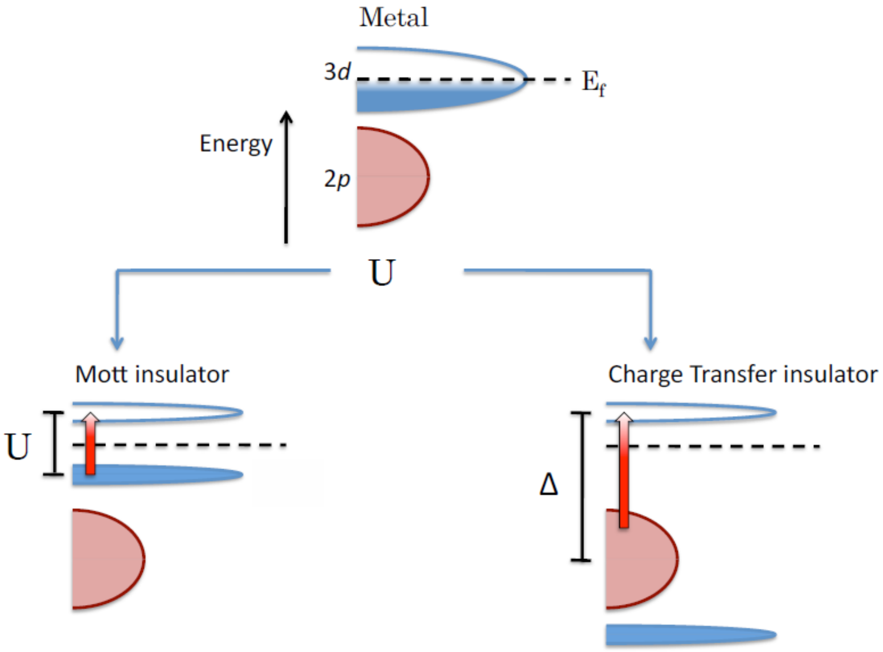

Figure 2.10: Band diagram of a transition metal compound, consisting of a partially full transition metal d-level and a full $2p$ anion band. When $t \gg U, \Delta$ the Hubbard bands are not split resulting in the Fermi level lying in the middle of the d-band. When $U \gg t$ the $3d$ band is split into the upper and lower Hubbard bands resulting in an insulator. If $U < \Delta$ the material is a Mott insulator and excitations correspond to electrons and holes in the upper and lower Hubbard bands respectively. Whereas, if $U > \Delta$, the anion valence band lies closer to the Fermi level and excitations correspond to electrons in the upper Hubbard band and holes in the anion valence band. This material is a charge-transfer insulator.

81], manganese compounds [82], and to describe charge ordering [83, 84, 85, 86] and phase separation [87, 88]. Our one-dimensional compound has non-negligible non-local interactions, and these make it ideal to explore properties which are at the heart of some of the most interesting phenomena that happen in two- or three-dimensions.

2.A Strongly correlated many-body systems

The aim of this appendix is to derive the Hubbard model. We are going to focus on the approximations that will lead, in Sec. 2.A.2, from the general many-body Hamiltonian, to Eq. (2.1). By using an approximate set of wave functions located at each atomic site (Wannier functions), we will also obtained the well-known tight-binding model. This arises in the limit of $t \gg U$, and it will be used in Ch. 5 to compare the relaxation of electronic excitations in a strongly-correlated material against the ones in metals or semiconductors.

Molecular solids are systems of molecules and electrons arranged in a three-dimensional crystalline structure. Due to the enormous mass difference between electrons and molecules, the latter are usually assumed to be static (Born-Oppenheimer approximation) and the dynamics of the electronic behavior is governed by the Hamiltonian

$$H = \sum_{j=1}^{N} \Big(\frac{\mathbf{p}_j^2}{2m_e} + V_I(\mathbf{r}_j) \Big) + \sum_{1 \le i \le j \le N} V_C(\mathbf{r}_j - \mathbf{r}_j), \tag{2.3}$$

where m_e and N are the mass and the total number of the electrons, respectively, $V_I(\mathbf{r})$ is the periodic potential of the molecules, $V_C(\mathbf{r}) = \mathrm{e}^2/|\mathbf{r}|$ is the Coulomb repulsion among electrons

Historically, a very successful approach to tackle this formidable problem has been the so-called “mean-field” single particle approximation, performed by adding an auxiliary potential, $V_A(\mathbf{r})$, to the one-particle part of the Hamiltonian and then subtracting it to the two body-part as

$$H = \sum_{j=1}^{N} \Big(\frac{\mathbf{p}_j^2}{2m_e} + V(\mathbf{r}_j) \Big) + \sum_{1 \le i \le j \le N} U(\mathbf{r}_i, \mathbf{r}_j),$$

where the effective one- and two-body potentials, $V(\mathbf{r})$ and $U(\mathbf{r}_1, \mathbf{r}_1)$, are

$$\begin{aligned} V(\mathbf{r}) &= V_I(\mathbf{r}) + V_A(\mathbf{r}), \\ U(\mathbf{r}_1, \mathbf{r}_2) &= V_C(\mathbf{r}_1 - \mathbf{r}_2) - \frac{1}{N-1} \big(V_A(\mathbf{r}_1) + V_A(\mathbf{r}_2) \big). \end{aligned}$$

The auxiliary potential is chosen in such a way that the matrix elements of the effective two-body potential $U(\mathbf{r}_1, \mathbf{r}_2)$ between the eigenstates of the one-particle Hamiltonian,

$$h_1(\mathbf{r}, \mathbf{p}) = \frac{\mathbf{p}^2}{2m_e} + V(\mathbf{r}), \tag{2.5}$$

become small. The idea behind this is that, if one inserts an additional electron in a system that has a large number of electrons N, the attractive ionic potential it will feel will be screened by the electrostatic potential which stems from the ground state density of the other electrons.

The total Hamiltonian can be studied by using the eigenstates of the single-particle Hamiltonian, h_1. The single-particle potential is periodic, i.e., $V_I(\mathbf{r}) = V_I(\mathbf{r}+a)$ (a is the lattice spacing), thus the eigenstates of h_1 are required to be eigenstates of the lattice translation operator $\hat{T}f(\mathbf{r}) = f(\mathbf{r}+a)$. The Bloch's theorem [13] states that they are of the form

$$\varphi_{\alpha\mathbf{q}}(\mathbf{r}) = \mathrm{e}^{i\mathbf{k}\cdot\mathbf{r}} u_{\alpha q}(\mathbf{r}), \quad \text{with} \quad u_{\alpha q}(\mathbf{r}) = u_{\alpha q}(\mathbf{r}+a),$$

i.e., plane-waves with wave-vector q modulated by a function, $u_{\alpha q}(\mathbf{r})$, with the same periodicity of the underlying lattice. α is a band index, while q is called quasi-momentum and has a finite range of values called the first Brillouin zone (BZ). The functions $\varphi_{\alpha\mathbf{q}}(\mathbf{r})$ are eigenfunctions of the single-particle Hamiltonian, h_1,

$$h_1 \varphi_{\alpha\mathbf{q}}(\mathbf{r}) = \epsilon_{\alpha\mathbf{q}}(\mathbf{r}). \tag{2.6}$$

Eq. (2.6) determines the band structure [13].

These states, known as Bloch states, are typically functions that extend over the entire system. To describe local interactions, it is convenient to use a complementary single-particle basis for which the states are spatially localized on each lattice site, at a distance R_j from the origin. This is the Wannier basis [13]. Formally, we write $\phi_\alpha(\mathbf{r}-\mathbf{R}_j)$, where $\phi_\alpha(\mathbf{r})$ is defined as

$$\phi_\alpha(\mathbf{r}) = \frac{1}{\sqrt{M}} \sum_{\mathbf{k}} \mathrm{e}^{i\mathbf{k}\cdot\mathbf{r}} \varphi_{\alpha\mathbf{k}}(\mathbf{r}), \tag{2.7}$$

and M is the number of lattice sites. The wave functions in Eq. (2.7) are the lattice analogous of the atomic states and are mutually orthogonal for different bands, α, and site indices, j. The Bloch states can be re-obtained from Wannier states by Fourier inversion:

$$\varphi_{\alpha\mathbf{k}}(\mathbf{r}) = \frac{1}{\sqrt{M}} \sum_{j} \mathrm{e}^{i\mathbf{k}\cdot\mathbf{R}_j} \phi_\alpha(\mathbf{r}-\mathbf{R}_j). \tag{2.8}$$

At this point, one can introduce creation and annihilation operators, $\hat{c}^\dagger_{\alpha\mathbf{k},\sigma}$ and

$\hat{c}_{\alpha\mathbf{k},\sigma}$. Correspondingly, their Fourier transforms are

$$\hat{c}^{\dagger}_{\alpha j,\sigma} = \frac{1}{\sqrt{M}} \sum_{\mathbf{k}} \mathrm{e}^{-i\mathbf{k}\cdot\mathbf{R}_j} \hat{c}^{\dagger}_{\alpha\mathbf{k},\sigma}, \quad \hat{c}_{\alpha j,\sigma} = \frac{1}{\sqrt{M}} \sum_{\mathbf{k}} \mathrm{e}^{-i\mathbf{k}\cdot\mathbf{R}_j} \hat{c}_{\alpha\mathbf{k},\sigma} \tag{2.9}$$

The creation operator $\hat{c}^{\dagger}_{\alpha\mathbf{k},\sigma}$ generates the space of states of the HM by acting on the vacuum state $|\mathrm{vac}\rangle$. These are canonical Fermi operators satisfying the standard anti-commutation relations

$$\{\hat{c}^{\dagger}_{\alpha j,\sigma}, \hat{c}^{\dagger}_{\alpha k,\sigma'}\} = \{\hat{c}_{\alpha j,\sigma}, \hat{c}_{\alpha k,\sigma'}\} = 0, \quad \{\hat{c}_{\alpha j,\sigma}, \hat{c}^{\dagger}_{\alpha k,\sigma'}\} = \delta_{jk}\delta_{\sigma\sigma'},$$

for $j,k = 1,\dots,M$ and $\sigma,\sigma' =\uparrow,\downarrow$. One can express the field operator which creates an electron of spin σ at position $\mathbf{r}$, Eq. (2.8), as

$$\hat{\Psi}^{\dagger}_{\sigma}(\mathbf{r}) = \sum_{\alpha\mathbf{k}} \varphi^{*}_{\alpha\mathbf{k}}(\mathbf{r}) \hat{c}^{\dagger}_{\alpha\mathbf{k},\sigma} = \sum_{\alpha j} \phi^{*}_{\alpha}(\mathbf{r}-\mathbf{R}_j) \hat{c}^{\dagger}_{\alpha j,\sigma}. \tag{2.10}$$

Here * stands for complex conjugation. The general formula [89] relating first and second quantized formalisms

$$\begin{aligned} \hat{H} = {} & \sum_{\sigma=\uparrow,\downarrow} \int \mathrm{d}\mathbf{r} \hat{\Psi}^{\dagger}_{\sigma}(\mathbf{r}) h_1 \hat{\Psi}_{\sigma}(\mathbf{r}) \\ & + \tfrac{1}{2} \sum_{\sigma,\bar{\sigma}=\uparrow,\downarrow} \int \mathrm{d}\mathbf{r}_1 \, \mathrm{d}\mathbf{r}_2 \hat{\Psi}^{\dagger}_{\sigma}(\mathbf{r}_1) \hat{\Psi}^{\dagger}_{\bar{\sigma}}(\mathbf{r}_2) U(\mathbf{r}_1,\mathbf{r}_2) \hat{\Psi}_{\sigma}(\mathbf{r}_1) \hat{\Psi}_{\bar{\sigma}}(\mathbf{r}_2), \end{aligned} \tag{2.11}$$

enables us to express the Hamiltonian Eq. (2.3) in second quantized form in the basis of Wannier states:

$$\begin{aligned} \hat{H} = {} & \sum_{\alpha,i,j,\sigma} t^{\alpha}_{ij} \hat{c}^{\dagger}_{\alpha i,\sigma} \hat{c}_{\alpha j,\sigma} \\ & + \sum_{\alpha,\beta,\gamma,\delta} \sum_{i,j,k,l} \sum_{\sigma,\bar{\sigma}} U^{\alpha\beta\gamma\delta}_{ijkl} \hat{c}^{\dagger}_{\alpha i,\sigma} \hat{c}^{\dagger}_{\beta j,\bar{\sigma}} \hat{c}_{\gamma k,\bar{\sigma}} \hat{c}_{\delta l,\sigma}. \end{aligned} \tag{2.12a}$$

The hopping matrix elements, t^{α}_{ij}, and the interaction parameters, $U^{\alpha\beta\gamma\delta}_{ijkl}$, are:

$$t^{\alpha}_{ij} = -\int \mathrm{d}\mathbf{r} \phi^{*}_{\alpha}(\mathbf{r}-\mathbf{R}_i) h_1 \phi_{\alpha}(\mathbf{r}-\mathbf{R}_j), \tag{2.12b}$$

$$U^{\alpha\beta\gamma\delta}_{ijkl} = \int \mathrm{d}\mathbf{r}_1 \, \mathrm{d}\mathbf{r}_2 \phi^{*}_{\alpha}(\mathbf{r}_1-\mathbf{R}_i) \phi^{*}_{\beta}(\mathbf{r}_2-\mathbf{R}_j) U(\mathbf{r}_1,\mathbf{r}_2) \phi_{\gamma}(\mathbf{r}_2-\mathbf{R}_k) \phi_{\delta}(\mathbf{r}_1-\mathbf{R}_l). \tag{2.12c}$$

The Hamiltonian Eq. (2.12a) is completely equivalent to Eq. (2.3), but by choosing highly localized single-particle states, it may be rendered a model dominated by a few local terms. Any band α with energies

$$E_{\alpha\mathbf{q}} = \langle \varphi_{\alpha\mathbf{q}} | h_1 | \varphi_{\alpha\mathbf{q}} \rangle,$$

satisfying the condition that $E_{\alpha\mathbf{q}}$ is much bigger than the kinetic, potential, and thermal energy for all $\mathbf{q}$ will not contribute to the physics and can be ignored. If, in addition, the Fermi surface lies inside a single conduction band, it is reasonable to assume that the interesting physics happens in that band, while the main effect of the high energy bands is simply to change the hopping and interaction matrix elements of the electrons in the conduction band. This is the reason of the aforementioned single-band assumption in the Hubbard model. Thus, from this point on, we shall assume that these conditions hold and consequently drop the band indices.

2.A.1 The tight-binding model

The simplest model with the form of Eq. (2.11) is the so called tight-binding model [13] (or Hückel model in a chemistry context [90]). In this model one makes the approximation $U_{ijkl}^{\alpha\beta\gamma\delta} = 0$, therefore neglecting the interactions between electrons.

We take the basis to consist of orbitals centered on particular sites, an assumption that we will carry on throughout this thesis. Another common simplification arises by assuming that the two-center integrals, Eq. (2.12b), are only non-zero for electrons in the same or in neighboring orbitals, i.e.,

$$\begin{aligned} t_{j,j} \equiv -\epsilon_j &= \int \mathrm{d}\mathbf{r}\phi_\alpha^*(\mathbf{r}-\mathbf{R}_j)h_1\phi_\alpha(\mathbf{r}-\mathbf{R}_j). \\ t_{\langle i,j\rangle} \equiv t &= -\int \mathrm{d}\mathbf{r}\phi_\alpha^*(\mathbf{r}-\mathbf{R}_i)h_1\phi_\alpha(\mathbf{r}-\mathbf{R}_j), \end{aligned} \tag{2.13}$$

where $\langle ij\rangle$ indicates that the sum is over nearest-neighbors only. If we consider materials with only a single atomic species, $\epsilon_j = 0$, yielding

$$\hat{H}_{\mathrm{TB}} - \mu\sum_j \hat{n}_j = -t\sum_{\langle ij\rangle} \hat{c}_{i,\sigma}^\dagger \hat{c}_{j,\sigma} - \mu\sum_{j\sigma}\hat{n}_j,$$

where μ is the chemical potential. For a one-dimensional chain the sites have a natural ordering, thus the Hamiltonian may be written as

$$\hat{H}_{\mathrm{TB}} - \mu\sum_j \hat{n}_j = (\hat{c}_{j,\sigma}^\dagger \hat{c}_{j+1,\sigma} + \hat{c}_{j+1,\sigma}^\dagger \hat{c}_{j,\sigma}) - \mu\sum_{j,\sigma}\hat{n}_{j,\sigma}. \tag{2.14}$$

This model can be solved exactly by Fourier transform. By using the reciprocal space creation and annihilation operators (Eq. (2.9)), we obtain for Eq. (2.14)

$$\hat{H}_{\mathrm{TB}} - \mu \sum_j \hat{n}_j = \frac{1}{N} \sum_{jkk'\sigma} \hat{c}^{\dagger}_{k,\sigma} \hat{c}_{k',\sigma} \mathrm{e}^{i(k'-k)R_j} \left[-t(\mathrm{e}^{ik'a} + \mathrm{e}^{-ika}) - \mu \right],$$

Using the δ function property: $\delta(k-k') = 1/M \sum_j \mathrm{e}^{i(k-k')R_j}$, we finally obtain

$$\hat{H}_{\mathrm{TB}} - \mu \sum_j \hat{n}_j = \sum_{k,\sigma} \left[-2t\cos(ka) \hat{c}^{\dagger}_{k,\sigma} \hat{c}_{k,\sigma} - \mu \hat{c}^{\dagger}_{k,\sigma} \hat{c}_{k,\sigma} \right] = \sum_{k,\sigma} (\epsilon_k - \mu) \hat{c}^{\dagger}_{k,\sigma} \hat{c}_{k,\sigma},$$

where $\epsilon_k = -2t\cos(ka)$ is the dispersion relation. This equation is diagonal: it depends only on the number operator terms. The energy is the sum of ϵ_k for the $k\sigma$ occupied states.

Changes in the chemical potential move the Fermi energy up or down the band, and hence alter the number of electrons in the system. For an half-filled band $\mu = 0$: this is the case of interest in this thesis, and we will set $\mu = 0$ from now on.

2.A.2 The Hubbard Model

The single-band HM originates from Eq. (2.12a) when the interaction parameters cannot be neglected compared to the hopping matrix elements, and are short range. Specifically, the four-center integral Eq. (2.12c) is dominated by electrons in the same orbital,

$$U_{jjjj} \equiv U = \int \mathrm{d}\mathbf{r}_1\, \mathrm{d}\mathbf{r}_2 \phi_1^*(\mathbf{r}_1 - \mathbf{R}_j) \phi_1^*(\mathbf{r}_2 - \mathbf{R}_j) U(\mathbf{r}_1, \mathbf{r}_2) \phi_1(\mathbf{r}_2 - \mathbf{R}_j) \phi_1(\mathbf{r}_1 - \mathbf{R}_j).$$

Finally, we recover Eq. (2.1):

$$\hat{H}_{\mathrm{HM}} = -t \sum_{\langle ij \rangle} \hat{c}^{\dagger}_{i,\sigma} \hat{c}_{j,\sigma} + U \sum_j \hat{n}_{j,\uparrow} \hat{n}_{j,\downarrow}.$$

The space of states of the HM for N electrons can be constructed from the creation operators once an ordering on the operators is imposed as

$$|\mathbf{r}, \vec{\sigma}\rangle = \hat{c}^{\dagger}_{r_1,\sigma_1} \hat{c}^{\dagger}_{r_2,\sigma_2} \cdots \hat{c}^{\dagger}_{r_N,\sigma_N} |\mathrm{vac}\rangle,$$

where electrons of spin σ_j are located on lattice sites r_j, $j = 1, \ldots, M$. We also define the row vectors of electrons and spin coordinates, $\mathbf{r} = (r_1, r_2, \cdots, r_N)$ and $\vec{\sigma} = (\sigma_1, \sigma_2, \cdots, \sigma_N)$ $(r_j = \{1, \ldots, M\})$ and impose that the elements of

$\mathbf{r}$ are arranged in ascending order so that $r_j \leq r_{j+1}$, and if $r_j = r_{j+1}$ (something clearly only permitted if the spin configurations differ) then $\uparrow < \downarrow$. Thus, associated to each lattice site there are four states

$$\begin{aligned}
|\mathrm{vac}\rangle =& |0\rangle_j, \quad \text{holon} \\
\hat{c}^\dagger_{j,\uparrow}|\mathrm{vac}\rangle =& |\uparrow\rangle_j, \quad \text{singlon} \\
\hat{c}^\dagger_{j,\downarrow}|\mathrm{vac}\rangle =& |\downarrow\rangle_j, \quad \text{singlon} \\
\hat{c}^\dagger_{j,\uparrow}\hat{c}^\dagger_{j,\downarrow}|\mathrm{vac}\rangle =& |\Updownarrow\rangle_j, \quad \text{doublon}
\end{aligned}$$

corresponding to an empty site (holon), a single occupied site with a spin up or down electron (singlon), or a doubly occupied site (doublon).

Chapter 3

Computing Optical Properties

Physical and chemical systems are characterized by their natural frequencies and energy scales. The effects of strong correlation are reflected in the response of solids to small amplitude perturbations at their natural frequencies. In complex solids, these natural frequencies span an enormous range range from zero Hz to beyond x-ray energies. Large regions of such energy scales can be studied with various photon spectroscopies.

In this chapter, we concentrate on absorptive and conductive properties, and more specifically on the frequency-dependent conductivity, $\sigma(\omega)$, or alternatively on the dielectric constant, $\epsilon(\omega)$. We will start by introducing the complex optical constants and their most important properties. Despite being well known, this part is necessary because it will be widely used in the analysis of the experiments of the next chapters.

In the second part of the chapter, we will focus on the calculations of the optical conductivity for a quantum system described by the Hubbard Hamiltonian.

3.1 The complex optical constants

The optical properties of a medium are described by the dielectric constant ϵ, the optical conductivity σ, and the refractive index. They are all, in general, complex quantities:

$$\epsilon(\omega) = \epsilon_1(\omega) + i\epsilon_2(\omega),$$
$$\sigma(\omega) = \sigma_1(\omega) + i\sigma_2(\omega),$$
$$n(\omega) = n(\omega) + i\kappa(\omega),$$

where n is the complex refractive index, κ the absorption coefficient [91], and we use the subscripts 1 and 2 to denote real and imaginary part, respectively. The complex refractive index is related to the complex dielectric constant by [92] $n^2(\omega) = \epsilon(\omega)$. The general relation between the dielectric function and complex conductivity may be shown to be [92]

$$\epsilon(\omega) = \tilde{\epsilon}(\omega) + i\frac{\tilde{\sigma}(\omega)}{(\omega)}\omega\epsilon_0, \tag{3.1}$$

where ϵ_0 is the vacuum permittivity, $\tilde{\epsilon}$ describes the motion of bound charges, and $\tilde{\sigma}$ describes that of free charges, in the limit of a very low frequency or DC field. However, at higher frequencies, especially optical frequencies, the response of free and bound charges to the rapidly varying field changes dramatically from the low frequency case, and the distinction between bound and free charges becomes one of convention [13]. It is therefore possible to redefine $\tilde{\epsilon}$ using an arbitrary function of frequency, so long as $\tilde{\sigma}(\omega)$ is correspondingly redefined and satisfies Eq. (3.1). The relation between the dielectric constant and complex conductivity is redefined to place the response of all electrons into the conductivity term [93]

$$\epsilon(\omega) = 1 + i\frac{\sigma(\omega)}{\omega\epsilon_0}.$$

This definition is well justified so long as the conductivity remains greater than unity. It also allows easy conversion between ϵ and σ, since the real and imaginary parts of $\epsilon(\omega) = \epsilon_1(\omega) + i\epsilon_2(\omega)$ and $\sigma(\omega) = \sigma_1(\omega) + i\sigma_2(\omega)$ can be now be expressed as

$$\sigma_1(\omega) = \omega\epsilon_0\epsilon_2(\omega), \quad \sigma_2(\omega) = \omega\epsilon_0(1 - \epsilon_1(\omega)).$$

All the optical constants outlined so far determine the response of a medium to an external electromagnetic wave.

3.1.1 Linear response

When a linear relationship is assumed between the applied field E and the response of the polarization, P, or of the current, J, one finds [94]:

$$P = \epsilon_0 \chi_e E, \qquad J = \sigma E. \tag{3.2}$$

The electric susceptibility χ_e is related to the dielectric function as $\epsilon = (1+\chi_e)\epsilon_0$. The response functions ϵ and σ connect the field E at time τ and position r with the field D and current, respectively, at some later time and position as

$$D(r,\tau) = \int_{-\infty}^{\tau} \int \epsilon(r, r', \tau, \tau') E(r', \tau')\, \mathrm{d}^3 r'\, \mathrm{d}\tau', \tag{3.3a}$$

$$J(r,\tau) = \int_{-\infty}^{\tau} \int \sigma(r, r', \tau, \tau') E(r', \tau')\, \mathrm{d}^3 r'\, \mathrm{d}\tau'. \tag{3.3b}$$

To compare with experimental optical spectra, we need the to Fourier transform Eqs. 3.3a and 3.3b, into the momentum- and frequencies-dependent quantities $\sigma(q,\omega)$ and $\epsilon(q,\omega)$. How to explicitly calculate these quantities is discussed at length in Sec. 3.3.

Due to the great mismatch between the velocity of light and the typical velocity of electrons in solids, it is a good assumption to study Eq. (**??**) in the $q = 0$ limit. In other words, we shall adopt a local relationship between the quantities in Eq. (3.2) valid over a microscopic distance.

3.1.2 Kramer-Kronig relations

Exploiting the principle of causality [95], one can obtain a fundamental connection between the real and imaginary part of linear complex optical functions. From causality, the conductivity memory function satisfies $\sigma(\tau,\tau') = \sigma(\tau-\tau' < 0) \equiv \sigma(\Delta\tau < 0) = 0$, so that the current becomes

$$J(\tau) = \int_{-\infty}^{\tau} \sigma(\tau - \tau') E(\tau')\, \mathrm{d}\tau',$$

and its Fourier transform

$$\sigma(\omega) = \int_{0}^{\tau} \sigma(\Delta\tau) \mathrm{e}^{i\omega\Delta\tau}\, \mathrm{d}(\Delta\tau).$$

We can perform the integral in the complex frequency plane by substituting $\omega \to z = \omega_1 + i\omega_2$:

$$\sigma(\omega) = \int_0^\infty \sigma(\Delta\tau) \mathrm{e}^{i\omega_1 \Delta\tau} \mathrm{e}^{-\omega_2 \Delta\tau} \, \mathrm{d}(\Delta\tau).$$

The second exponent is bound in the upper (lower) half of the complex plane for $\Delta\tau > 0$ ($\Delta\tau < 0$). Since $\sigma(\Delta\tau < 0) = 0$, $\sigma(\omega)$ is analytic in the upper half of the complex plane in which we can apply Cauchy's theorem [96]:

$$\int \frac{\sigma(\omega')}{\omega' - \omega_0} \, \mathrm{d}\omega' = \mathcal{P} \int_{-\infty}^{\infty} \mathrm{d}\omega' \frac{\sigma(\omega')}{\omega' - \omega} - i\pi\sigma(\omega) = 0,$$

where $\mathcal{P}$ denotes the principal part. Using the fact that in time domain $\mathrm{Im}[\sigma(\tau)] = 0$, then $\sigma(-\omega) = \sigma^*(\omega)$, and the Kramers-Kronig (KK) [97, 98] relations follow as

$$\sigma_1(\omega) = \frac{2}{\pi} \mathcal{P} \int_0^\infty \mathrm{d}\omega' \frac{\omega' \sigma_2(\omega')}{\omega'^2 - \omega^2}, \tag{3.4a}$$

$$\sigma_2(\omega) = -\frac{2\omega}{\pi} \mathcal{P} \int_0^\infty \mathrm{d}\omega' \frac{\omega' \sigma_1(\omega')}{\omega'^2 - \omega^2}, \tag{3.4b}$$

The KK relations describe a fundamental connection between the real and imaginary part of linear complex optical functions: $\sigma_1(\omega)$ and $\sigma_2(\omega)$ are connected by a special form of Hilbert transforms. Physically, this means that it is possible to perform the so-called inversion of optical data, i.e., to acquire knowledge on dispersive phenomena by measurements of absorptive phenomena over the *whole* spectrum (e.g., with transmission spectroscopy) or vice versa.

3.2 Drude-Lorentz classical conductivity

The simplest model of charge conduction we can imagine is of a single charge e, driven by an electric field $\mathbf{E}$, subject to a viscous damping force that relaxes momentum on a timescale τ_R, and to a harmonic restoring force $-Kr$, where r denotes its average position. The equation of motion is

$$m_e(\ddot{\mathbf{r}} + \frac{\dot{\mathbf{r}}}{\tau_R} + \omega_0^2 \mathbf{r}) = -e\mathbf{E},$$

where $w_0^2 = K/m_e$. We assume harmonic motion, so that $x = x_0 \mathrm{e}^{-i\omega\tau}$ and $E = E_0 \mathrm{e}^{-i\omega\tau}$. If we consider an ensemble of charge with density n, the maximum current density is $J_0 = ne\dot{x}_0$. Using the relation $J = \sigma E$, the relation for the optical conductivity is [13]

$$\sigma(\omega) = \frac{Ne^2}{m_e} \frac{\omega}{i(\omega_0^2 - \omega^2) + \omega/\tau_R}. \tag{3.5}$$

Strictly speaking, this model describes quite accurately only the low frequency features of simple metals (for a metal there is no restoring force, i.e. the $\omega_0 = 0$). Despite its classical nature, the Drude-Lorentz model can anyway be used to quantify finite frequency absorptions [99] in complex materials. Since any lineshape can be fitted arbitrarily well using a large enough number of oscillators, and because the imaginary part of the response can be extracted by KK transformation of the real part, it is perfectly feasible to parametrize the response using Eq. (3.5). This is indeed the way the experimental results in the following chapters were fitted.

However, if we wish to use the optical conductivity to extract physical information about the underlying microscopic physics, a quantum mechanical treatment is required. This is what we set about to discuss in the next section.

3.3 Quantum optical conductivity

The most commonly used method for quantum mechanical calculation of the electronic response is the Kubo formalism [100]. It is based on the fluctuation-dissipation theorem, which relates the spontaneous fluctuations of a system at equilibrium described through its correlation functions to its driven linear response [101]. The Kubo formula is a very general equation, and its application spans from the computation of charge and spin susceptibilities of electron systems due to external electric or magnetic field, to responses to external mechanical forces or vibrations.

In the remaining of this chapter, we are going to specialize to the case of interest for this thesis, namely how the one-band Hubbard model in the tight-binding approximation has to be modified in the presence of an external eletro-magnetic field. This way, the sought formula for the conductivity of a periodic Hubbard chain is found. Let us remark that this is the central quantity investigated in the results chapters, hence it is worthwhile to show its derivation in detail.

3.3.1 Hubbard Hamiltonian in an external field

In a typical optical experiment, an electric field impinges on a system and light creates a localized disturbance at some point $\mathbf{r}$ at some time τ. The response of the system is then measured at some later time $\tau' > \tau$.

As mentioned above, we consider a one-dimensional system with periodic boundary conditions [1], i.e., a ring of radius R with M lattice sites. We are interested in the electronic response to a spatially homogeneous, time-dependent electric field, $\mathbf{E}(\mathbf{r},\tau) = -E(\rho,\tau)\mathbf{e}_\varphi$. $\mathbf{e}_\varphi$ is the unit vector along the ring and ρ is the distance of the point $\mathbf{r}$ from the axis perpendicular to the ring plane through the center of the ring, that we take to be the z-axis.

We work in the Weyl gauge, where the scalar potential Φ is set zero: $\Phi(\mathbf{r},\tau) = 0$. The electric field $\mathbf{E}(\mathbf{r},\tau)$, and the vector potential $\mathbf{A}(\mathbf{r},\tau)$, become

$$\mathbf{E}(\mathbf{r},\tau) = -\frac{1}{c}\partial_t \mathbf{A}(\mathbf{r},\tau), \qquad \mathbf{A}(\mathbf{r},\tau) = -A(\rho,\tau)\mathbf{e}_\varphi.$$

The field affects only the individual momenta $\mathbf{p}$ of the electrons, and thus the single-particle part of the Hamiltonian, Eq. (2.5), is

$$h_1(\tau) = \frac{1}{2m_e}\left(\mathbf{p} + \frac{e\mathbf{A}(\mathbf{r},\tau)}{c}\right)^2 + V(\mathbf{r}). \tag{3.6}$$

The magnetic field $\mathbf{B} = \nabla \times \mathbf{A}$ couples only to the spin part of the wave function [102], and can be treated separately. We disregard this effect here, but it can be introduced in the calculation at any stage. The general hopping matrix elements, Eq. (2.12b), for a single-band Hamiltonian with nearest-neighbor terms only, are modified by Eq. (3.6) as

$$\begin{aligned}
t_{j,j+1}(\tau) &= -\int \mathrm{d}\mathbf{r}\phi^*(\mathbf{r}-\mathbf{R}_j)h_1(\tau)\phi(\mathbf{r}-\mathbf{R}_{j+1}),\\
&= \int \mathrm{d}\mathbf{r}\phi^*(\mathbf{r}-\mathbf{R}_j)\left[\frac{1}{2m_e}\left(\mathbf{p}+\frac{e\mathbf{A}}{c}\right)^2 + V(\mathbf{r})\right]\phi(\mathbf{r}-\mathbf{R}_{j+1}),\\
&= \int \mathrm{d}\mathbf{r}\phi^*(\mathbf{r}-\mathbf{R}_j)\mathrm{e}^{-ie\lambda(\mathbf{r},\tau)/c}\left[\frac{1}{2m_e}\left(\mathbf{p}+\frac{e(\mathbf{A}-\partial\lambda(\mathbf{r},\tau)}{c}\right)^2 + V(\mathbf{r})\right]\\
&\qquad \times \mathrm{e}^{ie\lambda(\mathbf{r},\tau)/c}\phi(\mathbf{r}-\mathbf{R}_{j+1}).
\end{aligned} \tag{3.7}$$

---

[1] We are interested in the bulk properties, therefore the choice of boundary conditions should not change the physics. We choose periodic boundary conditions for convenience. In this section, we are going work in Gaussian units.

The third equality holds for any differentiable complex valued function $\lambda(\mathbf{r}, \tau)$. The terms $\mathrm{e}^{\pm ie\lambda(\mathbf{r},\tau)/c}$ are called Peierls phases and we choose them as

$$\lambda_{j,j+1}(\tau) = \frac{e}{c} \int_{\mathbf{R}_j}^{\mathbf{R}_{j+1}} \mathrm{d}\mathbf{r}\mathbf{A}(\mathbf{r}, \tau) = \frac{ea}{c} A(R, \tau),$$

where the lattice spacing for the ring is $a = 2\pi R/M$. The electric field is related to $\lambda(\tau)$ as

$$E(\tau) = -\frac{1}{c}\frac{\partial A(\tau)}{\partial \tau} = -\frac{1}{ea}\frac{\partial \lambda(\tau)}{\partial \tau}.$$

The current flowing through the system is determined by measuring the current operator

$$\hat{J} = -it \sum_{j,\sigma} (\hat{c}^{\dagger}_{j,\sigma}\hat{c}_{j+1,\sigma} - \hat{c}^{\dagger}_{j+1,\sigma}\hat{c}_{j,\sigma}),$$

which satisfies the continuity equation for the total number of electrons. In the presence of external field, $\hat{J}$ is modified similarly to the hopping operator to obtain

$$\hat{J}(\tau) = -it \sum_{j,\sigma} (\mathrm{e}^{i\lambda(\tau)}\hat{c}^{\dagger}_{j,\sigma}\hat{c}_{j+1,\sigma} - \mathrm{e}^{-i\lambda(\tau)}\hat{c}^{\dagger}_{j+1,\sigma}\hat{c}_{j,\sigma}). \tag{3.8}$$

The corresponding electric current is $\hat{J}_{el}(\tau) = -ea\hat{J}(\tau)$, while the electric current density[2] is given by

$$j_{el}(\tau) = -\frac{e}{a^2}\hat{J}(\tau).$$

If the Wannier functions $\phi(\mathbf{r} - \mathbf{R}_j)$ are strongly localized around $\mathbf{R}_j$, and if the vector potential A^{α} varies slowly with respect to a, the full Extended Hubbard Hamiltonian, Eq. (2.2), becomes

$$\begin{aligned}\hat{H}_{\mathrm{EHM}}(\tau) = &- t \sum_{j} (\mathrm{e}^{i\lambda_{j,j+1}(\tau)}\hat{c}^{\dagger}_{j,\sigma}\hat{c}_{j+1,\sigma} + \mathrm{e}^{-i\lambda_{j,j+1}(\tau)}\hat{c}^{\dagger}_{j+1,\sigma}\hat{c}_{j,\sigma}) + U \sum_{j} \hat{n}_{j,\uparrow}\hat{n}_{j,\downarrow} \\ &+ V \sum_{j} \hat{n}_j \hat{n}_{j+1} \equiv \hat{H}_t(\tau) + \hat{H}_U + \hat{H}_V. \end{aligned} \tag{3.9}$$

Moreover, if the electric field is weak as it customarily is for a probe, we can take into account its effects by retaining only linear terms in Eq. (3.9) and Eq. (3.8):

$$\begin{aligned}\hat{H}_{\mathrm{EHM}}(\tau) &= \hat{H}_t + \hat{H}_U + \hat{H}_V + \lambda(\tau)\hat{J}, \\ \hat{J}(\tau) &= \hat{J} - \lambda(\tau)\hat{H}_t, \end{aligned} \tag{3.10}$$

where $\hat{H}_t$ and $\hat{J}$ are the hopping and current operators in zero external field ($\lambda(\tau) = 0$), respectively.

---

[2] The electric current is conventionally normalized to a 3D unit volume, even in 1D systems.

3.3.2 Optical Conductivity Kubo formula

At this point, we have all the elements to obtain an expression for the optical conductivity, that is the linear response function connecting the induced electric current density, $\Delta j_{el}(\tau) = \langle j_{el}(\tau)\rangle - \langle j_{el}(-\infty)\rangle_0$, to the applied electric field $E(\tau)$:

$$\Delta j_{el}(\tau) = \int_{-\infty}^{\infty} \mathrm{d}\tau' \sigma(\tau - \tau')E(\tau').$$

With $\langle\cdot\rangle = \mathrm{tr}(\cdot\ \rho(\tau))$ we denote the expectation value with respect to the time-evolved state, and $\langle\cdot\rangle_0 = \mathrm{tr}(\cdot\ \rho_0)$.

We start from a general stationary initial state of the unperturbed Hamiltonian, $\hat{H}_{\mathrm{EHM}}$, with density matrix ρ_0, and compute the expectation value of $\hat{J}(\tau)$ with respect to the time evolution of ρ_0 under the influence of the small perturbation $\lambda(\tau)$.

In the distant past ($\tau \to \infty$), ρ_0 is taken to be in a statical mixture possessing the diagonal form

$$\rho_0 = \sum_n p_n |\psi_n\rangle\langle\psi_n|, \tag{3.11}$$

where we assume that $\hat{H}_{\mathrm{EHM}} = \sum_n \epsilon_n |\psi_n\rangle\langle\psi_n|$, and $|\psi_n\rangle$ is an eigenstate of energy ϵ_n. In time, it evolves according to $\rho(\tau) = \hat{V}(\tau, -\infty)\rho_0\hat{V}^\dagger(\tau, -\infty)$, where $\hat{V}(\tau, -\infty)$ is the full time-ordered propagator of $\hat{H}_{\mathrm{EHM}}(\tau)$:

$$\hat{V}(\tau, -\infty) = \mathbb{T}\left\{\exp\left[-i\int_{-\infty}^{\tau} \mathrm{d}\tau' \hat{H}_{\mathrm{EHM}}(\tau')\right]\right\}. \tag{3.12}$$

By using Eq. (3.10), we obtain

$$\langle\hat{J}(\tau)\rangle = \mathrm{tr}\left[\hat{V}^\dagger(\tau, -\infty)\hat{J}(\tau)\hat{V}(\tau, -\infty)\rho_0\right] \tag{3.13}$$

Seeing that we are interested in the linear response of $\hat{H}_{\mathrm{EHM}}$ to a small perturbation, it is sufficient to consider $\hat{V}$ in the so-called Born approximation:

$$\hat{V}(\tau, -\infty) = \hat{U}(\tau, -\infty) - i\int_{-\infty}^{\tau} \mathrm{d}\tau' \hat{U}(\tau, \tau')\hat{J}\hat{U}(\tau', -\infty)\lambda(\tau'),$$

where $\hat{U}(\tau, \tau') = \hat{U}(\tau - \tau')$ is the propagator of the unperturbed time-independent Hamiltonian, $\hat{H}_{\mathrm{EHM}}$. Inserting this back into $\langle\hat{J}(\tau)\rangle$ yields the Kubo formula for $\Delta\hat{J}(\tau) = \langle\hat{J}(\tau)\rangle - \langle\hat{J}\rangle_0$:

$$\Delta\hat{J}(\tau) = -\mathrm{tr}(\hat{H}_{\mathrm{EHM}}\rho_0)\lambda(\tau) - i\int_{-\infty}^{\tau} \mathrm{d}\tau' \mathrm{tr}\left([\hat{J}_H(\tau), \hat{J}_H(\tau')]\rho_0\right)\lambda(\tau'). \tag{3.14}$$

Here the suffix H specifies that the current operator is time evolved in the Heisenberg picture $\hat{J}_H(\tau) = \hat{U}^\dagger(\tau, -\infty)\hat{J}\hat{U}(\tau, -\infty)$. Eq. (3.14) is our starting point to compute the optical conductivity.

We have chosen ρ_0 to be exactly stationary, thus it commutes with $\hat{U}(\tau, \tau')$. This allows to simplify Eq. (3.14) to a form which is translationally invariant in the time domain, i.e., is a function only of the time interval $\tau - \tau'$:

$$\Delta\hat{J}(\tau) = -\mathrm{tr}(\hat{H}_{\mathrm{EHM}}\rho_0)\lambda(\tau) - i\int_{-\infty}^{\infty} \mathrm{d}\tau'\Theta(\tau-\tau')\langle[\hat{J}_H(\tau-\tau'), \hat{J}_H(0)]\rho_0\rangle_0\lambda(\tau'). \tag{3.15}$$

The Heaviside function

$$\Theta(\tau-\tau') \equiv \begin{cases} 0, & \tau-\tau' < 0 \\ 1, & \tau-\tau' \geq 0 \end{cases}$$

enforces causality within the integral. The central quantity in this expression is the causal unequal time current-current correlation function

$$\chi_{JJ}(\Delta\tau) = \Theta(\Delta\tau)\mathrm{tr}\left(\hat{J}_H(\Delta\tau)\hat{J}_H(0)\rho_0\right) = \Theta(\Delta\tau)\langle\hat{J}_H(\Delta\tau)\hat{J}_H(0)\rangle_0, \tag{3.16}$$

where $\Delta\tau = \tau - \tau'$. Using $\chi^*_{JJ}(\Delta\tau) = \Theta(\Delta\tau)\langle\hat{J}_H(0)\hat{J}_H(\Delta\tau)\rangle_0$, Eq. (3.15) becomes

$$\Delta J(\tau) \quad = \quad -\langle\hat{H}_{\mathrm{EHM}}\rangle\lambda(\tau) - i\int_{-\infty}^{\infty} \mathrm{d}\tau'\left(\chi_{JJ}(\Delta\tau) - \chi^*_{JJ}(\Delta\tau)\right)\lambda(\tau').$$

Notice that the relation $\chi_{JJ}(\Delta\tau) - \chi^*_{JJ}(\Delta\tau) = 2\mathrm{Im}\{\chi_{JJ}(\Delta\tau)\}$ ensures that, despite $\chi_{JJ}(\Delta\tau)$ being complex valued, the current response is real overall. Using the diagonal decomposition of both ρ_0 and $\hat{H}_{\mathrm{EHM}}$ we can evaluate $\chi_{JJ}(\Delta\tau)$ as

$$\begin{aligned}
\chi_{JJ}(\Delta\tau) &= \Theta(\Delta\tau)\sum_m p_m\langle\psi_m|U^\dagger(\Delta\tau)\hat{J}U(\Delta\tau)\hat{J}|\psi_m\rangle, \\
&= \Theta(\Delta\tau)\sum_m p_m\langle\psi_m|\mathrm{e}^{i\epsilon_m\Delta\tau}\hat{J}\sum_n|\psi_n\rangle\langle\psi_n|\mathrm{e}^{-i\epsilon_n\Delta\tau}\hat{J}|\psi_m\rangle, \\
&= \Theta(\Delta\tau)\sum_m p_m\sum_{n\neq m}|\langle\psi_m|\hat{J}|\psi_n\rangle|^2\mathrm{e}^{-i\omega_{nm}\Delta\tau},
\end{aligned}$$

where $\omega_{nm} = \epsilon_n - \epsilon_m$ are the eigenstate transition frequencies. We have also assumed here that $\langle\psi_m|\hat{J}|\psi_m\rangle = 0$ vanishes for all eigenstates $|\psi_m\rangle$. Inserting this into Eq. (3.15), yields

$$\Delta J(\tau) \quad = \quad \int_{-\infty}^{\infty} \mathrm{d}\tau'\Big[i\sum_m p_m\sum_{n\neq m}|\langle\psi_m|\hat{J}|\psi_n\rangle|^2$$

$$\times(\mathrm{e}^{i\omega_{nm}\Delta\tau}-\mathrm{e}^{-i\omega_{nm}\Delta\tau})\Theta(\Delta\tau)-\langle\hat{H}_t\rangle_{\mathrm{EHM}}\delta(\Delta\tau)\Big]\lambda(\tau').$$

To identify $\sigma(\Delta\tau)$, we need to link $\Delta J(\tau)$ to the electric field $E(\tau)$, rather than to $\lambda(\tau)$. By using

$$\int_{-\infty}^{\tau}\mathrm{d}\tau'\frac{\partial\lambda(\tau')}{\partial\tau'}=\lambda(\tau)-\lambda(-\infty)=\lambda(\tau),$$

where $\lambda(-\infty)=0$, and by integrating by parts as

$$\int_{-\infty}^{t}\mathrm{d}\tau'\lambda(\tau')\mathrm{e}^{\pm i\omega\Delta\tau}=\mp\frac{\lambda(\tau)}{i\omega}\pm\int_{-\infty}^{t}\mathrm{d}\tau'\frac{\partial\lambda(\tau')}{\partial\tau'}\frac{\mathrm{e}^{\pm i\omega\Delta\tau}}{i\omega},$$

we obtain

$$\begin{aligned}\Delta J(\tau) &= \int_{-\infty}^{\infty}\mathrm{d}\tau'\Theta(\Delta\tau)\Big[-\langle\hat{H}_{\mathrm{EHM}}\rangle_0-2\sum_m p_m\sum_{n\neq m}\frac{|\langle\psi_m|\hat{J}|\psi_n\rangle|^2}{\omega_{nm}}\\ &\quad+2\sum_m p_m\sum_{n\neq m}\frac{|\langle\psi_m|\hat{J}|\psi_n\rangle|^2}{\omega_{nm}}\cos(\omega_{nm}\Delta\tau)\Big]\frac{\partial\lambda(\tau')}{\partial\tau'}.\end{aligned}$$

Finally,

$$\begin{aligned}\sigma(\Delta\tau) &= \frac{2\mathrm{e}^2}{a}\Theta(\Delta\tau)\Big[-\tfrac{1}{2}\langle\hat{H}_{\mathrm{EHM}}\rangle_0-\sum_m p_m\sum_{n\neq m}\frac{|\langle\psi_m|\hat{J}|\psi_n\rangle|^2}{\omega_{nm}}\\ &\quad+\sum_m p_m\sum_{n\neq m}\frac{|\langle\psi_m|\hat{J}|\psi_n\rangle|^2}{\omega_{nm}}\cos(\omega_{nm}\Delta\tau)\Big],\end{aligned}$$

where we used $\Delta j_{el}(\tau)=-(e/a^2)\Delta J(\tau)$ and $E(\tau)=-(1/ea)\partial\lambda(\tau)/\partial\tau$.

Transport experiments measure the Fourier transform of the optical conductivity, $\sigma(\omega)$, rather than $\sigma(\Delta\tau)$. Moreover, we want to distinguish between real and imaginary part, as they give different (but complementary), physical information. Typically, for a linear response, the real part of the response function gives the in-phase reactive response, and the imaginary part gives the out-of-phase delayed response [103]. However, in our case the probe perturbation within the Hamiltonian couples to $E(\omega)=i\omega A(\omega)/c$. Thus, the out-of-phase response is actually $\mathrm{Re}\{\sigma(\omega)\}$, proportional to the optical absorption.

We can obtain real and imaginary part by using the identity

$$\int_{-\infty}^{\infty}\mathrm{d}(\tau-\tau')\Theta(\tau-\tau')\mathrm{e}^{i(\omega\pm\omega_n)\tau-\tau'}=\pi\delta(\omega\pm\omega_n)+\mathcal{P}\left(\frac{i}{\omega\pm\omega_n}\right).$$

The real part becomes

$$\sigma_1(\omega) = \frac{2\pi\mathrm{e}^2}{a}\Bigg\{\left(-\frac{\langle\hat{H}_{\mathrm{EHM}}\rangle_0}{2}-\sum_m p_m\sum_{n\neq m}\frac{|\langle\psi_m|\hat{J}|\psi_n\rangle|^2}{\omega_{nm}}\right)\delta(\omega)$$

$$+\sum_m p_m \sum_{n\neq m} \frac{|\langle\psi_m|\hat{J}|\psi_n\rangle|^2}{2\omega_{nm}} \left[\delta(\omega+\omega_{nm})+\delta(\omega-\omega_{nm})\right] \Bigg\},$$

This expression has the general form

$$\sigma_1(\omega) = D\delta(\omega) + \sigma_1^{\text{reg}}(\omega),$$

where the zero-frequency contribution is called Drude weight, D, and equals

$$D = -\frac{2\pi \mathrm{e}^2}{a}\left(\tfrac{1}{2}\langle\hat{H}_{\text{EHM}}\rangle_0 + \sum_m p_m \sum_{n\neq m} \frac{|\langle\psi_m|\hat{J}|\psi_n\rangle|^2}{\omega_{nm}}\right),$$

and the regular finite-frequency part, $\sigma_1^{\text{reg}}(\omega)$, becomes

$$\begin{aligned}\sigma_1^{\text{reg}}(\omega) &= \frac{\pi \mathrm{e}^2}{a}\sum_m p_m \sum_{n\neq m} \frac{|\langle\psi_m|\hat{J}|\psi_n\rangle|^2}{\omega_{nm}}\Big(\delta(\omega-\omega_{nm})+\delta(\omega+\omega_{nm})\Big),\\ &= \frac{\pi \mathrm{e}^2}{a}\sum_m \sum_{n\neq m} \frac{(p_m-p_n)}{\omega_{nm}}|\langle\psi_m|\hat{J}|\psi_n\rangle|^2\delta(\omega-\omega_{nm}).\end{aligned}$$

Up to this point, we have computed $\sigma_1(\omega)$ by diagonalizing $\hat{H}_{\text{EHM}}$ and constructing the sequence of appropriately weighted δ at each eigenfrequencies ω_{nm}. However, in numerical simulation, $\sigma_1^{\text{reg}}(\omega)$ is computed directly from $\chi_{JJ}(\tau-\tau')$. By taking the real part of the Fourier transform of $\chi_{JJ}(\Delta\tau)$, we have

$$\sigma_1^{\text{reg}}(\omega) \quad = \quad \frac{e^2}{a\omega}\text{Re}\left\{\chi_{JJ}(\omega)-\chi_{JJ}(-\omega)\right\}.$$

Thus,

$$\sigma_1^{\text{reg}}(\omega) \quad = \quad \frac{e^2}{\ell\omega}\text{Re}\left\{\int_{-\infty}^{\infty} d\tau\; e^{i\omega\tau}\Theta(\tau)\text{Tr}\left([\hat{J}_H(\tau),\hat{J}_H(0)]\rho_0\right)\right\}.$$

Similarly one can obtain the imaginary part, $\sigma_2(\omega) = \text{Im}\{\sigma(\omega)\}$, as

$$\begin{aligned}\sigma_2(\omega) \quad = \quad & \frac{2\mathrm{e}^2}{a}\Bigg\{\left(-\tfrac{1}{2}\langle\hat{H}_{\text{EHM}}\rangle_0 - \sum_m p_m \sum_{n\neq m}\frac{|\langle\psi_m|\hat{J}|\psi_n\rangle|^2}{\omega_{nm}}\right)\mathcal{P}\left(\frac{1}{\omega}\right)\\ & + \sum_m p_m \sum_{n\neq m}\frac{|\langle\psi_m|\hat{J}|\psi_n\rangle|^2}{2\omega_{nm}}\mathcal{P}\left(\frac{\omega}{\omega^2-\omega_{nm}^2}\right)\Bigg\}.\end{aligned}$$

Nonetheless, it is not strictly necessary to compute $\sigma_2(\omega)$ explicitly, as $\sigma_1(\omega)$ and $\sigma_2(\omega)$ are connected via the KK transformations [94], Eq. (3.4a) and Eq. (3.4b).

3.3.3 Two-time correlation functions

As we shall see in Ch. 6, on-site molecular vibrations can cause the Coulomb interaction matrix-elements, and hence the Hamiltonian, to become time-dependent [3]. The current-current correlation functions Eq. (3.16) of a system which is not in an initial steady state is not simply a function of the time difference $\Delta\tau = \tau - \tau'$, but rather dependent on two time coordinates, τ *and* τ'. In the most general form

$$\chi_{JJ}(\tau, \tau') = \Theta(\tau - \tau')\mathrm{tr}\left(\hat{J}_H(\tau)\hat{J}_H(\tau')\rho_0\right) = \Theta(\tau - \tau')\langle\hat{J}_H(\tau)\hat{J}_H(\tau')\rangle_0.$$

The time at which the two-current operators are individually applied now becomes relevant: the Hamiltonian has a different value at different instants of time. The relevant quantity to compute in the Kubo formula, is then (with $\tau > \tau'$)

$$\begin{aligned}\chi_{JJ}(\tau, \tau_0) - \chi^*_{JJ}(\tau, \tau_0) =& \langle\left[\hat{J}_H(\tau + \tau_0), \hat{J}_H(\tau_0)\right]\rangle_0, \\ =& \langle\left[\hat{U}^\dagger(\tau + \tau_0)\hat{J}\hat{U}(\tau + \tau_0), \hat{U}^\dagger(\tau_0)\hat{J}\hat{U}(\tau_0)\right]\rangle_0, \qquad (3.17)\end{aligned}$$

where now in the time evolution operator the Hamiltonian is explicitly time dependent: $\hat{U}(\tau_0) = \exp(-i\hat{H}_{\mathrm{EHM}}(\tau_0)\tau_0)$. To distinguish $\chi_{JJ}(\tau, \tau_0)$, Eq. (3.17), from $\chi_{JJ}(\Delta\tau)$, we will refer to it as *two-time* correlation function.

3.4 Summary

In this chapter, we have discussed the experimentally observable quantities that characterize the response of a material to an applied electromagnetic field. We have focused in particular on the optical conductivity, and obtained the Kubo formula that permits theoretical and numerical calculations within the framework of linear response theory.

---

[3] The energy is obviously not conserved anymore, due to the external driving pulse.

Chapter 4

Hubbard Model in the Strong Coupling Limit

4.1 Exact solutions in one dimension

Despite its apparent simplicity, exact solutions for the Hubbard Model (HM) exist only in one or infinite dimensions [20, 102]. In 1D, the Bethe Ansatz provides very elegant expressions for the eigenvalues and eigenstates of the HM. The thermodynamics of the one-dimensional HM has been investigated for both nearest-neighbor [104, 105, 106, 107] and long-range [108] hopping.

Unfortunately, integrability is a fragile property: adding extra terms to an integrable Hamiltonian will in general break it. This is a crucial point for us: in Ch. 2 we mentioned that the original Hubbard Hamiltonian doesn't capture completely the physics of ET-F_2TCNQ, and a nearest-neighbor interaction needs to be added [76]. Therefore, an Extended Hubbard Hamiltonian has to be considered. For general values of the hopping t and interaction parameters U and V, the Extended Hubbard Model (EHM) is known to be non-integrable [109]. Moreover, even for the "simple" Hubbard Model, the exact expressions for eigenstates and eigenvalues are impossible to exploit for practical calculations of correlation functions, and only allow to express local properties.

The aim of this chapter is to explore in some detail two limits in which solutions for the EHM exist, and allow for exact expression for the optical conductivity, $\sigma(\omega)$: the atomic limit, and the strong coupling limit. We will make extensive use of both results. Specifically the atomic limit will serve as a starting point to estimate $\sigma(\omega)$ in Ch. 7; while the strong-coupling limit expansion will help us to extract the values of the Hubbard parameters from experimental data both in Ch. 5 and Ch. 8.

4.2 Atomic limit

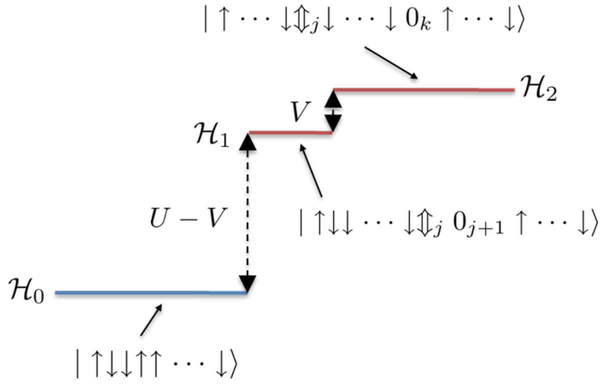

Figure 4.1: A schematic of the half-filled Extended Hubbard model spectrum in the atomic limit. The ground state manifold $\mathcal{H}_0$ is spanned by spin configurations in the Mott Insulator (MI). The first excited Hubbard band $\mathcal{H}_1$ at an energy $U-V$ above this is spanned by MI states with an adjacent holon-doublon pair. The second excited Hubbard band $\mathcal{H}_2$ at an energy U above the ground state is spanned by MI states with a non-adjacent holon-doublon pair. Representative for each manifold of eigenstates are illustrated in the figure.

The difficulties in extending solutions for the HM to models including long-range Coulomb interactions have led to the investigation of the so-called narrow band, or atomic, limit, where t can be neglected with respect to the interaction coupling U and V. Even with this simplification, this model has many interesting features and a very rich phase diagram with multicritical behavior [110, 111, 112, 113].

Given the wide separation between the ground state energy and the lowest excited state, it is often sufficient for studying optical properties to focus on three lowest subspaces: (a) $\mathcal{H}_0$, where all the sites are are singly occupied the eigenstates have energy 0, (b) $\mathcal{H}_1$, with a single adjacent doublon-holon pair excited from $\mathcal{H}_0$ (energy $U - V$), and (c) $\mathcal{H}_2$ where the doublon and the holon are non adjacent (energy U). This is schematically represented in Fig. 4.1. We will use the atomic limit to investigate the effects of onsite molecular vibrations on the optical response of ET-F_2TCNQ in Ch. 6 and Ch. 7.

An additional advantage of this approach is that the results for the atomic model can be used as a starting point for a perturbation expansion in powers of the hopping t, thereby giving information beyond the zero-bandwidth limit [114]. This strategy has allowed Gebhard *et al.* [50] to describe the optical properties of the Extended Hubbard Model (EHM) in the limit $U \gg V, t$, by mapping it onto the Harris-Lange model. This specific model can be solved exactly in 1D, as will be shown in the next section.

4.3 Strong coupling limit

As already mentioned in a few occasions now, the EHM in the strong coupling limit ($t, V \ll U$) reproduces the electronic properties of ET-F_2TCNQ [76]. In this regime, it is possible to obtain the exact spectrum and eigenstates for the model, and interpret the results in terms of two parallel bands for the charges. When the system is at temperatures large compared to the spin exchange energy, no magnetic ordering is expected and all the spin configurations can be assumed to be equally probable in the thermal state. In this instance, the optical absorption in the presence of a nearest-neighbor interaction between the charges can be exactly computed. This is the main advantage of the Harris-Lange model with respect to the Bethe Ansatz [20]: the latter does not allow the direct calculation of transport properties at finite frequencies.

We have already seen in Sec. 2.A.2 that, when $V = 0$, a charge excitation from the LHB to the UHB creates an unbound particle-hole pair, and the energies of the pair creates a band that we will call the “particle-hole continuum”. When $V \neq 0$, a holon and a doublon are attracted with an energy V, creating an exciton. In molecular crystals, these neutral excitation states may have long lifetimes [115, 50, 116, 117], and an excitation energy which is smaller than the energy required to excite an electron from the valence band into the particle-hole continuum. Therefore, when the quantum energy of the photons is not too great, the photo-excitation in molecular crystals does not produce free charge carriers, but rather bound electron-hole pairs.

4.4 Harris-Lange model

In the extreme limit $t/U \to 0$, the charge and spin degrees of freedom completely decouple [118, 119]. For $N \leq M$ and $U = \infty$, the eigenenergies are the same as those of a Fermi gas of with $N_h = M - N$ holes, with dispersion $\epsilon(k) = -2t\cos(ka)$.

Following [50], we can map the HM onto a problem for which the number of double occupancies is conserved. Thus, we can decompose the operators into those which act solely in the upper or lower Hubbard band, and eliminate the parts which couple the two bands. The resulting effective Hamiltonian, to lowest order in t/U, is called "Harris-Lange" model. The kinetic energy operator, $\hat{H}_t$, may be split into four terms

$$\hat{H}_t = \hat{H}_t^{\text{UHB}} + \hat{H}_t^{\text{LHB}} + \hat{H}_t^{+} + \hat{H}_t^{-},$$

where

$$\begin{aligned}
\hat{H}_t^{\text{LHB}} &= -t\sum_{j,\sigma}(1-\hat{n}_{j,-\sigma})\left(\hat{c}^\dagger_{j,\sigma}\hat{c}_{j+1,\sigma} + \hat{c}^\dagger_{j+1,\sigma}\hat{c}_{j,\sigma}\right)(1-\hat{n}_{j+1,-\sigma}),\\
\hat{H}_t^{\text{UHB}} &= -t\sum_{j,\sigma}\hat{n}_{j,-\sigma}\left(\hat{c}^\dagger_{j,\sigma}\hat{c}_{j+1,\sigma} + \hat{c}^\dagger_{j+1,\sigma}\hat{c}_{j,\sigma}\right)\hat{n}_{j+1,-\sigma},\\
\hat{H}_t^{+} &= -t\sum_{j,\sigma}\left[\hat{n}_{j,-\sigma}\hat{c}^\dagger_{j,\sigma}\hat{c}_{j+1,\sigma}(1-\hat{n}_{j+1,-\sigma}) + \hat{n}_{j+1,-\sigma}\hat{c}^\dagger_{j+1,\sigma}\hat{c}_{j,\sigma}(1-\hat{n}_{j,-\sigma})\right],\\
\hat{H}_t^{-} &= (\hat{H}_t^{+})^\dagger.
\end{aligned}$$

$\hat{H}_t^{\text{LHB}}$ and $\hat{H}_t^{\text{UHB}}$ describe holons and doublons moving in the Lower Hubbard Band (LHB) and Upper Hubbard Band (UHB), respectively, while conserving their number. On the contrary, $\hat{H}_t^{+}$ ($\hat{H}_t^{-}$) increases (decreases) the doublon number and can be eliminated to lowest order in t/U by performing a canonical transformation [120, 121], $\hat{c}_{j,\sigma} = \exp\{i\hat{S}(\tilde{c})\}\tilde{c}_{j,\sigma}\exp\{-i\hat{S}(\tilde{c})\}$, with $\left(\hat{S}(\tilde{c})\right)^\dagger = \hat{S}(\tilde{c})$ and

$$\hat{S}(\tilde{c}) = \frac{it}{U}\left(\hat{H}_t^{\tilde{c},+} - \hat{H}_t^{\tilde{c},-}\right).$$

Using $[\hat{H}_U/U, \hat{H}_t^{\pm}] = \pm\hat{H}_t^{\pm}$, the Hubbard Hamiltonian for the transformed fermions, $\tilde{c}$, becomes the Harris-Lange model

$$\hat{H}_{\mathrm{HL}}^{\tilde{c}} = \hat{H}_t^{\tilde{c},\mathrm{LHB}} + \hat{H}_t^{\tilde{c},\mathrm{UHB}} + \hat{H}_U^{\tilde{c}}.$$

The energies obtained from the Harris-Lange model agree with those of the HM with a second order error. Thus, at this level of approximation, there is no distinction between $\tilde{c}_{j,\sigma}$ and $\hat{c}_{j,\sigma}$. The hopping term acting within the Lower Hubbard Band $\hat{H}_t^{\mathrm{LHB}}$, can be mapped onto its UHB counterpart $\hat{H}_t^{\mathrm{UHB}}$, by exploiting particle-hole symmetry [50]: this allows for an exact solution of the model since there is no difference in the motion of double occupancies in the UHB and holes in the LHB.

Crucially, when the nearest-neighbor Coulomb interaction is included ($V \neq 0$) in the HM, the Harris-Lange picture still holds. The Hamiltonian simply becomes

$$\hat{H}_{\mathrm{HL}}^{\mathrm{ext}} = \hat{H}_t^{\mathrm{LHB}} + \hat{H}_t^{\mathrm{UHB}} + \hat{H}_U + \hat{H}_V.$$

The doublon and the holon in the excited states now experience a nearest-neighbor attraction.

We are now ready to compute the optical conductivity, $\sigma_1(\omega)$.

4.5 Optical conductivity in the Strong Coupling limit

Let us begin with the simplest case, namely $V = 0$. An optical absorption process excites one hole in the LHB that has dispersion relation $\epsilon_{\mathrm{LHB}} = -U/2+\epsilon(k)$, and one double occupancy in the UHB, with $\epsilon_{UHB}(k) = U/2-\epsilon(k)$, as schematically depicted in Fig. 4.2. Here $\epsilon(k) = -2t\cos(ka)$ is the usual dispersion relation for electrons in the tight-binding approximation (see Appendix 2.A.1). The two charge excitations have total energy and momentum equal to ω and q, respectively.

For high temperatures, all the states with no double occupancy are possible ground states in the Harris-Lange model at half-filling. Instead of looking at the optical absorption for a specific ground state, it is more reasonable to calculate

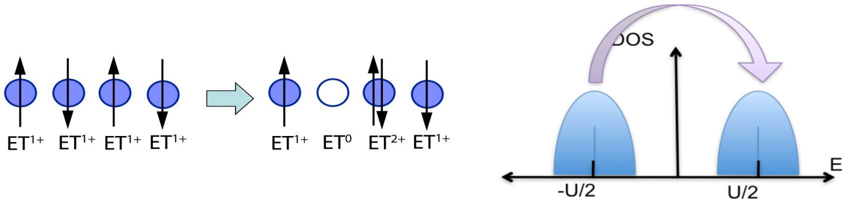

Figure 4.2: Mott transition $\mathrm{ET}^{+}\mathrm{ET}^{+} \rightarrow \mathrm{ET}^{2+}\mathrm{ET}^{0}$ and expected density of states (DOS).

the average absorption. This would be a formidable calculation, if the spin-charge separation property of one-dimensional system wouldn't come to our aid.

In particular, Gebhard *et al.* [50] showed that the spin contribution to the current-current correlation function boils down to a multiplicative factor. More specifically, this factor is momentum-dependent, and reads:

$$g_q = 2\langle 0|\hat{Z}^{\dagger}_{r,r+1}(q)\left(\frac{1}{4} - \hat{\mathbf{S}}_r\hat{\mathbf{S}}_{r+1}\right)\hat{Z}^{\dagger}_{r,r+1}(q)|0\rangle, \tag{4.1}$$

$$\hat{Z}^{\dagger}_{r,r+1}(q) = \frac{1}{M}\sum_j \mathrm{e}^{-iqj}\mathcal{T}_S^{(j-r)}\mathcal{T}_{S'}^{-(j-r)},$$

where $\mathcal{T}_S$ shifts all spins by one site and $\mathcal{T}_{S'}$ performs the same operation on the lattice with sites r and $r+1$ removed. The spin operators $\hat{\mathbf{S}}$ are, in terms of fermionic operators:

$$\hat{\mathbf{S}} \equiv (\hat{S}^{+}_i, \hat{S}^{-}_i, \hat{S}^{z}_i) = (\hat{c}^{\dagger}_{j\uparrow}\hat{c}_{j\downarrow}, \hat{c}^{\dagger}_{j\downarrow}\hat{c}_{j\uparrow}, (\hat{n}_{j\uparrow} - \hat{n}_{j\downarrow})/2), \tag{4.2}$$

A very difficult problem has thus been "hidden" in the form factor g_q. The exact result for g_q is very involved, but one can argue (and confirm with numerical simulations [116]) that the dominant contributions come from its value at $q = 0$ and $q = \pi/a$. This approximation is called "no-recoil approximation", and retains the vertical transitions between two parallel bands for $q = 0$, i.e., $\epsilon_{\mathrm{LHB}}(k) \rightarrow \epsilon_{\mathrm{UHB}}(k)$, and between two anti-parallel bands for $q = \pi/a$, i.e., $\epsilon_{\mathrm{LHB}}(k) \rightarrow \epsilon_{\mathrm{UHB}}(k+\pi)$. The values of g_q in Eq. (4.1) have been estimated by means of numerical DMRG simulations [122, 123]. The results, $g_{q=0} \equiv g_0 = 2.65$ and $g_{q=\pi/a} \equiv g_\pi = 0.05 \pm 0.03$, suggest that it is the transition between parallel bands that dominates the optical transition. Physically, this reflects the fact that states with antiferromagnetic spin correlations are best suited to optical absorption since they contain many neighboring single pairs.

When a finite nearest-neighbor Coulomb repulsion ($V \ll U$) is introduced, the doublon and holon mutually attract. They behave like spinless hard-core bosons and, if the value of V exceeds a critical threshold ($V_c = 2t$), an exciton peak appears in the expression for the reduced optical conductivity, σ_1 [116]:

$$\begin{aligned}\omega\sigma_1 =& \pi g_\pi t^2 e^2 \delta(\omega - \omega_2) + g_0 t^2 \Bigg\{ \Theta(V - 2t)\pi \Big[1 - \big(\frac{2t}{V}\big)^2\Big] \delta(\omega - \omega_1) \\ &+ \Theta(4t - |\omega - U|) \frac{2t\sqrt{1 - [(\omega - U)/4t]^2}}{V(\omega - \omega_1)} \Bigg\}. \end{aligned} \tag{4.3}$$

where $\Theta(x)$ is the Heaviside step function. We can see that there are two δ-peaks corresponding to two different Mott-Hubbard excitons: (a) one at energy

$$\hbar\omega_1 = U - V - \frac{4t^2}{V},$$

and (b) one at energy

$$\hbar\omega_2 = U - V,$$

with the $\Theta(V - 2t)$ factor expressing that the ω_1 exciton exists only when $V > V_C$. The peak associated to ω_1 in the optical conductivity is sometimes called *charge-transfer* (CT) resonance. Seeing that $q_0 \gg q_\pi$, ω_2 carries very little spectral weight and doesn't affect the physics too much, we thus drop it from now on. Hence, the $q = \pi/a$ exciton dominates over the $q = 0$ exciton for $V > V_C$. The final term represents the continuum of states associated with unbound particle-hole (PH) excitations, centered at U and with bandwidth of $8t$.

4.6 Summary

Summarizing the results obtained so far, ultrafast pump-probe techniques applied to a one-dimensional organic salt, ET-F$_2$TCNQ, enable us to explore the physics of the Extended Hubbard Model in a room temperature, macroscopic material. The central experimental observable we are going to study is the optical response, which can be numerically computed in linear response theory, and for which exact analytic expressions exist.

We are now in place to present our novel results.

Part II

Tuning and modulating the Hubbard Model

Chapter 5

Tuning the Hubbard parameters with pressure

5.1 Pressure control of the coherent parameters

The aim of this chapter is twofold.

- Firstly, we want to study how the Hubbard parameters, and the binding energy of the excitons, change in conjunction with an adiabatic compression of the material. We are going to investigate how the on-site and nearest-neighbor Coulomb interaction, U and V respectively, and the bandwidth $W = 4t$ change as a function of the pressure P. As an experimental reference, we shall analyze the results of measurements of the optical conductivity as a function of pressure of the organic Mott insulator ET-F$_2$TCNQ.
- Secondly, we argue that the relaxation of holon-doublon pairs can expose the competition between the pairs' tendency to bind, due to V, and to delocalize because of the hopping amplitude t. We will develop and test a model for the relaxation rates by comparing predictions with the measured femtosecond relaxation of pairs of photo-excited holon-doublon pairs.

Before dealing with complex materials, it is instructive to analyze how the recombination rate depends on microscopic parameters with reference to two well known situations: metals and direct band semiconductors.

5.1.1 Non-equilibrium electron relaxation in metals

For metals, the Two-Temperature Model (TTM) [124] describes the state that results after photo-excitation. Anisimov *et al.* [125] focused on the particular case of a metal been exposed to a ultrashort (femto-second) laser pulse, with the pulse provoking a non-equilibrium distribution. At room temperature, the heat capacities of the electrons and lattice, C_e and C_l, respectively, differ considerably. As a result of the fact that $C_l \gg C_e$, the lattice temperature is essentially unchanged.

Over a time scale of hundreds of femto-seconds, the non-equilibrium electrons redistribute their energies among themselves and return to a local equilibrium at some temperature $T_e > T$. Then, this excited thermalized electron gas relaxes (or cools) via electro-phonon interactions giving up the excess energy to the phonon bath. The large difference between the time scales on which these two processes happen motivates the TTM.

With these approximations in place, it is possible to obtain [126] coupled differential equations to describe hot electron cooling. The one governing the relaxation of the electronic temperature reads

$$\frac{\mathrm{d}T_e}{\mathrm{d}\tau} = -\frac{G}{C_e}(T_e - T),$$

where the bosonic phonon distribution is taken at ambient room temperature, T, and G is the electron-phonon interaction coefficient.

The specific heat of an electron gas is proportional to the density of states at the Fermi level ϵ_F [13]: $C_e \sim g(\epsilon_F)$. We want to compare theoretical predictions with experimental observations in the 1D (half-filled) Mott insulator ET-F_2TCNQ. To draw an analogy, we describe the metallic electronic band as a one-dimensional tight-binding model with hopping amplitude t and lattice spacing a. As explained in Appendix 2.A.1, the energy-dispersion relation for periodic boundary (PB) conditions is $\epsilon(k) = -2t\cos(ka)$, hence the general density of states is readily obtained as:

$$g(k) = \frac{4}{|2t\sin(ka)|}, \qquad g(\epsilon_F) = \frac{2}{t}, \tag{5.1}$$

where we used the general relation $g(\epsilon) = g(k)\, \mathrm{d}k/\, \mathrm{d}\epsilon$.

To summarize, we expect the decay time τ_R for metals to vary as

$$\tau_R \sim \frac{1}{t},$$

i.e. to accelerate linearly with the bandwidth.

5.1.2 Direct band semiconductors

For direct band semiconductors, the recombination rate, R, between electrons excited in the conduction band and holes in the valence band, is proportional to the product of the density of electron in the conduction bands, n_c, and of holes in the valence band, p_v [13]:

$$R = K n_c p_v, \qquad K = \text{constant}. \tag{5.2}$$

The number of carriers present at a temperature T is given by

$$\begin{aligned} n_c(T) &= \int_{\epsilon_c}^{\infty} \mathrm{d}\epsilon g_c(\epsilon) \frac{1}{\mathrm{e}^{(\epsilon-\mu)/k_B T} + 1}, \\ p_v(T) &= \int_{-\infty}^{\epsilon_v} \mathrm{d}\epsilon g_v(\epsilon) \frac{1}{\mathrm{e}^{(\mu-\epsilon)/k_B T} + 1}, \end{aligned} \tag{5.3}$$

where $g_c(\epsilon)$ and $g_v(\epsilon)$ are the density of states in the conduction and valence band, respectively. To determine the value of the chemical potential μ, the exact knowledge of the impurity levels is required. Nevertheless, there is a large class of values of the energy gap $E_g = \epsilon_c - \epsilon_v$ (ϵ_c and ϵ_v are the energies at the bottom of the conduction band and at the top of the valence band, respectively) and temperature, for which the following conditions are satisfied:

$$\epsilon_c - \mu \gg k_B T, \qquad \mu - \epsilon_v \gg k_B T.$$

In this case, Eq. (5.3) reduces to

$$n_c(T) = N_c(T) \mathrm{e}^{-(\epsilon_c - \mu)/k_B T}, \qquad p_v(T) = P_v(T) \mathrm{e}^{-(\mu - \epsilon_v)/k_B T},$$

where

$$N_c(T) = \int_{\epsilon_c}^{\infty} \mathrm{d}\epsilon g_c(\epsilon) \mathrm{e}^{-(\epsilon - \epsilon_c)/k_B T}, \qquad P_v(T) = \int_{-\infty}^{\epsilon_v} \mathrm{d}\epsilon g_v(\epsilon) \mathrm{e}^{-(\epsilon_v - \epsilon)/k_B T}.$$

We are interested in the rate, R, hence simply in the product $n_c p_v$ (Eq. (5.2)). Notably, the μ dependence disappears from the product of the two densities:

$$n_c p_v = N_c P_v \mathrm{e}^{-E_g/k_B T},$$

where

$$N_c = \int_{\epsilon_c}^{\infty} \mathrm{d}\epsilon g_c(\epsilon), \qquad N_v = \int_{-\infty}^{\epsilon_v} \mathrm{d}\epsilon g_v(\epsilon).$$

From this result, sometimes called "law of mass action", we deduce that the number of electrons and holes is a function of the integral of the density of states. With the help of the general relation $g(\epsilon) = g(k)\ \mathrm{d}k/\ \mathrm{d}\epsilon$, R is found to be proportional to both $\propto \partial g_c(k)/\partial k$ and $\propto \partial g_v(k)/\partial k$.

Once again, we want to draw a comparison with ET-F_2TCNQ. This time we use a two one-dimensional tight-binding models, one to describe the conduction band, and one for the valence band, separated by an energy gap E_g. The energy-dispersion relation for periodic boundary (PB) conditions turns out to be: $\epsilon_c(k) = E_g - 2t\cos(ka)$ and $\epsilon_v(k) = -2t\cos(ka)$. With the help of Eq. (5.1) we predict that the recombination rate for direct band semiconductors will be $R \sim t^{-2}$, and consequently the decay time

$$\tau_R \sim t^2.$$

In conclusion, the recombination is expected to slow down with the square of the bandwidth.

5.2 Fitting to static conductivities

With external hydrostatic pressure, P, we can adiabatically tune the microscopic parameters of $\hat{H}_{\mathrm{EHM}}$ by slowly reducing the lattice spacing between molecular sites. Generally, the π-orbitals governing the conduction properties of organic salts are well described by hydrogenic wave functions [49]. In this case, t depends exponentially on the lattice spacing, a, as $t(a) \sim (1 + \alpha a)\mathrm{e}^{-\alpha a}$, where α is a constant depending on the specific compound. Simultaneously, V also increases as $V(a) \sim 1/a$ [103]. On the contrary, we assume that the reduction of lattice spacing doesn't change the on-site properties of the model, so that $U(a) \sim U$.

The first part of the experiment that we are about to describe measures the static reflectivity of the material for different values of pressure. The fits to the data are performed by recalling that the reflectance of a material at normal incidence is given by Fresnel formula [127] as

$$R(\omega) = \left| \frac{1 - \sqrt{\tilde{\epsilon}(\omega)}}{1 + \sqrt{\tilde{\epsilon}(\omega)}} \right|^2,$$

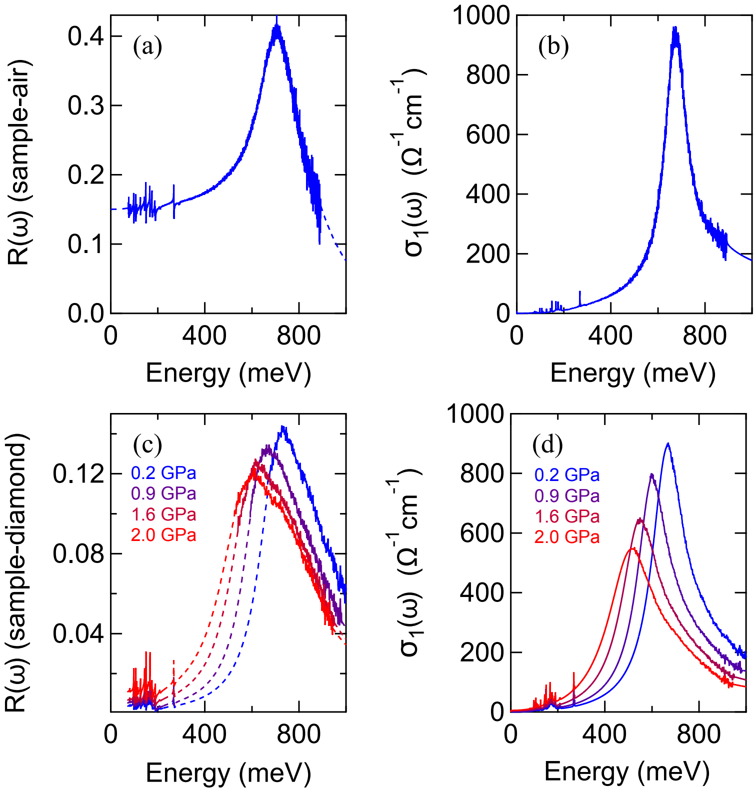

Figure 5.1: (a) Static reflectivity at ambient pressure of the ET-F$_2$TCNQ, measured with the electric field parallel to the a axis . (b) Real part of the optical conductivity, $\sigma_1(\omega)$ at ambient pressure. (c) Steady state reflectivity of the ET-F$_2$TCNQ along the a axis for selected pressures. (d) Pressure dependence of the optical conductivity $\sigma_1(\omega)$.

where $\tilde{\epsilon}(\omega)$ is the complex dielectric function of the material. This quantity may be analyzed according to the Drude-Lorentz model introduced in Sec. 3.2, a phenomenological model using a set of N uncoupled harmonic oscillators to describe the response as a sum of Lorentzian line shapes [128],

$$\frac{\tilde{\epsilon}(\omega)}{\epsilon_0} = 1 + \sum_{i=1}^{N} \frac{A_i^2}{\omega_{0i}^2 - \omega^2 - i\gamma_i\omega},$$

where A_i is the oscillator strength, ω_{0i} is the natural frequency of the resonance and γ_i the damping constant. These equations were used to fit the static reflectivities shown in Fig. 5.1(a)-(c). From these, the optical conductivity has been extracted and is shown in Fig. 5.1(b)-(d). For details about the measurements and setup, see Appendix 5.B and the Supplementary Material of [1].

At ambient pressure, the optical conductivity exhibits a prominent Charge Transfer (CT) peak near 700 meV. We observe that it red-shifts at a rate of 70 meV/GPa, as well as broadening towards high frequencies. Moreover, the lack of observation of any Drude response confirms that the material remains insulating for all measured photon energies ($>$ 75 meV), and at any applied pressure ($0-2$ GPa). The vibrational peaks at frequencies below 400 meV, associated to vibrational modes, show no dependence on pressure. This excludes significant intra-molecular structural rearrangement, that would provoke changes in the intensity and/or position of these peaks. As hinted in Sec. 2.1, the latter is a well known feature of organic crystals, where the weakness and the short range of the Van der Waals bonding is such that individual molecules retain their individual properties to a much greater extent than those of the bonding units observed in other material classes.

In order to analyze the data, we want to use the analytic results for the optical conductivity based on the strong coupling expansion of the EHM. As detailed in Sec. 4.5, we can use a strong coupling expansion in $1/U$ to achieve this goal. We showed that one can obtain an analytic expression for the reduced optical conductivity (Eq. (4.3)), as

$$\begin{aligned}\omega\sigma_1 =& \pi g_\pi t^2 e^2 \delta(\omega-\omega_2) + g_0 t^2 \Bigg\{ \Theta(V-2t)\pi\Big[1-\Big(\frac{2t}{V}\Big)^2\Big]\delta(\omega-\omega_1) \\ &+\Theta(4t-|\omega-U|)\frac{2t_0\sqrt{1-[(\omega-U)/4t]^2}}{V(\omega-\omega_1)}\Bigg\}.\end{aligned}$$

Since the experiment has finite resolution, the sharp theoretical features (i.e. the δ peaks and the Θ functions) in Eq. (4.3), have been convolved with a Lorentzian of finite width η, of the order of the hopping amplitude. The subsequent best-fit with free parameters V and t, focuses on the features near the CT resonance and provides the results shown in Fig. 5.2. In Fig. 5.2(a)-(c) we report a comparison of measured and fitted $\omega\sigma_1(\omega)$, normalized to the peak value of the spectrum measured at ambient pressure. In grey we find the curves based on the conductivity predicted by Eq. (4.3), whereas the measured data are in black. Both V and t are observed to increase with pressure, ranging from 120 to 203 meV and from 40 to 203 meV, respectively (see Fig. 5.2(e)).

The fit highlights the two dominant contributions to $\omega\sigma_1(\omega)$. As explained in Sec. 4.5, the first peak is the Mott-Hubbard exciton composed of a bound holon-doublon (HD) pair; the second broad feature is the continuum of states associated with unbound particle-hole (PH) excitations [116, 129]. These two types of excitations are visualized in Fig. 5.2(d). As a function of pressure, the exciton peak shifts to the red, whereas the continuum remains centered at U, thus confirming our hypothesis that U is not affected by pressure.

We already mentioned, in Sec. 1.3.1, how tools used to study the physics of optical lattices could be of great help to develop a physical intuition of the behavior of much more complex systems. In next section we want to estimate how the parameters of the Hubbard model would change following a reduction of the lattice parameters, if the system under consideration was a perfect lattice. This procedure will help us to confirm the basic picture for a well understood lattice system.

5.3 Pressure in optical lattices

In Ref. [4] we developed a code that allows to estimate the Hubbard parameters for any kind of optical lattice geometry. The method allows to find a set of highly localized basis states (or Wannier states), and thereby systematically derive the parameters of a generic HM realized using cold atoms and optical lattice. The general features of the procedure are discussed in Appendix 5.A. The MATLAB code was made freely available online at `http://ccpforge.cse.`

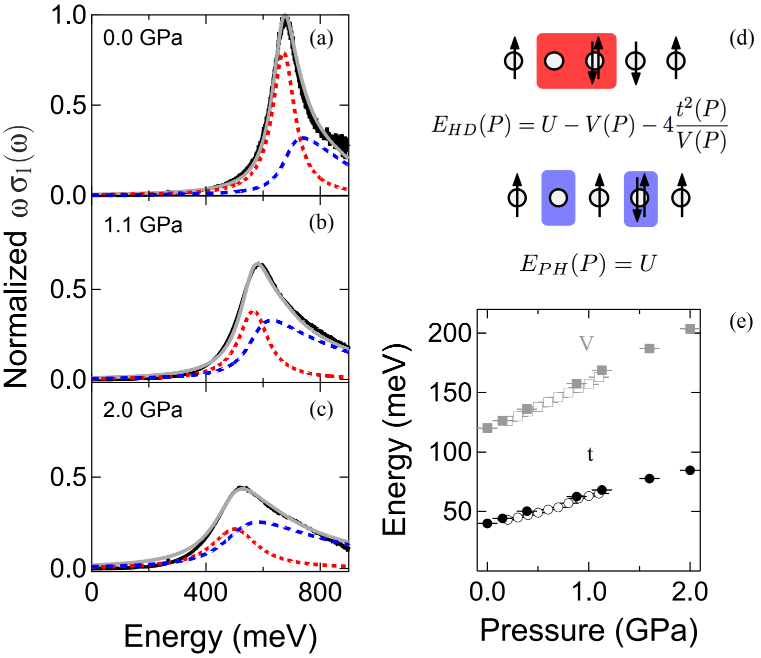

Figure 5.2: (a)-(c) Normalized reduced optical conductivity for selected pressures (black solid line), with corresponding fit (grey solid line). The contributions of the holon-doublon pair (red) and of the PH continuum (blue) are shown as dashed lines. (d) Sketch of a holon-doublon pair (top) and of a typical PH continuum excitation (bottom). (e) Pressure dependence of the EHM parameters V (squares) and t (circles) extracted from the fit of the steady state $\omega\sigma_1(\omega)$. U is assumed to be fixed to 845 meV. Filled and empty symbols identify measurements performed with different setups (see Supplementary Material of [1] for details).

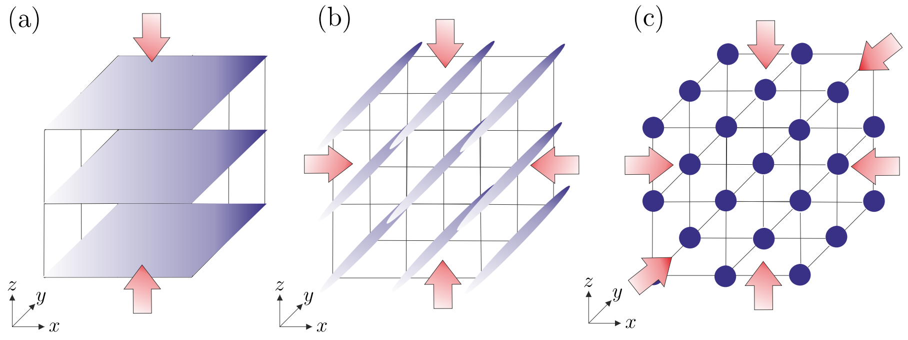

Figure 5.3: (a) Two counter-propagating lasers along the z-axis create a 1D optical lattice, and constrain the motion of the atoms to one of a set of xy planes. (b) With an additional pair of counter-propagating lasers along the x-axis, one creates a 2d optical lattice where the motion of atoms is constrained to one of a set of tubes along the y-axis. (c) A further pair of counter-propagating lasers along the y-axis generates a full 3d optical lattice which localizes the atoms to of the lattice sites [130].

`rl.ac.uk/gf/project/mlgws/`, and several examples were reported.

In this section, we are going to use the code to estimate on how U, V and t would change if we wished to simulate an adiabatic reduction of the lattice parameter in a one-dimensional optical lattice. Let us recall that an optical lattice potential can be formed by interfering a set of lasers to create a standing wave intensity pattern [131]. For example, we take two counter-propagating beams of amplitude E_0, described by plane-waves with wave-vectors $\mathbf{k}_1 = (0, 0, k)$ and $\mathbf{k}_2 = (0, 0, -k)$ and both polarized in the x-direction, i.e., $\mathbf{e}_1 = \mathbf{e}_2 = \mathbf{i}$ with $\mathbf{i} = (1, 0, 0)$. The sum of the fields is given by

$$\mathbf{E}(z, \tau) = E_0 \mathbf{i} \mathrm{e}^{i(\omega\tau + kz)} + E_0 \mathbf{i} \mathrm{e}^{i(\omega\tau - kz)},$$

which has an intensity $I(z) = |\mathbf{E}(z)|^2 = 4|\mathbf{E}_0|^2 = \cos^2(kz)$ independent of time. The potential experienced by the atom due to the interaction with the field is $V_{\mathrm{OL}}(x) \propto \cos^2(kx)$. We introduce the potential strength $\tilde{V}$ expressed in units of the recoil energy $E_R = \hbar^2 k^2 / 2\mu$ [132], where μ is the mass of the atom. We set it equal to the full energy range of the optical lattice potential so that $\tilde{V} = \max[V_{\mathrm{OL}}(\mathbf{r})]$. The potential becomes $V_{\mathrm{OL}} = \tilde{V} \cos^2(kx)$, with "av-

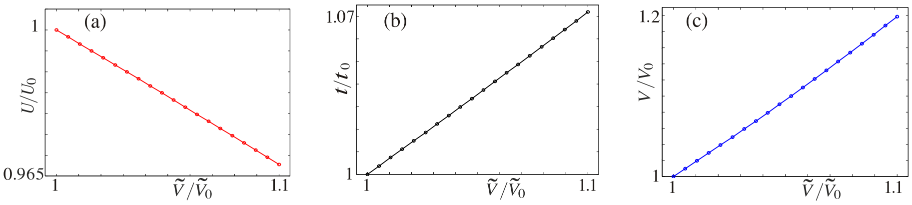

Figure 5.4: Relative change of (a) U, (b) t, and (c) V, as a function of the change in the optical lattice depth. Here we took $V_0 = 2.7\ E_R$.

eraged" wavevector k[1]. We are going to consider a one-dimensional lattice as in Fig. 5.3(a): periodic potentials in 1D can be created by superimposing additional laser beams to the setup for higher dimensions, as illustrated in Fig. 5.3(b) for a 2d square and Fig. 5.3(c) for a 3d cubic lattice.

In this system, the lattice parameter is $a = \lambda/2$. Typical values for the potential depth are $1 - 30\ E_R$ [133]. The fact that $\tilde{V} \sim E_r = 2\pi/(2\mu\lambda^2) = 2\pi/(8\mu a^2)$ suggests that it might be possible to qualitatively mimic the reduction of the lattice spacing, a by increasing the lattice depth.

To evaluate U, V and t as a function of the adiabatic change of the lattice spacing we proceed as follows. Firstly, we find the maximally localized generalized Wannier states by tuning the initial value of $\tilde{V}$ so to reproduce the experimentally observed ratio at room temperature, $U/t \sim 21$. Consequently, we increase the lattice depth of 10% and recompute the Wannier states at each step to obtain the changes in U, V and t.

The results are shown in Fig. 5.4(a)-(c) and qualitatively confirm the expected trend. Both t and V increase as anticipated, while U is slightly reduced. Obviously, it would have been unreasonable to look for a quantitative agreement, given the enormous simplification implicit in assuming such a complex system to be reproduced by a simple cosinusoidal potential.

---

[1] The word "averaged" here acknowledges that the wavevectors of the lasers used to produce the lattice must be slightly detuned from each other to avoid unwanted interference

5.4 Modelling holon-doublon decay

At this point, we are ready to move to the second task of this chapter, namely understanding the dynamics of holon-doublon pairs. To this end, we focus on the time-resolved reflectivity changes when the applied pressure is adjusted. In Sec. 5.4.1 we report the measurements of decay times as a function of pressure. We are going to model the energy dissipation of the electronic excitations via a coupling to a bosonic reservoir mimicking molecular vibrations (Sec. 5.4.2). We find that the dissipation process taking place via holon-doublon recombination into two singlons is in competition with hopping processes that tend to separate the holon and the doublon, thus slowing down the recombination process. Finally, in Sec. 5.4.3 we obtain an effective model that encompasses all of these features.

5.4.1 Experiments

Time resolved pump-probe experiments were carried out[2] by using excitation pulses of duration 100 fs and average photon energy of 1.5 eV. Renormalized time-resolved reflectivity changes, $(\Delta R)/R$, have been measured as a function of pressure. Subsequently, we have extracted the pressure-dependent holon-doublon recombination lifetimes, τ.

The experiments have been performed in two different ways: (i) the central frequency of the femtosecond pulses has been tuned in such a way so as to match the maximum of the charge-transfer (CT) resonance for each pressure (Fig. 5.5(a)-(b)), (ii) both pump and probe wavelength have been kept fixed on the center of the pressure-independent PH continuum band (Fig. 5.5(a)-(b)). The main reason to perform these two separate measurements was to investigate the possible difference of behavior between the two main features of the optical conductivity: (i) the holon-doublon (HD) bound pair, and (ii) the PH continuum.

The renormalized time-resolved reflectivity changes for of both cases are reported in Fig. 5.5(a) and (c). They show a prompt reduction of the holon-doublon band and particle hole continuum following photo-excitation, followed

---

[2] All the measurements in this section were performed by M. Mitrano with two different setups as explained in Supplementary Material of Ref. [1]

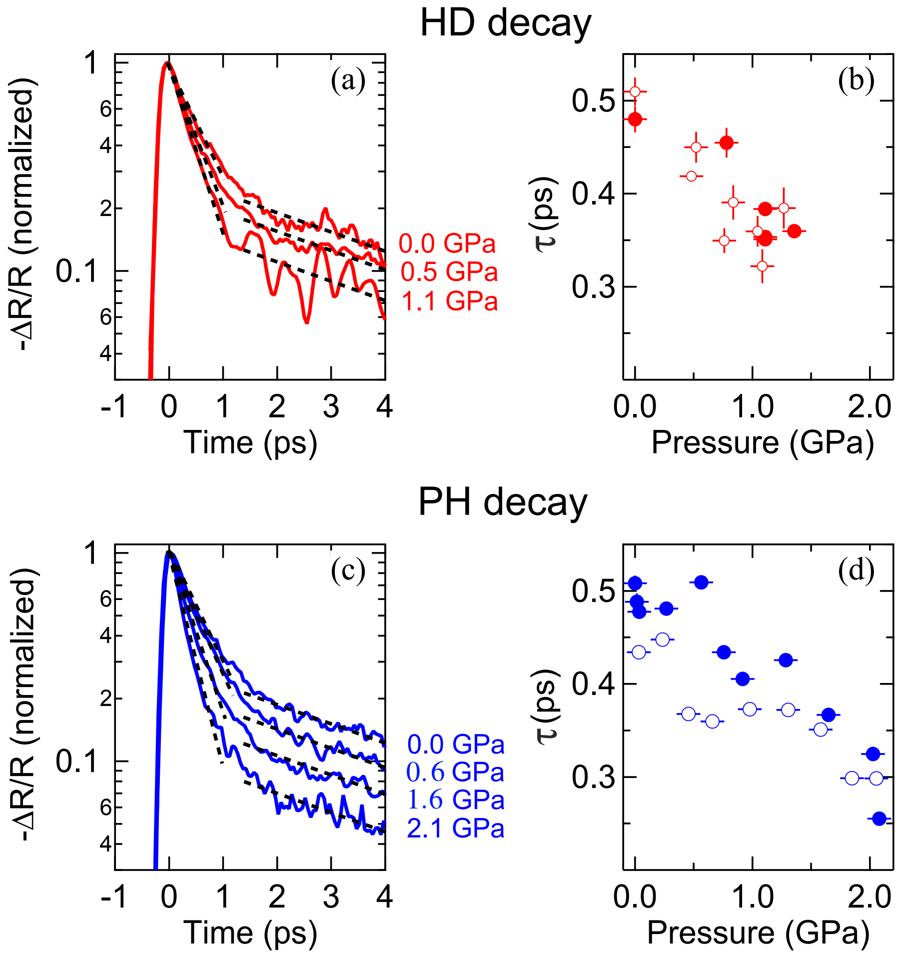

Figure 5.5: (a) Normalized $(\Delta R)/R$ time domain curves on the holon-doublon pair peak (HD) for selected pressures (solid lines). Black dashed lines are guides to the eye showing the bi-exponential decay, straight lines on a log scale. (b) Holon-doublon recombination lifetimes extracted from a fit to the data of (a). Filled and empty symbols identify distinct experimental runs. (c) Normalized $(\Delta R)/R$ time domain curves on the PH continuum peak (HD) for selected pressures (solid lines). (d) Holon-doublon recombination lifetimes extracted from a fit to the data of (c).

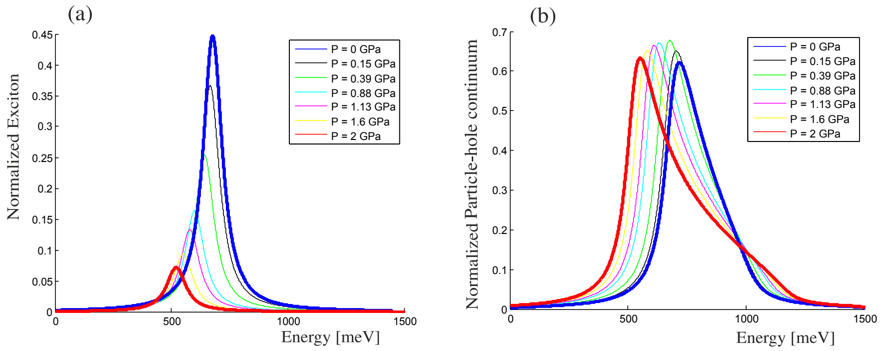

Figure 5.6: (a) Holon-doublon pair, and (b) PH continuum contributions to the optical conductivity as a function of pressure. The blue thick line is the ambient pressure initial value, the blue red line the highest pressure (2 Gpa) value. In general terms, electrons can couple both to low-frequency, collective lattice modes (phonons), and higher frequency intra-molecular molecular vibrations. Nevertheless, ET-F_2TCNQ shows very weak electron-phonon coupling so it is reasonable to assume that high-frequency molecular modes are the primary scattering partner for the observed rapid decay.

by a recovery of the signal with a time dependence that is well described by a double exponential function [76, 67]. Thus we have two decay times, one fast and one slow, but only the fast one shows pressure dependence, while the second 2.5 ps time constant is independent of pressure.

Both excitation channels exhibit a similar dependence on pressure. This behavior can be interpreted as a proof of significant intermixing of the HD and PH upon photo-excitation from the earliest time scales. This conjecture is validated by the static fitting results, showing that the ratio $V(P)/t(P)$ is reduced from ~ 3.0 to ~ 2.4. This latter value is close to the critical $V/t = 2$ in which case the exciton peak cannot be isolated from the continuum. In Fig. 5.6 we show that with increasing pressure the exciton peak indeed becomes less and less relevant.

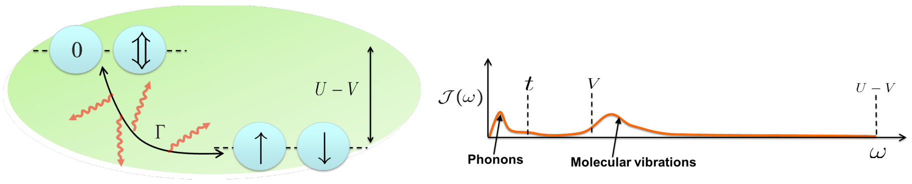

Figure 5.7: (a) Recombination of the holon-doublon configuration into a singlon-singlon pair is pictured as a two level systems separated in energy by $U - V$. The electron density is in turn coupled to a dissipative bath. (b) The bath is completely characterized by the spectral function $\mathcal{J}(\omega)$ which combines the frequency of the oscillators with their coupling. We show the relevant energies of our system: the bias $U - V$, much higher in energy than phonons and molecular vibrations, as well as t and V. The picture is a schematic, and not derived from a real calculation.

5.4.2 Holon-doublon decay in the spin-boson model

The recombination of a holon and a doublon within a pair should involve a dissipation of an energy in excess of order $\sim U - V$ by coupling to a bath. In the range explored in the experiment, the signal scales linearly with the laser fluence (i.e., the radiative flux integrated over time), but the relaxation rates are independent from it. This strongly indicates that different holon-doublon pairs do not interact with each other (sparse regime) and that the relaxation occurs locally between each pair.

To model this process we apply a generic, still well-established, description based on the celebrated spin-boson model [134]. We take a dimer of sites and label the singlon configuration as ground state, $|g\rangle$, and the holon-doublon configuration as excited state, $|e\rangle$: thus, we obtain an effective two-level system where the potential energy gap (or bias) between $|g\rangle$ and $|e\rangle$ is $U - V$. This model describes exclusively on-site decay process, hence it is necessarily incomplete since it neglect inter-site effects due to V and t. It is nevertheless convenient to introduce and study it on its own as a start. We are going to add the additional features in the following section, Sec. 5.4.3.

By coupling the electron density linearly to a continuum of bosonic modes, the following spin-boson Hamiltonian is obtained:

$$\hat{H}_F = -t\left(|0\rangle\langle g| + |g\rangle\langle 0|\right) + (U - V)|0\rangle\langle 0| + \sum_n \lambda_n \left(\hat{a}_n^\dagger + \hat{a}_n\right)|0\rangle\langle 0| \sum_n \omega_n \hat{a}_n^\dagger \hat{a}_n,$$

where $\hat{a}_n$ is the bosonic annihilation operator of the bath. This process is schematically illustrated in Fig. 5.7(a).

The environment is completely characterized by the spectral function

$$\mathcal{J}(\omega) = \pi \sum_n \lambda_n^2 \delta(\omega - \omega_n),$$

which combines the frequencies of the oscillators, ω_n, with their couplings, λ_n.

This kind of description of the electron transfer in a dissipative environment is the quantum mechanical equivalent [135] of the classical electron transfer encountered in chemistry, physics and biology [136, 137, 138, 139], used to model a wide variety of processes such as chemical redox processes, charge transfer in semiconductors, and the primary steps of photosynthesis. In condensed polar environments one observes strong electron coupling to the underlying nuclear motion, and the process is usually dominated by the nuclear reorganization that accompanies the charge rearrangement. The spectral function, $\mathcal{J}(\omega)$, is in fact the quantum version of the reorganization energy.

Depending on the particular form of $\mathcal{J}(\omega)$, the spin-boson model can have solutions which exhibit non-Markovian behavior, as well as Markovian [140]. We do not have precise knowledge of $\mathcal{J}(\omega)$, but we can approximate its form as

$$\mathcal{J}(\omega) \sim \omega^s \mathrm{e}^{-\omega/\omega_c}.$$

The parameter s is likely to be in the regime $s > 1$ for the most relevant intra- or inter-molecular vibrations [141], and its cut-off frequency, ω_c, obeys the relation $t < \omega_c < U - V$. This implies that the bath is non-adiabatic with respect to the hopping. Furthermore, the condition $U - V \gg t$ means that the model operates in the “large-bias” regime.

The super-ohmic and large-bias regime of the spin-boson model is known to exhibit overdamped behavior [134]. This causes non-Markovian memory effects (such as recurrences and oscillations in the populations due to the back-action of the environment [142]) to be highly suppressed. The dynamics of the large-bias super-ohmic regime is therefore effectively Markovian [143, 144], although not necessarily weak-coupling. This conjecture is confirmed by the experimentally measured short-time decay of the reflectivity (Fig. 5.5). This quantity is an approximate measure of the carrier density and displays a monotonic profile that is highly indicative of a Markovian process.

Within these limits, the decay rate Γ for an initial state $|e\rangle$ to arrive in $|g\rangle$ due to its interaction with the environment is

$$\Gamma = \tfrac{1}{2}\Big(\frac{t}{U-V}\Big)^2 \mathcal{J}(U-V).$$

Only the value of the spectral function at the bias energy $U - V$ to be dissipated is relevant. This value is above the cut-off energy: the closest high frequency modes are intra-molecular vibrations which, as observed in Sec. 5.2, are unaffected by pressure to leading order (see Fig. 5.7(b)). This wide energy separation makes the exact form of the spectral function not-relevant to our purposes, so that the (unknown) pressure independent value of $\mathcal{J}(U - V)$ can be taken as constant. This feature allows us to predict the recombination rate scaling with pressure P as

$$\frac{\Gamma(P)}{\Gamma_0} = \Big(\frac{t(P)}{t_0}\Big)^2 \Big(\frac{U-V_0}{U-V(P)}\Big)^2, \tag{5.4}$$

where the suffix 0 stands for ambient pressure. We remark that U is assumed to be independent of pressure. The scaling of the rate sensibly encodes: (i) an increase in the decay rate Γ with increasing hopping t (which is the process ultimately responsible for recombination), and (ii) an increase with decreasing bias $U - V$ between the levels.

It is important to notice that the introduction of a bath (i.e. of a dissipative, bosonic, decay channel) is necessary to explain the fact that the decay process becomes faster with increasing pressure. Let us assume, for sake of argument, that the only channel of holon-doublon recombination is the purely electron one. The EHM has three main energy scales: the energy of double occupancies, given by the Hubbard repulsion $U - V$, the kinetic energy given by the tunneling t, and the superexchange scale $J_{ex} = 4t^2/(U - V)$, which governs the spin dynamics. For large values of $(U - V)/t$, these three energy scales are well separated from each other: $U \gg t \gg J_{ex}$. In order for the pair to recombine, it has to dissipate the energy $U - V$ in other excitations of the system. If we denote a typical energy of an accessible excitation to be ϵ_0, this can be either $\sim t$ or $\sim J_{ex}$

depending on the background state that the doublon is propagating through. As a results of the separation of energy scales, $\epsilon_0 \ll U$, a large number $n \sim U/\epsilon_0$ of excitations must be created for doublon decay to satisfy energy constraints. For this reason, Sensarma *et al.* [145] argued that the scaling of doublon decay rate, due exclusively to dissipation via electronic excitation, is exponential which leads to a small recombination rate.

In particular, the matrix element for a doublon decay process can be calculated in n-th order perturbation theory as

$$M \sim \frac{t}{\epsilon_0} \times \frac{t}{2 \times \epsilon_0} \times \cdots \times \frac{t}{n \times \epsilon_0}.$$

The decay rate, expressed in units of t, is $\sim M^2$. Using Stirling's formula, and the fact that $n\epsilon_0 = U - V$, one finds that for large n the decay rate scales as

$$\Gamma \sim t \left(\frac{t}{U-V} \right)^{\frac{U-V}{t}} \sim t \exp\left\{ -\frac{\kappa(U-V)}{\epsilon_0} \log\left(\frac{t}{U-V} \right) \right\},$$

where κ is a constant to be extracted from experimental data. When the system is a homogeneous Mott insulator at half-filling, the only possible candidate for transfer energies are spin excitations with bandwidth $\epsilon_0 \sim J_{ex}$. This leads to the decay rate scaling as

$$\Gamma \propto \exp\left\{ -\frac{\kappa(U-V)^2}{t^2} \log\left(\frac{t}{U-V} \right) \right\}, \tag{5.5}$$

This conjecture has been confirmed by DMRG simulations [146] demonstrating that the decay mechanism of the holon-doublon pair to spin excitations is very inefficient. By applying Eq. (5.5) to the pressure dependent Hubbard parameters found previously, we find that $(U - V(P))/t(P)$ decreases from ~ 18 to ~ 7.5. Thus we would expect the decay time to increase with pressure and thus the decay time to get slower. This is exactly the opposite of what has been found in the experiments reported here in real materials.

5.4.3 Dissociation of the Holon-Doublon beyond the Spin-Boson picture

In the light of the results obtained so far, we integrate the two site model of the previous section with an effective model that takes into account the

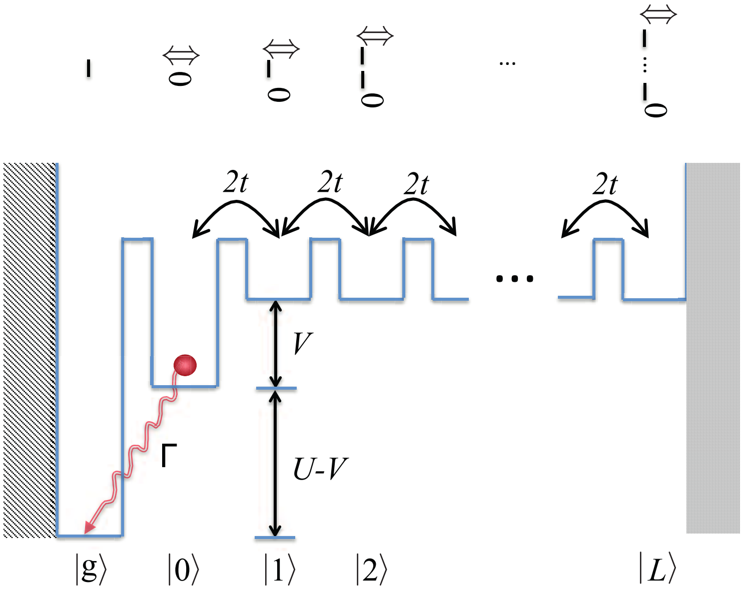

Figure 5.8: Effective model describing holon-doublon dynamics in the strong-coupling limit. The state $|g\rangle$ is the ground state containing no holon-doublon states, whereas the state $|0\rangle$ represents an adjacent holon-doublon pair. The remaining states $|l\rangle$ represent the holon and doublon being separated by l sites. In the limit $L \to \infty$ these unbound states form the PH continuum. The relaxation to $|g\rangle$ at a bare rate Γ only occurs from state $|0\rangle$.

competition between the decay mechanism, the tendency of the holon-doublon pair to separate due to hopping amplitude t, and to bind owing to V.

As already shown in previous time resolved spectroscopy experiments, at least three sites are necessary to account for the photo-response [76]. This takes into account the possibility for the bound holon-doublon pairs to tunnel into a configuration of the type, $|0, \uparrow, \Updownarrow, \downarrow, \ldots\rangle$ (of course, in adherence to a *sine qua non* condition: the pairs should be placed next to singly occupied sites, as $|0, \Updownarrow, \uparrow, \downarrow, \ldots\rangle$). This separation occurs at a rate which is determined by the hopping amplitude t and limited by a barrier V. Since we have a local decay process, the configuration $|0, \uparrow, \Updownarrow, \downarrow, \ldots, \rangle$ has a lower probability to recombine than $|0, \Updownarrow, \uparrow, \downarrow, \ldots\rangle$, as two hopping event are necessary.

In Sec. 4.3 we used a well known procedure [147, 50] that, via a unitary transformation S, renders the effective double occupation a good quantum number provided that one neglects terms $\sim t/U$. In this limit, exact eigensolutions to the EHM can be found [148] and it is possible to define spinless fermionic operators, $\hat{a}_j$ and $\hat{a}_j^\dagger$ which act only on the $\vec{n} \equiv (n_1, \ldots, n_M)$ indices in the basis kets, where n_j counts the number of particles at site j. Charge excitations of such a system are described by a spinless fermion Hamiltonian

$$\hat{H}_{\text{exc}} = U - V \sum_{j=1}^{M} \hat{n}_j \hat{n}_{j+1} - \sum_{j=1}^{M} \left(\hat{a}_j^\dagger \hat{a}_{j+1} + \hat{a}_{j+1}^\dagger \hat{a}_j \right),$$

where $n_j = 0$ or 1.

A convenient basis for the description of these charge excitations (or excitons) is in terms of a centre-of-mass coordinate, R, and a relative coordinate, r, between holons and doublons with the form

$$|\Psi_{\text{HD}}\rangle = \sum_{rR} |R + \frac{r}{2}, R - \frac{r}{2}\rangle,$$

where $|R + r/2, R - r/2\rangle = \hat{a}_{R+r/2}^\dagger \hat{a}_{R-r/2} |0\rangle$ is the vacuum of the two-body problem. The exciton is a two-particle bound state, so we look for a solution as a function of r and R. The scalar product $\langle R + r/2, R - r/2 | \hat{H}_{\text{exc}} | \Psi_{\text{HD}} \rangle$ gives a difference equation for the exciton wave function [51]. We can take the center-of-mass momentum K, equal to $K = 0$ without loss of generality. The Schrödinger equation becomes

$$2t[2\psi_n(r) - \psi_n(r - a) - \psi_n(r + a)] - 4t\psi_n(r) - V\delta_{ra} = E\psi_n(r).$$

Seeing that the reduced mass of the double occupancies and vacancies is roughtly the same, the effective hopping of the "particle" described by the relative coordinate will be double the one of holon and doublon individually. Eventually, we obtain a single particle effective Hamiltonian defined on a single-infinite tight-binding chain:

$$\hat{H}_{\text{eff}} = -2t\sum_{\alpha=1}^{L}(\hat{a}^{\dagger}_{\alpha}\hat{a}_{\alpha+1} + \hat{a}^{\dagger}_{\alpha+1}\hat{a}_{\alpha}) + U\sum_{\alpha=1}^{L}\hat{n}_{\alpha} - V\sum_{\alpha=1}^{L}\delta_{\alpha 0}\hat{n}_{\alpha}. \tag{5.6}$$

The ground state configuration, $|g\rangle$, of all singly-occupied sites has zero potential energy and is not connected by hopping to any other configuration. The configuration with adjacent holon-doublon pair, $|0\rangle$, has energy $U - V$, and all the more distant holon-doublon configurations, $|n\rangle$ $(n = 1, \ldots, L)$, have energy U and hopping amplitude $2t$. The current operator in this picture can be taken as $\hat{J} \propto \big(|g\rangle\langle 0| + |0\rangle\langle g|\big)$, which mimics the optical photo-excitation of $|g\rangle$ through the creation of an adjacent (bound) holon-doublon configuration $|0\rangle$.

The optical conductivity of the model, $\sigma_1(z) = \langle g|\hat{J}(z - \hat{H})^{-1}\hat{J}|g\rangle$, is then equivalent to the Green function $G(z) = \langle 0|(z - \hat{H})^{-1}|0\rangle$ [103], with complex frequency z. In the limit $L \to \infty$

$$G(z) = \frac{2}{z - U + 2V \pm \sqrt{(z-U)^2 - 4t^2}}. \tag{5.7}$$

By expanding the imaginary part of Eq. (5.7), and by extracting the residue of the poles, it is possible to reproduce the dominant ω_1 Mott-Hubbard exciton δ peak and the PH continuum we had previously found in the strong-coupling analytic result, Eq. (4.3). In other words, apart from the small term proportional to g_0, we can reproduce the analytic results of Eq. (4.3) via this much simpler effective model. The value of the hopping amplitude equal to $2t$ proves to play a crucial role so as to get a bandwidth of $8t$ for the PH continuum.

We account for the recombination in the strong-coupling effective model, Eq. (5.6), by introducing a local Markovian quantum dissipation process which incoherently drives $|0\rangle \to |g\rangle$ as described in Sec. 5.4.2. In more specific terms, a Lindblad mater equation [149] describes the evolution of the density matrix ρ as

$$\frac{\mathrm{d}}{\mathrm{d}\tau}\rho(\tau) = -i[\hat{H}_{\text{eff}}, \rho(\tau)] + \Gamma\Big(\hat{C}\rho(\tau)\hat{C}^{\dagger} - \tfrac{1}{2}\hat{C}^{\dagger}\hat{C}\rho(\tau) - \tfrac{1}{2}\rho(\tau)\hat{C}^{\dagger}\hat{C}\Big),$$

where $\hat{C} = |g\rangle\langle 0|$ is the jump operator. The resulting dynamics describe the competition between the local dissipation of a bound holon-doublon and the coherent evolution which acts to unbind the pair.

The addition of even one ionized holon-doublon state $|1\rangle$ (i.e. $L = 1$) which is unaffected by the decay, causes the suppression of the actual decay rate Γ_{eff} to $|g\rangle$ to the bare rate Γ as

$$\Gamma_{\text{eff}} = \frac{\Gamma}{2}\left(1 + \frac{V}{\sqrt{V^2 + 16t^2}}\right).$$

Analytic expressions for more then $L = 1$ become increasingly cumbersome, and difficult to interpret. Nevertheless, the simplicity of the model presents the advantage of making numerical calculations straightforward and easy to compare to experimental data, as we will see in the next section.

5.5 Results

We compute the population $n_g(\tau) = \text{tr}(\rho(\tau)|g\rangle\langle g|)$ in the ground state as a function of time up to 4 ps. This way, we realize that it fitted well with a trial function $n_g(\tau) = A(1 - \text{e}^{-\Gamma_{\text{eff}}\tau})$, thereby allowing a determination of the effective quasi-particle decay rate Γ_{eff} for each value of V and t.

The bare rate Γ is fitted to reproduce the experimentally measured zero pressure decay rate. Subsequently, we obtain the values of the decay rate for all other pressures by using the values for t, V, as they are reported in Fig. 5.2. This calculation is repeated for different sizes L. As L increases, we notice that the suppression of Γ_{eff} becomes more pronounced. This happens because the ionized holon-doublon pair can ballistically separate to larger distances, but remain immune to the decay. Thus, we observe that with reference to more than two sites (accounting for the ionization of the holon-doublon pair) coherent dynamics compete and slow down the relaxation caused by the local decay process.

In Fig. 5.9 we plot HD and PH continuum decay rates normalized to the ambient pressure decay rate τ_0 as a function of $(U - V)/t$, against the calculated HD lifetimes with the effective L-site model. The value of $L = 20$ physically expresses the fact that there is a finite number of double occupancies excited in

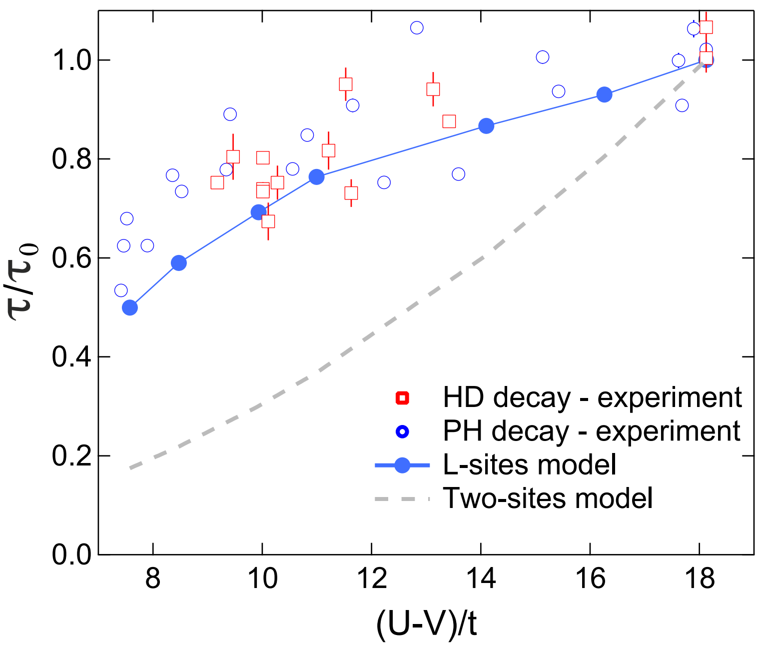

Figure 5.9: *Empty circles*: Experimental relaxation times for both HD and PH resonant excitation. *Filled circles*: Calculated holon-doublon lifetimes as function of $(U-V)/t$ using an L-site model ($L=20$) based on a numerical solution of the time dependent one-dimensional Hubbard Hamiltonian. *Dashed Curve*: Calculated holon-doublon lifetimes as function of $(U-V)/t$ using a two-site model based on the spin boson model.

the system. In other words, after L sites the propagating doublon encounters another doublon, represented here by a hard-boundary.

Notice that the two-site model developed in Sec. 5.4.2 alone is not able to reproduce the experimentally measured scaling. The dashed line in Fig. 5.9 shows the change in the relaxation rate obtained using Eq. (5.4): it gives more than five-fold increase at the largest pressure.

5.6 Summary

In this chapter, we have investigated the pressure dependence of hot holon-doublon recombination in a one-dimensional Mott insulator. By fitting the steady state IR properties with a model based on the extended Hubbard Hamiltonian, we have extracted the pressure dependence of the Hubbard parameters t and V up to 2.0 GPa, and correlated them to the recombination rates. A key inference made by comparing the experimentally determined dependence to theory is that the decay of quasi-particles is likely connected to the coherent evolution of holon-doublon pairs immediately after excitation. Based on this idea, it may be possible in the future to accelerate or decelerate the photo-induced dynamics of correlated electron systems by pulse shaping and by coherent optical control techniques.

5.A Maximally localized Wannier states

Repulsive fermions in an optical lattice allow one to realize an ideal and tunable version of the HM [44]. The perfect control and tunability of the interactions in these systems provide a "quantum-simulator" [150] for studying problems in many body physics [45, 46]. It is then crucial to be able to justify the description of a system in terms of a HM dominated by a few local terms, in order for the simulation of a complex system via an optical lattice to be ideal. The aim of this section is to discuss how to choose a set of Maximally Localized Wannier States in an optical lattice framework.

When deriving the HM in Appendix 2.A, we assumed that all the physics happened in a single band, and the effects of the others were simply to change the value of U, V and t. Here we are going to consider a more general case, in which we focus solely on a small number $J \geq 1$ of the lowest-energy bands. They may be degenerate amongst themselves but are separated in energy from the others. We shall see that considering more than one band can help the localization of the orbitals' wave functions.

To describe local interactions within this J-band subspace, a good choice of basis are states of the form

$$|\mathbf{R}\alpha\rangle = \frac{\Upsilon}{(2\pi)^D} \int_{\mathrm{BZ}} \mathrm{d}\mathbf{k} e^{-i\mathbf{k}\cdot\mathbf{R}} \sum_{\alpha=1}^{J} U_{\alpha\beta,\mathbf{k}} |\varphi_{\beta\mathbf{k}}\rangle, \tag{5.8}$$

where $|\mathbf{R}\alpha\rangle = \int \mathrm{d}\mathbf{r}\phi_\alpha(\mathbf{r}-\mathbf{R})|\mathbf{r}\rangle$, Υ is the volume of the primitive cell of the D-dimensional direct lattice. In the case $U_{\alpha\beta,\mathbf{k}}$ is diagonal, i.e., there is no band mixing, these states are exactly those first considered by Wannier [151]. The states appearing in Eq. (5.8) are commonly referred to as generalized Wannier states.

The separation in energy of the J lowest bands from the others ensures that some states $|\mathbf{R}n\rangle$ exist with mode functions $\phi_{\alpha\mathbf{R}}(\mathbf{r})$ that are exponentially localized at lattice site $\mathbf{R}$ in coordinate space [152, 153, 154, 155, 156]. This exponential localization occurs if and only if the Bloch superpositions

$$|\tilde{\varphi}_{\alpha,\mathbf{k}}\rangle = \sum_{\alpha=1}^{J} U_{\alpha\beta,\mathbf{k}} |\varphi_{\beta,\mathbf{k}}\rangle,$$

are analytic (infinitely differentiable) in $\mathbf{k}$ across the whole Brillouin zone [157]. This is a rigorous way of saying that only smoothed-out Bloch superpositions will lead to localization when Fourier transformed. When there are no degeneracies between bands can one simply use the phases of elements of a diagonal $U_{\mathbf{k}}$ (representing the freedom in the phase of each $|\varphi_{\beta,\mathbf{k}}\rangle$) to ensure the smoothness of the Bloch states $|\tilde{\varphi}_{\alpha,\mathbf{k}}\rangle$. Hence simple Wannier states provide an exponentially localized basis.

This is no longer the case when degeneracies and crossings in the band structure lead to non-analytic $|\varphi_{\beta,\mathbf{k}}\rangle$. In this situation band mixing (and therefore a non-diagonal $U_{\mathbf{k}}$) are required to obtain smooth Bloch superpositions and an exponentially-localized basis. Even when exponential localization is possible using simple Wannier states, generalized Wannier states may still significantly improve the localization. Generalized Wannier states therefore have the potential to provide a well-localized basis for the derivation of a HM. In [4] we calculate the maximally localized generalized Wannier basis by implementing an algorithm originally proposed by Marzari and Vanderbilt [158]. We also show how to derive *ab initio* local Hubbard models for several optical-lattice potential in one and two dimensions. This is very important because justifies the simulation of local Hubbard models, used to describe many condensed matter phenomena, using cold atoms in optical lattices.

5.B High-pressure pump-probe measurements

In this appendix we wish to give some information on how to perform pump-probe measurements on samples under pressure. In this chapter we reported the results of Ref. [1], aimed to measure the pressure-induced changes of the holon-doublon "quasiparticle" in ET-F_2TCNQ. Notable examples of previous ultrafast experiment have been performed under high pressure conditions, are the experiments of Hess *et al.* [159] and Trigo *et al.* [160].

The application of pressure on a solid results in a change of its lattice parameters, and in turn the electronic properties [161]. Pressure has the advantage of allowing continuous changes of both structural and electronic changes in a more gradual and flexible way with respect to chemical doping. The range of pressures routinely used in condensed matter experiments varies from ~ 0.1 GPa to ~ 300 GPa.

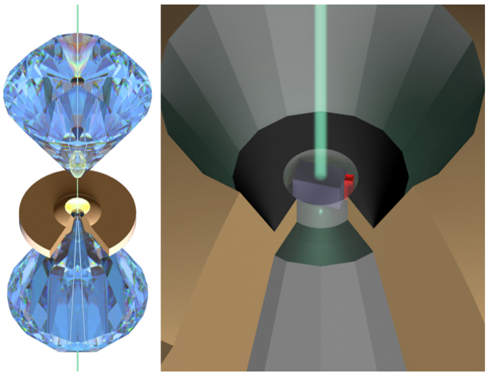

Figure 5.10: (Left) Diamond Anvil Cell scheme. (Right) Zoom of the sample chamber inside the gasket. [Image courtesy of Matteo Mitrano]

There are two ways of applying pressure to a sample: quasi-static or dynamic. In the former case, the sample is compressed using presses, anvils or diamond anvil cells (DAC, shown in Fig. 5.10); in the latter one uses shock waves. In a DAC, in order to obtain a high pressure P, instead of increasing the applied force (hydraulic press approach), one shrinks the area where the force is exerted. In this way, a modest force applied on the supporting plate where the diamond anvil sits, generates high pressures thanks to the sharpness of the diamond tip ($\sim 100-500\ \mu$m) with multiplication factors with respect to the actual pressure applied of the order $\sim 10^3$. The diamond transparency in a wide photon energy range (far IR, near IR, visible and hard X-rays) makes it an ideal tool for equilibrium spectroscopy experiments. Nevertheless, especially regarding the investigation of far IR optical properties, extreme care is required: on one hand the generation of high pressures requires the smallest possible dimension, one the other the specimen needs to be much larger than the photon wavelengths to avoid diffraction effects.

Chapter 6

Origin of the Dynamic Hubbard Model

6.1 Missing physics in the Hubbard model

As is well known in atomic physics, double occupancy of an atomic orbital gives rise to electronic angular correlations. The orbital expands, thereby reducing the Coulomb repulsion between the electrons that in turn acquire angular correlations as they try to avoid each other. Thus, a fundamental problem arises within the Hubbard Hamiltonian since it implicitly assumes that the state of two electrons in a molecular orbital is represented by a Slater determinant of the singly occupied orbital [162]. Yet, in a doubly occupied atomic orbital, actual values of Coulomb repulsion between two electrons are smaller than those predicted from a Slater determinant wave function [162, 163]. This observation suggests that molecular orbitals are not infinitely rigid.

The ordinary single band Hubbard Model (HM) may be adequate to explain systems with low filling, as the electrons can avoid each other. In contrast, when the band occupation equals or exceeds half-filling, the dynamics of the system will necessarily involve doubly occupied molecular orbitals. As a consequence, the large cost in Coulomb energy cannot be avoided. Thus, it is precisely the existence of the electron-electron interaction, which the Hubbard U attempts to model, that makes it somewhat questionable to describe the doubly occupied orbital by using a single Slater determinant.

Attempting at overcoming this deficiency, Hirsch [164] has introduced the so-called Dynamic Hubbard Model (DHM): this includes, in the most minimal way, the physics of orbital relaxation by coupling the on-site interaction term (Hubbard U) with an auxiliary degree of freedom modeled either as an additional orbital, spin or boson mode. This model appears to resemble closely the standard Holstein model [165], where the electron density couples linearly to phonons, leading to the formation of polarons. However, in a DHM the vibrational modes couple to the double occupancy, rather than to the electron density. The terms coupling the electronic degrees of freedom to the oscillator position, $\hat{q}$, will be of the form $\sim (\hat{n}_\uparrow \hat{n}_\downarrow)\hat{q}$, rather then the conventional Holstein coupling: $\sim (\hat{n}_\uparrow + \hat{n}_\downarrow)\hat{q}$. This way, the bosons dress the electron double occupancies alone, causing an intrinsic electron-hole asymmetry [166] and leading to an unconventional mechanism of superconductivity [167, 168].

Apart from including crucial physics, the DHM also points to new ways in which solid state systems can be measured and manipulated by means of ultrafast optical techniques. In this and the next two chapters, we shall advocate mode selective modulation spectroscopy as a mean of exposing information about the nature and strength of coupling to a given local vibrational mode.

In the previous chapter, we took into account all the local vibrational modes together, and modeled their effects simply as a bath used by the electronic excitations to dissipate energy. Here we use a completely different approach: we strongly drive just *one* selected mode as explained in Sec. 2.1.3, and amplify its influence on macroscopic observables.

Our goal is to show that mode selective driving elevates the contribution of the chosen modes beyond a simple scalar renormalization of U. This way it *deconstructs* the HM by requiring the vibrations' quantum mechanical DOF to be explicitly accounted for in a DHM. Such information, previously hidden within an effective renormalized Hubbard description, can reveal missing physics which proves to be relevant to the out-of-equilibrium and dynamical properties. We are going to start by developing a model able to capture the essential features of the coupling between valence electron orbitals and molecular vibrations with different symmetries.

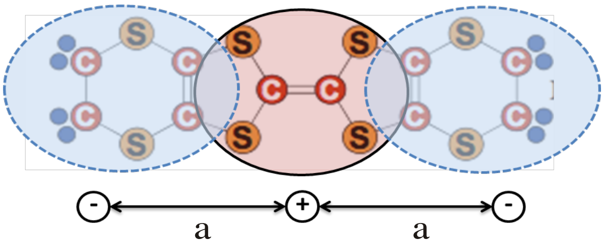

Figure 6.1: Minimal three-ion toy model describing the BEDT-TTF (ET) molecule. The outer ions have a charge $q_0 < 0$, whereas the central ion has a charge $q_c > 0$ and is separated from the outer ones by a distance a. The expected polarity is shown.

6.2 Toy model for intramolecular vibrations

The "toy" model developed in this section focus on reproducing some of the basic symmetries which are expected for real vibrations, and the difference of their coupling to valence electrons. In the case of ET-F$_2$TCNQ, the ET molecule acts as the electron donor and therefore dictates the conduction properties of the material. As explained in Sec. 2.1.2, there is one single valence π-electron per molecular site.

The complex charge distribution of the molecule is assumed to be contained within a region of radius R. We suggest a minimal model describing the backbone of the molecule as an effective system of 3 point charges which are located at the origin and at $\pm a$ of the z-axes taken as reference (Fig. 6.1). The valence electron located at a radius $r > R$ sees only the backbone because of the screening of inner electrons, and has a symmetrical extended charge distribution about the origin. The donor molecule, ET, possesses an overall positive charge, say Δq, that we model by assigning a charge q_c to the central ion, and q_0 to the two outer ions. This way, the distribution is symmetric and once the valence electron is included, the total charge is $q_c + 2q_0 - 1 = \Delta q$.

We wish to explore the properties of a valence electron mostly determined by the part of the electrons' wave function lying outside the charge distribution. The valence orbital needs to be modeled so that its value is significant over distances $r \gg a$ and $r > R$. We are going to consider the effects of both

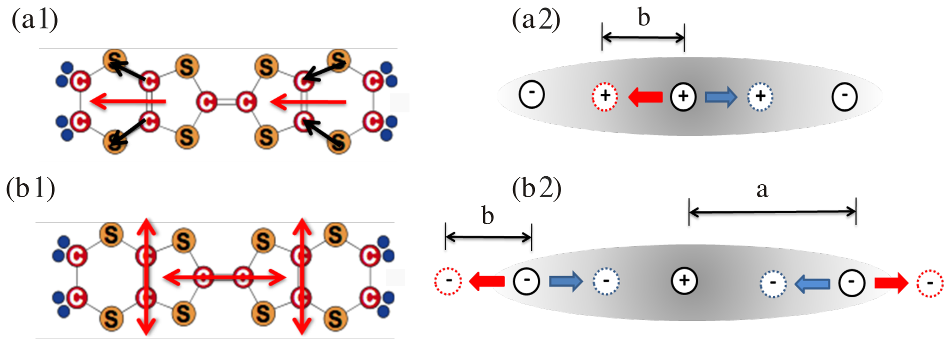

Figure 6.2: (a1) Vibrational IR active mode excited in the ET molecule and (a2) its implementation in our three-ion model. (b1) Vibrational Raman active mode excited in the ET molecule and (b2) its implementation in our three-ion model.

antisymmetric (Fig. 6.2(a1)) and symmetric (Fig. 6.2) driving, motivated by the fact that they can be realized via IR and Raman excitations, respectively [2]. The former is akin to an oscillating dipole breaking the initial symmetry of the molecule; the latter is instead captured by an oscillating quadrupole leaving the initial symmetry intact. We model the IR antisymmetric excitations by displacing the central charge of a quantity b along the axis of the three charges (Fig. 6.2(a2)). Then we mimic the Raman symmetric driving by displacing the outer two charges by $+b$ and $-b$ ($b < a$) as shown in Fig. 6.2(b2), respectively. To lowest order in b, the resulting perturbation to the potential energy function for the valence electron is $\Delta V_{IR} \sim b/r^2$ for an IR excitation and $\Delta V_{Ra} \sim ab/r^3$ for a Raman one. To analyze the influence of vibrations on the electronic system we work in the Born-Oppenheimer (BO) approximation, in which the motion of the ions is assumed to be much slower than the electron motion in the valence orbital.[1] The vibrational perturbation, then, causes adiabatic mixing of unperturbed valence states with higher-lying excited states. The effects of this mixing can be computed with time-independent perturbation theory.

In general a spin-independent coupling between a local harmonic oscillator

---

[1] Notice that this BO approximation refers to rearrangement of the valence electron within the orbital, and has nothing to do with the relation between inter-orbital dynamics (dependent on t and V) and vibrations.

and the electronic configuration of a site can be written in terms of $\hat{n}_j = \hat{n}_{j\uparrow} + \hat{n}_{j\downarrow}$ and $\hat{n}_{j\uparrow}\hat{n}_{j\downarrow}$ only, as the number operator $\hat{n}_j$ is fermionic. We assume that this coupling can be expressed as $\hat{n}_j f(\hat{q}_j) + \hat{n}_{j\uparrow}\hat{n}_{j\downarrow} g(\hat{q}_j)$, where $f(\hat{q}_j)$ and $g(\hat{q}_j)$ are two functions of the local mode coordinate that are not known a priori. By expanding the functions f and g into a Taylor series we obtain

$$\hat{H}_I = \sum_j \hat{n}_j (A_1 \hat{q}_j + A_2 \hat{q}_j^2 + \ldots) + \hat{n}_{j\uparrow}\hat{n}_{j\downarrow}(B_1 \hat{q}_j + B_2 \hat{q}_j^2 + \ldots),$$

with coupling constants A_i, B_i which are constrained by the symmetry of the molecular modes [169]. An antisymmetric infrared vibration causes admixing of the valence orbital with higher-lying excited state of differing parity and induces an energy shift that is an even function of $\hat{q}_j$, meaning e.g. that $A_1 = 0$. This already precludes that such a vibration can be described by a conventional Holstein-Hubbard type interaction. In contrast, a symmetric Raman vibration admixes higher-lying states of the same parity and causing a linear energy shift with non-zero A_1.

The second term in the expression for $\hat{H}_I$, which includes coupling to the double occupancy, is determined by computing the Coulomb repulsion arising from both electrons occupying the admixed vibrational orbital

$$|\psi(b)\rangle = |g\rangle + c(b)|e\rangle + \ldots .$$

Here $|g\rangle$ and $|e\rangle$ denote the bare unperturbed valence orbital and the higher-lying excited states, respectively, while $c(b)$ is a displacement dependent admixing coefficient. The variation in U is then given by

$$U(b) = \langle\psi(b)|_1 \langle\psi(b)|_2 \Big(\frac{1}{r_{12}}\Big) |\psi(b)\rangle_1 |\psi(b)\rangle_2,$$

where $r_{12} = |\vec{r}_1 - \vec{r}_2|$ is the modulus of the distance between the two electrons. Retaining these terms is crucial to properly describing how vibrations modify the on-site Hubbard U interaction.

For the infrared vibration the differing parity of the states in the admixture causes $U(b)$ to again vary, to lowest order, quadratically with displacement q (implying $B_1 = 0$), while the Ramain vibration retains a linear dependence. It is found that $B_2 < 0$ for the infrared mode because the admixed vibrational orbital spatially expands for any non-zero displacement in this simple mode, as

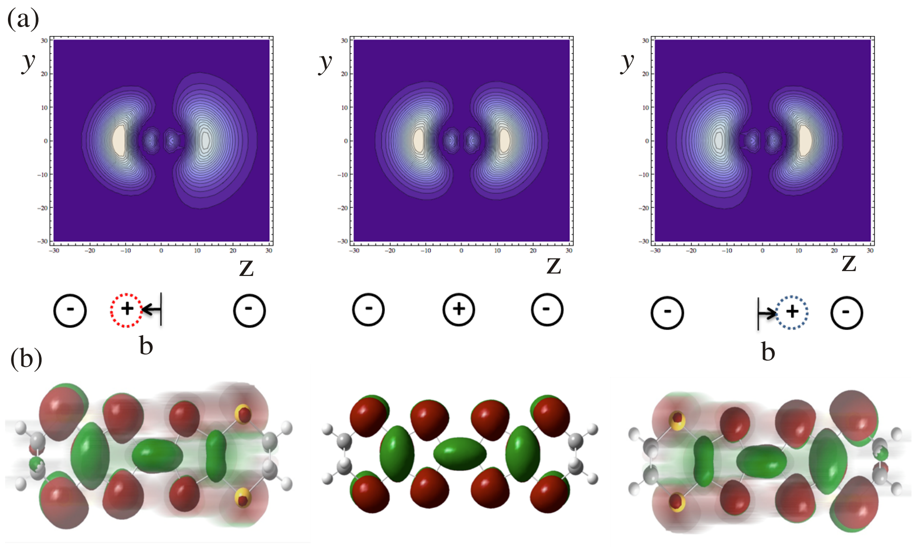

Figure 6.3: (a) Contour plot of the charge distribution in $z-y$ plane of an orbital composed of an admixture of $4d$ and $3p$ states with a $|g\rangle = |4s\rangle$, as it adiabatically follows the underlying vibration. The plots show from left to right a displacement of the central ion with charge $q_c > 0$ by $c(b) = -0.2$, $c(b) = 0$, and $c(b) = 0.2$. (b) Snapshot of the electron charge distribution computed within the frozen phonon approximation for large normal mode displacement. The normal displacement leads to an effectively enlarged molecular orbital distribution in time average.

illustrated in the caricature of the ET orbital (Fig. 6.2). This conjecture has been confirmed by approximating the eigenstates of the 3 ion system by hydrogenic states and by computing the charge distribution of an orbital composed of an admixture of states with opposite parity. The orbital is taken to adiabatically follow the underlying vibration. An example of this is shown Fig. 6.3.

We remark that the inclusion of these interaction terms accounts only for the energy changes caused by $|\psi(b)\rangle$, but it neglects any change to the valence orbital itself. The DHM therefore retains the standard Hubbard electronic state for double occupancy as the Slater determinant of $|g\rangle$, but models the energetics of orbital relaxation.

6.3 Forming a Dynamic Hubbard model

In this section, we use the intuition developed so far with our toy model to formally obtain a Dynamic Hubbard Hamiltonian. We have shown that a *local* molecular vibration is sensitively dependent on the electronic configuration of the site. Thus, we shall allow local electron-oscillator coupling to holon, singlon and doublon states which can be either linear of quadratic in $\hat{q}_j$ based on the symmetry of the vibrational model.

This situation is intrinsically different from a lattice phonon, which consists of the *collective* motion of many molecules in the solid and is extremely heavy in comparison to a single electron. It is therefore customary to neglect the effects of the electronic configuration on the phonon frequency itself. Likewise, one considers the coupling between them to take place via the electron density and phonon displacement.

We are going to introduce formally the the oscillator's degrees of freedom (DOF) and their coupling to the electronic DOF. By using a generalized Lang-Firsov transformation [170], we will subsequently show that the spectrum of the Hamiltonian can be obtained in the atomic limit. Owing to the very different physics emerging for the linear and quadratic coupling, the two cases will be studied separately.

With reference to a vibration localized on a single molecule this assumption is no longer valid and different forms of back-action, or coupling, between the oscillators are expected. Let us take as reference oscillator the one determined for the singlon state and assign it a "free" Hamiltonian for an oscillator of mass m and frequency Ω for site j as

$$\hat{H}_{s,j} = \frac{\hat{\mathbf{p}}_j^2}{2m} + \tfrac{1}{2}m\Omega^2\hat{q}_j^2 = \Omega\big(\hat{a}_j^\dagger\hat{a}_j + \tfrac{1}{2}\big),$$

where $\hat{a}_j^\dagger$ and $\hat{a}_j$ are the oscillators raising and lowering operators. We shall denote the eigenstates of this reference oscillator as $|n_j\rangle$ with an energy $\epsilon_s(n_j) = \Omega(n_j + \frac{1}{2})$. The corresponding harmonic oscillator length scale is the Bohr radius $a_0 = 1/\sqrt{m\Omega}$, and the entire chain has a free oscillator Hamiltonian $\hat{H}_s = \sum_j \hat{H}_{s,j}$. The singlon states are decoupled relative to this oscillator, while the holon and doublon states for any site will experience additional coupling terms.

6.3.1 Raman mode - linear coupling

Following the discussion in Sec. 6.2, for the symmetric Raman mode the doublon and holon coupling terms are linear and of the form $\hat{H}^d_{R,j} = g^d_R \mathbb{P}^d_j \hat{q}_j$, and $\hat{H}^h_{R,j} = g^h_R \mathbb{P}^h_j \hat{q}_j$, respectively, so that in total

$$\hat{H}_{R,j} = \left(g^d_R \mathbb{P}^d_j + g^h_R \mathbb{P}^h_j\right)\hat{q}_j.$$

Here g^d_R and g^h_R are coupling parameters, and $\mathbb{P}^h_j = \mathbb{1}_j - \hat{n}_{j\uparrow}\hat{n}_{j\downarrow}$, $\mathbb{P}^s_j = \hat{n}_{j\uparrow} - 2\hat{n}_{j\uparrow}\hat{n}_{j\downarrow}$, $\mathbb{P}^d_j = \hat{n}_{j\uparrow}\hat{n}_{j\downarrow}$ are the local projectors on site j on to the holon, singlon, and doublon states, respectively. The full interaction, $\hat{H}_R = \sum_j \hat{H}_{R,j}$, in combination with the free evolution, gives the total oscillator terms for site j as

$$\begin{aligned}\hat{H}_{s,j} + \hat{H}_{R,j} =& \Omega(\hat{a}^\dagger_j \hat{a}_j + \tfrac{1}{2})\mathbb{P}^s_j + \left[\Omega(\hat{a}^\dagger_j \hat{a}_j + \tfrac{1}{2}) + g^h_R \frac{a_0}{\sqrt{2}}(\hat{a}^\dagger_j + \hat{a}_j)\right]\mathbb{P}^h_j \\ &+ \left[\Omega(\hat{a}^\dagger_j \hat{a}_j + \tfrac{1}{2}) + g^d_R \frac{a_0}{\sqrt{2}}(\hat{a}^\dagger_j + \hat{a}_j)\right]\mathbb{P}^d_j. \\ =& \hat{H}_{s,j}\mathbb{P}^s_j + \hat{H}_{h,j}\mathbb{P}^h_j + \hat{H}_{d,j}\mathbb{P}^d_j.\end{aligned}$$

New oscillator Hamiltonians arise for the holon and doublon due to the couplings, generically denoted as $\hat{H}_{h,j}$ and $\hat{H}_{d,j}$, respectively. As it is well known, a linear coupling means that when the local electronic state is a holon or doublon, the oscillator behaves as a displaced version of the reference singlon oscillator [171]. Formally the oscillators are related by the unitary displacement transformation $\hat{D}_j(\chi) = \exp\left[\chi(\hat{a}^\dagger_j - \hat{a}_j)\right]$, where for holon and doublon we choose the real dimensionless scalars $\chi_h = g^h_R a_0/\Omega\sqrt{2}$ and $\chi_d = g^d_R a_0/\Omega\sqrt{2}$. We obtain the energy shifts: $\hat{H}_{h,j} = \hat{D}^\dagger_j(\chi_h)\hat{H}_{s,j}\hat{D}_j(\chi_h)$ and $\hat{H}_{d,j} = \hat{D}^\dagger_j(\chi_d)\hat{H}_{s,j}\hat{D}_j(\chi_d)$. As a result, the complete on-site oscillator Hamiltonian is

$$\begin{aligned}\hat{H}_{s,j} + \hat{H}_{R,j} =& \Omega(\hat{a}^\dagger_j \hat{a}_j + \tfrac{1}{2})\mathbb{P}^s_j + \left\{\Omega\left(\hat{D}^\dagger_j(\chi_h)\hat{a}^\dagger_j \hat{a}_j \hat{D}_j(\chi_h) + \tfrac{1}{2}\right)\right\}\mathbb{P}^h_j \\ &+ \left\{\Omega\left(\hat{D}^\dagger_j(\chi_d)\hat{a}^\dagger_j \hat{a}_j \hat{D}_j(\chi_d) + \tfrac{1}{2}\right)\right\}\mathbb{P}^d_j. \end{aligned} \tag{6.1}$$

Eq. (6.1) shows that the eigenstates of the holon and doublon oscillator are related to those of the reference singlon oscillator via $|n_j\rangle_h = \hat{D}^\dagger_j(\chi_h)|n_j\rangle$ and $|n_j\rangle_d = \hat{D}^\dagger_j(\chi_d)|n_j\rangle$, with $n_j \in \{0, 1, 2, \cdots\}$ being the phonon occupation of the reference singlon oscillator for each site. The energies of these eigenstates are $\epsilon_h(n_j) = \Omega(n_j + \frac{1}{2}) - \Omega\chi_h^2$ and $\epsilon_d(n_j) = \Omega(n_j + \frac{1}{2}) - \Omega\chi_d^2$, respectively. Aside from an energy shift, they are identical to the singlon oscillator spectrum.

By including the linear coupling we have finally obtained a DHM describing the full electronic-oscillator Hamiltonian

$$\hat{H}_{\mathrm{DHM}} = \hat{H}_{\mathrm{EHM}} + \hat{H}_s + \hat{H}_R, \tag{6.2}$$

where $\hat{H}_{\mathrm{EHM}} = -t\sum_j(\hat{c}^\dagger_{j,\sigma}\hat{c}_{j+1,\sigma} + \hat{c}^\dagger_{j+1,\sigma}\hat{c}_{j,\sigma}) + U\sum_j \hat{n}_{j,\uparrow}\hat{n}_{j,\downarrow} + V\sum_j \hat{n}_j\hat{n}_{j+1}$ is the EHM Hamiltonian, $\hat{H}_s = \sum_j \hat{H}_{s,j}$ and $\hat{H}_R = \sum_j \hat{H}_{R,j}$. Notice that the overall oscillator state depends explicitly on the electronic configuration.

The effects of the coupling on the Hamiltonian become much more clear if we decouple the two contributions. In the atomic limit, this is achieved by performing a Lang-Firsov transformation [170] on each site of the form

$$\begin{aligned}\hat{X}_j =& \exp\left[-\chi_h(\hat{a}_j - \hat{a}^\dagger_j)\mathbb{P}^h_j\right]\exp\left[-\chi_d(\hat{a}_j - \hat{a}^\dagger_j)\mathbb{P}^d_j\right],\\ =& \left[(\mathbb{1}_j - \mathbb{P}^h_j) + \hat{D}^\dagger_j(\chi_h)\mathbb{P}^h_j\right]\left[(\mathbb{1}_j - \mathbb{P}^d_j) + \hat{D}^\dagger_j(\chi_d)\mathbb{P}^d_j\right]\\ =& \mathbb{P}^s_j + \hat{D}^\dagger_j(\chi_h)\mathbb{P}^h_j + \hat{D}^\dagger_j(\chi_d)\mathbb{P}^d_j.\end{aligned}$$

While $\hat{X}_j$ has no effect on a local singlon state, it performs an inverse displacement transformation $\hat{D}^\dagger_j(\chi_h)$ and $\hat{D}^\dagger_j(\chi_d)$ on the holon and doublon states, respectively. The overall effect on site j, by using the identity $\mathbb{1}_j = \mathbb{P}^h_j + \mathbb{P}^s_j + \mathbb{P}^d_j$, is

$$\begin{aligned}\hat{X}^\dagger_j\left(\hat{H}_{s,j} + \hat{H}_{R,j}\right)\hat{X}_j =& \Omega(\hat{a}^\dagger_j\hat{a}_j + \tfrac{1}{2})\mathbb{P}^s_j + \left[\Omega(\hat{a}^\dagger_j\hat{a}_j + \tfrac{1}{2}) - \Omega\chi_h^2\right]\mathbb{P}^h_j +\\ & \left[\Omega(\hat{a}^\dagger_j\hat{a}_j + \tfrac{1}{2}) - \Omega\chi_d^2\right]\mathbb{P}^d_j.\\ =& \hat{X}^\dagger_j\left(\hat{H}_{s,j} + \hat{H}_{R,j}\right)\hat{X}_j = \hat{H}_{s,j} - \Omega\chi_h^2\mathbb{P}^h_j - \Omega\chi_d^2\mathbb{P}^d_j.\end{aligned}$$

Considering that both Coulomb terms, $U\hat{n}_{j,\uparrow}\hat{n}_{j,\downarrow} = U\mathbb{P}^d_j$ and $V\hat{X}^\dagger_j\hat{n}_j\hat{n}_{j+1}\hat{X}_j = V\hat{n}_j\hat{n}_{j+1}$, commute with this transformation, the electronic system is completely decoupled from the oscillators, and $\hat{n}_j$ is a good quantum number. We have therefore managed to remove the configuration dependence on the oscillator part of the eigenstates for the total Hamiltonian.

6.3.2 Infrared mode - quadratic coupling

The analysis for the quadratic coupling is less straightforward. In Sec. 6.2 we have found that an antisymmetric IR vibration leads to a quadratic term coupling to the electronic density and double occupancy as

$$\Delta\hat{H}_1 = -\sum_j C_1(\hat{n}_{j,\uparrow} + \hat{n}_{j,\downarrow})\hat{q}_j^2 - \sum_j C_2\hat{n}_{j,\uparrow}\hat{n}_{j,\downarrow}\hat{q}_j^2,$$

respectively, where C_1 and C_2 are two positive constants. The total interaction term at site j can be written in a more transparent way as

$$\begin{aligned}\hat{H}_{h,j} + \hat{H}^s_{I,j} + \hat{H}^d_{I,j} = & \left[\frac{\hat{p}_j^2}{2m} + \tfrac{1}{2}m\Omega_h^2\hat{q}_j^2\right]\mathbb{P}^h_j + \left[\frac{\hat{p}_j^2}{2m} + \tfrac{1}{2}m\left(\Omega_h^2 - 2\frac{C_1}{m}\right)\hat{q}_j^2\right]\mathbb{P}^s_j\hat{q}_j^2 \\ & + \left[\frac{\hat{p}_j^2}{2m} + \tfrac{1}{2}m\left(\Omega_h^2 - 2\frac{C_2 + 2C_1}{m}\right)\hat{q}_j^2\right]\mathbb{P}^d_j\hat{q}_j^2,\end{aligned}$$

so that we can identify how the frequencies of the oscillators depend on the electronic configuration. The positivity of C_1 and C_2 implies that $\Omega_h > \Omega > \Omega_d$, where the suffices h and d denote holon and doublon, respectively.

The full interaction term $\hat{H}_I = \sum_j \hat{H}_{I,j}$ can be further simplified by defining two positive coupling constants $g_I^d = C_2 + 2C_1$ and $g_I^h = C_1$, so that doublon and holon interaction terms become $\hat{H}^d_{I,j} = -g_I^d\mathbb{P}^d_j\hat{q}_j^2$, and $\hat{H}^h_{I,j} = g_I^h\mathbb{P}^h_j\hat{q}_j^2$, respectively. In total,

$$\hat{H}_{I,j} = \left(g_I^h\mathbb{P}^h_j - g_I^d\mathbb{P}^d_j\right)\hat{q}_j^2. \tag{6.3}$$

The signs in Eq. (6.3) highlight a very important property: an empty site will vibrate with a frequency $\Omega_h > \Omega$, whereas a doubly occupied site will perform harmonic motion with frequency $\Omega_d < \Omega$.

In combination with the free evolution of the singlons this interaction gives the total oscillator terms for site j as

$$\begin{aligned}\hat{H}_{s,j} + \hat{H}_{I,j} = & \Omega(\hat{a}_j^\dagger\hat{a}_j + \tfrac{1}{2})\mathbb{P}^s_j + \left[\Omega(\hat{a}_j^\dagger\hat{a}_j + \tfrac{1}{2}) + \tfrac{1}{2}g_I^h a_0^2(\hat{a}_j^\dagger + \hat{a}_j)^2\right]\mathbb{P}^h_j \\ & + \left[\Omega(\hat{a}_j^\dagger\hat{a}_j + \tfrac{1}{2}) - \tfrac{1}{2}g_I^d a_0^2(\hat{a}_j^\dagger + \hat{a}_j)^2\right]\mathbb{P}^d_j. \\ = & \hat{H}_{s,j}\mathbb{P}^s_j + \hat{H}_{h,j}\mathbb{P}^h_j + \hat{H}_{d,j}\mathbb{P}^d_j.\end{aligned}$$

Encouraged by the results of the linear coupling analysis, we wish to find a transformation that decouples the electronic and oscillators' terms.

The oscillators for holons and doublons are related to the singlon ones by the unitary squeezing transformation [172, 173, 174]

$$\hat{S}(\xi) = \exp\left[\tfrac{1}{2}\xi(\hat{a}_j^{\dagger\,2} - \hat{a}_j^2)\right],$$

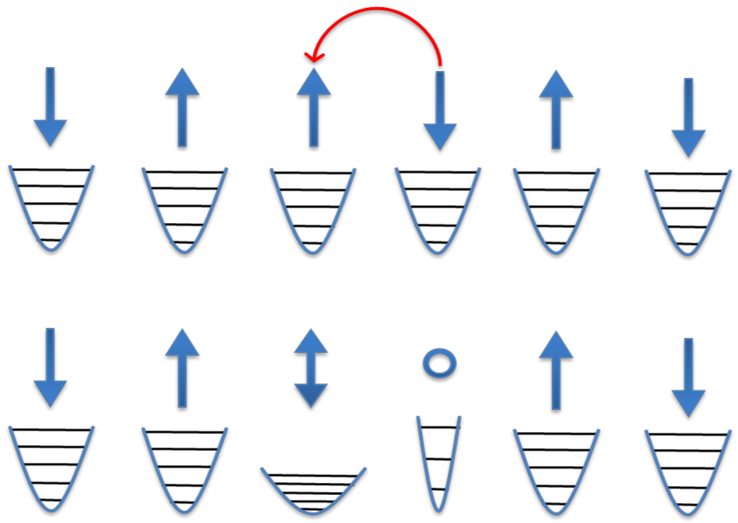

Figure 6.4: A schematic of the DHM used here for the IR mode. Each site has an electronic and harmonic oscillator DOF associated to it. In the thermal state of the system each site is singly occupied and the frequency of the oscillator is Ω. If an electron hops to its neighbor via probing or fluctuations, a holon-doublon pair is created. As a consequence the electronic state is in the first excited Hubbard band. In the doublon-site the corresponding oscillator slackens with an abrupt frequency reduction to $\Omega_d < \Omega$, whereas in the hole site the oscillator tightens with a frequency increase to $\Omega_h > \Omega$.

as $\hat{h}_j = \hat{S}^\dagger(\xi_h)\hat{a}_j\hat{S}(\xi_h)$ and $\hat{d}_j = \hat{S}^\dagger(\xi_d)\hat{a}_j\hat{S}(\xi_d)$, with real squeezing parameters $\xi_h = \log(\sqrt{\Omega_h/\Omega})$ and $\xi_d = \log(\sqrt{\Omega_d/\Omega})$, respectively. The holon and doublon frequencies are defined as $\Omega_h = \Omega\sqrt{1+2g_I^h a_0^2/\Omega}$ and $\Omega_d = \Omega\sqrt{1-2g_I^d a_0^2/\Omega}$. The corresponding oscillators are the *squeezed* versions of the reference singlon oscillator, as schematically illustrated in Fig. 6.4. Once more, in the atomic limit the explicit dependence on the electronic configuration can be removed by means of a generalized Lang-Firsov transformation on each site of the form

$$\begin{aligned}\hat{X}_j =& \exp\left[-\tfrac{1}{2}\xi_h(\hat{a}_j^{\dagger\,2} - \hat{a}_j^2)\mathbb{P}_j^h\right]\exp\left[-\tfrac{1}{2}\xi_d(\hat{a}_j^{\dagger\,2} - \hat{a}_j^2)\mathbb{P}_j^d\right], \\ =& \mathbb{P}_j^s + \hat{S}^\dagger(\xi_h)\mathbb{P}_j^h + \hat{S}^\dagger(\xi_d)\mathbb{P}_j^d.\end{aligned}$$

The operator $\hat{X}_j$ does not affect the local singlon state, while implementing an inverse squeezing transformation, $\hat{S}^\dagger(\xi_h)$ and $\hat{S}^\dagger(\xi_d)$, on the holon and doublon states, respectively. Locally on-site j we find

$$\hat{X}_j^\dagger \left(\hat{H}_{s,j} + \hat{H}_{I,j}\right) \hat{X}_j = \Omega(\hat{a}_j^\dagger \hat{a}_j + \tfrac{1}{2})\mathbb{P}_j^s + \Omega_h(\hat{a}_j^\dagger \hat{a}_j + \tfrac{1}{2})\mathbb{P}_j^h + \Omega_d(\hat{a}_j^\dagger \hat{a}_j + \tfrac{1}{2})\mathbb{P}_j^d.$$

The eigenstates of the holon and doublon oscillator are related to those of the reference singlon oscillator via $|n_j\rangle_h = \hat{S}^\dagger(\xi_h)|n_j\rangle$ and $|n_j\rangle_d = \hat{S}^\dagger(\xi_d)|n_j\rangle$. Their energies are $\epsilon_h(n_j) = \Omega_h(n_j + \frac{1}{2})$ and $\epsilon_d(n_j) = \Omega_d(n_j + \frac{1}{2})$, respectively.

We can immediately notice one crucial difference with the linear case: the frequency of the oscillators changes depending on the electronic configurations, causing the holon and doublon spectra to be different from the one of the singlon oscillator. This is schematically shown in Fig. 6.5. In the next chapter, we shall see that this has very deep consequences on the optical response.

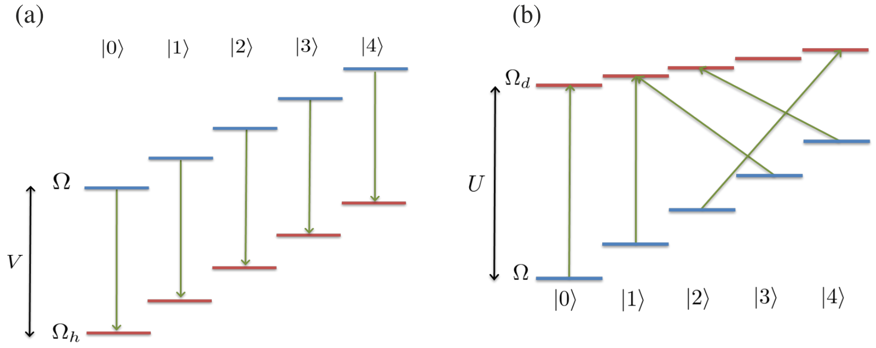

Figure 6.5: (a) A depiction of the singlon and holon oscillator energy ladder with frequencies Ω and Ω_h, respectively, where $\Omega_h \sim \Omega$. The holon ladder energy includes the $-V$ electron interaction energy below the singlon ladder. This reflects its binding to the adjacent doublon. (b) A depiction of the singlon and doublon oscillator energy ladder with frequencies Ω and Ω_d, respectively, where Ω_d 0.3Ω. The doublon ladder includes the U electron interaction energy above the singlon ladder. In both (a) and (b) some of the possible transitions are highlighted.

6.4 Stationary and excited states of the system

In the previous sections, we have introduced the DHM to take into account the effects of local vibrations on the energy of the system. Since our aim is to apply this model to compute observable quantities, we also need to characterize the initial state of our system. All the experiments we are going to consider in this thesis are performed at room temperature, $T \sim 300$ K. Let us recall that the ET-F$_2$TCNQ is a half-filled Mott insulator (MI), with one-dimensional transport properties described by the EHM with $U/t \sim 21$ [1]. At this temperature, the system does not display any long-range Neél order. In the strong coupling limit $U \gg t > k_B T$, and electron double-occupancies are highly suppressed.

These observations suggest that the thermal state of the electron system is well approximated by the half-filled "hot" spin MI state:

$$\rho_s = \frac{1}{2^M} \sum_{\vec{\sigma}} |\vec{\sigma}\rangle\langle\vec{\sigma}|, \tag{6.4}$$

where $|\vec{\sigma}\rangle$ is a spin configuration space, e.g., $|\uparrow\downarrow \ldots \downarrow\uparrow\uparrow\rangle$. The state in Eq. (6.4) models an infinite temperature spin configuration (that is $k_B T \gg t^2/U$), and a zero temperature motional configuration (consistent with $k_B T \ll t$).

The oscillators, in turn, are assumed to be initially in their ground state, $|0\rangle$: the condition $k_B T < \Omega$ is satisfied for either vibrational mode[2], so that higher vibrational states of the localized molecular oscillator are essentially unoccupied at room temperature. The full thermal state of the electron-oscillator system can be expressed $\rho_T = \rho_s \otimes \prod_{j=1}^{M} |0\rangle\langle 0|$.

When the initial state is vibrationally excited, we can assume each free singlon oscillator as prepared instantaneously in an identical coherent state $|\alpha\rangle$, where $\alpha = |\alpha| \mathrm{e}^{i\phi}$. If the excitation pulse has no carrier-envelope-phase stability, we average over ϕ which is equivalent to using a Poissonian statistical mixture of singlon vibrational number states, $|n\rangle$,

$$\rho_\alpha = \mathrm{e}^{-|\alpha|^2} \sum_n \frac{|\alpha|^{2n}}{n!} |n\rangle\langle n|. \tag{6.5}$$

The total vibrationally driven initial state of the system is, finally

$$\rho_{\mathrm{ex}} = \rho_s \otimes \prod_{j=1}^{M} \rho_\alpha. \tag{6.6}$$

---

[2] At 300 K, $k_B T \sim 200$ cm^{-1}, while the two vibrational modes we use in the experiment [2] are ≥ 1000 cm^{-1}.

6.5 Finite hopping

Up to this point, we have analyzed the DHM in the atomic limit. This is motivated by the fact that, as we will detail in the next chapter, by neglecting the hopping term it is possible to compute the optical conductivity analytically.

Physically, the atomic limit is a good approximation for our system, in which the Coulomb interaction is dominant $U \gg t$. Nonetheless, it is worth studying more carefully how the local vibrations act on the hopping amplitude. We will find that molecular vibrations further reduce the hopping amplitude. This suggests the interpretation of the transformed operator as creation and annihilation of a quasi-particle, known as *polaron* [165]. Physically, the vibrations cause the coherent part of the hopping amplitude to a neighboring site to reduce, since the particle has to drag its vibrationally-induced deformation in order to move. The atomic limit is thereby justified as plausible approximation. In other words, we wish to determine how the *coherent* band-like motion of electrons is is modified by the local vibrational coupling.

We want to use the Lang-Firsov transformation introduced in the previous section to account for electron-oscillator coupling. Special care is needed in this case though, since the transformation may have two undesired effects on the electron motion: (i) enable energy to be exchanged between the electrons and oscillators (leading the energy dissipation), (ii) correlate electronic configurations and oscillator occupation numbers (leading to dephasing). Both of these processes do not preserve electron coherence, and hence should be dealt with in combination with other incoherent processes not considered here. Thus, we shall truncate the transformed hopping as $\tilde{H}_t \to \tilde{H}_t^\circ$, by retaining only a subset of transitions which preserve electron coherence.

The full DHM is composed of two parts,

$$\tilde{H}_{\text{DHM}} = \tilde{H}^a_{\text{DHM}} + \tilde{H}_t. \tag{6.7}$$

We have already studied the effects of the Lang-Firsov transformation on the atomic part, $\tilde{H}^a_{\text{DHM}} = \hat{X}^\dagger \hat{H}^a_{\text{DHM}} \hat{X}$. The hopping operator is transformed as

$$\tilde{H}_t = -t \sum_{j\sigma} \hat{X}_j^\dagger \hat{X}_{j+1}^\dagger \big(\hat{c}^\dagger_{j\sigma} \hat{c}_{j+1\sigma} + \hat{c}^\dagger_{j+1\sigma} \hat{c}_{j\sigma} \big) \hat{X}_j \hat{X}_{j+1}, \tag{6.8}$$

where $\tilde{H}_t$ induces transitions between electron-oscillator eigenstates, written as (electron) (oscillators), as $|\mathbf{x}_i, \vec{\sigma}_i\rangle, |\vec{n}_i\rangle \to |\mathbf{x}_f, \vec{\sigma}_f\rangle, |\vec{n}_f\rangle$ (i and f stand for "initial" and "final", respectively).

It is noteworthy that the canonical transformation does not alter the initial driven state Eq. (6.6), $\tilde{\rho}_{\mathrm{ex}} = \rho_{\mathrm{ex}}$. The equality holds due to the lack of holons and doublons in the initial state.

6.5.1 Linear coupling

The canonically transformed Hamiltonian, Eq. (6.7), with $\hat{X}_h = \hat{D}(\chi_h)$ and $\hat{X}_d = \hat{D}(\chi_d)$, becomes

$$\tilde{H}_{\mathrm{DHM}} = \tilde{H}_t + \hat{H}^a_{\mathrm{DHM}} - \sum_j (\Omega\chi_h^2 + \Omega_d^2)\mathbb{P}_j^d + \sum_j \hat{H}_{s,j},$$

after dropping terms proportional to the conserved total number of electrons, $\sim \sum_j \hat{n}_j$, that lead to a global phase or a constant energy shift. The coupling has dressed the hopping via a displacement transformation, which was applied while decoupling electrons and oscillators decouple.

In order to extract the resulting coherent motion, we use an approach inspired by the seminal work of Holstein [165]. We distinguish between transitions in which the number of vibrational quanta is changed during the hop (inelastic scattering), and processes where they do not change. The former processes lead to loss of phase coherence during the absorption and emission of a phonon, and to non-coherent electron motion, since they correlate electrons and oscillators. Again we focus only on coherent contribution. On the other hand, the latter (called "diagonal" transitions), $|\mathbf{x_i}, \vec{\sigma}_i\rangle|\vec{n}\rangle \to |\mathbf{x_f}, \vec{\sigma}_f\rangle|\vec{n}\rangle$, leave the vibrational occupation numbers $|\vec{n}\rangle$ unchanged by the hopping process. We shall focus on these ones, which preserve phase coherence.

In order to estimate the amplitudes $\langle\vec{n}|\langle\mathbf{x_f}, \vec{\sigma}_f|\langle\vec{n}|\tilde{H}_t|\mathbf{x_i}, \vec{\sigma}_j\rangle|\vec{n}\rangle$, we trace out (i.e., average over) the bosonic operator by dressing the hopping with each local oscillator stationary states. We have separate amplitudes depending on the electronic occupation of the sites involved. Specifically, we get

$$\tilde{t}^{hx} = t \quad \mathrm{tr}\left[\hat{D}(\chi_h)\rho_\alpha\right]\left[\hat{D}^\dagger(\chi_h)\rho_\alpha\right] = t\mathrm{e}^{-\chi_h^2}\mathcal{J}_0^2(2\chi_h|\alpha|),$$

for holon-singlon exchange,

$$\tilde{t}^{dx} = t \quad \mathrm{tr}\left[\hat{D}(\chi_d)\rho_\alpha\right]\left[\hat{D}^\dagger(\chi_d)\rho_\alpha\right] = t\mathrm{e}^{-\chi_d^2}\mathcal{J}_0^2(2\chi_d|\alpha|),$$

for doublon-singlon exchange, and

$$\tilde{t}^{hd} = t \quad \mathrm{tr}\left[\hat{D}^{\dagger}(\chi_h)\rho_{\alpha}\right]\left[\hat{D}^{\dagger}(\chi_d)\rho_{\alpha}\right] = t\mathrm{e}^{-\frac{1}{2}(\chi_h^2+\chi_d^2)}\mathcal{J}_0(2\chi_h|\alpha|)\mathcal{J}_0(2\chi_d|\alpha|),$$

for holon-doublon creation and annihilation. Here $\mathcal{J}_0$ is the Bessel function of the first kind. By averaging over the phases of the coherent states, the effective translationally invariant holon-doublon antisymmetric hopping becomes

$$\begin{aligned}\tilde{H}_t = \sum_{j\sigma} \Big[& \tilde{t}^{hx}\mathbb{P}^{hx}_{j,j+1}\left(\hat{c}^{\dagger}_{j\sigma}\hat{c}_{j+1\sigma} + \hat{c}^{\dagger}_{j+1\sigma}\hat{c}_{j\sigma}\right) + \tilde{t}^{hd}\mathbb{P}^{hd}_{j,j+1}\left(\hat{c}^{\dagger}_{j\sigma}\hat{c}_{j+1\sigma} + \hat{c}^{\dagger}_{j+1\sigma}\hat{c}_{j\sigma}\right) \\ & + \tilde{t}^{dx}\mathbb{P}^{dx}_{j,j+1}\left(\hat{c}^{\dagger}_{j\sigma}\hat{c}_{j+1\sigma} + \hat{c}^{\dagger}_{j+1\sigma}\hat{c}_{j\sigma}\right)\Big],\end{aligned}$$

where we have defined projectors for the allowed hopping processes as

$$\begin{aligned}\mathbb{P}^{hx}_{j,j+1} &= \mathbb{P}^{h}_{j}\mathbb{P}^{s}_{j+1} + \mathbb{P}^{s}_{j}\mathbb{P}^{h}_{j+1}, && \text{holon-singlon exchange}\\ \mathbb{P}^{dx}_{j,j+1} &= \mathbb{P}^{d}_{j}\mathbb{P}^{s}_{j+1} + \mathbb{P}^{s}_{j}\mathbb{P}^{d}_{j+1}, && \text{doublon-singlon exchange}\\ \mathbb{P}^{hd}_{j,j+1} &= \mathbb{P}^{h}_{j}\mathbb{P}^{d}_{j+1} + \mathbb{P}^{d}_{j}\mathbb{P}^{h}_{j+1} + \mathbb{P}^{s}_{j}\mathbb{P}^{s}_{j+1}, && \text{holon-doublon creation/annihilation.}\end{aligned}$$

6.5.2 Quadratic coupling

For quadratic coupling, $X_h = \hat{S}^{\dagger}(\xi_h)$ and $X_d = \hat{S}^{\dagger}(\xi_d)$, so that Eq. (6.7) transforms into

$$\tilde{H}_{\mathrm{DHM}} = \tilde{H}_t + \sum_j(\Omega\mathbb{P}^s_j + \Omega_h\mathbb{P}^h_j + \Omega_d\mathbb{P}^d_j)(\hat{a}^{\dagger}_j\hat{a}_j + \tfrac{1}{2}).$$

Coherent hopping transitions must neither correlate the electronic and oscillator configurations, nor exchange energy between them. This implies that there can be no coherent contributions from holon-doublon creation and annihilation processes, since they result in two oscillators having their frequencies to switch from $\Omega \leftrightarrow \Omega_h$ and $\Omega \leftrightarrow \Omega_d$. The total energy changes, even if the vibrational occupation numbers do not change (see Fig. 6.6(a1)-(c1)): as a result, these processes are prohibited regardless of the vibrational state in the effective coherent Hamiltonian.

As for holon-singlon and doublon-singlon exchange, we observe that if the vibrational occupations of the oscillators before and after the transitions are different, even diagonal transitions are not allowed. Non-diagonal transitions that preserve energy, like the ones in Fig. 6.6(b2) and (c2), are prohibited because

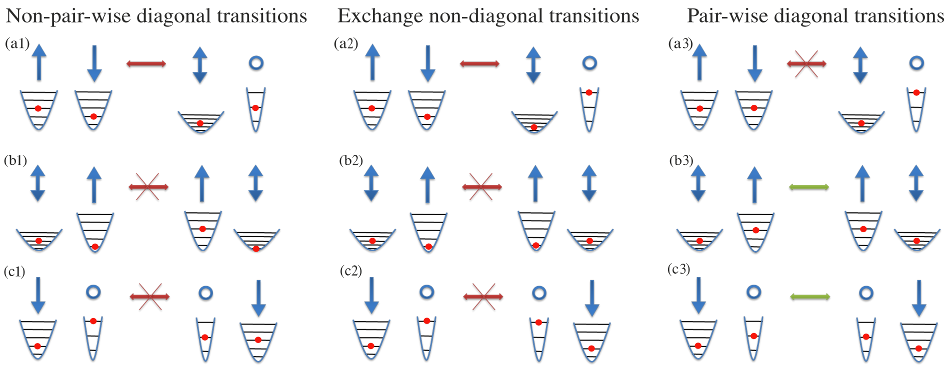

Figure 6.6: A diagram of some hopping transitions. *Left*: the vibrational occupation numbers in these transitions is identical for both oscillators, thus they are all diagonal. The oscillator occupation is not the same: they are forbidden since they are not pair-wise diagonal. (a1) Holon-doublon creation and annihilation, (b1) singlon-doublon exchange, (c1) singlon-holon exchange. *Center*: Non-diagonal transitions where the vibrational quanta numbers are exchanged. (a2) Holon-doublon creation and annihilation, (b2) singlon-doublon exchange, (c2) singlon-doublon exchange. (a2) is prohibited because the energy of the oscillators changes, (b2) and (c2) because they correlate the electronic configuration with the vibrational occupation number resulting in dephasing. Right: pair diagonal transitions where the vibrational occupation numbers are unchanged and identical for both oscillators. (a3) Holon-doublon creation, (b3) singlon-doublon exchange, (c3) singlon-doublon exchange. (a3) is prohibited because the energy of the oscillators is changed, (b3) and (c3) are allowed: they are both energy conserving and occur without changing any vibrational occupations. These latter processes are the only ones permitted in the effective coherent hopping Hamiltonian.

they lead to dephasing. The only permitted ones are what we call *pair-wise diagonal* transitions (like the ones shown in Fig. 6.6(b3) and (c3)), in which the occupancy numbers of the neighboring oscillators are identical.

Once more, we need to estimate the quantity $\langle\vec{n}|\langle\mathbf{x_f},\vec{\sigma}_f|\langle\vec{n}|\tilde{H}_t|\mathbf{x_i},\vec{\sigma}_j\rangle|\vec{n}\rangle$, in which an electron of spin σ hops from site $j+1$ to j and has occupation number $n_j = n_{j+1}$. By averaging over the local oscillator stationary state, we obtain a translationally invariant amplitude

$$\begin{aligned}\tilde{t}^{hx} =& t\sum_{n_j=0}^{\infty} p_{n_j} \sum_{n_{j+1}=0}^{\infty} p_{n_{j+1}} \left[\langle n_j|\hat{S}_j(\xi_h)|n_j\rangle\langle n_{j+1}|\hat{S}_{j+1}(\xi_h)|n_{j+1}\rangle\right]\delta_{n_j,n_{j+1}},\\ =& \sum_{n=0}^{\infty} p_n^2 |\langle n|\hat{S}(\xi_h)|n\rangle|^2,\end{aligned}$$

where we used that the local oscillator stationary state ρ_α with a Poisson number distribution p_n is independent on the site. An identical calculation reveals that

$$\tilde{t}^{dx} = \sum_{n=0}^{\infty} p_n^2 |\langle n|\hat{S}(\xi_d)|n\rangle|^2.$$

After taking $\tilde{t}^{hd} = 0$, the effective coherent hopping takes the form

$$\tilde{H}_t = \sum_{j\sigma}\left[\tilde{t}^{hx}\mathbb{P}^{hx}_{j,j+1}\left(\hat{c}^\dagger_{j\sigma}\hat{c}_{j+1\sigma} + \hat{c}^\dagger_{j+1\sigma}\hat{c}_{j\sigma}\right) + \tilde{t}^{dx}\mathbb{P}^{dx}_{j,j+1}\left(\hat{c}^\dagger_{j\sigma}\hat{c}_{j+1\sigma} + \hat{c}^\dagger_{j+1\sigma}\hat{c}_{j\sigma}\right)\right].$$

By eliminating the coherent dynamical creation or annihilation of holon-doublon pair, we have obtained a Harris-Lange-like model [50]. In its original formulation, we have already used it in Ch. 5 to compute the optical conductivity of the EHM. The crucial difference here is that the lower and upper Hubbard bands have different bandwidths.

6.6 Summary

In this chapter we have demonstrated how to modulate individual parameters of the HM by selectively driving localized vibrational states of the molecule. We have developed a toy model to build a physical intuition about the coupling of local molecular vibration to valence electrons. The Dynamical Hubbard Hamiltonian has been shown to be the appropriate minimal model to account for these vibrations, and a suitable basis state has been obtained.

In the next chapters, we shall look for experimental signatures of the physics described here.

Chapter 7

Dynamic Hubbard Model: optical properties

Control of phases in correlated-electron systems is typically achieved by applying physical or chemical pressure [175]. In Ch. 5 we studied an example of this procedure: by applying hydrostatic pressure we manipulated the inter-molecular distance, and therefore the intermolecular parameters of the Hubbard model. On the other hand, on-site correlations parameters are molecular properties that descend from the electronic structure itself, and cannot be easily affected with any static perturbation.

The goal of this chapter is to demonstrate a new type of optical control, acting directly on the electronic structure and on the on-site correlation, U. In Ch. 6 we explained how intra-molecular vibrations directly influence the wave function and the on-site energies of molecular crystals. The effective $U = U_C - U_s$ on a molecular site is given by the bare Coulomb repulsion of the electrons (U_C) reduced by the screening effects of the lower orbitals of the molecule (quantified by U_S). A resonant excitation of an intra-molecular vibration of the molecular wave function changes the screening of the orbital and therefore changes the effective on-site U.

Experimentally, mid-infrared (MIR) optical pulses have been used to excite localized molecular vibrations in ET-F_2TCNQ, while a broadband ultrafast probe interrogates the resulting optical spectrum. After reporting the results of the measurements in Sec. 7.1, the response is compared to computations based on the Dynamic Hubbard Model (DHM) introduced in Ch. 6. Among the main results of this comparison, we are going to find that the coupling to holon and doublon are asymmetric, and that the doublons strongly squeeze the vibrational mode.

7.1 Experimental results

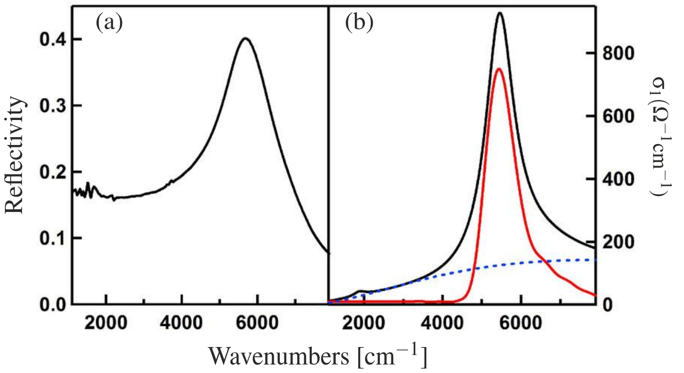

Figure 7.1: (a) Equilibrium reflectivity of the ET-F_2TCNQ for light polarized along the ET chains. (b) Black curve: equilibrium optical conductivity extracted from the optical conductivity. Red curve: numerical simulation of the optical conductivity with Hubbard parameters: $t \sim 40$ meV, $V \sim 120$ meV and $U \sim 850$ meV. These values are in agreement with the ones obtained in Ch. 5. A quantitative match with the experimental conductivity is achieved by adding a Lorentzian oscillator centered at 8000 cm^{-1}, which takes into account contributions by higher-lying transitions (blue dashed curve).

Pump-probe experiments were performed with two optical parametrical amplifiers (OPAs)[1]. Excitation was achieved via MIR pulses from difference frequency mixing of signal and idler in $AgGaS_2$, resonant with two different intramolecular vibrations: an asymmetric, IR active mode [176] at 10 μm and a symmetric, Raman active mode [177] at 6 μm. The latter is highly coupled to

---

[1] The experimental measurements reported in this section were carried out by S. Kaiser, D. Nicoletti and R. I. Tobey.

the electronic system via e-mv-coupling that leads to a symmetric break and makes the IR mode active [178, 179].

The probe was tuned to several wavelengths around the charge transfer (CT) resonance at 700 meV $= 1.77$ μm to trace the shift and the changes of the band as direct evidence of control of the on-site U. The measurements were taken in reflection geometry and the system was probed along the direction of the largest overlap of the one-dimensional conductors, i.e., along the chain of ET molecules. A time resolution of about 80 fs was achieved.

The results of the static measurements are reported in Fig. 7.1. One observes a charge-transfer (CT) resonance at photon energies ~ 5500 cm^{-1}. This feature reflects the existence of a correlation gap and corresponds to excitations of the type $(\mathrm{ET}^{+}\mathrm{ET}^{+}) \rightarrow (\mathrm{ET}^{2+}\mathrm{ET}^{0})$. The broadband reflectivity spectra was fitted with a Drude-Lorentz model [180], and transformed in optical conductivity using the Kramers-Kronig relations (Sec. 3.1.2). In Fig. 7.1(b) we have used the procedure developed in Ch. 5 to reproduce the static measurement of optical conductivity. We were able to obtain a very good agreement once a background contribution from a high frequency oscillator (dashed blue curve) was added.

The excitation of the molecular vibrations induces changes on the charge transfer band. The reflectivity changes along the ET molecules were probed at frequencies in the mid (1800-3000 cm^{-1}) and near-infrared (4000-7000 cm^{-1}).

The vibration-induced absolute reflectivity is shown Fig. 7.2(a) for the mode at 10 μm wavelength, selectively excited by light pulses with a 10% bandwidth and field strengths up to 10 MV/cm. One observes: (a) a red-shift of the CT band from its equilibrium position at $\omega \simeq 5500$ cm^{-1} toward 5000 cm^{-1}; (b) a new band approximately at 4200 cm^{-1}; (c) a mid-gap resonance and a weaker peak at ~ 3000 cm^{-1} and ~ 2000 cm^{-1}, respectively. No change in the reflectivity signal above the CT resonance was detected.

When the excited modes relax, the vibrational oscillations are reduced, and the CT band shifts back to its equilibrium, while the the peaks inside the gap reduce substantially. The relaxation back to to ground state can be described with a double-exponential function. The two time-decay values are $\tau_1 = 230$ fs and $\tau_2 = 4.5$ ps. We interpret the first time constant, τ_1, as the direct relaxation of the system in the vibrational excited state. On the other hand, we explain the second long time constant, τ_2, with a thermalization of the "hot" mode with the crystal lattice, i.e., with low frequency phonon modes. This interpretation is confirmed by the value of τ_2 in the ps region, typical of phonon modes at THz frequencies. It is noteworthy that the response is mode selective: when the excitation was tuned away from the frequency of the selected vibration, the MIR resonances disappeared.

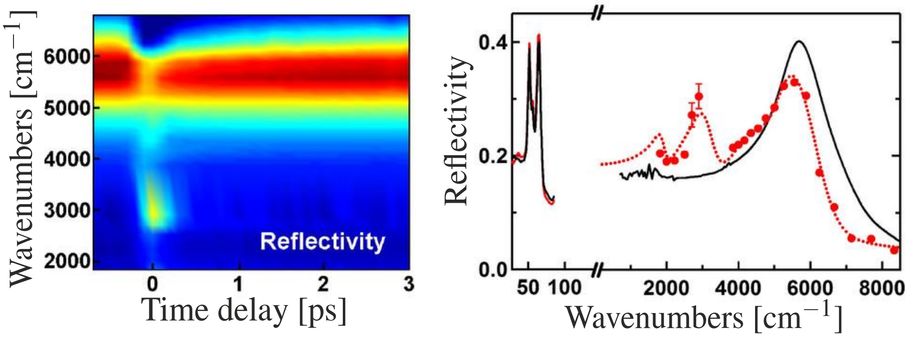

Figure 7.2: (a) Time and frequency dependent reflectivity after selective modulation of the IR active molecular mode at 1000 cm^{-1}. (b) Frequency dependent reflectivity at equilibrium (black) and at the peak of the modulating IR field (red). Full circles indicate experimental data, whilst the dashed like is a Lorentzian fit to the data to extract the optical conductivity. In the low-frequency range (below 100 cm^{-1}), the full lines indicate the equilibrium (black) and transient (red) reflectivity measured with single-cycle THz-pulses. The two peaks are phonon modes of the molecular crystal.

The same measurement, performed by exciting the molecule with the totally symmetric, Raman active, mode at 6 μm, gives the response reported in Fig. 7.2(b). In this case, one observes a reduction of the spectral weight at the charge resonance but, importantly, there is neither a shift of the CT resonance nor any significant response at other wavelengths.

It is important to mention that in both cases there has been no detection of metallic response in the THz range; the reflectivity remained low and the phonon resonances stayed unscreened. We can clearly state that the results are not a consequence of the photo-induced formation of a metallic state. Actually, if an optical excitation above gap had taken place, one would have observed a Drude-like metallic response [27].

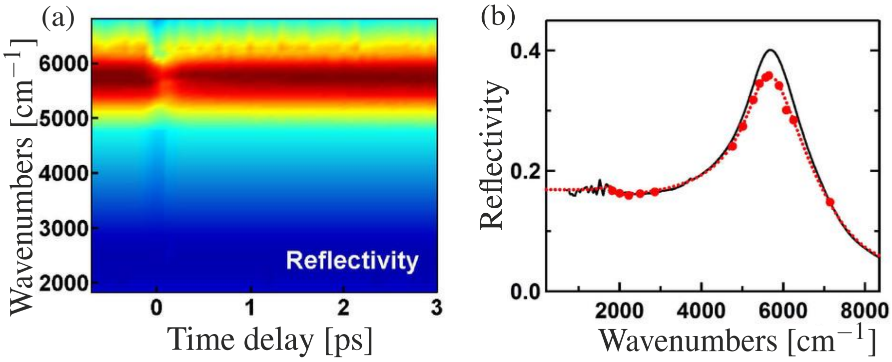

Figure 7.3: (a) Time and frequency dependent reflectivity after modulation at $\omega \sim 1670$ cm^{-1}. (b) Frequency dependent reflectivity at equilibrium (black) and at the peak of the modulating field (red). Full circles indicate experimental data whilst the dashed line is a Lorentz fit to the data.

To analyze the experimental data, we are going to compute the real part of the optical conductivity $\sigma(\omega)$ of the Dynamic Hubbard Model (DHM) via the unequal time current-current correlation function. The narrow hopping bandwidth of ET-F$_2$TCNQ, as well as the strong binding of holon-doublon pairs, justifies $\sigma(\omega)$ being calculated analitically in the atomic limit. In the final section of the chapter we are going to show that the latter approximation holds even more so when vibrational driving is on.

7.2 Optical conductivity in the Atomic Limit

As discussed in Sec. 6.4, when $U \gg k_B T \gg t^2/U$, we can approximate the initial electronic state by a half-filled completely spin-mixed state $\rho_s = \frac{1}{2^M} \sum_{\vec{\sigma}} |\vec{\sigma}\rangle\langle\vec{\sigma}|$. With regard to the vibrationally driven state, we assume that each oscillator is prepared instantaneously in a phase-averaged coherent state, ρ_α. Let us recall that this assumption is motivated by the following considerations: (i) higher vibrational states of the localized molecular oscillators are essentially unoccupied at room temperature since $k_B T < \Omega$; (ii) despite the phase of the oscillator on each site being expected to be identical across the sample, it is not controlled shot-to-shot in the experiment. We shall use the total initial state:

$$\rho_{\text{ex}} = \rho_s \otimes \prod_{j=1}^{M} \rho_\alpha,$$

to compute the optical conductivity of the system, $\sigma(\omega)$.

In Ch. 3 we studied the optical conductivity. Let us recall here briefly the key facts. The optical conductivity $\sigma(\omega)$ is defined as the linear response function connecting the finite frequency electrical current in the system, $J(\omega)$, to the applied electric field, $E(\omega)$, via $\hat{J}(\omega) = \sigma(\omega)E(\omega)$ [103]. The real part of $\sigma(\omega)$ describes the out-of-phase response of the system and is proportional to optical absorption (see Ch. 3). It has the general form $\text{Re}\,\{\sigma(\omega)\} = D\delta(\omega) + \sigma_1^{\text{reg}}(\omega)$, where D is the Drude weight, and $\sigma_1^{\text{reg}}(\omega)$ is the regular finite frequency optical conductivity which is the focus of our calculation. The central quantity determining $\sigma_1^{\text{reg}}(\omega)$ is the unequal time current-current correlation function $\chi_{JJ}(\omega)$, defined in real time ($\Delta\tau = \tau - \tau'$) as $\chi_{JJ}(\Delta\tau) = \Theta(\Delta\tau)\langle \hat{J}_H(\Delta\tau)\hat{J}_H(0)\rangle$. If the we apply the first current operator at time 0, $\tau' = 0$, so that $\Delta\tau = \tau$. $\hat{J}_H(\tau)$ is the time evolved current operator in the Heisenberg picture with respect to the atomic limit Dynamic Hubbard Hamiltonian.

The regular part of the optical conductivity, $\sigma_1^{\text{reg}}(\omega)$, is related to $\chi_{JJ}(\omega)$ as [102]

$$\sigma_1^{\text{reg}}(\omega) = \frac{e^2}{\omega a}\text{Re}\,\{\chi_{JJ}(\omega) - \chi_{JJ}(-\omega)\}\,.$$

In the atomic limit, for a system with M lattice sites, the Fourier transform of the current-current correlation function of the DHM assumes for both vibration modes the general form (see Appendix 7.B for a full derivation)

$$\chi_{JJ}(\omega) = \frac{t^2 M}{4\pi^2}\int_{-\infty}^{+\infty}\int_{-\infty}^{+\infty} G_0(\omega'')G_h(\omega'-\omega'')G_d(\omega-\omega')\,\mathrm{d}\omega'\,\mathrm{d}\omega\text{”}. \tag{7.1}$$

That is, a convolution of the bare atomic limit HM Green's function

$$G_0(\omega) = \int_{-\infty}^{\infty} \Theta(\tau)\mathrm{e}^{i(U-V)\tau}\mathrm{e}^{i\omega\tau}\,\mathrm{d}\tau,$$

with the vibrational Green's function for a site with a holon, $G_h(\omega)$, and doublon, $G_d(\omega)$, present. These functions are identical for any site j and have the general form

$$G_x(\omega) = \int_{-\infty}^{\infty} \text{tr}\left[\mathrm{e}^{i\hat{H}_{s,j}\tau}\mathrm{e}^{-i\hat{H}_{x,j}\tau}\rho_\alpha\right]\mathrm{e}^{i\omega\tau}\,\mathrm{d}\tau, \tag{7.2}$$

where $x = \{h, d\}$ labels holons and doublons, $\hat{H}_{x,j}$.

In other words, the oscillator Green’s functions are a Fourier transform of the overlap of the driven coherent state when evolved in the presence of a singlon, with the evolution of the same state in the presence of a doublon or holon. The bare Hubbard contribution $G_0(\omega)$ is responsible for a single CT peak $U - V$. In the presence of a vibrational coupling, but absence of any excitation, $G_h(\omega)$ and $G_d(\omega)$ cause the bare $\sigma_1^{\text{reg}}(\omega)$ response to shift slightly. Correspondingly, once the vibrational modes are driven, the effects on the conductivity are entirely contained in $G_h(\omega)$ and $G_d(\omega)$, as we will study in detail in the next sections.

7.3 Classical “heavy” oscillator limit

A good starting point to understand the influence of vibrations on $\sigma_1(\omega)$ is to consider the molecular modes as infinite mass classical oscillators. This limit embodies the physical situation in which the mass of the molecular oscillator far exceeds the mass of a valence electron either lost or gained: its motion remains essentially unchanged and independent of the electronic configuration. We thus ignore any “back-action” on the oscillators and consider them as having a position coordinate described by a scalar $q_j(\tau)$, oscillating as $q_j(\tau) = Q\cos(\Omega\tau + \phi_j)$. Q is the maximum displacement (identical for all the oscillators), and ϕ_j is the initial phase. $\chi_{JJ}(\tau)$ is obtained by replacing the operator $\hat{q}_j$ by the scalar coordinate $q_j(\tau)$ within the DHM. In turn this causes the Coulomb interaction U to become time-dependent.

With regard to the linear Raman mode (see Appendix 7.A) we obtain the oscillator Green’s functions

$$G_x = 2\pi \sum_{n=-\infty}^{\infty} \mathcal{J}_n^2(\nu_x)\delta(\omega - n\Omega_R),$$

where $\mathcal{J}_n$ is the order n Bessel function of the first kind, and $\nu_x = g_R^x Q/\Omega$ is a dimensionless measure of the driving energy. Let us recall that g_R^x $(x = h, d)$ is a positive coupling parameter. The optical conductivity for the Raman mode is then

$$\frac{\sigma_1^{\text{reg}}(\omega)}{t^2} = \frac{\pi M e^2}{a\omega} \sum_{m,n=-\infty}^{\infty} \mathcal{J}_n^2(\nu_h)\mathcal{J}_m^2(\nu_d)\left[\delta(\omega - \omega_{mn}) - \delta(\omega + \omega_{mn})\right], \quad (7.3)$$

where $\omega_{mn} = U - V + (n+m)\Omega_R$. The excitation of the Raman vibrations results in additional δ-peaks at integer multiples of Ω_R either side of the stationary CT peak at $U - V$.

Pertaining to the IR mode, the oscillator Green's functions are

$$G_x(\omega) = 2\pi \sum_{n=-\infty}^{\infty} \mathcal{J}_n^2(\eta_x)\delta[\omega \pm 2\Omega_I(n + \eta_x)],$$

where $\eta_x = g_I^x Q^2/4\Omega_I$ is a dimensionless measure of the driving energy, and the $'-'$ sign applies to holons. Again, g_I^x is a positive coupling parameter with units of Jm^{-1}. The resulting optical conductivity for the IR mode is then

$$\frac{\sigma_1^{\text{reg}}(\omega)}{t^2} = \frac{\pi M e^2}{a\omega} \sum_{n,m=-\infty}^{\infty} \mathcal{J}_n^2(\eta_h)\mathcal{J}_m^2(\eta_d)\left[\delta(\omega - \omega_{mn}) - \delta(\omega + \omega_{mn})\right], \tag{7.4}$$

where $\omega_{mn} = U - V + 2\Omega_I(n-m) + 2\Omega_I(\eta_h - \eta_d)$. Once more, the IR vibrations result in additional peaks at higher and lower frequencies than the main resonance. We observe two main difference between Eq. (7.3) and Eq. (7.4): (a) as a result of the quadratic coupling, in Eq. (7.4) the peaks appear at multiples of $2\Omega_I$ rather then Ω_I; (b) the central band at $U - V$ is now shifted by a driving dependent frequency $(g_I^h - g_I^d)Q^2/2$.

In both cases, the appearance of additional peaks arises because of the time-dependence of the interaction U. These resonances are the sidebands expected from classical frequency modulation caused by the oscillating interaction strength U in the dynamical phase of the time-evolution. If the driving or the coupling goes to zero then the optical conductivity reduces to the one of the bare Extended Hubbard Model in the atomic limit, as expected.

7.4 Quantum limit

Having developed an intuition for the expected physics in the limit of infinitely heavy oscillators, we shall now treat both the electrons and the oscillators quantum mechanically. In this limit, the ectrons can cause a back-action on the oscillators, and Eq. (7.2) gives (see Sec. 7.B)

$$G_x(\omega) = 2\pi \sum_{nm} p_n |\langle n|\hat{D}(\chi_x)|m\rangle|^2 \delta(\omega - \omega_{mn}^x),$$

in Raman limit. As before, $\hat{D}$ is the oscillator displacement operator, with $\chi_x = g_R^x a_0/\Omega_R\sqrt{2}$, and $\omega_{mn}^x = \Omega_R(m-n) - \Omega_R\chi_x^2$ $(x = h, d)$. The driving dependence now appears exclusively through the Poisson distribution of the phase averaged driven oscillator state: $p_n = \exp(-|\alpha|^2)|\alpha|^{2n}/n!$.

The optical conductivity for the Raman mode optical conductivity is then

$$\begin{aligned}\frac{\sigma_1^{\mathrm{reg}}(\omega)}{t^2} = \frac{\pi M e^2}{a\omega} \sum_{n,n',m,m'} & |\langle n|\hat{D}(\chi_d)|m\rangle|^2 |\langle n'|\hat{D}(\chi_h)|m'\rangle|^2 \\ & \times \left[\delta(\omega - \omega_{mm'nn'}) - \delta(\omega + \omega_{mm'nn'})\right], \end{aligned} \tag{7.5}$$

where

$$\omega_{mm'nn'} = U - V + \omega_{mn}^d + \omega_{mn}^h = U - V + \Omega_R(m + m' - n - n') - \Omega_R\chi_h^2 - \Omega_R\chi_h^2.$$

The "oscillator strengths" $|\langle n|\hat{D}(\chi_d)|m\rangle|^2$ appearing in Eq. (7.5) are Franck-Condon factors describing the overlap of vibrational eigenstates for the oscillator Hamiltonian when a singlon is present, with the eigenstates when a holon or doublon is present. They are called the photon-number distribution of number displaced states [181] and have a known analytic form (Eq. (7.12)).

We can proceed in a similar way for the IR case. The oscillator Green's functions are

$$G_x(\omega) = 2\pi \sum_{nm} p_n |\langle n|\hat{S}(\xi_x)|m\rangle|^2 \delta(\omega - \omega_{mn}^x).$$

Here $\hat{S}$ is the oscillator squeezing operator, with $\xi_x = \log(\sqrt{\Omega_x/\Omega_I})$ $(x = h, d)$. The optical conductivity for the IR mode in the quantum limit is then

$$\begin{aligned}\frac{\sigma_1^{\mathrm{reg}}(\omega)}{t^2} = & \frac{\pi M e^2}{a\omega} \sum_{n,n',m,m'} |\langle n|\hat{S}(\xi_d)|m\rangle|^2 |\langle n'|\hat{S}(\xi_h)|m'\rangle|^2 \\ & \times \left[\delta(\omega - \omega_{mm'nn'}) - \delta(\omega + \omega_{mm'nn'})\right]. \end{aligned} \tag{7.6}$$

We have defined the frequencies $\omega_{mm'nn'} = U - V + \omega_{mn}^d + \omega_{m'n'}^h$ which expand to

$$\omega_{mm'nn'} = U - V + \Omega_I^d m - \Omega_I m + \Omega_I^h m' - \Omega_I n' + \tfrac{1}{2}(\Omega_I^h + \Omega_I^d - 2\Omega_I).$$

In this case the "oscillator strengths" $|\langle n|\hat{S}(\xi_x)|m\rangle|^2$ are again Franck-Condon factors describing the overlap of vibrational eigenstates of the singlon with the holon and doublon. Once more, the latter have a known analytic formula (Eq. (7.12)), and are known as photon-number distribution of number squeezed states [173]. In conclusion, we can compute the optical conductivity for all drivings in the atomic limit.

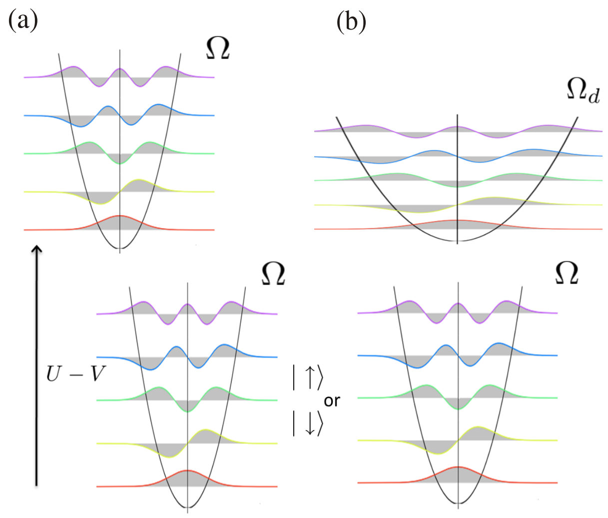

Figure 7.4: A schematic of the Franck-Condon principle for (a) linear coupling and (b) quadratic coupling. In the vibrational mode is modified by the local electronic configuration making a transition from a singlon to a doublon state with a ground state energy difference of $U - V$. In the case of linear coupling the doublon oscillator is displaced from the singlon one by an amount χ_d. In the case of quadratic coupling the doublon oscillator has a lower frequency $\Omega_d < \Omega$. In either case the vibronic (vibrational-electronic) transitions are weighted by the overlaps of the oscillator states of these two oscillators.

7.4.1 Vibrational sidebands

The most striking effect found in the conductivity is that exciting the vibrational mode causes the CT peak to acquire sidebands. Physically, they indicate that the CT transitions can occur at frequencies above and below the stationary value by either absorbing energy from the oscillator or emitting energy into it. Thus, by exciting the vibrational mode, thereby pumping energy into this degree of freedom, it becomes possible for the probe at a lower frequency of $U - V$ to transfer enough energy from the oscillator to become resonant with the CT peak. Likewise, a probe at a frequency higher than the CT peak can emit excess energy into the oscillator through the electron-oscillator coupling, again becoming resonant.

In other words, a system coupled to a local vibrational mode has numerous CT transitions. Upon driving, the oscillator transitions from higher vibrational eigenstates become more probable and represent energy exchange between the electronic and vibrational degrees of freedom initiated by the probe.

In both the classical and quantum limit the origin of transition strengths is the Franck-Condon principle: during an electronic transition, a change from one vibrational energy level to another will be more likely to happen if the two vibrational wave functions overlap more significantly. Indeed, both the Bessel functions $\mathcal{J}_n$ found in the classical limit, as well as the weights $|\langle n|\hat{D}(\chi_x)|m\rangle|^2$ and $|\langle n|\hat{S}(\xi_x)|m\rangle|^2$ determined in the quantum limit, are Franck-Condon factors. A schematic representation of the Franck-Condon principle for both linear and quadratic coupling is shown in Fig. 7.4.

7.5 Results and fitting

We are now ready to use the analytic expression for $\sigma_1^{\mathrm{reg}}(\omega)$ obtained above to interpret the detailed structure of the optical conductivity when the IR mode is vibrated. The key effects of vibrational excitation are revealed by considering the infinitely heavy oscillator limit of Sec. 7.3, where the optical conductivity is given by Eq. (7.4). The classical displacement varies harmonically in time as $q(\tau) = Q\cos(\Omega\tau)$, with amplitude Q and frequency of the driven molecular vibration $\Omega = 1000\ \mathrm{cm}^{-1}$.

The modulation of the on-site interaction matrix element U by $(g_I^h - g_I^d)q^2$ results in two crucial features. First, the $q^2 \propto Q^2[1+\cos(2\Omega\tau)]$ dependence predicts a shift of the CT resonance, by an amount that depends on the amplitude Q of the driven mode. The CT resonance is observed to red-shift: this implies that the doublon coupling exceeds that of the holon, therefore reducing the time averaged U. Second, the classical frequency modulation generates sidebands at multiples of $\pm\Omega$ on each side of the shifted CT resonance. Indeed, in Fig. 7.2 one sees a shift of the CT resonance, along with the emergence of a mid-gap peak at 2Ω below CT.

In addition to these effects, we notice that in the experiment we see only one sideband, and some additional sub-structure that emerges. These features can

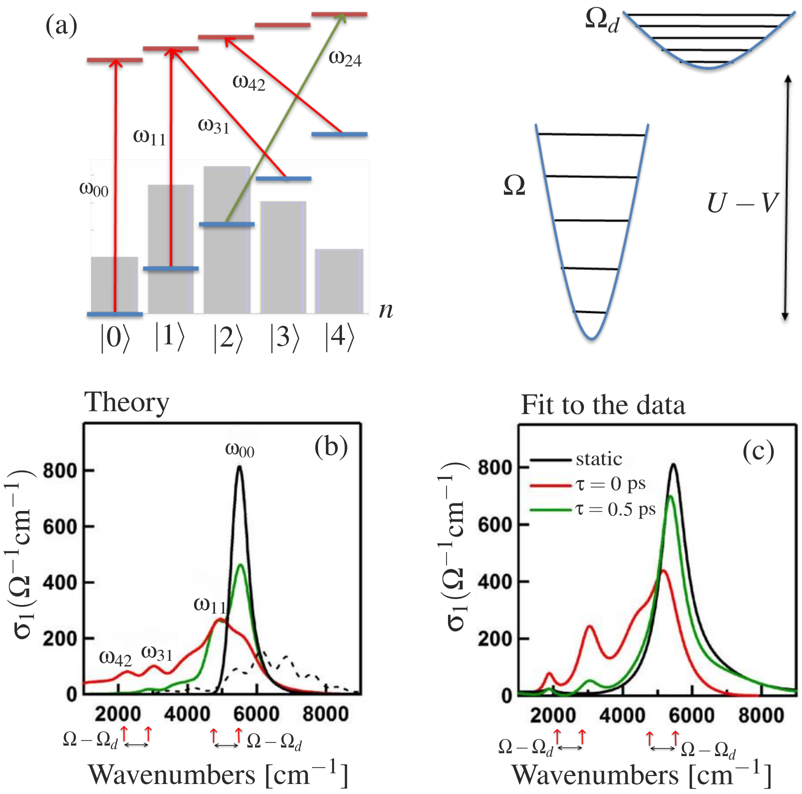

Figure 7.5: (a) Schematic representation of the vibrational transitions assuming for simplicity $\Omega_h = \Omega$. The doubly-occupied site has a significantly renormalized vibration Ω_d, which results in new transitions in the optical conductivity. In grey we represent the occupation of the driven lower vibrational ladder. (b) Theoretical optical conductivity at equilibrium (as in Fig. 7.1(b), represented in black), and upon coherent excitation of the local vibrational mode. The green and red curves represent two different driving amplitudes. The various peaks are labeled according to the transitions in (a). The dashed line represents the case in which the asymmetry between holons and doublons inverted, i.e., in where the holons are stiffened by a factor of 4 are the doublons remain almost unperturbed. (c) Optical conductivity calculated via Drude-Lorentz fit to the reflectivity spectra of Fig. 7.2, at two selected pump-probe delays. The background oscillator of Fig. 7.1(b) has been subtracted.

be explained by taking into account full quantum result, Eq. (7.6). As described in Sec. 7.4, the electronic configuration applies a back-action on a finite mass oscillator. Specifically, the oscillator "stiffens" on the holon site ($\Omega_h > \Omega$) and "slackens" on the doublon one ($\Omega_d < \Omega$).

In Fig. 7.5(b) and (c) we show the comparison between the optical conductivity extracted from the reflectivity data and a calculation with strong coupling and strong holon-doublon asymmetry. We obtain a driving strength $Q/a_0 \sim 2$, a doublon oscillator that suffers a significant frequency reduction to $\Omega_d \sim 0.26$ Ω, and a holon's $\Omega_h \sim 1.10$ Ω that is only marginally increased. The additional sub-structure seen in Fig. 7.5(b) can be attributed to the "slackening" of the doublon oscillator as schematically shown in Fig. 7.5(a). Crucially, the reduced spacing between energy levels of the doublon oscillator causes the transition frequencies to move into the gap, an effect that is significant only if the vibrational mode is appreciably populated. This finding is in agreement with the strong experimental excitation of the molecular oscillator. The remnants of the classical sidebands are now located only at low frequencies and are split into multiples of $\Omega - \Omega_d$.

The 10% modulation of the holon frequency is in agreement with the expectations [182, 68] for a thermal molecular state. The charge distribution of double occupancies lies predominantly near the the central bond $C = C$ [183, 184] of the ET molecules. This is exactly the place where the driven oscillation takes places, which may explain the reason why the doublons frequency is far more affected (about a factor of 4) then the holon one.

Finally, let us shortly comment on the lack of response seen when tuning the pump wavelength to 6 μm. This vibrational mode is expected to have a linear coupling, and thus exhibit the features obtained in Eq. (7.5). Nevertheless, we do observe only a slight reduction of the CT peak without any shift, or any response at other frequencies. This is consistent with a weak linearly coupled model which suggests that the totally symmetric vibration plays a minor part in the renormalization of the effective parameters of the HM.

7.5.1 Effect of finite hopping

In order to reproduce experimental results, we used the results for the optical conductivity in the zero-bandwidth limit, where $\sigma_1^{\text{reg}}(\omega)/t^2$ can be obtained exactly. This is justified by the parameters of ET-F$_2$TCNQ, and by the suppression of the hopping amplitude with driving, analogous to polaronic effects [180]. The former indicate that, once optically excited, an adjacent holon-doublon pair is bound. Thus, when driven the contributions of the oscillators at the initial holon and doublon locations will be dominant.

To estimate the suppression of t caused by driving, we use the results of Sec. 6.5. We need to compute $\tilde{t}^{hx}$ and $\tilde{t}^{dx}$ for the parameters used to fit the data in Fig. 7.5:

$$\tilde{t}^{hx} = \text{tr}\left[\hat{S}(\xi_h)\rho_\alpha\right] \text{tr}\left[\hat{S}(\xi_h)\rho_\alpha\right] t, \quad \text{and} \quad \tilde{t}^{dx} = \text{tr}\left[\hat{S}(\xi_d)\rho_\alpha\right] \text{tr}\left[\hat{S}(\xi_d)\rho_\alpha\right] t.$$

The traces of the squeezing transformation and phase averaged-coherent state can be computed using some of the SU(1,1) disentangling theorems discussed in Appendix 7.D. We obtain,

$$\begin{aligned}\text{tr}\left[\hat{S}(\xi)\rho_\alpha\right] &= \int_0^{2\pi} \frac{\mathrm{d}\phi}{2\pi} \langle |\alpha|\mathrm{e}^{i\phi}|\hat{S}(\xi)||\alpha|\mathrm{e}^{i\phi}\rangle, \\ &= \frac{\mathrm{e}^{|\alpha|^2[\text{sech}(\xi)-1]/2}}{\sqrt{\cosh(\xi)}} \int_0^{2\pi} \frac{\mathrm{d}\phi}{2\pi} \mathrm{e}^{i\xi|\alpha|^2 \sin(2\phi)} = \frac{\mathrm{e}^{|\alpha|^2[\text{sech}(\xi)-1]/2}}{\sqrt{\cosh(\xi)}} \mathcal{J}_0(\xi|\alpha|^2).\end{aligned}$$

Owing to the phase averaging, $\hat{S}^\dagger(\xi)$ has the same expression, apart from the sign of the exponential of $\sin(2\phi)$. Finally,

$$\tilde{t}^{hx} = t\frac{\mathrm{e}^{|\alpha|^2[\text{sech}(\xi_h)-1]/2}}{\sqrt{\cosh(\xi_h)}} \mathcal{J}_0^2(\xi_h|\alpha|^2), \quad \text{and} \quad \tilde{t}^{dx} = t\frac{\mathrm{e}^{|\alpha|^2[\text{sech}(\xi_d)-1]/2}}{\sqrt{\cosh(\xi_d)}} \mathcal{J}_0^2(\xi_d|\alpha|^2).$$

For both results the $\cosh(\xi)$ in the denominator describes the stationary reduction in the coherent hopping amplitude, while the numerator exponential and Bessel function explain the further suppression caused by the driving.

Using the fitting parameters $g_I^d a_0^2 = 1.12\ t$, $g_I^h a_0^2 = 0.250\ t$, we have that $\xi_h = 0.0473$, $\xi_d = -0.0677$, $\Omega_d = 0.26\ \Omega$, while $\Omega_h = 1.10\ \Omega$. Using the fitted value of the maximum driven displacement $Q/a_0 = 2.14$, we obtain $\tilde{t}^{dx} = 0.051\ t_0$ and $\tilde{t} = 0.19\ t$. Therefore, driving the vibration mode dramatically quenches the coherent hopping amplitude of both the doublon and holons. The atomic limit is indeed an appropriate approximation for the driven system. Let us also add that, because the oscillator coupling here is to a local molecular mode on each site, as opposed to a collective bath of lattice phonons typical for a conventional Holstein model, the vibrational excitation makes the hopping amplitudes disordered through the chain, which further inhibits holon-doublon motion via Anderson localization [185].

We conclude that the effects of a finite t are simply to broaden the dominant contribution to the optical conductivity already captured by on-site vibrational dynamics. To account for these mechanisms, as well as the spectral limitations of the measurement itself, we have introduced an artificial broadening of 0.5 t to the results presented in Fig. 7.5(b).

7.A Optical conductivity - Classical

In the classical derivation of $\sigma_1(\omega)$, we treat each oscillator by tracking its position and momentum coordinates $q(\tau)$ and $p(\tau)$. The motion of these coordinates for each oscillator is governed by an unchanging rigid classical oscillator, with mass m and frequency Ω. Namely, we have $q_j(\tau) = Q\cos(\Omega\tau + \phi_j)$ and $p_j(\tau) = -m\Omega Q\sin(\Omega\tau + \phi_j)$, where Q is the maximum displacement, identical for all oscillators, and ϕ_j is the initial phase of the jth oscillator.

7.A.1 Raman mode

In the subspace $\mathcal{H}_0 \oplus \mathcal{H}_1$ (see Sec. 4.2), the DHM becomes a time-dependent Hubbard Hamiltonian

$$\begin{aligned} \hat{H}_{\rm cl}(\tau) &= \tfrac{1}{2}Mm\Omega^2Q^2(\mathbb{P}_0+\mathbb{P}_1) + (U-V)\mathbb{P}_1 \\ &\quad + \sum_j \left\{\mathbb{P}^{hd}_{j,j+1}\left[g^h_R q_j(\tau) + g^d_R q_{j+1}(\tau)\right]\right. \\ &\quad \left. + \mathbb{P}^{dh}_{j,j+1}\left[g^d_R q_j(\tau) + g^h_R q_{j+1}(\tau)\right]\right\}. \end{aligned}$$

In the atomic limit, $\hat{H}_{\rm cl}(\tau)$ commutes with itself at different times τ: the propagator in this subspace is $\hat{U}_{\rm cl}(\tau) = \exp(-i\int_0^\tau \hat{H}_{\rm cl}(\tau')d\tau')$. After defining the integration over position as

$$\int_0^\tau q_j(\tau')d\tau' = \frac{Q}{\Omega}\left[\sin(\Omega\tau+\phi_j) - \sin(\phi_j)\right] \equiv \frac{Q}{\Omega}\Upsilon_j(\tau),$$

and the total energy of all the oscillators as $\mathcal{E} = \frac{1}{2}Mm\Omega^2Q^2$, we get

$$\begin{aligned} \hat{U}_{\rm cl}(\tau) &= {\rm e}^{-i\mathcal{E}\tau}\mathbb{P}_0 + {\rm e}^{-i\mathcal{E}\tau}{\rm e}^{-i(U-V)\tau} \\ &\quad \times \sum_j \left\{\mathbb{P}^{hd}_{j,j+1}{\rm e}^{-i[\nu_h\Upsilon_j(\tau)+\nu_d\Upsilon_{j+1}(\tau)]} + \mathbb{P}^{dh}_{j,j+1}{\rm e}^{-i[\nu_d\Upsilon_j(\tau)+\nu_h\Upsilon_{j+1}(\tau)]}\right\}. \end{aligned}$$

Here $\nu_d = g^d_R Q/\Omega$ and $\nu_h = g^h_R Q/\Omega$. By using these propagators we can compute the phase averaged current-current correlation function in the classical limit via

$$\chi_{JJ,{\rm cl}}(\tau) = \frac{\Theta(\tau)}{2^L}\int_0^{2\pi}\frac{d\phi_1}{2\pi}\cdots\int_0^{2\pi}\frac{d\phi_L}{2\pi}\sum_{\vec{\sigma}}\langle\vec{\sigma}|\hat{U}^\dagger_{\rm cl}(\tau)\hat{J}\hat{U}_{\rm cl}(\tau)\hat{J}|\vec{\sigma}\rangle.$$

The essential part of this correlation stems from the scalar product of two states which depends on the configuration $\vec{\sigma}$: $|\Phi_{\vec{\sigma}}(\tau)\rangle = \hat{U}_{\rm cl}(\tau)\hat{J}|\vec{\sigma}\rangle$ and $|\Psi_{\vec{\sigma}}(\tau)\rangle =$

$\hat{J}\hat{U}_{\mathrm{cl}}(\tau)|\vec{\sigma}\rangle$. With regard to the state $|\Psi_{\vec{\sigma}}(\tau)\rangle$ we have

$$|\Psi_{\vec{\sigma}}(\tau)\rangle \quad = \quad -it\,\mathrm{e}^{-i\mathcal{E}\tau}\left(\sum_{(j<k)\in x(\vec{\sigma})}|\vec{\sigma}_{jk}\rangle - \sum_{(j>k)\in x(\vec{\sigma})}|\vec{\sigma}_{jk}\rangle\right), \tag{7.7}$$

while $|\Phi_{\vec{\sigma}}(\tau)\rangle$ reads

$$\begin{aligned} |\Phi_{\vec{\sigma}}(\tau)\rangle = \quad & -it\,\mathrm{e}^{-i\mathcal{E}\tau}e^{-i(U-V)\tau}\left(\sum_{(j<k)\in x(\vec{\sigma})} e^{-i[\nu_h\Upsilon_j(\tau)+\nu_d\Upsilon_{j+1}(\tau)]}|\vec{\sigma}_{jk}\rangle\right. \\ & \left. -e^{-i[\nu_d\Upsilon_j(\tau)+\nu_h\Upsilon_{j+1}(\tau)]}\sum_{(j>k)\in x(\vec{\sigma})}|\vec{\sigma}_{jk}\rangle\right). \end{aligned}$$

Upon computing the overlap $\langle\, \Phi_{\vec{\sigma}}(\tau)\,|\,\Psi_{\vec{\sigma}}(\tau)\,\rangle$, the global phase arising from $\mathcal{E}$ cancels and leaves

$$\begin{aligned} \chi_{JJ,\mathrm{cl}}(\tau) \quad &= \quad t^2\frac{\Theta(\tau)}{2^M}\,\mathrm{e}^{-i(U-V)\tau}\sum_{\vec{\sigma}}\sum_{(j,k)\in x(\vec{\sigma})} \\ & \quad \times\int^{2\pi}\frac{\mathrm{d}\phi_j}{2\pi}e^{-i\nu_d\Upsilon_j(\tau)}\int_0^{2\pi}\frac{\mathrm{d}\phi_k}{2\pi}\mathrm{e}^{-i\nu_h\Upsilon_k(\tau)} \\ &= \quad t^2 M\Theta(\tau)\,\mathrm{e}^{-i(U-V)\tau}G_d(\tau)G_h(\tau). \end{aligned}$$

We have defined the oscillator correlation functions as

$$G_{\mathrm{p}}(\tau) \quad = \quad \int_0^{2\pi}\frac{d\phi}{2\pi}e^{-i\nu_{\mathrm{p}}\Upsilon(\tau)},$$

where $\mathrm{p} = \{h, d\}$ designates the holon and doublon functions which differ only by the dimensionless driving energy ν_{p}. To evaluate these functions we use the Jacobi-Anger expansion

$$\mathrm{e}^{\pm iz\sin(\theta)} = \sum_{n=-\infty}^{\infty}\mathcal{J}_n(z)\mathrm{e}^{\pm in\theta},$$

and the identity

$$\int_0^{2\pi}\frac{d\phi}{2\pi}\,\mathrm{e}^{\pm i(m-n)\phi} = \delta_{mn}.$$

In this way, the oscillator correlation functions reduce to

$$\begin{aligned} G_{\mathrm{p}}(\tau) \quad &= \quad \int_0^{2\pi}\frac{d\phi}{2\pi}e^{-i\nu_{\mathrm{p}}[\sin(\Omega\tau+\phi)-\sin(\phi\tau)]} \\ &= \quad \sum_{n=-\infty}^{\infty}\mathcal{J}_n(\nu_{\mathrm{p}})e^{-in\Omega\tau}\int_0^{2\pi}\frac{d\phi}{2\pi}\sum_{m=-\infty}^{\infty}\mathcal{J}_m(\nu_{\mathrm{p}})e^{i(n-m)\phi}, \\ &= \quad \sum_{n=-\infty}^{\infty}J_n^2(\nu_{\mathrm{p}})e^{-in\Omega\tau}. \end{aligned}$$

Putting this altogether yields the classical Raman current-current correlation function as

$$\chi_{JJ,\mathrm{cl}}(\tau) \quad = \quad t^2\Theta(\tau)L\,\mathrm{e}^{-i(U-V)\tau}\sum_{n=-\infty}^{\infty}\sum_{m=-\infty}^{\infty}J_n^2(\nu_h)J_m^2(\nu_d)e^{-i(n+m)\Omega\tau}.$$

We can finally obtain the expression for the classical Raman mode optical conductivity, Eq. (7.3):

$$\begin{aligned}\sigma_{1,\mathrm{cl}}^{\mathrm{reg}}(\omega) \quad &= \quad \frac{\pi t_0^2 L e^2}{\ell\omega}\sum_{n=-\infty}^{\infty}\sum_{m=-\infty}^{\infty}J_n^2(\nu_h)J_m^2(\nu_d)\\ &\quad\quad \times\left[\delta(\omega-\omega_{mn})-\delta(\omega+\omega_{mn})\right],\end{aligned}$$

where $\omega_{mn} = U - V + (n+m)\Omega$. If either of the coupling strengths goes to zero, i.e., $\nu_d \to 0$ and/or $\nu_h \to 0$, the optical conductivity reduces to the standard HM atomic limit ($\mathcal{J}_0(0) = 1$, while $\mathcal{J}_n(0) = 0$ for $|n| > 0$).

7.A.2 IR mode

The analysis can be repeated for the IR case. In this case we have the Hamiltonian

$$\begin{aligned}\hat{H}_{\mathrm{cl}}(\tau) = &\left(\tfrac{1}{2}Mm\Omega^2Q^2\right)(\mathbb{P}_0+\mathbb{P}_1) + (U-V)\mathbb{P}_1\\ &+\sum_j\left\{\mathbb{P}_{j,j+1}^{hd}\left[g_I^h q_j^2(\tau) - g_I^d q_{j+1}^2(\tau)\right]\right.\\ &\left.+\mathbb{P}_{j,j+1}^{dh}\left[-g_I^d q_j^2(\tau) + g_I^h q_{j+1}^2(\tau)\right]\right\},\end{aligned}$$

taking note of the signs of the interaction for the holon and doublon couplings as discussed earlier. In order compute the propagator $\hat{U}_{\mathrm{cl}}(\tau)$ we again define the position integration as

$$\begin{aligned}\int_0^\tau q_j^2(\tau')d\tau' \quad &= \quad \frac{Q^2}{4}\left[\sin(2\Omega\tau+\phi_j) - \sin(2\phi_j) + 2\tau\right],\\ &= \quad \frac{Q^2}{4\Omega}\Upsilon_j(\tau) + \tfrac{1}{2}Q^2\tau.\end{aligned}$$

This leads to the expression for the propagator, $\hat{U}_{\mathrm{cl}}(\tau)$:

$$\begin{aligned}\hat{U}_{\mathrm{cl}}(\tau) =&\mathrm{e}^{-i\mathcal{E}\tau}\Bigg(\mathbb{P}_0 + \mathrm{e}^{-i[U-V+\Omega(\eta_h-\eta_d)]\tau}\times\\ &\sum_j\left\{\mathbb{P}_{j,j+1}^{hd}\mathrm{e}^{-\frac{1}{2}i[\eta_h\Upsilon_{j+1}(\tau)-\eta_d\Upsilon_j(\tau)]} + \mathbb{P}_{j,j+1}^{dh}\mathrm{e}^{-\frac{1}{2}i[\eta_h\Upsilon_{j+1}(\tau)-\eta_d\Upsilon_j(\tau)]}\right\}\Bigg),\end{aligned}$$

where $\eta_d = g_I^d Q^2/2\Omega$ and $\eta_h = g_I^h Q^2/2\Omega$ are dimensionless measures of the driving energy. We are now ready to compute the current-current correlation function $\chi_{JJ,\mathrm{cl}}(\tau)$:

$$\chi_{JJ,\mathrm{cl}}(\tau) = \frac{\Theta(\tau)}{2^L}\int_0^{2\pi}\frac{d\phi_1}{2\pi}\cdots\int_0^{2\pi}\frac{d\phi_L}{2\pi}\sum_{\vec{\sigma}}\langle\,\Psi_{\vec{\sigma}}\,|\,\Phi_{\vec{\sigma}}\,\rangle\,.$$

The state $|\Psi_{\vec{\sigma}}(\tau)\rangle$ has the same expression as Eq. (7.7), while for $|\Phi_{\vec{\sigma}}(\tau)\rangle$ we obtain

$$\begin{aligned}|\Phi_{\vec{\sigma}}(\tau)\rangle = -\,it\,\mathrm{e}^{-i\mathcal{E}\tau}e^{-i[U-V+\Omega(\eta_h-\eta_d)]\tau}\Bigg(&\sum_{(j<k)\in x(\vec{\sigma})}\mathrm{e}^{-\frac{1}{2}i[\eta_h\Upsilon_{j+1}(\tau)-\eta_d\Upsilon_j(\tau)]}|\vec{\sigma}_{jk}\rangle\\ &-\mathrm{e}^{-\frac{1}{2}i[\eta_h\Upsilon_j(\tau)-\eta_d\Upsilon_{j+1}(\tau)]}\sum_{(j>k)\in x(\vec{\sigma})}|\vec{\sigma}_{jk}\rangle\Bigg)\,.\end{aligned}$$

Explicitly, $\chi_{JJ,\mathrm{cl}}(\tau)$ is

$$\begin{aligned}\chi_{JJ,\mathrm{cl}}(\tau) &= t^2\frac{\Theta(\tau)}{2^L}\,\mathrm{e}^{-i[U-V+\Omega(\eta_h-\eta_d)]\tau}\sum_{\vec{\sigma}}\sum_{(j,k)\in x(\vec{\sigma})}\\ &\quad\times\int_0^{2\pi}\frac{d\phi_j}{2\pi}\mathrm{e}^{\frac{1}{2}i\eta_d\Upsilon_j(\tau)}\int_0^{2\pi}\frac{d\phi_k}{2\pi}\mathrm{e}^{-\frac{1}{2}i\eta_h\Upsilon_k(\tau)}.\end{aligned}$$

We define once more the holon and doublon oscillator correlation functions as

$$G_{\mathrm{p}}(\tau) = \mathrm{e}^{(-1)^{\mathrm{p}}i\Omega\eta_{\mathrm{p}}\tau}\int_0^{2\pi}\frac{d\phi}{2\pi}\mathrm{e}^{-\frac{1}{2}(-1)^{\mathrm{p}}i\eta_{\mathrm{p}}\Upsilon(\tau)},$$

where $(-1)^{\mathrm{p}}$ is shorthand for 1 when $\mathrm{p} = h$ and -1 when $\mathrm{p} = d$. This correlation function evaluates as

$$\begin{aligned}G_{\mathrm{p}}(\tau) &= \mathrm{e}^{(-1)^{\mathrm{p}}i\Omega\eta_{\mathrm{p}}\tau}\int_0^{2\pi}\frac{d\phi}{2\pi}\mathrm{e}^{-i(-1)^{\mathrm{p}}\frac{1}{2}\eta_{\mathrm{p}}[\sin(2\Omega\tau+\phi)-\sin(2\phi\tau)]}\\ &= \mathrm{e}^{(-1)^{\mathrm{p}}i\Omega\eta_{\mathrm{p}}\tau}\sum_{n=-\infty}^{\infty}\mathcal{J}_n(\tfrac{1}{2}\eta_{\mathrm{p}})\mathrm{e}^{-(-1)^{\mathrm{p}}2in\Omega\tau}\\ &\quad\times\int_0^{2\pi}\frac{d\phi}{2\pi}\sum_{m=-\infty}^{\infty}\mathcal{J}_m(\tfrac{1}{2}\eta_{\mathrm{p}})\mathrm{e}^{(-1)^{\mathrm{p}}2i(m-n)\phi}\\ &= \mathrm{e}^{(-1)^{\mathrm{p}}i\Omega\eta_{\mathrm{p}}\tau}\sum_{n=-\infty}^{\infty}J_n^2(\tfrac{1}{2}\eta_{\mathrm{p}})e^{-(-1)^{\mathrm{p}}2in\Omega\tau}.\end{aligned}$$

Putting this altogether yields the classical IR current-current correlation function:

$$\chi_{JJ,\mathrm{cl}}(\tau) = t^2\Theta(\tau)L\,\mathrm{e}^{-i[U-V+\Omega(\eta_h-\eta_d)]\tau}\sum_{n=-\infty}^{\infty}\sum_{m=-\infty}^{\infty}$$

$$\times J_n^2(\tfrac{1}{2}\eta_h)J_m^2(\tfrac{1}{2}\eta_d)\mathrm{e}^{-2i(m-n)\Omega\tau}.$$

Finally, we find the results Eq. (7.4) for the optical conductivity

$$\begin{aligned}\sigma_{1,\mathrm{cl}}^{\mathrm{reg}}(\omega) &= \frac{\pi t_0^2 L e^2}{\ell\omega}\sum_{n=-\infty}^{\infty}\sum_{m=-\infty}^{\infty} J_n^2(\tfrac{1}{2}\eta_h)J_m^2(\tfrac{1}{2}\eta_d) \\ &\quad \times\left[\delta(\omega-\omega_{mn})-\delta(\omega+\omega_{mn})\right],\end{aligned}$$

where $\omega_{mn} = U - V + 2\Omega(m-n) + \Omega(\eta_h - \eta_d)$. If $\eta_d \to 0$ and/or $\eta_h \to 0$, the optical conductivity reduces to the standard HM atomic limit result.

7.B Optical conductivity - Quantum limit

In this Appendix we compute the unequal time causal current-current correlation function for the driven stationary state $\rho_{\mathrm{ex}} = \rho_s \otimes \prod_{j=1}^{M}\rho_\alpha$ defined in Sec. 6.4:

$$\chi_{JJ}(\tau) = \Theta(\tau)\mathrm{tr}\left(\hat{J}(\tau)\hat{J}(0)\rho_{\mathrm{ex}}\right),$$

ρ_s and ρ_α are defined in Eq. (6.4) and Eq. (6.5), respectively. We decompose ρ_{ex} as

$$\begin{aligned}\rho_{\mathrm{ex}} =& \frac{1}{2^M}\sum_{\vec{\sigma}}|\vec{\sigma}\rangle\langle\vec{\sigma}|\otimes\Bigg(\int_0^{2\pi}\frac{d\phi_1}{2\pi}\cdots\int_0^{2\pi}\frac{d\phi_M}{2\pi} \\ &\times ||\alpha|e^{i\phi_1}\rangle\cdots||\alpha|e^{i\phi_L}\rangle\langle|\alpha|e^{i\phi_1}|\cdots\langle|\alpha|e^{i\phi_M}|\Bigg). \qquad (7.8)\end{aligned}$$

This leaves the correlation functions as

$$\begin{aligned}\chi_{JJ}(\tau) =& \frac{\Theta(\tau)}{2^M}\sum_{\vec{\sigma}}\Bigg(\int_0^{2\pi}\frac{d\phi_1}{2\pi}\cdots\int_0^{2\pi}\frac{\mathrm{d}\phi_M}{2\pi}\times \\ &\langle\vec{\sigma}|\langle|\alpha|e^{i\phi_1}|\cdots\langle|\alpha|e^{i\phi_M}|e^{i\hat{H}^a_{\mathrm{DHM}}\tau}\hat{J}e^{-i\hat{H}^a_{\mathrm{DHM}}\tau}\hat{J}|\vec{\sigma}\rangle||\alpha|e^{i\phi_1}\rangle\cdots||\alpha|e^{i\phi_M}\rangle\Bigg).\end{aligned}$$

The essential part of the correlation stems from the scalar product of two states

$$\begin{aligned}|\Phi(\tau)\rangle =& e^{-i\hat{H}^a_{\mathrm{DHM}}\tau}\hat{J}|\vec{\sigma}\rangle||\alpha|e^{i\phi_1}\rangle\cdots||\alpha|e^{i\phi_L}\rangle, \\ |\Psi(\tau)\rangle =& \hat{J}e^{-i\hat{H}^a_{\mathrm{DHM}}\tau}|\vec{\sigma}\rangle||\alpha|e^{i\phi_1}\rangle\cdots||\alpha|e^{i\phi_M}\rangle,\end{aligned}$$

where the perturbation by the current operator $\hat{J}$ is applied before and after the time evolution, respectively. Notice that both of these states depend explicitly on $|\alpha|$, $\vec{\sigma}$ and $\{\phi_j\}$. The current-current correlation function for M sites is then

$$\chi_{JJ}(\tau) \quad = \quad \frac{\Theta(\tau)}{2^M}\sum_{\vec{\sigma}}\int_0^{2\pi}\frac{d\phi_1}{2\pi}\cdots\int_0^{2\pi}\frac{\mathrm{d}\phi_M}{2\pi}\,\langle\,\Psi(\tau)\,|\,\Phi(\tau)\,\rangle\,.$$

In the atomic limit, we can compute exactly the time evolution in the subspace $\mathcal{H}_0 \oplus \mathcal{H}_1$. We start from a ground state with only singly occupied state. With regard to $|\Psi(\tau)\rangle$, we find that the evolution is entirely in $\mathcal{H}_0$:

$$\begin{aligned}|\Psi(\tau)\rangle \quad = \quad & -it\,\mathrm{e}^{-\frac{1}{2}iM\Omega\tau}\left(\sum_{(j<k)\in x(\vec{\sigma})}|\vec{\sigma}_{jk}\rangle - \sum_{(j>k)\in x(\vec{\sigma})}|\vec{\sigma}_{jk}\rangle\right)\\ & \times|\,|\alpha|\mathrm{e}^{i(\phi_1-\Omega\tau)}\rangle\cdots|\,|\alpha|e^{i(\phi_M-\Omega\tau)}\rangle.\end{aligned}$$

Here we have chosen a convenient notation, $|\vec{\sigma}_{jk}\rangle$, for a half-filled system by introducing a shorthand for states which are minimally perturbed out of the subspace $\mathcal{H}_0$: site j is occupied by a doublon and site k by a holon. The total spin must be conserved: if we start with a given spin configuration $|\vec{\sigma}\rangle$, after applying the current operator and before the time evolution, jth and kth elements of the vector $\vec{\sigma}(j,k)$ must have been either $(\uparrow_j,\downarrow_k)$ or $(\downarrow_j,\uparrow_k)$. For each $\vec{\sigma}$ we denote the complete set of permissible pairs of locations (j,k) as $z(\vec{\sigma})$. We will also split this set up into two parts: (i) a subset $x(\vec{\sigma})$ that contains all adjacent holon-doublon locations, i.e., $(j,k)=(j,j+1)$ or $(j,k)=(j,j-1)$; (ii) a subsect $y(\vec{\sigma}) = z(\vec{\sigma}) - x(\vec{\sigma})$ of the remaining non-adjacent configurations.

On the other hand, the evolution of the state $|\Phi(\tau)\rangle$ is entirely in $\mathcal{H}_1$:

$$\begin{aligned}|\Phi(\tau)\rangle = -it\,\mathrm{e}^{-\frac{1}{2}i(M-2)\Omega\tau}\mathrm{e}^{-i(U-V)\tau}\Bigg(&\sum_{(j<k)\in x(\vec{\sigma})}|\vec{\sigma}_{jk}\rangle|\,|\alpha|\mathrm{e}^{i(\phi_1-\Omega\tau)}\rangle\cdots\\ &\mathrm{e}^{-i\hat{H}_{d,j}\tau}|\,|\alpha|\mathrm{e}^{i\phi_j}\rangle\mathrm{e}^{-i\hat{H}_{h,j+1}\tau}|\,|\alpha|\mathrm{e}^{i\phi_{j+1}}\rangle\cdots|\,|\alpha|\mathrm{e}^{i(\phi_M-\Omega\tau)}\rangle - \sum_{(j>k)\in x(\vec{\sigma})}|\vec{\sigma}_{jk}\rangle\\ &\times|\,|\alpha|\mathrm{e}^{i(\phi_1-\Omega\tau)}\rangle\cdots\mathrm{e}^{-i\hat{H}_{h,j-1}\tau}|\,|\alpha|\mathrm{e}^{i\phi_{j-1}}\rangle\mathrm{e}^{-i\hat{H}_{d,j}\tau}|\,|\alpha|\mathrm{e}^{i\phi_j}\rangle\cdots|\,|\alpha|\mathrm{e}^{i(\phi_M-\Omega\tau)}\rangle\Bigg)\,.\end{aligned}$$

It is clear that the evolution of the oscillators on the holon and doublon sites is different from the remaining $(M-2)$ singlons sites. By taking the scalar product of these states, $\langle\,\Psi(\tau)\,|\,\Phi(\tau)\,\rangle$, we obtain with a bit of algebra

$$\begin{aligned}\chi_{JJ}(\tau) \quad = \quad & t^2\frac{\Theta(\tau)}{2^M}\,\mathrm{e}^{-i(U-V)\tau}\sum_{\vec{\sigma}}\sum_{(j,k)\in x(\vec{\sigma})}\\ & \times\left(\int_0^{2\pi}\frac{\mathrm{d}\phi_j}{2\pi}\mathrm{e}^{\frac{1}{2}i\Omega\tau}\langle|\alpha|e^{i(\phi_j-\Omega\tau)}|\mathrm{e}^{-i\hat{H}^{a}_{\mathrm{DHM},d,j}\tau}||\alpha|\mathrm{e}^{i\phi_j}\rangle\right.\end{aligned}$$

$$\times \int_0^{2\pi} \frac{\mathrm{d}\phi_k}{2\pi} \mathrm{e}^{\frac{1}{2} i\Omega\tau} \langle |\alpha| \mathrm{e}^{i(\phi_k-\Omega\tau)} | \mathrm{e}^{-i\hat{H}^{\alpha}_{\mathrm{DHM},h,k}\tau} | \, |\alpha| \mathrm{e}^{i\phi_k} \rangle \Bigg).$$

This expression becomes more transparent by defining two correlation functions $G(\tau)$ as

$$\begin{aligned} G_d(\tau) &= \int_0^{2\pi} \frac{\mathrm{d}\phi}{2\pi} \langle |\alpha| \mathrm{e}^{i\phi} | \mathrm{e}^{i\hat{H}_s\tau} \mathrm{e}^{-i\hat{H}_d\tau} | \, |\alpha| \mathrm{e}^{i\phi} \rangle, \\ G_h(\tau) &= \int_0^{2\pi} \frac{\mathrm{d}\phi}{2\pi} \langle |\alpha| \mathrm{e}^{i\phi} | \mathrm{e}^{i\hat{H}_s\tau} \mathrm{e}^{-i\hat{H}_h\tau} | \, |\alpha| \mathrm{e}^{i\phi} \rangle. \end{aligned} \tag{7.9}$$

These function are composed by the overlap of two terms: (i) a driven oscillator time evolved according to the free singlon oscillator Hamiltonian $\hat{H}_s$, (ii) the very same oscillator evolved according to the doublon or holon oscillator Hamiltonian $\hat{H}_d$ or $\hat{H}_h$. These correlation functions characterize the correlation function $\chi_{JJ}(\tau)$. We have assumed that every oscillator was driven identically, which causes Eq. (7.9) to be independent on the site j or k. Therefore, χ_{JJ} simplifies to $\chi_{JJ}(\tau) = S\, t^2 \Theta(\tau)\, \mathrm{e}^{-i(U-V)\tau} G_d(\tau) G_h(\tau)/2^M$. Here S is a scalar factor arising from

$$S = \sum_{\vec{\sigma}} \sum_{(j,k)\in x(\vec{\sigma})} 1,$$

and S counts the total number of holon-doublon pairs which can be generated from every MI spin configuration $\vec{\sigma}$. We compute this sum explicitly in Appendix 7.C, and obtain $S = M\, 2^M$ (Eq. (7.13)). Thus

$$\chi_{JJ}(\tau) = t^2 M \Theta(\tau)\, \mathrm{e}^{-i(U-V)\tau} G_d(\tau) G_h(\tau).$$

$\chi_{JJ}(\tau)$ is a product of functions $f(\tau)g(\tau)$ in the time-domain: consequently its Fourier transform will be a convolution

$$\chi_{JJ}(\omega) = \frac{1}{2\pi} \int_{-\infty}^{\infty} \mathrm{d}\omega' \; f(\omega') g(\omega - \omega'). \tag{7.10}$$

By choosing $f(\tau) = \Theta(\tau)\, \mathrm{e}^{-i(U-V)\tau} G_d(\tau)$ and $g(\tau) = G_h(\tau)$, the doublon and holon oscillator correlation functions reduce to

$$\begin{aligned} G_d(\tau) &= \mathrm{tr}\left(\mathrm{e}^{i\hat{H}_s\tau} \mathrm{e}^{-i\hat{H}_d\tau} \rho_\alpha \right) = \sum_n p_n \langle n | \mathrm{e}^{i\hat{H}_s\tau} e^{-i\hat{H}_d\tau} | n \rangle \\ &= \sum_n p_n \mathrm{e}^{i\Omega(n+\frac{1}{2})\tau} \langle n | \mathrm{e}^{-i\hat{H}_d\tau} | n \rangle, \end{aligned}$$

and similarly

$$G_h(\tau) = \sum_n p_n \mathrm{e}^{i\Omega(n+\frac{1}{2})\tau} \langle n | \mathrm{e}^{-i\hat{H}_h\tau} | n \rangle.$$

7.B.1 Raman mode

The doublon and holon oscillators are related to the singlon oscillator by displacement transformations. By using

$$\begin{aligned}\langle n|e^{-i\hat{H}_d\tau}|n\rangle &= \langle n|\hat{D}^\dagger(\chi_d)e^{i\Omega\chi_d^2\tau}e^{-i\Omega(\hat{a}^\dagger\hat{a}+\frac{1}{2})\tau}\hat{D}(\chi_d)|n\rangle,\\ &= e^{i\Omega\chi_d^2\tau}\sum_m e^{-i\Omega(m+\frac{1}{2})\tau}|\langle n|\hat{D}(\chi_d)|m\rangle|^2,\end{aligned}$$

the Green function for the doublon results to be

$$G_d(\tau) = \sum_n p_n \sum_m e^{-i\omega_{mn}^d\tau}|\langle n|\hat{D}(\chi_d)|m\rangle|^2,$$

where $\omega_{mn}^d = \Omega(m-n) - \Omega\chi_d^2$. Similarly, the correlation function for the holon is

$$G_h(\tau) = \sum_n p_n \sum_m e^{-i\omega_{mn}^h\tau}|\langle n|\hat{D}(\chi_h)|m\rangle|^2,$$

where $\omega_{mn}^h = \Omega(m-n) - \Omega\chi_h^2$. We can now compute the Fourier transforms of $f(\tau)$ and $g(\tau)$ by using the well known expressions

$$\int_{-\infty}^{\infty} d\tau\ e^{i(\omega\pm W)\tau} = 2\pi\delta(\omega\pm W),$$

and

$$\int_{-\infty}^{\infty} d\tau\ \Theta(\tau)e^{i(\omega\pm W)\tau} = \pi\delta(\omega\pm W) + \mathcal{P}\left(\frac{i}{\omega\pm W}\right).$$

We obtain

$$\begin{aligned}f(\omega) &= \sum_n p_n \sum_m |\langle n|\hat{D}(\chi_d)|m\rangle|^2\\ &\times\left[\pi\delta(\omega-\omega_{mn}^d-U+V) + \mathcal{P}\left(\frac{i}{\omega-\omega_{mn}^d-U+V}\right)\right],\\ g(\omega) &= 2\pi\sum_n p_n\sum_m |\langle n|\hat{D}(\chi_h)|m\rangle|^2\delta(\omega-\omega_{mn}^h),\end{aligned}$$

and their convolution

$$\begin{aligned}\chi_{JJ}(\omega) =& t^2 M\sum_{n,n'} p_n p_{n'}\sum_{m,m'}|\langle n|\hat{D}(\chi_d)|m\rangle|^2|\langle n'|\hat{D}(\chi_h)|m'\rangle|^2\\ &\times\left[\pi\delta(\omega-\omega_{mm'nn'}) + \mathcal{P}\left(\frac{i}{\omega-\omega_{mm'nn'}}\right)\right].\end{aligned}$$

Here $\omega_{mm'nn'} = U - V + \omega_{mn}^d + \omega_{m'n'}^h$ which reduces to

$$\omega_{mm'nn'} = U - V + \Omega(m+m'-n-n') - \Omega\chi_h^2 - \Omega\chi_d^2.$$

Finally, we obtain Eq. (7.5) for $\sigma_1^{\mathrm{reg}}(\omega)$:

$$\begin{aligned}\sigma_1^{\mathrm{reg}}(\omega) &= \frac{e^2}{a\omega}\mathrm{Re}\left\{\chi_{JJ}(\omega)-\tilde{\chi}_{JJ}(\omega)\right\}\\ &= \frac{\pi t^2 M e^2}{a\omega}\sum_{n,n'} p_n p_{n'} \sum_{m,m'} |\langle n|\hat{D}(\chi_d)|m\rangle|^2 |\langle n'|\hat{D}(\chi_h)|m'\rangle|^2\\ &\quad\times\left[\delta(\omega-\omega_{mm'nn'})-\delta(\omega+\omega_{mm'nn'})\right].\end{aligned}$$

If $\chi_d \to 0$ and $\chi_h \to 0$ then the optical conductivity reduces to

$$\sigma_1^{\mathrm{reg}}(\omega) = \frac{\pi t^2 M e^2}{a\omega}\left[\delta(\omega-\omega_{\mathrm{CT}})-\delta(\omega+\omega_{\mathrm{CT}})\right],$$

where $\omega_{\mathrm{CT}} = U - V$. When the driving is zero, we simply find optical peaks at the CT resonance.

The "oscillator strengths" $|\langle n|\hat{D}(\zeta)m\rangle|^2$, or photon-number distribution of number displaced states, have the form (for $n \geq m$)

$$|\langle n|\hat{D}(\chi)|m\rangle|^2 = \frac{\mathrm{e}^{-|\chi|^2}|\chi|^{2(n-m)}}{m!n!}\mathcal{D}(\chi,n,m), \tag{7.11}$$

where

$$\mathcal{D}(\chi,n,m) = \left|\sum_{k=0}^{m}\frac{m!n!(-1)^k|\chi|^{2(m-k)}}{k!(m-k)!(n-k)!}\right|^2.$$

7.B.2 IR mode

We use a very similar procedure for the IR case. We start from the overlap

$$\begin{aligned}\langle n|\mathrm{e}^{-i\hat{H}_d\tau}|n\rangle &= \langle n|\hat{S}^\dagger(\xi_d)\mathrm{e}^{-i\Omega_h(\hat{a}^\dagger\hat{a}+\frac{1}{2})\tau}\hat{S}(\xi_d)|n\rangle\\ &= \sum_m \mathrm{e}^{-i\Omega_h(m+\frac{1}{2})\tau}|\langle n|\hat{S}(\xi_d)|m\rangle|^2,\end{aligned}$$

so that the Green's function for the doublon is

$$G_d(\tau) = \sum_n p_n \sum_m \mathrm{e}^{-i\omega^d_{mn}\tau}|\langle n|\hat{S}(\xi_d)|m\rangle|^2,$$

with $\omega^d_{mn} = \Omega_d m - \Omega n + \frac{1}{2}(\Omega_d - \Omega)$. Similarly for the holon:

$$G_h(\tau) = \sum_n p_n \sum_m \mathrm{e}^{-i\omega^h_{mn}\tau}|\langle n|\hat{S}(\xi_h)|m\rangle|^2,$$

with $\omega^h_{mn} = \Omega_h m - \Omega n + \frac{1}{2}(\Omega_h - \Omega)$. The two functions, $f(\omega)$ and $g(\omega)$ in this case are

$$f(\omega) = \sum_n p_n \sum_m |\langle n|\hat{S}(\xi_d)|m\rangle|^2$$

$$
\begin{aligned}
&\times\left[\pi\delta(\omega-\omega^d_{mn}-U+V)+\mathcal{P}\left(\frac{i}{\omega-\omega^d_{mn}-U+V}\right)\right],\\
g(\omega) &= 2\pi\sum_n p_n\sum_m |\langle n|\hat{S}(\xi_h)|m\rangle|^2\delta(\omega-\omega^h_{mn}),
\end{aligned}
$$

and their convolution

$$
\begin{aligned}
\chi_{JJ}(\omega) &= t^2M\sum_{n,n'}p_np_{n'}\sum_{m,m'}|\langle n|\hat{S}(\xi_d)|m\rangle|^2|\langle n'|\hat{S}(\xi_h)|m'\rangle|^2\\
&\times\left[\pi\delta(\omega-\omega_{mm'nn'})+\mathcal{P}\left(\frac{i}{\omega-\omega_{mm'nn'}}\right)\right].
\end{aligned}
$$

The frequency $\omega_{mm'nn'}=U-V+\omega^d_{mn}+\omega^h_{m'n'}$ reduces to

$$
\omega_{mm'nn'}=U-V+\Omega_dm-\Omega n+\Omega_hm'-\Omega n'+\tfrac{1}{2}(\Omega_h+\Omega_d-2\Omega).
$$

The optical conductivity for the IR case is then Eq. (7.6):

$$
\begin{aligned}
\sigma_1^{\text{reg}}(\omega) &= \frac{\pi t^2M\mathrm{e}^2}{\ell\omega}\sum_{n,n'}p_np_{n'}\sum_{m,m'}|\langle n|\hat{S}(\xi_d)|m\rangle|^2|\langle n'|\hat{S}(\xi_h)|m'\rangle|^2\\
&\times\left[\delta(\omega-\omega_{mm'nn'})-\delta(\omega+\omega_{mm'nn'})\right].
\end{aligned}
$$

Once more, if $\xi_d\to 0$ and $\xi_h\to 0$ the optical conductivity reduces to the standard HM atomic limit result.

The "oscillator strengths" $|\langle n|\hat{S}(\xi)|m\rangle|^2$, or photon-number distribution of number squeezed states, have analytic form

$$
|\langle n|\hat{S}(\xi)|m\rangle|^2=\frac{n!m!}{[\cosh(\xi)]^{2n+1}}[\tanh(\xi)]^{m-n}\mathcal{S}(\xi,n,m), \tag{7.12}
$$

when $|n-m|=2$, otherwise it is zero. The latter condition reflects the fact that squeezing is a two photon process. Here we have defined

$$
\mathcal{S}(\xi,n,m)=\left|\sum_{k=k_{\min}}^{k_{\max}}\frac{(-1)^k[\frac{1}{2}\sinh(\xi)]^{2k}}{k!(n-2k)!(k+(m-n)/2)!}\right|^2,
$$

where k is a non-negative integer running from $k_{\min}=\max\{0,\frac{1}{2}(n-m)\}$ to $k_{\max}=\lfloor\frac{1}{2}n\rfloor$.

7.C Computing the configuration sum

In the calculation of the optical conductivity in the atomic limit we need to evaluate the sum

$$
S=\sum_{\vec{\sigma}}\sum_{(j,k)\in x(\vec{\sigma})}1.
$$

Let us recall that $x(\vec{\sigma})$ is the set of all adjacent locations (j,k) of the doublon and hole in the configuration string $\vec{\sigma}$. $\vec{\sigma}$ has either $(\uparrow_j,\downarrow_{j+1})$ or $(\downarrow_j,\uparrow_{j+1})$. The holon and doublon can be created on either side: as a consequence $x(\vec{\sigma})$ will contain two locations $(j,j+1)$ and $(j+1,j)$. For this reason the sum $\sum_{(j,k)\in x(\vec{\sigma})} 1$ counts twice the number of such pairs within the configuration $\vec{\sigma}$.

We can formulate this problem by taking an arbitrary bit string b_M of length $M \geq 3$ and creating a function $F(b_M)$ which counts the number of occurrences of adjacent "01" and "10" substrings within b_M allowing for periodic boundary conditions. As an example, a string like $b_{11} = 01100100111$ has $F(b_{11}) = 6$. This way, $S_M = \sum_{b_M} F(b_M)$ for strings of length M. We then note that the set of all bit strings $\{b_M\}$ can be created from the set of strings $\{b_{M-1}\}$ by inserting an additional bit $z = \{0,1\}$ between the first and second bit of every string. So if $b_{M-1} = xyb_{M-3}$ then $b_M = xzyb_{M-3}$, where b_{M-3} is an arbitrary $M-3$ length string. We thus spawn two new b_M's through z from each b_{M-1}. The newly created b_M's have the same number of substrings as the b_{M-1} they were created from (see 7.1). Let us denote the set of 3-bit strings xzy in this as A. The remaining $\frac{1}{4}$ of the b_M's have 2 more substrings in addition to those in the b_{M-1} string, and we denote this set of 3-bit strings xzy as B. This allows us to write S_M as

$$\begin{aligned}
S_M &= \sum_{b_M} F(b_M) = \sum_{xzy}\sum_{b_{M-3}} F(xzyb_{M-3}) \\
&= \sum_{xzy\in A}\sum_{b_{M-3}} F(xzyb_{M-3}) + \sum_{xzy\in B}\sum_{b_{M-3}} F(xzyb_{M-3}).
\end{aligned}$$

By using that $F(xzyb_{M-3}) = F(xyb_{M-3})$ $xzy \in A$, and that $F(xzyb_{M-3}) = 2 + F(xyb_{M-3})$ for $xzy \in B$, we obtain

$$\begin{aligned}
S_M &= \sum_{xzy\in A}\sum_{b_{M-3}} F(xyb_{M-3}) + \sum_{xzy\in B}\sum_{b_{M-3}} [2 + F(xyb_{M-3})] \\
&= \sum_{z}\sum_{xy}\sum_{b_{M-3}} F(xyb_{M-3}) + \sum_{xzy\in B}\sum_{b_{M-3}} 2 \\
&= \sum_{z} S_{M-1} + 2^{M-3}\sum_{xzy\in B} 2 \\
&= 2S_{M-1} + 2^{M-1}.
\end{aligned}$$

Here we have also used

$$\sum_{xzy\in A} + \sum_{xzy\in B} = \sum_{xzy}, \quad \text{and}$$

$$\sum_{xy} \sum_{b_{M-3}} F(xyb_{M-3}) = S_{M-1}.$$

By inspection we can evaluate $S_3 = 2^3 + 2^2 = 12$ and consequently

$$\begin{aligned}
S_4 &= 2(2^3 + 2^2) + 2^3 = 2^4 + 2 \times 2^3, \\
S_5 &= 2(2^4 + 2 \times 2^3) + 2^4 = 2^5 + 3 \times 2^4, \\
S_6 &= 2(2^5 + 3 \times 2^4) = 2^6 + 4 \times 2^4, \\
&\vdots \\
S_M &= 2^M + (M-2) \times 2^{M-1} = M \times 2^{M-1}.
\end{aligned}$$

Finally, we have obtained the results used in Appendix 7.B:

$$S = 2S_M = M \times 2^M. \tag{7.13}$$

Table 7.1: Configurations of the bit strings upon enlargement.

x	z	y	$F(b_{M+1}) - F(b_M)$
0	0	0	0
0	1	0	**2**
0	0	1	0
0	1	1	0
1	0	0	0
1	1	0	0
1	0	1	**2**
1	1	1	0

7.D Operator ordering SU(1,1) theorem

In this appendix we expand upon the SU(1,1) disentangling theorem [171], useful for computing the action of squeezing operators and squeezed Hamiltonians on coherent states. The SU(1,1) algebra $\hat{K}$-operators is defined as

$$\hat{K}_0 = \frac{1}{4}(\hat{a}^\dagger \hat{a} + \hat{a}\hat{a}^\dagger), \quad \hat{K}_- = \frac{1}{2}\hat{a}^2, \quad \hat{K}_+^\dagger = \frac{1}{2}(\hat{a}^\dagger)^2.$$

The SU(1,1) disentangling theorem allows to decompose the exponentials as

$$\mathrm{e}^{\gamma_0 \hat{K}_0 + \gamma_+ \hat{K}_+ + \gamma_- \hat{K}_-},$$

where one defines

$$\Gamma_0 = \left(\cosh(\beta) - \frac{\gamma_0}{2\beta}\sinh\beta\right)^{-2}, \qquad \Gamma_\pm \frac{2\gamma_\pm \sinh(\beta)}{2\beta\cosh(\beta) - \gamma_0\sinh(\beta)},$$

and $\beta^2 = \gamma_0^2/4 - \gamma_+\gamma_-$. We need to compute the matrix element $\langle\alpha|\hat{S}(\xi)|\alpha\rangle$. The operator $\hat{S}(\xi)$ has coefficients $\gamma_\pm = \mp\xi$ and $\gamma_0 = 0$. Thus $\beta^2 = \xi^2$. Irrespective of choosing $\beta = \xi$ or $\beta = -\xi$, we obtain $\Gamma_\pm = \mp\tanh(\xi)$, and $\Gamma_0 = \cosh(\xi)^{-2}$. Let us consider the action of the $\hat{K}$ operators on coherent states:

$$\begin{aligned}
\exp(\Gamma_- \hat{K}_-)|\alpha\rangle &= \exp\left(\Gamma_- \frac{\alpha^2}{2}\right)|\alpha\rangle, \\
\langle\alpha|\exp(\Gamma_+ \hat{K}_+) &= \langle\alpha|\exp\left(\Gamma_+ \frac{(\alpha^*)^2}{2}\right), \\
\exp(z\hat{K}_0)|\alpha\rangle &= \mathrm{e}^{z/4}\mathrm{e}^{\frac{|\alpha|^2}{2}(|\mathrm{e}^{z/2}|^2-1)}|\alpha\mathrm{e}^{z/2}\rangle,
\end{aligned}$$

where we defined the modified normalized coherent state as

$$|\alpha\mathrm{e}^{z/2}\rangle = \mathrm{e}^{-\frac{|\alpha|^2|\mathrm{e}^{z/2}|^2}{2}}\sum_{n=0}^{\infty}\frac{(\alpha\mathrm{e}^{z/2})^n}{\sqrt{n!}}|n\rangle.$$

For the case $z = \ln(\Gamma_0)$, then $\mathrm{e}^{z/2} = \sqrt{\Gamma_0}$ so the result simplifies to

$$\exp[\ln(\Gamma_0)K_0]|\alpha\rangle = (\Gamma_0)^{1/4}\mathrm{e}^{\frac{|\alpha|^2}{2}(|\Gamma_0|-1)}|\alpha\sqrt{\Gamma_0}\rangle.$$

Using the values for $\Gamma_\pm$ and Γ_0 given by the squeezing operator then leaves

$$\begin{aligned}
\langle\alpha|\mathrm{e}^{\Gamma_+\hat{K}_+}\mathrm{e}^{\ln(\Gamma_0)\hat{K}_0}\mathrm{e}^{\Gamma_-\hat{K}_-}|\alpha\rangle =& \frac{\exp\left[\frac{1}{2}|\alpha|^2(\mathrm{sech}^2(\xi) - \xi\mathrm{e}^{-2i\phi} + \xi\mathrm{e}^{2i\phi} - 1)\right]}{\sqrt{\cosh(\xi)}} \\
& \times \langle\alpha|\alpha\mathrm{sech}(\xi)\rangle,
\end{aligned}$$

where we used that $\mathrm{sech}(\xi) = \cosh(\xi)^{-1}$ and set $\alpha = |\alpha|\mathrm{e}^{i\phi}$. Note that for squeezing operator we also have that $\Gamma_0 > 0$. The overlap of the two coherent states becomes

$$\langle\alpha|\alpha\mathrm{sech}(\xi)\rangle = \exp\left\{-\tfrac{1}{2}|\alpha|^2[1 + \mathrm{sech}^2(\xi) - 2\mathrm{sech}(\xi)]\right\},$$

giving in total

$$\langle\alpha|\hat{S}(\xi)|\alpha\rangle = \frac{\exp\left[\frac{1}{2}|\alpha|^2(\mathrm{sech}(\xi) - 1 + i\xi\sin(2\phi))\right]}{\sqrt{\cosh(\xi)}}.$$

This indicates that the special case of the vacuum expectation value of the squeezing operator is simply $\langle 0|\hat{S}(\xi)|0\rangle = \sqrt{\mathrm{sech}(\xi)}$.

Chapter 8

Phase controlled driving

8.1 Phase locked vibrational driving

In the previous chapter we showed that by strongly driving an intra-molecular mode we can modulate the on-site Coulomb interaction in time, and reveal its effects on observable optical properties of the systems. By driving an anti-symmetric IR active mode at frequency $\Omega_I \sim 1000$ cm^{-1}, and by using ultrafast probes, we observed a transient red-shift of the charge transfer (CT) peak and the appearance of a sideband at a frequency $\sim 2\Omega_I$. The quantum nature of the oscillator, and thus the back-action on the electrons, was revealed by the asymmetry of the response: the doublon oscillators "slackens" much more than the holon oscillators "stiffens", and the sidebands appear only within the gap.

In this chapter, we wish to further substantiate our physical picture using a new experimental and therefore numerical approach. Our goal is to find signatures of the U modulation by tracking the reflectivity (or optical conductivity) directly in the time domain. Experimentally, this is a very challenging task. First of all, if we drive the anti-symmetric 10 μm mode introduced previously, we need a time resolution $\lesssim 17$ fs to observe the $2\Omega_I$ oscillations. Moreover, in order for the oscillations to be visible, the driving needs to be performed with phase "locked" pulses. In fact, if the pulse has random phase for each experimental run, the oscillations in the time domain are averaged out. As a consequence, one can obtain only indirect signatures of the time dependence,

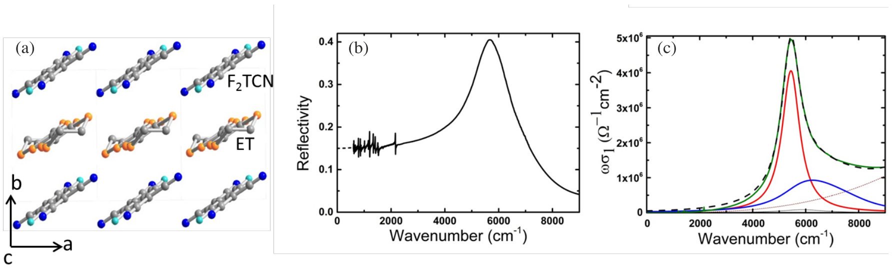

Figure 8.1: (a) Crystal structure of ET-F_2TCNQ (b) Static reflectivity of ET-F_2TCNQ along a-axis (c) Reduced optical conductivity is shown in green with model fit in dashed black curve. Red and blue curves are contributions from holon-doublon pair and particle-hole continuum to the charge transfer peak.

namely peaks in the optical response.

We will perform our experiment once again on the ET-F_2TCNQ system. In Fig. 8.1 are summarized the key properties of the compounds that are going to be useful in the following. In particular, in Fig. 8.1(a) the crystal structure is shown; in Fig. 8.1(b) and (c) we report the reflectivity and optical conductivity. Furthermore, in Fig. 8.1(c) we highlight the contributions of holon-doublon (HD) and particle-hole (PH) continuum to the charge transfer peak, extracted in the same way as in Ch. 5.

The plan of the chapter is the following. In Sec. 8.2 we report the experimental results[1], and extract the Hubbard parameters by using the fitting procedure developed in Ch. 5. Consequently, in Sec. 8.3 we compute the non time-translationally invariant conductivity. This calculation requires the computation of two-time correlation functions, owing to the explicit time dependence of the Hamiltonian. We will exploit the effective Hamiltonian, Eq. (5.6), to simulate the broadband optical properties as the Coulomb interaction is periodically modulated.

In this chapter we are going to treat the system as classical, rather then quantum as in the previous chapter. This is justified by the much weaker excitation energy of the vibrations of the current experiment (pump fluence of 0.9

---

[1] The experimental measurements reported in this section have been performed by R. Singla.

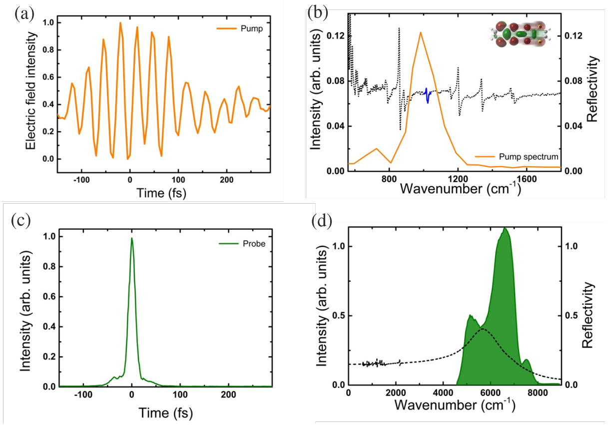

Figure 8.2: (a) Electric field time trace of MIR pump pulse. (b) Spectra of pump pulse (orange) together with reflectivity of ET-F_2TCNQ along c-axis (dashed black). Infrared active vibrational mode at 1000 wavenumber is highlighted in blue with its pictorial representation in the inset. (c) Auto-correlation of nearly transform limited near-infrared (NIR) probe pulse. (d) Spectra of probe pulse (green).

mJ/cm^2) with respect to the one described in Ch. 7 (pump fluence up to 35 mJ/cm^2).

8.2 Experimental results and fitting

We start by describing the measurements of the the reflectivity changes along the chain of ET molecules, probed when the antisymmetric, IR active mode is driven. In the experiment, an amplified Ti:sapphire laser at 800 nm with repetition rate of 1 kHz has been used to seed two NIR optical parameter amplifier (OPA) setups. Difference frequency mixing of the two NIR beams generates carrier-envelope phase stable pulses in the mid-infrared region at 10 μm [186]. In Fig. 8.2. Fig. 8.2(a) shows the phase stable electric field of the pump pulse over time with width of 10 fs. The corresponding spectrum in Fig. 8.2(b) resonantly pumps the IR mode of the ET molecule along the c-axis. The pump beam is incident normally to the sample surface with fluence of 0.9 mJ/cm^2.

Subsequently, the CT band along the a-axis has been probed with an over-

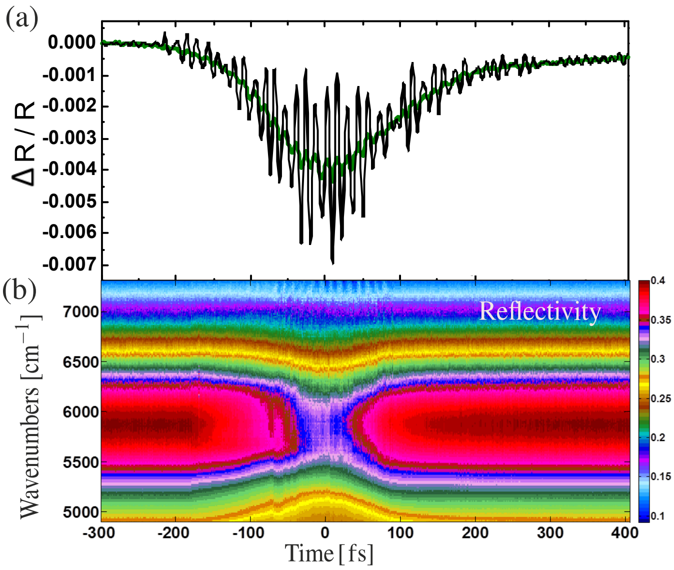

Figure 8.3: (a) Integrated experimental relative reflectivity changes (green) together with deconvolved (i.e., with the probe signal subtracted) data (grey). (b) Frequency resolved reflectivity as a function of pump-probe delay time.

lapping NIR spectrum covering the range $4700 - 7500$ cm^{-1}. The probe beam is parallel to the a-axis to highlight the one-dimensionality of the conduction along the ET chain. In the experiment, this is achieved by using the same Ti:sapphire laser that drives another OPA, which in combination with deformable mirror compression generates pulses in the NIR region [187]. Fig. 8.2(c) and (d) show the time profile and the spectrum of the probe pulse.

Driving the infrared mode at 1000 cm^{-1}, the reflectivity changes in the way reported in Fig. 8.3. Time-dependent oscillations are clearly observed both in the integrated reflectivity (Fig. 8.3(a)), and in the frequency resolved reflectivity (b). To interpret these data, we are going to use exact analytic results for the optical conductivity, and extract the Hubbard parameters from experimental measurements as in Sec. 5.2. Let us recall that in that experiment, the data were analyzed using a model of the optical conductivity based on a $1/U$ strong coupling expansion of the extended Hubbard model. In that case, the onsite repulsion U was assumed to be constant at all pressures, while V and t were modified by the applied pressure. This assumption was justified by the fact

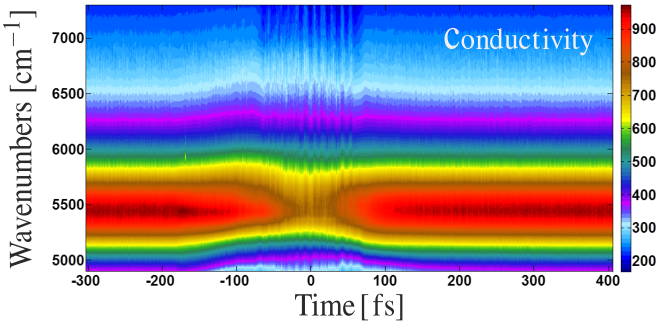

Figure 8.4: Time and frequency dependent experimental optical conductivity after the vibrational modulation.

that, to leading order, one expects the reduction of lattice spacing to affect the inter-site parameters rather then the intra-site ones.

In the current experiment, this picture is not valid anymore. On the contrary, since the excited mode is local, we expect the on-site effects to be dominant, as extensively discussed in Ch. 2 as well as in Ch. 7.

With this strategy, we extract the changes in U/t as a function of time difference (τ) between the pump and the probe, after transforming the reflectivity results of Fig. 8.3(b) in reduced optical conductivity, shown in Fig. 8.4. We observe two main effects: (a) a U decrease as a consequence of the expansion of the electronic wave function (hence the interaction between two electrons in the same orbital decreases), and (b) oscillations with a $2\Omega_I$ frequency. To accurately fit the data, it was necessary to let the ratio V/t be a free parameter as well.

The absolute effect on the V/t ratio is similar to the one of U/t, but shows much less visible oscillations (see Fig. 8.5(a)). Despite the relative reduction effect on $V/t \gg U/t$, the fact that the oscillations are mostly prominent on U/t confirms that the leading effect of the local modulation is to modify the on-site contribution.

In Fig. 8.5(b) we plot the conductivities fit for selected instants of time. Alongside the total result, we show the exciton and particle-hole (PH) continuum contributions in red and blue, respectively. The exciton contribution decreases as a function of pressure, which suggests the holon and doublon be-

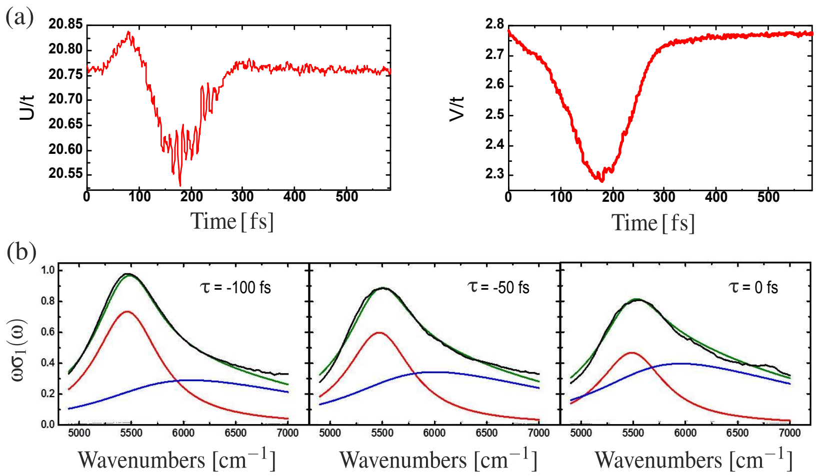

Figure 8.5: (a) Time dependence of the Coulomb parameters U and V as extracted from the fit of the steady state $\omega\sigma_1(\omega)$. (b) Frequency dependent optical conductivity after the vibrational modulation at selected time delays between pump and probe, τ. In black we show the experimental data, in green the fit results (see main text for details), while in red and blue the exciton and PH contributions are displayed.

come less bounded with driving.

Before moving to the theoretical analysis, one remark is necessary. The fitting procedure is not completely justified in this case, since the analytic formula used to extract the Hubbard parameters is strictly valid only for *equilibrium* optical conductivities. In the experiment, the state of the system is probed while the driving is still on, that causes the Hamiltonian to be explicitly time-dependent. Nonetheless, the fitting procedure is very useful to give an insight into the overall effects on the Hubbard parameters, and confirm our physical intuition.

The results of this section will be used as a starting point for the simulations of the optical conductivity in the next section as follows. Firstly, the functional form extracted for the U/t and V/t will be used to shape their time dependence. Then, we will compute the two-time correlation function and the resulting optical conductivity. Finally, we will show that this reproduces the experimental results thereby confirming the reliability of our assumptions.

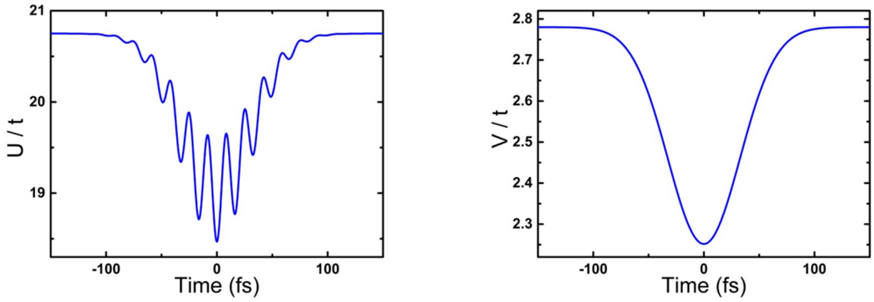

Figure 8.6: Time-dependent Coulomb parameters U and V used in the effective model. We use this sensible form for the perturbation based on the fits performed previously (see main text).

8.3 Two-time correlation functions

We take into account the influence of vibrations by considering the oscillators as having a position coordinate described by a scalar $q_j(\tau) = Q_0 \sin(\Omega_I \tau + \phi)^2$, where Q_0 and ϕ are the maximum displacement and the phase, respectively, identical for all oscillators. This was called classical limit in Sec. 7.3, and it was shown to have the effect of making the U interaction time dependent.

An implicit assumption of this result was that the modulation was kept switched on indefinitely. On the contrary, here we are going to superimpose the sinusoidal oscillation of U on a gaussian envelope to reproduce the finite duration of the pulse. The width and amplitude of the Gaussian is extracted from the fit of Fig. 8.5(a). Simultaneously, also the V is assumed to decrease, but without periodic modulation. Overall,

$$P_U(\tau) = \mathrm{e}^{-\frac{\tau-\tau_P}{T_P}} \left[1 - P_0 \sin(\Omega_I \tau + \phi)^2\right], \quad P_V(\tau) = \mathrm{e}^{-\frac{\tau-\tau_P}{T_P}},$$

where τ_P and T_P are the center and width of the pulse-like modulation. P_0 and ϕ are the amplitude and the phase of the modulating function superimposed to the gaussian envelope, respectively. U and V then change in time as

$$U(\tau) = U(1 - A_U P_U(\tau)), \qquad V(\tau) = V(1 - A_V P_V(\tau)), \tag{8.1}$$

where A_U and A_V quantify the reduction of U and V ensuing the molecular vibration.

As explained in detail in Ch. 3, the central quantity in the Kubo formula is the unequal time current-current correlation function of the initial state, defined as

$$\chi_{JJ}(\tau,\tau') = \langle 0|\hat{U}^\dagger(\tau+\tau')\hat{J}\hat{U}(\tau+\tau')\hat{U}^\dagger(\tau')\hat{J}\hat{U}(\tau')|0\rangle.$$

We use the effective model, Eq. (5.6), with $|0\rangle$ ground state, as Hamiltonian that governs the time evolution in $\hat{U}$. Let us recall that $|0\rangle$ represents all the configurations with only singly occupied sites, but no specific spin order due to being at room temperature. The current-operator, in this picture, creates a particle at "site" 2, with energy $U - V$, i.e., the energy to create a nearest-neighbor holon-doublon pair. The explicit time-dependence of U and V, expressed by Eq. (8.1), mimics the effects of molecular vibrations.

8.3.1 Results

Having described the parameters that enter our simulation, we now describe how they are pieced together.

1. We choose a time interval for which to compute the correlation function $\tau_{\text{int}} \in [\tau_i', \tau_f']$, and we divide it in equal sub-intervals of length $\mathrm{d}\tau' = 1$ fs;
2. we evolve the system up to τ_i';
3. we apply the first current operator $\hat{J}$;
4. we time-evolve the resulting state up to $\tau' + \tau$, where τ is a fixed time window over which the system is probed: $\tau = \tau_{\text{probe}}$;
5. we apply the second current operator, and compute the current-current correlation function;
6. at this point, we start again from $|0\rangle$, time evolve it up to time $\tau_i' + \mathrm{d}\tau'$, and repeat the steps from number 3., until the value $\tau' = \tau_f'$ is reached.

As for the time intervals, we have chosen $\tau_{\text{int}} = 400$ fs, $N_{\tau'} = 400$, $\tau_{\text{probe}} = 100$ fs. The values of A_U and A_V are deduced from the fitting in Sec. 8.2, and equal $A_U \sim 1.5\%$ and $A_V \sim 20\%$. The energy changes in U result thus to be bigger, in absolute value, then those in V. We take the phase to be $\phi = 0$: as long as

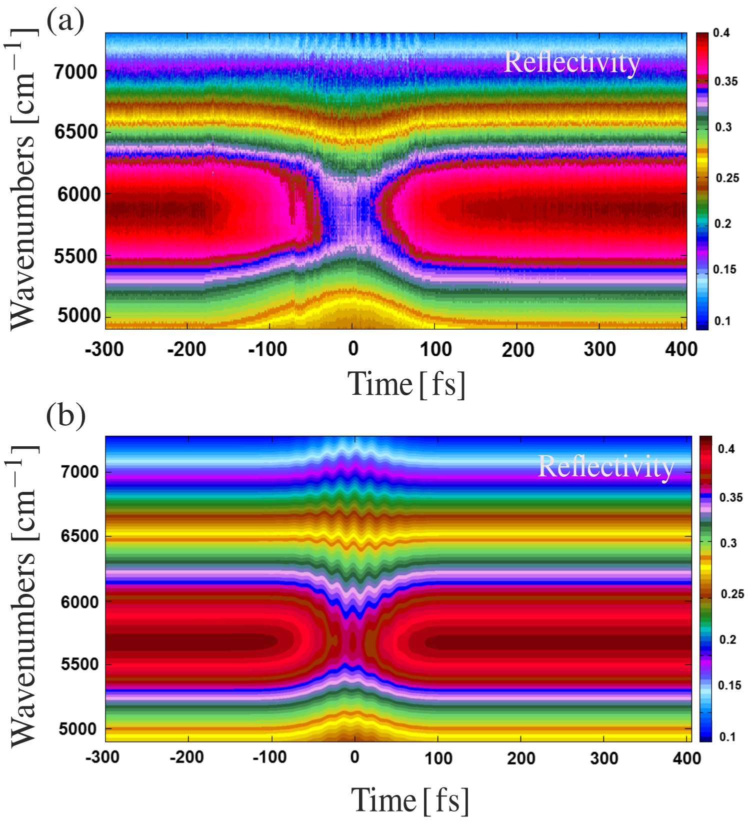

Figure 8.7: Comparison between the (a) numerically computed, and (b) experimentally measured, time and frequency dependent reflectivity.

its value is fixed (or “locked”), the actual initial value is not relevant. Finally, we will find that, in order to reproduce the data, a value $P_0 = 0.5$ has to be chosen.

The results of this procedure are shown in Fig. 8.7(a), compared with the experimental data in the same range in Fig. 8.7(b). In the figure the data have been shifted so that the pulse is centered at time $\tau = 0$. The main features observed in the experiment are reproduced.

By combining the tools developed in the previous chapters we can thus combine the physics of the DHM with a single-particle effective model and reliably predict the time and frequency dependent reflectivity.

8.4 Summary

This and the previous chapters have attempted to demonstrate that the selective modulation of one degree of freedom, when combined with probing of the electronic system, raises the tantalizing prospect of experimentally deconstructing the Hubbard Hamiltonian, by exposing one specific coupling that would otherwise have a vanishingly small contribution to the the equilibrium properties. We have investigated the optical signatures of selective vibrational excitations of intra-molecular modes to ET-F_2TCNQ, and argued that the lineshape of the optical conductivity carries important information about the microscopic interactions of the material, such as holon-doublon asymmetry. Most importantly, the response to such strongly driven vibrational modes reveals the strength of their coupling to the electronic structure.

Such control is not easily accomplished by other means and the method is likely to be applicable to a broader class of organic materials, beside ET-F_2TCNQ, which exhibit other phases such as charge-density waves, high-T_c superconductivity, and higher dimensionality.

Chapter 9

Spin ordering via vibrational control

9.1 Magnetism in a strongly-correlated Mott insulator

In Ch. 6 we have studied the effects of local vibrations on the charge degrees of freedom (DOF). By exploiting the spin-charge separation property of one-dimensional system, we were able to trace out the contributions of the spins to the optical conductivity, and bundle their effect into a multiplicative factor (Sec. 4.5). The assumption of having a spin-mixed state was justified by the fact that the experiments were performed at room temperature. In this chapter, on the contrary, we are going to focus on the effects of vibrations on the magnetic properties of a strongly correlated material, i.e., on the spins' DOF. For this to be the case, we will be working at low temperatures. Notice that differently from the last chapters, here we are not going to interpret experimental results, but rather discuss a proposal for a future experiments.

For large values of the local repulsion U, the low-energy properties of the Hubbard Model can be described by the $t-J$ model [188] (see Appendix 9.A

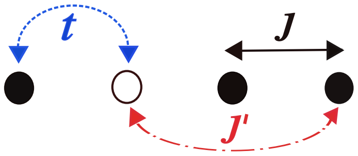

Figure 9.1: Schematic view of the interactions between a hole and spins in the $t-J$ model.

for the derivation based on strong-coupling perturbation theory):

$$\begin{aligned}\hat{H}_{tJ} =&\mathbb{P}_0 \left\{ -t \sum_{\langle ij\rangle,\sigma} \hat{c}^\dagger_{i\sigma}\hat{c}_{j,\sigma} + \frac{J}{2}\sum_{\langle ij\rangle}\left(\mathbf{S}_i\cdot\mathbf{S}_j - \frac{\hat{n}_i\hat{n}_j}{4}\right)\right.\\ &\left.\underbrace{-\frac{t^2}{2U}}_{J'} \sum_{ijk}^{i\neq k}\left[\sum_{\sigma} (\hat{c}^\dagger_{i,\sigma}\hat{c}_{k,\sigma}\hat{n}_j) - \hat{c}^\dagger_i\vec{\sigma}\hat{c}_k\cdot\hat{c}^\dagger_j\vec{\sigma}\hat{c}_j\right]\right\}\mathbb{P}_0,\end{aligned} \tag{9.1}$$

where $\mathbb{P}_0$ projects the Hilbert space onto the subspace of zero and one electron per site, $\hat{\mathbf{S}}$ are the spin-operators expressed in terms of fermionic operators (Eq. (4.2)), and $\vec{\sigma}$ are the Pauli matrices. With $\hat{c}^{(\dagger)}_{j,\sigma}$ we denote, as usual, the creation (annihilation) operator for electrons with spin σ on site j.

It is customary to call the exchange interaction term $J = 4t^2/U$, from which the name $t-J$ model arises. Physically, the three terms of Eq. (9.1) represent the following processes:

1. the first one corresponds to an electron hopping from singly occupied site onto an empty site;

2. the second is the full kinetic-exchange part in which the spin-1/2 operators $\{\mathbf{S}_j\}$ are
$$\mathbf{S}_j \equiv \frac{1}{2}\sum_{\sigma\sigma'} \hat{c}^\dagger_{j\sigma}\vec{\sigma}_{\sigma\sigma'}\hat{c}_{j\sigma'},$$
and $\vec{\sigma}$ are the Pauli matrices;

3. finally, the third denotes hopping between three sites without and with spin flip in the middle site.

At half-filling, the expectation value of the number operator, $\langle\hat{n}\rangle_j = 1$. The first and third term annihilate, as there can be no low-energy hopping process if every site has exactly one electron. This is the Mott insulating (MI) phase, and the only terms that survive in Eq. (9.1) are the magnetic interactions. We obtain the Heisenberg model with antiferromagnetic (AF) exchange interaction:

$$\hat{H}_{\text{Heis}} = J \sum_j \big(\hat{\mathbf{S}}_j \cdot \hat{\mathbf{S}}_{j+1} - \frac{1}{4}\big).$$

Notice that if we take into account the nearest neighbor interaction term, the exchange coupling term takes the form $J = 4t^2/(U - V)$ and an additional term $V \sum_j \hat{n}_j \hat{n}_{j+1}$.

Away from half-filling, the $t - J$ model describes a system of interacting spins and mobile holes, i.e., a *doped* AF. A fundamental problem is to understand the evolution of an AF Mott-type insulator into a metal or superconductor at a certain hole concentration.

Since large U/t implies that $t \gg J, J'$, the hopping term is not small. As a consequence, the motion of the holes disturbs the AF correlations. This is a quite challenging theoretical problem: the Heisenberg model, which is believed to be fairly well understood, is strongly perturbed by addition of mobile holes. The properties of the $t - J$ model have been widely explored, since it is believed to describe features of high-T_c superconductors. A famous semi-classical solution has been obtained using the Swinger boson mean field-theory [189, 190], that shows that the propagation of charge carriers interacting strongly with AF spin-fluctuations favors spin-ordering.

When studying Eq. (9.1), it is customary to omit the third term from the Hamiltonian, by arguing that its effects are small in comparison to the ones dictated by the hopping t. Furthermore, in bipartite lattices, the three site terms do not “mess up” the spin ordering since they move holes on the same sublattice. On the contrary, the hopping term can move holes between different sublattices, thereby disturbing AF correlations. This is schematically illustrated in Fig. 9.1. The Hamiltonian that we will consider in the following is then

$$\hat{H}_{tJ} = \mathbb{P}_0 \left\{ -t \sum_{\langle ij \rangle, \sigma} \hat{c}^\dagger_{i\sigma} \hat{c}_{j,\sigma} + \frac{J}{2} \sum_{\langle ij \rangle} \left(\mathbf{S}_i \cdot \mathbf{S}_j - \frac{\hat{n}_i \hat{n}_j}{4} \right) \right\} \mathbb{P}_0. \tag{9.2}$$

It is important to notice that the projected version of creation, annihilation, and particle-number operators, $\hat{b}^\dagger_{j,\sigma} \equiv \hat{c}^\dagger_{j,\sigma}(1 - \hat{n}_{j,-\sigma})$, $\hat{b}_{j,\sigma} \equiv \hat{c}_{j,\sigma}(1 - \hat{n}_{j,-\sigma})$, $\hat{\nu}_{j,\sigma} \equiv \hat{b}^\dagger_{j,\sigma} \hat{b}_{j,\sigma} = \hat{n}_{j,\sigma}(1 - \hat{n}_{j,-\sigma})$, have non-fermionic anticommutation relations [188, 191, 192]. As a consequence, the hopping and exchange part do not commute with each other, causing the motion of single electrons and the spin interactions to be entangled with each other. For large enough t, this results in a strongly correlated metallic state, which can be described as a Luttinger Liquid [22].

When the kinetic $\sim t$ and the exchange $\sim t^2/U$ energies become comparable, the Luttinger liquid (metallic) state may have a transition to a localized state induced by the exchange interaction [193]. Alternatively, one could have phase separation into AF islands immersed in the ferromagnetic sea of holes [194].

Based on our success from earlier chapters, here we propose selective vibrational excitation as a tool to cause a transition between a metallic-like and a localized state. We shall exploit the results of Sec. 6.5, in which we have shown that driving can greatly reduce the coherent hopping amplitude to a new value $t \to \tilde{t} < t$.

9.2 Dynamic $t - J$ model

The effects of local vibrations can be taken into account within the $t - J$ model, by adding a coupling term between the local electron density and the oscillator displacement. We obtain a Dynamic $t - J$ model, that can written as

$$\begin{aligned}\hat{H}_{DtJ} = & -t \sum_{\langle ij \rangle, \sigma} \hat{b}^{\dagger}_{i,\sigma} \hat{b}_{j,\sigma} + J \sum_{\langle ij \rangle} \left(\mathbf{S}_i \cdot \mathbf{S}_j - \frac{\hat{\nu}_i \hat{\nu}_j}{4} \right) \\ & + g \frac{a_0}{\sqrt{2}} \sum_j \hat{\nu}_j (\hat{a}^{\dagger}_j + \hat{a}_j) + \Omega \sum_j (\hat{a}^{\dagger}_j \hat{a}_j + \tfrac{1}{2}), \end{aligned} \tag{9.3}$$

where $\hat{a}^{\dagger}_j$ and $\hat{a}_j$ are the oscillator raising and lowering operators of on-site molecular vibrations, coupled to the electron density with coupling g and oscillating with frequency Ω. In other words, here we are considering the simplest possible coupling between on-site vibrations and electrons, i.e., a Holstein-type linear coupling.

In analogy to Ch. 6, we perform a canonical Lang-Firsov transformation so as to move to a quasi-particle picture, and investigate how the various terms in Eq. (9.3) are affected by the coupling. We choose the simplest possible form of coupling, i.e., linear coupling to the electron density. In this case, the operator for the Lang-Firsov transformation is $\hat{X}_j = \hat{D}_j(\chi) \mathbb{P}^s_j$, where $\mathbb{P}^s$ is the projector over the singly occupied state and $\chi = ga_0/\Omega\sqrt{2}$, the transformed Hamiltonian is

$$\begin{aligned}\hat{H}^{\bullet}_{DtJ} = & -t\overbrace{\sum_{\langle ij\rangle,\sigma}\hat{D}_j(\chi)\hat{D}^{\dagger}_{j+1}(\chi)\hat{b}^{\dagger}_{i,\sigma}\hat{b}_{j,\sigma}}^{\hat{H}^{\bullet}_t}+J\sum_{\langle ij\rangle}\left(\mathbf{S}_i\cdot\mathbf{S}_j-\frac{\hat{\nu}_i\hat{\nu}_j}{4}\right)\\ & +\sum_j\underbrace{\Omega(\hat{a}^{\dagger}_j\hat{a}_j+\tfrac{1}{2})}_{\hat{H}_{s,j}}-\Omega\chi^2\sum_j\hat{\nu}_j.\end{aligned} \tag{9.4}$$

We have succeeded in locally decoupling the oscillators and the electrons, whilst reducing the local potential by $-\Omega\chi^2$ and "dress" the hopping term. As anticipated above, the hopping operator ($\hat{H}^{\bullet}_t$) is transformed in such a way that an electron is *dressed* by a displaced state of the local oscillator. Crucially, the exchange term in the Hamiltonian is unaffected by the transformation.

9.2.1 Hopping quench

To estimate quantitatively how the coherent motion is affected by the vibration, we need to evaluate the modifications caused by the vibrations on the hopping amplitude. As already argued in Sec. 6.5, this is tantamount to limit the allowed hopping processes only to diagonal transitions: $|\mathbf{x}_i,\vec{\sigma}_i\rangle|\vec{n}\rangle \to |\mathbf{x}_f,\vec{\sigma}_f\rangle|\vec{n}\rangle$. Let us recall that these are the hopping processes in which all the vibrational occupation numbers $\vec{n}$ stay unchanged.

If $|\mathbf{x}_i,\vec{\sigma}_i\rangle$ and $|\mathbf{x}_f,\vec{\sigma}_f\rangle$ are the initial and final electronic configurations, and assuming that the original $\hat{H}_t$ has the same amplitude t for any permissible hopping transition, we can consider the amplitude of just one transition of a single electron with spin σ to hop from site $j+1$ to j:

$$\begin{aligned}(\tilde{t})_{n_j,n_{j+1}} =&\langle\mathbf{x}_f,\vec{\sigma}_f|\hat{c}^{\dagger}_{j,\sigma}\hat{c}_{j+1,\sigma}|\mathbf{x}_i,\vec{\sigma}_i\rangle\langle\vec{n}|\hat{D}_j(\chi)\hat{D}_{j+1}(\chi)|\vec{n}\rangle,\\ =&t\langle n_j|\hat{D}_j(\chi)|n_j\rangle\langle n_{j+1}|\hat{D}^{\dagger}_{j+1}(\chi)|n_{j+1}\rangle.\end{aligned} \tag{9.5}$$

Keeping only diagonal terms, the truncated Dynamic $t-J$ Hamiltonian, Eq. (9.4), is transformed as

$$\hat{H}^{\circ}_{DtJ} = \left\{\hat{H}^{\circ}_t + J\sum_{\langle ij\rangle}\left(\mathbf{S}_i\cdot\mathbf{S}_j-\frac{\hat{\nu}_i\hat{\nu}_j}{4}\right)-\Omega\chi^2\hat{\nu}_j+\hat{H}_{s,j}\right\}\otimes|\vec{n}\rangle\langle\vec{n}|,$$

that formally can be written as

$$\hat{H}^{\circ}_{DtJ} = \sum_{\vec{n}}\hat{H}_{\vec{n}}\otimes|\vec{n}\rangle\langle\vec{n}|.$$

We have bundled all the electronic terms into a $\hat{H}_{\vec{n}}$ with hopping amplitudes dependent on $\vec{n}$, so that the time evolution operator in the polaron picture is readily given by $\hat{U}(\tau) = \sum_{\vec{n}} \exp(-i\hat{H}_{\vec{n}}\tau) \otimes |\vec{n}\rangle\langle\vec{n}|$. Let us take an initial state of the form $\rho_i = \rho_{\mathrm{el}} \otimes \rho_{\mathrm{os}}$, where ρ_{os} is a number-diagonal stationary state of the oscillators described by a vibrational occupation probability distribution $p_{\vec{n}}$, and ρ_{el} and ρ_{el} a generic thermal state of the electron system. $\rho(\tau)$ evolves in time as

$$\rho(\tau) = \hat{U}^{\dagger}(\tau)\rho_i\hat{U}(\tau) = \sum_{\vec{n}} p_{\vec{n}} \left(\mathrm{e}^{i\hat{H}_{\vec{n}}\tau}\rho_{\mathrm{el}}\mathrm{e}^{-i\hat{H}_{\vec{n}}\tau}\right) \otimes |\vec{n}\rangle\langle\vec{n}|. \tag{9.6}$$

Following Mahan [103], we evaluate $(\tilde{t})_{n_j,n_{j+1}}$ by averaging over the (initially identical) stationary states of the oscillators. We end up with a single, translationally invariant, hopping amplitude:

$$\begin{aligned}\tilde{t} &= \sum_{n_j,n_{j+1}} p_{n_j,n_{j+1}} (\tilde{t})_{n_j,n_{j+1}} = \sum_{n_j,n_{j+1}} \mathrm{tr}\left[\hat{D}(\chi)\rho_\alpha\right] \mathrm{tr}\left[\hat{D}^{\dagger}(\chi)\rho_\alpha\right] \\ &= t\mathrm{e}^{-\chi^2} J_0^2(2\chi|\alpha|). \end{aligned} \tag{9.7}$$

The matrix element in Eq. (9.7) is suppressed exponentially with the coupling g^2, regardless of the driving, and further suppressed by the square of the J_0 Bessel function with increasing driving $|\alpha|$.

To conclude, by exploiting the fact that the vibrational driving affects the hopping amplitude but *does not* change the spin exchange interaction strength, we advocate vibrational driving as a tool to inhibit the hole motion and thus dynamically induce spin ordering.

9.2.2 Vibrationally induced disorder

Up to this point, we have focused on localized vibrations, since we would like to apply this idea to our organic salt ET-F$_2$TCNQ. It is worthwhile to consider in some detail what kind of differences would arise if we rather considered phonons, i.e., collective normal modes of the lattice. In this instance, the electron-phonon coupling takes the form [165]: $\sum_{jk} g_{k,j}\hat{n}_j\hat{q}_k$, i.e., the electron density at each site couples linearly to all collective phonon modes, with quasi-momentum k and coupling strength $g_{k,j}$. In particular, $g_{k,j}$ is $g_{k,j} = M_k \exp(ikj)$: the site dependence is a phase factor multiplying a momentum dependent coupling.

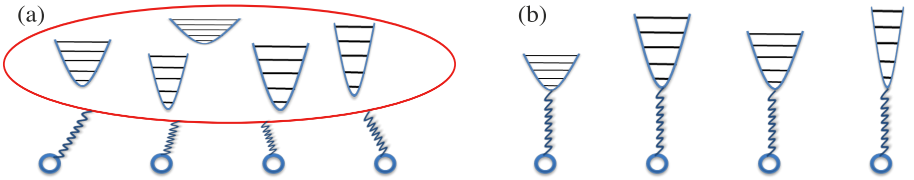

Figure 9.2: (a) Holstein-like coupling between electrons on the molecular site and a bath of oscillators. (b) Local electron-vibration coupling.

The difference between electron-phonon and electron-local vibration coupling is schematically illustrated in Fig. 9.2.

Strictly speaking, averaging the hopping transition amplitudes $\tilde{t}$ over the stationary state of the oscillators is more justified in the case of phonon coupling than for local vibrations. In fact, in the former situation the eigenstates of the hopping term are all Bloch states independent of $\vec{n}$, but with bandwidth dependent on $\vec{n}$. On the contrary, for a local Dynamic $t-J$ model, the eigenstates of the hopping term differ considerably with $\vec{n}$ and will in general be localized. The system can be seen as disordered, since the hopping will be different depending on the pair of sites taken into account. This effect is neglected by averaging the amplitude[1].

Despite this approximation being quite crude, the final physical result should not be affected. Indeed, as shown by Anderson [185, 195], disordered hopping leads to hole-localization as well. Thus, the effective result will be that “vibrationally induced” disorder leads to a further reduction of hole motion within the system.

9.3 Correlation functions

Up to this point, we have demonstrated that local vibrations reduce the hopping amplitude rather then the exchange coupling. To get some insight on how the

---

[1] To see this, suppose we had an Hamiltonian with some disordered coupling $\epsilon \in \{-1, 1\}$ distributed with zero mean $\langle \epsilon \rangle = 0$. If the Hamiltonian itself is averaged directly, the disorder disappears completely. Yet, if the evolution is performed first for each disorder realization of the original Hamiltonian and the results are averaged at the end, the Anderson localization will emerge.

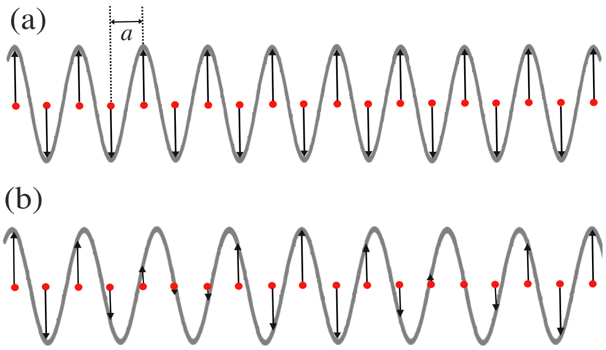

Figure 9.3: (a) Commensurate spin-density wave, with wave vector $q = \pi/a$. (b) Incommensurate spin-density wave.

magnetic state of the system is affected by this process, in this section we discuss the spin structure factors.

In general, the study of dynamic structure factors provides information about the dispersion and intensity of electronic excitations. Importantly, they are related to observables that can be experimentally measured, e.g., by inelastic neutron scattering [196].

In this section, we are going to focus on the longitudinal spectral function S^{zz}. By taking z as the longitudinal axis along which the spins are aligned if the system shows magnetic order, the Fourier transform of the spin operator $\hat{S}^z$ is

$$\hat{S}^z_q = \frac{1}{\sqrt{M}} \sum_j \hat{S}^z_j \mathrm{e}^{-iqj}.$$

If we set periodic boundary conditions (PBC) for a chain of M lattice sites, we obtain values for the momentum $q = 2\pi a Z/M$, where $-M/2 < Z \leq M/2$ (a is the lattice spacing). On the contrary, if we have open boundary conditions (OBC), the Fourier transform needs to be slightly modified as

$$\hat{S}^z_q = \sqrt{\frac{2}{M+1}} \sum_j \hat{S}^z_j \sin(qj),$$

where now the quasi-momentum values are $q = \pi Z a/M$, for integers $1 \leq Z \leq M$. The results obtained with either boundary condition should be equivalent in the thermodynamic limit.

The longitudinal dynamical structure factor is defined as the imaginary part of the spin-spin correlation function

$$\begin{aligned} S^{zz}(q,\omega) =& \frac{1}{\pi}\mathrm{Im}\left[\sum_{j,j'=1}^{M} \mathrm{e}^{-iq(j-j')}\int_{-\infty}^{+\infty}\mathrm{d}\tau \mathrm{e}^{i\omega\tau}\langle\psi_0|\hat{S}_j^z(\tau)\hat{S}_j^z(0)|\psi_0\rangle\right] \\ =& \frac{1}{\pi}\mathrm{Im}\left[\langle\psi_0|\hat{S}_q^{z\dagger}\frac{1}{\hat{H}+\omega-E_0}\hat{S}_q^z|\psi_0\rangle\right], \end{aligned} \tag{9.8}$$

where $|\psi_0\rangle$ and E_0 are the ground state wave function and energy of the Hamiltonian $\hat{H}$, respectively.

One of the most important properties that can be extracted from Eq. (9.8) is the existence of ordered phases. For example, the spin structure factor at $q = \pi/a$ is a measure of AF correlations. When the nesting wave vector

$$q = 2k_F = n\pi,$$

where k_F and n are the Fermi wave vector and the filling, respectively, turns out to be π/a, there is a spin-density wave commensurate with the lattice and AF order results (Fig. 9.3(a)) [197]. On the contrary, when $\mathbf{q}$ is not a simple multiple of π/a, the spin density wave is incommensurate (Fig. 9.3(b)). Correspondingly, a peak at $q = 0$ is indicative of a ferromagnetic behavior.

9.4 Quenched hopping

From Fig. 9.4 we find that in a system with low-energy physics described by the $t - J$ model, the AF order is destroyed when moving away from half-filling when the kinetic energy of the electron is sizable with respect to the exchange energy. On the contrary, if the latter becomes dominant, one would expect the spins to localize and align antiferromagnetically (for $J > 0$).

In Sec. 9.2 we argued that local vibrations can *dynamically* quench the hopping amplitude. Here we ask the following question: provided that the system is at time $\tau_0 = 0$ in its ground state, what happens in time if the hopping amplitude is suddenly quenched, e.g., by strongly driving the system?

To address this matter, we calculate the spin structure factor $S^{zz}(q)$ as a function of time. We start by computing the ground state of the $t - J$ Hamiltonian with $U/t = 20$, $J = 4t^2/U = 0.2$. Then, we let this state evolve in time

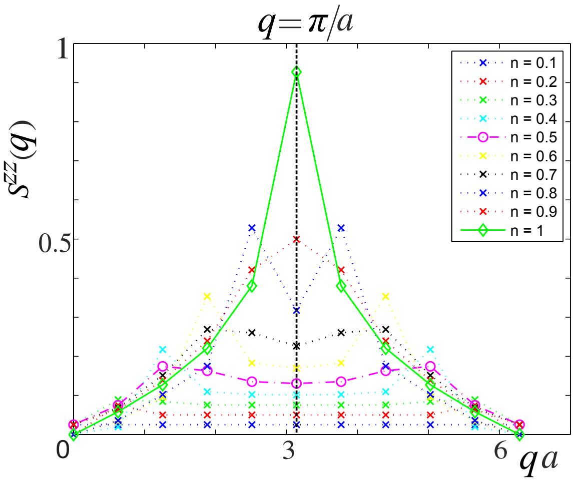

Figure 9.4: $S^{zz}(q)$ in a $t-J$ model as a function of the filling n. A clear peak at $q = \pi/a$ is observed for half-filling. The results have been obtained for a chain of $M = 10$ lattice sites with periodic boundary conditions. We choose a value of $U/t = 20$.

up to a final time τ_f, while the hopping amplitude is quenched to a value small that J: $\tilde{t} \ll J$.

The results for the time-dependent structure factor, computed in a chain with $M = 10$ lattice sites with PBC and $\tilde{t} = J/10$, are reported in Fig. 9.5 for different fillings. The thick red and blue lines show $S^{zz}(q, \tau)$ at initial ($\tau_0 = 0$) and at a much later time, that we take equal to $\tau_f = 30/t$. We have chosen a large value so that the electrons have enough time to perform multiple hops. It is clear the appearance of a peak at $q/a = \pi$, signaling AF order. This signature becomes less and less prominent as the filling decreases, given the increase in the number of holes.

9.5 Summary

In this chapter, we proposed vibrational driving as a tool to transiently induce magnetic order. Starting from a system with electronic properties described by the $t-J$ model, we showed that the excitation quenches the hopping amplitude while not affecting the exchange interaction. We presented some numerical

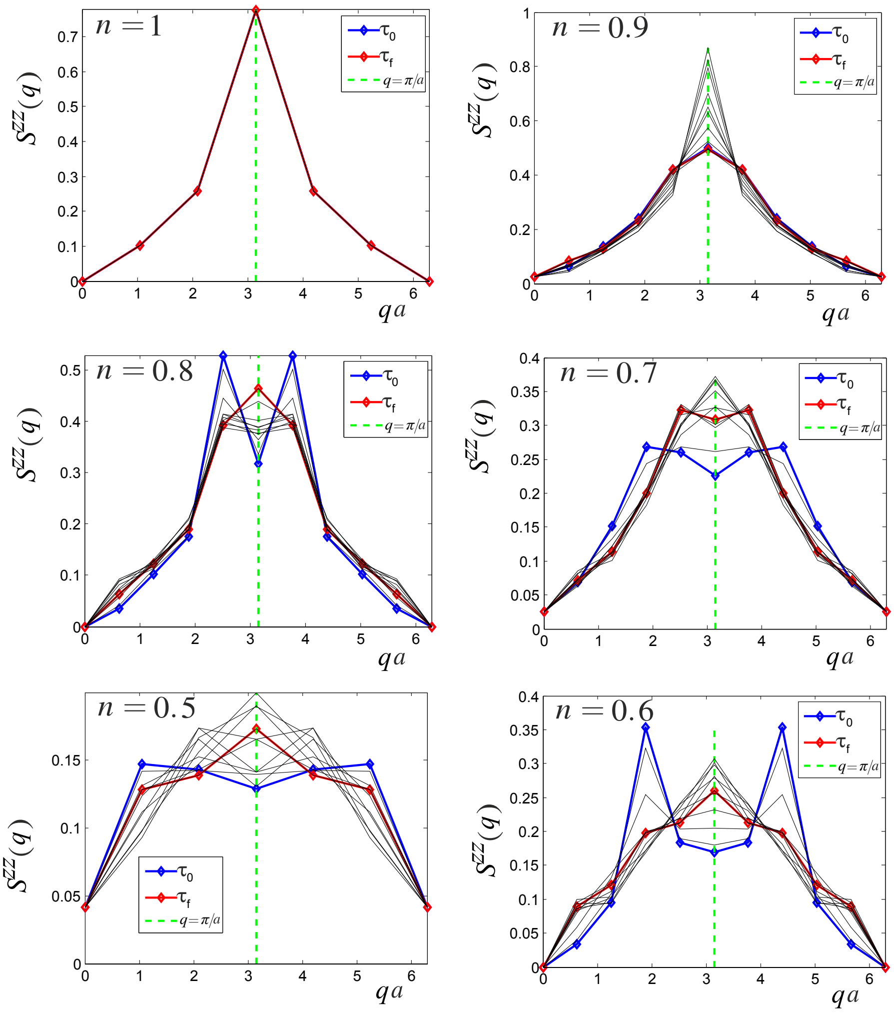

Figure 9.5: Time dependence of spin structure factor of a $t-J$ with quenched hopping $\tilde{t} = J/10$, for different fillings ($n = 1$ is half-filling, $n = 0.5$ quarter filling, and so on). The thick red and blue lines show $S^{zz}(q, \tau)$ at initial ($\tau_0 = 0$) and at final ($\tau_f = 30/t$) time, respectively, while the black lines are the results for intermediate times. We clearly see a peak appear at $q = \pi/a$, indicating AF order.

results to substantiate our claims.

These results are encouraging, but an extension to bigger systems (e.g. by using time-dependent DMRG algorithms [198]) is required. In parallel with this, it would be interesting to perform simulations with different values of the quenched hopping $\tilde{t}$ and establish what is the maximum value that allows to observe this effect. Furthermore, a deeper knowledge of the final state of the system is required, e.g., if we reach a out-of-equilibrium steady state.

Vibrational control of magnetism could be investigated in an experiment at low temperature, in which a simultaneous probe of the X-ray or neutron diffraction with vibration pumping, should show a transient formation of AF order.

9.A Strong coupling limit

In this appendix we formally derive the $t-J$ and Heisenberg model by means of large U perturbation theory of $\hat{H}_{\mathrm{HM}}$ Eq. (2.1). Following [102], we take $\hat{H}_t$ to be a small perturbation of $\hat{H}_U$. The double occupancy operator,

$$\hat{H}_d = \sum_{j=1}^{M} \hat{n}_{j\uparrow}\hat{n}_{j\downarrow},$$

counts the number of doubly occupied sites: its eigenvalues are thus $n = 0, \ldots, M$. The Hilbert space $\mathcal{H}^{(M)}$ of our model decomposes into $\mathcal{H}^{(M)} = \mathcal{H}_0 \oplus \cdots \oplus \mathcal{H}_M$, and $\hat{H}_d$ has spectral decomposition

$$\hat{H}_d = \sum_{n=1}^{M} n\mathbb{P}_n,$$

where $\mathbb{P}_n$ are the projectors onto the corresponding eigenspaces $\mathcal{H}_n$.

A fermionic representation of $\mathbb{P}_n$ is obtained by the generating function

$$G(\alpha) = \prod_{j=1}^{M}(1-\alpha\hat{n}_{j\uparrow}\hat{n}_{j\downarrow}),$$

that acts on Wannier states $|\mathbf{x},\vec{\sigma}\rangle$ as

$$G(\alpha)|\mathbf{x},\vec{\sigma}\rangle = (1-\alpha)^n|\mathbf{x},\vec{\sigma}\rangle. \tag{9.9}$$

Here n is the number of doublons in the state $|\mathbf{x},\vec{\sigma}\rangle$, i.e., $\hat{H}_d|\mathbf{x},\vec{\sigma}\rangle = n|\mathbf{x},\vec{\sigma}\rangle$. It follows from Eq. (9.9) that

$$\frac{(-1)^k}{k!}\partial_\alpha^k G(\alpha)|_{\alpha=1}|\mathbf{x},\vec{\sigma}\rangle = \delta_{kn}|\mathbf{x},\vec{\sigma}\rangle,$$

and thus

$$\mathbb{P}_n = \frac{(-1)^n}{n!}\partial_\alpha^n G(\alpha)\Big|_{\alpha=1}. \tag{9.10}$$

Obviously, for $n=0$ we have $\mathbb{P}_0 = G(1)$ from Eq. (9.9). Explicitly,

$$\mathbb{P}_0 = \prod_{j=1}^{M}(1-\hat{n}_{j\uparrow}\hat{n}_{j\downarrow}). \tag{9.11}$$

The Hamiltonian $\hat{H}_{\mathrm{HM}}$ conserves the number of electrons N, and we are going to consider the case $N \leq M$. For a fixed number of electrons N there are $2^N \begin{pmatrix} M \\ N \end{pmatrix}$ ground states of $\hat{H}_d$, which span the eigenspace $\mathcal{H}_0$ of $\mathbb{P}_0$.

Hence, the total number of Wannier states with no site doubly occupied is $\dim(\mathcal{H}_0) = 3^M$. The perturbation $\hat{H}_t$ partially lifts this degeneracy splitting the lowest energy level of $\hat{H}_U$ in many levels that are still well separated from the first excited one as long as $t \ll U$.

Let us consider a generic Hamiltonian $\hat{H}$ acting on a Hilbert space $\mathcal{H}$, $\mathbb{P}$ a projection on a subspace $\mathbb{P}\mathcal{H}$ of $\mathcal{H}$ and $\mathbb{Q} = 1 - \mathbb{P}$. $|\psi\rangle$ is a solution of the Schrödinger equation, $\hat{H}|\psi\rangle = E|\psi\rangle$, with eigenvalue E, if and only if

$$\mathbb{P}\hat{H}\mathbb{P}|\psi\rangle + \mathbb{P}\hat{H}\mathbb{Q}|\psi\rangle = E|\psi\rangle,$$
$$\mathbb{Q}\hat{H}\mathbb{P}|\psi\rangle + \mathbb{Q}\hat{H}\mathbb{Q}|\psi\rangle = E|\psi\rangle.$$

Solving the second equation for $\mathbb{Q}|\psi\rangle$ and inserting the result in the first one gets

$$\hat{H}(E)|\varphi\rangle = E|\varphi\rangle, \tag{9.12}$$

where

$$\hat{H}(E) = \mathbb{P}\hat{H}(1 + (E - \mathbb{Q}\hat{H})^{-1}\mathbb{Q}\hat{H})\mathbb{P}, \tag{9.13}$$

and $|\varphi\rangle = \mathbb{P}|\psi\rangle$. Thus, if $|\varphi\rangle \in \mathbb{P}\mathcal{H}$ solves Eq. (9.12), the vector

$$|\psi\rangle = (1 + (E - \mathbb{Q}\hat{H})^{-1}\mathbb{Q}\hat{H})|\varphi\rangle, \tag{9.14}$$

is a solution of the full stationary Schrödinger equation with eigenvalue E. Eqs. 9.13 and 9.12 are a convenient starting point for the perturbation theory around a given degenerate energy level.

Let us now split $\hat{H}$ into a contribution with known spectral decomposition, $\hat{H}_0 = \sum_n E_n\mathbb{P}_n$, and a perturbation $\hat{H}_1$ coupled to $\hat{H}_0$ by a constant λ:

$$\hat{H} = \hat{H}_0 + \lambda\hat{H}_1$$

Replacing $\mathbb{P}$ by $\mathbb{P}_n$ one obtains an operator $\hat{H}_n(E)$ that acts non-trivially only on the degeneracy subspace corresponding to the n-th energy level E_n of $\hat{H}_0$. Using the explicit form of $\hat{H}_0$ one can express $\hat{H}_n(E)$ in terms of the projectors $\mathbb{P}$

$$\hat{H}_n(E) = \left[E_n + \mathbb{P}_n\hat{H}_1\sum_{k=0}^{\infty}\left(\sum_{m(n\neq n)}\frac{\mathbb{P}\hat{H}_1}{E - E_m}\right)^k\right]\mathbb{P}_n. \tag{9.15}$$

and consequently the spectral problem Eq. (9.12) turns into

$$\mathbb{P}_n\hat{H}_1\sum_{k=0}^{\infty}\left(\sum_{m(n\neq n)}\frac{\mathbb{P}\hat{H}_1}{E - E_m}\right)^k|\varphi\rangle = (E - E_n)|\varphi\rangle, \tag{9.16}$$

for $|\varphi\rangle \in \mathbb{P}\mathcal{H}$.

We can finally perform perturbation theory around an energy level E_n in ascending orders of λ. For small λ we expect corrections to E_n of the form

$$E = E_n + \lambda E_n^{(1)} + \lambda^2 E_n^{(2)} + \mathcal{O}(\lambda^3).$$

To quadratic order in λ we obtain for Eq. (9.16)

$$\left[\mathbb{P}_n \hat{H}_1 \mathbb{P}_n + \lambda \sum_{m(m\neq n)} \frac{\mathbb{P}_n \hat{H}_1 \mathbb{P}_m \hat{H}_1 \mathbb{P}_n}{E_n - E_m}\right] = \frac{E - E_n}{\lambda}|\varphi\rangle. \tag{9.17}$$

The effective Hamiltonian on the restricted space $\mathbb{P}_n\mathcal{H}$ in $[\cdots]$ describes the splitting of the energy level E_n of $\hat{H}_0$ under the influence of the perturbation $\lambda\hat{H}_1$. The corresponding eigenstates of the full Hamiltonian are obtained by application of the operator $1 + (E - \mathbb{Q}_n\hat{H})^{-1}\mathbb{Q}_n\hat{H}\mathbb{P}_n$.

This formalism can now be readily applied to $\hat{H}_{\mathrm{HM}}$, by rescaling it as

$$\hat{H}_{\mathrm{HM}}/U = \hat{H}_d + \hat{H}_t/U.$$

$\hat{H}_{\mathrm{HM}}/U$ is in the form Eq. (9.15) with $\hat{H}_0 = \hat{H}_d$, $\hat{H}_1 = \hat{H}_t$ and $\lambda = 1/U$. Since the operator $\hat{H}_d$ has eigenvalues $E_n = n$ and we with to expand around the double occupancy degenerate ground state, we set $n = 0$ in Eq. (9.17) and obtain

$$\left[\mathbb{P}_0 \hat{H}_t \mathbb{P}_0 - \frac{1}{U}\sum_{m=1}^{M} \frac{\mathbb{P}_0 \hat{H}_t \mathbb{P}_m \hat{H}_t \mathbb{P}_0}{m}\right]|\varphi\rangle = E|\varphi\rangle. \tag{9.18}$$

The operator in $[\cdots]$ is called $t - J$ Hamiltonian, $\hat{H}_{tJ}$.

Substituting the explicit expressions and with a bit of algebra, we find Eq. (9.2):

$$\begin{aligned}\hat{H}_{tJ} =& \mathbb{P}_0 \Bigg\{ -t \sum_{\langle ij\rangle,\sigma} \hat{c}^\dagger_{i\sigma}\hat{c}_{j,\sigma} + \frac{J}{2}\sum_{ij}\left(\mathbf{S}_i \cdot \mathbf{S}_j - \frac{\hat{n}_j \hat{n}_j}{4}\right) \\ & -\frac{t^2}{U}\sum_{ijk}^{i\neq k}\left[\sum_{\sigma}(\hat{c}^\dagger_{i,\sigma}\hat{c}_{k,\sigma}\hat{n}_j) - \hat{c}^\dagger_i \vec{\sigma}\hat{c}_k \cdot \hat{c}^\dagger_j \vec{\sigma}\hat{c}_j\right]\Bigg\}\,\mathbb{P}_0.\end{aligned}$$

Chapter 10

Conclutions and outlook

10.1 Overview

Throughout this thesis we have used theoretical models and numerical tools to understand and characterize photo-induced effects in complex materials. Pump-probe experiments allow for an investigation of the electronic real-time dynamics, and manipulation of phase of correlated electron systems. We addressed these issues by investigating the one-dimensional organic charge-transfer compound ET-F_2TCNQ. This section highlights some of the more relevant contributions to this problem provided by this thesis.

- In Ch. 5 we have analyzed the pressure dependence of hot holon-doublon recombination in a one dimensional Mott insulator. By fitting the steady state infrared properties with a model based on the extended Hubbard Hamiltonian, we have extracted the pressure dependence of the Hubbard parameters t and V up to 2.0 GPa. We have succeeded in correlating these microscopic parameters to the recombination rates, and, crucially, in comparing their experimentally determined dependence to theoretical predictions. The key conclusion has been that the decay of quasi-particles is likely connected to the coherent evolution of holon-doublon pairs immediately after excitation.
- In Ch. 6, we have shown that the Extended Hubbard Hamiltonian has to be complemented with additional terms to properly take into account

the effects of local variations on the optical properties. The general features and the optical conductivity of the resulting model, called Dynamic Hubbard Model, have been explored analytically and with numerical simulations. The results of Ch. 7 and Ch. 8 have confirmed that it is possible to reproduce and thereby explain the broadband optical properties of ET-F_2TCNQ when specific modes are strongly driven.

- In Ch. 9 we have studied the effects of vibrations on the magnetic properties of a generic systems that satisfy the requirement that the Coulomb repulsion among electrons is much bigger than their kinetic energy. Differently from previous sections, in this case we consider non-half filled systems, and thus we are concerned with much lower energy scales. The model describing this physics, namely the $t - J$ model, is extended to include local molecular vibrations. We showed that, when driving a specific mode, the motion of holes is inhibited and magnetic order may be induced.

10.1.1 Further results

Motivated by the numerous similarities between the physics of ultra-cold quantum gases and correlated-electron systems, in Ref. [4] we have calculated, from first principles, the parameters of nearest-neighbor Hubbard models. We investigated several optical lattice potentials including the honeycomb and Kagomé potentials, demonstrating quantitatively for which lattice depths these models are accurate. Strongly-correlated phenomena probed in optical lattice experiments and quantum simulations depend delicately on the ratios of kinetic and interaction energies. Therefore, precisely determining them is essential for diagnosing and interpreting such experimental results, and for using optical lattices as quantum simulators of condensed matter systems. The ability to efficiently calculate the maximally-localized Wannier states for a given optical lattice potential will allow cold-atom researchers to easily and accurately determine Hubbard models realized by any laser setup.

More generally, having the capability to faithfully represent localized molecular orbitals in solid-state systems can be used in a large variety of applications [199], such as the analysis of chemical bonding, or as a local probe of phenomena related to electric polarization or orbital magnetization. Aside from their use in determining electronic structure theory and for modelling cold-atoms within optical lattices, maximally localized Wannier functions can be used for cases that include phonon excitations and photonic crystals.

10.2 Looking ahead

10.2.1 Strongly correlated organics: fundamental physics

In this work we have mainly addressed the fundamental physical processes of materials that exhibit strong electronic correlations. The one-dimensional conduction properties made our system ideal to explore and shed new light into the fundamental electron transfer mechanisms.

A possible question to address with regard to one-dimensional system is how much of our results can be applied to explain the physics of strongly correlated organic superconductors, such as the Bechgaard salts. These materials exhibit a Peierls transition from metallic to insulating behavior, and a spin-density wave is formed at the transition with a periodic antiferromagnetic order of conduction electrons. In these compounds, the application of pressure has already been investigated and shown to increase the dimensionality from one-dimensional to two- or three-dimensional [200]. In the future, mode-selective modulation spectroscopy may be used as an alternative method to dynamically induce phase transitions and switch between competing states with ordered charge or spin.

Another, possibly even more interesting, line of research could focus on the quasi-two dimensional CT superconductors that have the BEDT-TTF molecule as a structural unit. For example, one could study the effects of the very same vibrational excitations in salts with chemical composition $(\mathrm{ET})_2\mathrm{X}$. It is of crucial importance to understand the role that a time dependent Coulomb interaction plays in these compounds, since vibrational excitations can couple strongly to the superconducting order parameter [201].

10.2.2 Molecular electronics

The exploration of new territories and the subsequent discovery of novel phenomena often lead to unexpected technological applications. In recent years, molecular electronics has developed into an interdisciplinary research area which deals with the question of how molecular materials (such as organics) might find applications in electronics, photonics, and optoelectronics [202]. The future of this technology depends on our ability to understand the fundamental mechanism that governs the electronic conduction at the molecular scale.

In comparison with silicon-based technology, molecular electronics could in principle offer major advantages [203], ranging from higher packing density of devices and speed, as well as the capability of both switching and sensing electronic behavior on the single-molecule scale. Moreover, the existence of exotic phases, such as the ones investigated in this thesis, could lead to new electronic functions (e.g. ultrafast switches) that is not possible to implement in conventional semiconductor-based devices. Obviously, a number of issues have to be addressed, such as the fabrication of reliable molecular junctions, possible instabilities that might give rise to chemical reactions with their neighbors, etc. Anyway, the advantages described are sufficient to motivate a further exploration of electronics based on organic molecules.

We have shown that a light pulse permits the reversible selection of a specific physical property of the macroscopic system by means of an ultrafast stimulus. Such systems could be used as molecular switches, similarly to the ones based on polychromic compounds [204, 205, 206].

The control of magnetism with light is of interest precisely within the context of high speed switching applications.Vibrations could offer a neat way for achieving this goal. From an experimental point of view, it would be interesting to discover if mode selective vibrational driving can indeed transiently induce magnetic ordering, as proposed in Ch. 9. One could combine photo-doping and vibrational driving in ET-F_2TCNQ cooled below its Neél temperature, and track the electronic properties with THz probes. The mechanism proposed, though, is not limited to one-dimensional materials.

Additionally, further theoretical and numerical work is needed to substantiate the claims of Ch. 9. It is necessary to examine other correlation functions, e.g., transverse spin- or density-correlation functions. To achieve a better accuracy in the computation, we plan on simulating much larger system by using the Tensor Network Theory (TNT) library, developed within our group at Oxford `http://ccpforge.cse.rl.ac.uk/gf/project/tntlibrary/`.

Bibliography

[1] M. Mitrano, G. Cotugno, S.R. Clark, R. Singla, S. Kaiser, J. Stähler, R. Beyer, M. Dressel, L. Baldassarre, D. Nicoletti, A. Perucchi, T. Hasegawa, H. Okamoto, D. Jaksch, and A. Cavalleri, Phys. Rev. Lett. **112**, 117801 (2014).

[2] S. Kaiser, S. R. Clark, D. Nicoletti, G. Cotugno, R. I. Tobey, N. Dean, S. Lupi, H. Okamoto, T. Hasegawa, D. Jaksch, and A. Cavalleri, Sci. Rep. **4**, 3823 (2014).

[3] R. Singla, G. Cotugno, S. Kaiser, S. R. Clark, C. Manzoni, A. Cartella, H. Liu, M. Foerst, T. Hasegawa, H. Okamoto and A. Cavalleri, arXiv:1409.1088.

[4] R. Walters, G. Cotugno, T. H. Johnson, S. R. Clark, and D. Jaksch, Phys. Rev. A **87**, 043613 (2013).

[5] J. Hecht, Appl. Opt. **49**, F99 (2010).

[6] A. H. Zewail, J. Phys. Chem. A **104**, 5660 (2000).

[7] S. Koshihara, Y. Tokura, T. Mitani, G. Saito, and T. Koda, Phys. Rev. B **42**, 6853 (1990).

[8] G. Yu, C. H. Lee, A. J. Heeger, N. Herron, and E. M. McCarron, Phys. Rev. Lett. **67**, 2581 (1991).

[9] M. Sparks, and G. Teal, *Method of Making P-N Junctions in Semiconductor Materials*, U.S. Patent 2,631,356 (Filed June 15, 1950. Issued March 17, 1953).

[10] C. V. Shank, R. Yen, R. L. Fork, J. Orenstein, and G. L. Baker, Phys. Rev. Lett. **49**, 1660 (1982).

[11] C. W. Siders, A. Cavalleri, K. Sokolowski-Tinten, C. Toth, T. Guo, M Kammler, H. H. von Hoegen, K. R. Wilson, D. von der Linde, and C. P. J. Barty, Nature **286**, 1340 (1999).

[12] A. Sommerfeld, and H.Bethe, *Elektronentheorie der Metalle* (Springer Verlag, Heidelberg, 1933).

[13] N. W. Ashcroft, N. D. Mermin, *Solid State Physics* (Holt, Rinehardt and Winston, New York, 1976).

[14] L. D. Landau, Sov. Phys. JEPT **3**, 920 (1957).

[15] N. F. Mott, Proc. Phys. Soc. (London) **A62**, 416 (1949).

[16] E. Wigner, Phys. Rev. **46**, 1002 (1934).

[17] M. Imada, A. Fujimori, and A. Tokura, Rev. Mod. Phys. **70**, 1039 (1998).

[18] J. G. Bednorz, and K. A. Mller, Z. Phys. B **64**, 189 (1986).

[19] M. Matsubara, Y. Okimoto, T. Ogasawara, Y. Tomioka, H. Okamoto, and Y. Tokura, Phys. Rev. Lett. **99**, 207401 (2007).

[20] E. H. Lieb, and F. Y. Wu, Phys. Rev. Lett. **20**, 1445 (1968).

[21] A. M. Tsvelik, *Quantum Field Theory in Condensed Matter Physics* (Cambridge University Press, Cambridge, 1995).

[22] T. Giamarchi, *Quantum Physics in One Dimension* (Oxford University Press, Oxford, 2004).

[23] N. F. Mott, *Metal-Insulator Transitions* (Taylor and Francis, London, 1990).

[24] S. Iwai, M. Ono, A. Maeda, H. Matsuzaki, H. Kishida, H. Okamoto, and Y. Tokura, Phys. Rev. Lett. **91**, 057401 (2003).

[25] C. Kübler, H. Ehrke, R. Huber, R. Lopez, A. Halabica, R. F. Haglund, and A. Leitenstofer, Phys. Rev. Lett. **99**, 116401 (2007).

[26] T. Ogasawara, M. Ashida, N. Motoyama, H. Eisaki, S. Uchida, Y. Tokura, H. Ghosh, A. Shukla, S. Mazumdar, and M. Kuwata-Gonokami, Phys. Rev. Lett. **85**, 2204 (2000).

[27] H. Okamoto, H. Matsuzaki, T. Wakabayashi, Y. Takahashi, and T. Hasegawa, Phys. Rev. Lett. **98**, 037401 (2007).

[28] L. Perfetti, P. A. Loukakos, M. Lisowski, U. Bovensiepen, H. Berger, S. Biermann, P. S. Cornaglia, A. Georges, and M. Wolf, Phys. Rev. Lett. **97**, 067402 (2006).

[29] S. Hellmann, M. Beye, C. Sohrt, T. Rohwer, F. Sorgenfrei, H. Redlin, M. Kalläne, M. Marczynski-Bühlow, F. Hennies, M. Bauer, A. Föhlosch, L. Kipp, *et al.*, Phys. Rev. Lett. **105**, 187401 (2010).

[30] J. C. Petersen, S. Kaiser, N. Dean, A. Simoncig, H. Y. Liu, A. L. Cavalieri, C. Cacho, I. C. E. Turcu, E. Springate, F. Frassetto, L. Poletto, S. S. Dhesi, H. Berger, and A. Cavalleri, Phys. Rev. Lett. **107**, 177402 (2011).

[31] F. Schmitt, P. S. Kirchmann, U. Bovensiepen, R. G. Moore, L. Rettig, M. Krenz, J.-H. Chu, N. Ru, L. Perfetti, D. H. Lu, M. Wolf, I. R. Fisher, and Z.-X. Shen, Science **321**, 1649 (2008).

[32] E. Beaurepaire, J.-C. Merle, A. Daunois, and J.-Y. Bigot, Phys. Rev. Lett. **76**, 4250 (1996).

[33] H. Ehrke, R. I. Tobey, S. Wall, S. A. Cavill, M. Frst, V. Khanna, Th. Garl, N. Stojanovic, D. Prabhakaran, A. T. Boothroyd, M. Gensch, A. Mirone, P. Reutler, A. Revcolevschi, S. S. Dhesi, and A. Cavalleri, Phys. Rev. Lett. **106**, 217401 (2011).

[34] A. Takahashi, H. Itoh, and M. Aihara, Phys. Rev. B **77**, 205105 (2008).

[35] S. Wall, D. Prabhakaran, A. T. Boothroyd, and A. Cavalleri, Phys. Rev. Lett. **103**, 097402 (2009).

[36] A. D. Caviglia, R. Scherwitzl, P. Popovich, W. Hu, H. Bromberger, R. Singla, M. Mitrano, M. C. Hoffmann, S. Kaiser, P. Zubko, S. Gariglio, J.-M. Triscone, M. Frst, and A. Cavalleri, Phys. Rev. Lett. **108**, 136801 (2012).

[37] M. Rini, R. Tobey, N. Dean, J. Itatani, Y. Tomioka, Y. Tokura, R. W. Schoenlein, and A. Cavalleri, Nature **449**, 72 (2007).

[38] R. I. Tobey, D. Prabhakaran, A. T. Boothroyd, and A. Cavalleri, Phys. Rev. Lett. **101**, 197404 (2008).

[39] D. Fausti, R. I. Tobey, N. Dean, S. Kaiser, A. Dienst, M. C. Hoffmann, S. Pyon, T. Takayama, H. Takagi, and A. Cavalleri, Science **14**, 189 (2011).

[40] J. Hubbard, Proc. Roy. Soc. A **276**, 238 (1963).

[41] P. A. Lee, N. Nagaosa, and X.-G. Wen, Rev. Mod. Phys. **78**, 17 (2006).

[42] M. Greiner, O. Mandel, T. W. Hänsch, and I. Bloch, Nature **419**, 51 (2002).

[43] U. Schneider, L. Hackermüller, J. P. Ronzheimer, S. Will, S. Braun, T. Best, I. Bloch, E. Demler, S. Mandt, D. Rasch, and A. Rosch, Nature Physics **8**, 213 (2012).

[44] I. Bloch, J. Dalibard, and W. Zwerger, Rev. Mod. Phys. **80**, 885 (2008).

[45] M. Lewenstein, A. Sanpera, V. Ahufinger, B. Damski, A. Sen, U. Sen, Adv. Phys. **56**, 243 (2007).

[46] M. Lewenstein, A. Sanpera, V. Ahufinger, *Ultracold Atoms in Optical Lattices: Simulating Quantum Many-body Systems* (Oxford University Press, Oxford, 2012).

[47] H. Aoki, N. Tsuji, M. Eckstein, M. Kollar, T. Oka, and P. Werner, Rev. Mod. Phys. (2014).

[48] N. Strohmaier, D. Greif, R. Jördens, L. Tarruell, H. Moritz, T. Esslinger, R. Sensarma, D. Pekker, E. Altman, and E. Demler, Phys. Rev. Lett. **104**, 080401 (2010).

[49] M. Schwoerer, and H. C. Wolf, *Organic Molecular Solids* (WILEY-VCH GmbH & Co. KGaA, Weinheim, 2007).

[50] F. Gebhard, K. Born, M. Scheidler, P. Thomas, and S. W. Koch, Phil. Mag. B **75**, 1 (1997); F. Gebhard, K. Born, M. Scheidler, P. Thomas,

and S. W. Koch, Phil. Mag. B **75**, 13 (1997). F. Gebhard, K. Born, M. Scheidler, P. Thomas, and S. W. Koch, Phil. Mag. Part B **75**, 47 (1997).

[51] W. Barford, *Electronic and Optical Properties of Conjugated Polymers* (Clarendon Press, Oxford, 2005).

[52] M. J. Frisch, G. W. Trucks, H. B. Schlegel, G. E. Scuseria, M. A. Robb, *at al.*, and J. A. Pople, *Gaussian 03, Revision C.02*, (Gaussian, Inc., Wallingford, CT, 2004).

[53] E. B. Yagubskii, I. F. Schegolev, V. N. Laukhin, P. A. Kononovich, M. V. Kartsovnik, A. V. Zvarykina, L. I. Buravov, Sov. Phys. JEPT Lett. **39**, 12 (1984).

[54] J. M. Williams, T. J. Emge, H. H. Wang, M. A. Beno, P. T. Copps, L. N. Hall, K. D. Carlson, G. W. Crabtree, Inorg. Chem. **23**, 2558 (1984).

[55] J. M. Williams, A. J. Schultz, U. Geiser, K. D. Carlson, A. M. Kini, H. H. Wang, W.-K. Kwok, M.-H. Whangbo, J. E. Schirber, Science **252**, 1501 (1991).

[56] D. Jerome, Science **252**, 1509 (1991).

[57] R. H. McKenzie, Science **278**, 820 (1997).

[58] D. Jèrome, A. Mazaud, M. Ribault, and K. Bechgaard, J. Phys. Lett. **41**, L95 (1980).

[59] D. Jèrome, Physica **109/110B**, 1447 (1982).

[60] C. S. Jacobsen, K. Mortensen, N. Thorup, D. B. Tanner, M. Weger, and K. Bechgaard, Chem. Scri. **17**, 103 (1981).

[61] H. Kino, and H. Fukuyama, J. Phys. Soc. Jpn. **65**, 2158 (1996).

[62] P. Wzietek, H. Mayaffre, D. Jèrome, S. Brazovskii, Synth. Metals **85**, 1511 (1997).

[63] K. Kanoda, Hyperfine Interact. **104**, 235 (1997).

[64] T. Hasegawa, T. Mochida, R. Kondo, S. Kagoshima, Y. Iwasa, T. Akutagawa, T. Nakamura, and G. Saito, Phys. Rev. B, **62**(**15**), 10059 (2000).

[65] R. E. Peierls, *Quantum Theory of Solids* (Oxford University Press, 1955).

[66] G. Grüner, *Density Waves in Solids.* Frontiers in Physics (Perseus Publishing, 1994).

[67] T. Hasegawa, S. Kagoshima, T. Mochida, S. Sugiura, Y. Iwasa, Solid State Comm. **103**, 489 (1997).

[68] A. Girlando, J. Phys. Chem. C **115**, 19371 (2011).

[69] A. A. Ovchinnicov, Zh. Eksp. Teor. Fiz. **57**, 2137 (1969) (Sov. Phys. JEPT **30**, 1160 (1970)).

[70] S. K. Lyo, and J. P. Gallinar, J. Phys. C **10**, 1693 (1977). S. K. Lyo, Phys. Rev. B **18**, 1854 (1978).

[71] D. K. Campbell, J. T. Gammel, and E. Y. Loh, in *Interacting Electrons in Reduced Dimensions*, ed. by D. Baeriswyl and D. K. Campbell (NATO ASI Series B **213**, Plenum Press, New York, 1989).

[72] J. Zaanen, G. A. Sawatzky, and J. W. Allen, Phys. Rev. Lett. **55**, 418 (1985).

[73] D. I. Khomskii, *Basic Aspects of the Quantum Theory of Solids*, Ch. 12 (Cambridge University Press, New York, 2010).

[74] E. Boaknin, R. W. Hill, C. Proust, C. Lupien, L. Taillefer, and P. C. Canfield, Phys. Rev. Lett. **87**, 237001 (2001).

[75] S. Kaiser, M. Dressel, Y. Sun, A. Greco, J. A. Schlueter, G. L. Gard, and N. Drichko, Phys. Rev. Lett. **105**, 206402 (2010).

[76] S.Wall, D. Brida, S. R. Clark, H. P. Ehrke, D. Jaksch, A. Ardavan, S. Bonora, H. Uemura, Y. Takahashi, T. Hasegawa, H. Okamoto, G. Cerullo, and A. Cavalleri, Nature Materials **10**, 101 (2011).

[77] C. M. Varma, Phys. Rev. Lett. **75**, 898 (1995).

[78] P. B. Littlewood, C. M. Varma, and E. Abrahams, Phys. Rev. Lett. **63**, 2602 (1989).

[79] J. van den Brink, M. B. J. Meinders, J. Lorenzana, R. Eder, and G. A. Sawatzy, Phys. Rev. Lett. **75**, 4658 (1995).

[80] A. M. Gabovich, A. I. Voitenko, and M. Ausloos, Phys. Rep. **367**, 583 (2002).

[81] D. Basov, and T. Timusk, Rev. Mod. Phys. **77**, 721 (2005).

[82] E. Dagotto, *Nanoscale Phase Separation and Colossal Magnetoresistence* (Springer-Verlag, Berlin, 2002).

[83] R. Pietig, R. Bulla, and S. Blawid, Phys. Rev. Lett. **82**, 4046 (1999).

[84] A. T. Hoang and P. Thalmeier, J. Phys.: Condens. Matter **14**, 6639 (2002)

[85] N.-H. Tong, S.-Q. Shen, and R. Bulla, Phys. Rev. B **70**, 085118 (2004)

[86] H. Seo, J. Merino, H. Yoshioka, and M. Ogata, J. Phys. Soc. Jpn. **75**, 051009 (2006).

[87] J. E. Hirsch, E. Loh, Jr., D. J. Scalapino, and S. Tang, Phys. Rev. B **39**, 243 (1989).

[88] P. G. J. van Dongen, Phys. Rev. Lett. **74**, 182 (1995).

[89] L. D. Landau and E. M. Lifshitz, *Quantum Mechanics* (Oxford: Pergamon Press, 1977).

[90] J. P. Lowe, K. A. Peterson, *Quantum Chemistry* (Elsevier, Amsterdam, 2006).

[91] E. M. Lifshitz, L. D. Landau, and L. P. Pitaevskii, *Electrodynamics of Continuous Media*, 2nd ed. (Butterworth-Heinemann, 1984).

[92] M. Born, and E. Wolf, *Principles of Optics* (Cambridge University Press, 1998).

[93] G. Grüner (editor), *Millimiter and Submillimiter Wave Spectroscopy of Solids*, 1st ed. (Springer, 1998).

[94] M. Dressel, and G. Grüner, *Electrodynamics of Solids* (Cambridge University Press, Cambridge, 2003).

[95] H. M. Nussenzveig, *Causality and Dispersion Relations* (Academic, New York, 1972).

[96] J. D. Jackson, *Classical Electrodynamics*, 3rd ed. (Wiley).

[97] R. de L. Kronig, J. Opt. Soc. Am. **12**, 547 (1926).

[98] H. A. Kramers, "La diffusion de la lumiére par les atomes", in *Atti del Congresso Internazionale dei Fisici.* Vol. 2 (Zanichelli, Bologna, 1927), pp. 545-547.

[99] F. Wooten, *Optical Properties of Solids* (Academic Press, New York, 1972).

[100] R. Kubo, J. Phys. Soc. Jpn. **12** 570 (1957).

[101] D. Chandler, *Introduction to Modern Statistical Mechanics*, (Oxford University Press, 1987).

[102] F. H. L. Essler, H. Fram, F. Göhmann, A. Klümper, and V. Korepin, *The One-Dimensional Hubbard Model* (Cambridge University Press, 2005).

[103] G. D. Mahan, *Many-Particle Physics* (2nd ed., Plenum Press, New York, 1990).

[104] M. Takahashi, Prog. Theor. Phys. **52**, 103 (1974).

[105] N. Kawakami, T. Usuki, and A. Okiji, Phys. Lett. A **137**, 287 (1989).

[106] T. Usuki, N. Kawakami, and A. Okiji, J. Phys. Soc. Jpn **59**, 1357 (1990).

[107] A. Klümper, and J. Suzuki, Nucl. Phys. B **522**, 328 (1998).

[108] F. Gebhard, A. Girndt, and A. E. Ruckenstein, Phys. Rev. B **49**, 10926 (1994).

[109] D. Poilblanc, T. Ziman, J. Bellisard, F. Mila, and G. Montambaux, Europhys. Lett. **22**, 537 (1993).

[110] R. A. Bari, Phys. Rev. B **3**, 2662 (1971).

[111] D. Ihle, and B. Lorenz, Phys. Status Solidi B **60**, 319 (1973).

[112] S. Robaszkiewicz, Acta Phys. Pol. A **55**, 453 (1979).

[113] T. M. Rice, and L. Sneddon, Phys. Rev. Lett. **47**, 689 (1981).

[114] J. Hubbard, in *Quasi-One-Dimensional Conductors*, S. Barisic, A. Bjelis, J. R. Cooper, and B. Leontic, (Spinger, Berlin, 1979), Vol. 1.

[115] F. B. Gallagher, and S. Mazumdar, Phys. Rev. B **56**, 15025 (1997).

[116] F. H. L. Essler, F. Gebhard, and E. Jeckelmann, Phys. Rev. B **64**, 125119 (2001).

[117] W. Barford, Phys. Rev. B **65**, 205118 (2002).

[118] M. Ogata, and H. Shiba, Phys. Rev. B **41**, 2326 (1990).

[119] A. Parola, and S. Sorella, Phys. Rev. Lett. **60**, 1831 (1990).

[120] A. B. Harris, and R. V. Lange, Phys. Rev. **157**, 295 (1967).

[121] P. G. van Dongen, Phys. Rev. B **49**, 7904 (1994); *ibid.*, **50**, 14016 (1994).

[122] E. Jeckelmann, F. Gebhard, and F. H. Essler, Phys. Rev. Lett. **85**, 3910 (2000).

[123] E. Jeckelmann, Phys. Rev. B **66**, 045114 (2002).

[124] P. B. Allen, Phys. Rev. Lett. **59**, 1460 (1987).

[125] S. I. Anisimov, and B. Rethfeld, Sov. Phys.-JETP **39**, 375 (1974).

[126] S. D. Brorson, A. Kazeroonian, J. S. Moodera, D. W. Face, T. K. Cheng, E. P. Ippen, M. S. Dresselhaus, and G. Dresselhaus, Phys. Rev. Lett. **64**, 2172 (1990).

[127] W. J. Duffin, *Electricity and Magnetism*, 4th ed. (McGraw Hill Higher Education, 1990).

[128] Fabrice Vallée, Phys. Rev. B **49**, 2460 (1994).

[129] E. Jeckelmann, Phys. Rev. B, **67**, 075106 (2003).

[130] S. Clark, *Strongly correlated one-dimensional systems of cold atoms in optical lattices* (DPhil thesis, University of Oxford, 2007).

[131] D. Jaksch, C. Bruder, J. I. Cirac, C. W. Gardiner, and P. Zoller, Phys. Rev. Lett. **81**, 3108 (1998).

[132] D. Jaksch, P. Zoller, Ann. Phys. (N. Y.) **315**, 52 (2004).

[133] J. Struck, C. Ölschläger, R. Le Targat, P. Soltan-Panahi, A. Eckardt, M. Lewenstein, P. Windpassinger, and K. Sengstock, Science **333**, 996 (2011).

[134] A. J. Leggett, S. Chakravarty, A. T. Dorsey, Matthew P. A. Fisher, Anupam Garg, and W. Zwerger, Rev. Mod. Phys. **59**, 1 (1987).

[135] S. Tornow, R. Bulla, F. B. Anders, and A. Nitzan, Phys. Rev. B **78**, 035434 (2008).

[136] J. Jortner, and M. Bixon, Adv. in Chem. Phys. **106/107** (1999).

[137] V. May, and O. Kühn, *Charge and Energy Transfer Dynamics in Molecular Systems* (WILEY-VCH, Weinheim, 2004).

[138] R. A. Marcus, J. Chem. Phys. **24**, 966 (1956).

[139] A. Nitzan, *Chemical Dynamics in Condensed Phase: Relaxation, Transfer, and Reactions in Condensed Molecular Systems* (Oxford University Press, Oxford, 2006).

[140] G. Clos, and H.-P. Breuer, Phys. Rev. A **86**, 012115 (2012).

[141] U. Weiss, *Quantum Dissipative Systems*, 3rd ed. (World Scientific, 2008).

[142] P. Haikka, J. D. Cresser, and S. Maniscalco, Phys. Rev. A **83**, 012112 (2011).

[143] A. Nazir, Phys. Rev. Lett. **103**, 146404 (2009)

[144] D. P. S. McCutcheon, and A. Nazir, Phys. Rev. B **83**, 165101 (2011).

[145] R. Sensarma, D. Pekker, E. Altman, E. Demler, N. Strohmaier, D. Greif, R. Jördens, L. Tarruell, H. Moritz, and T. Esslinger, Phys. Rev. B **82**, 224302 (2010).

[146] K. A. Al-Hassanieh, F. A. Reboredo, A. E. Feiguin, I. Gonzàlez, E. Dagotto, Phys. Rev. Lett. **100**, 166403 (2008).

[147] S. K. Lyo, and J. P. Gallinar, J. Phys. C **10**, 1693 (1977); S. K. Lyo, Phys. Rev. B **18**, 1854 (1978).

[148] D. J. Klein, Phys. Rev. B **8**, 3452 (1973).

[149] H. J. Carmichael, *An Open System Approach to Quantum Noise* (Springer, Berlin, 2005).

[150] T. H. Johnson, S. R. Clark, and D. Jaksch, EPJ Quantum Technology **1**, 10 (2014).

[151] P. B. Blakie, and C. W. Clark, J. Phys. B: At. Mol. Opt. Phys. **37**, 1391 (2004).

[152] W. Kohn, Phys. Rev. **115**, 809 (1959)

[153] J. Des Cloizeaux, Phys. Rev. **135**, A698 (1964)

[154] G. Nenciu, Comm. Math. Phys. **91**, 81 (1983)

[155] C. Brouder, G. Panati, M. Calandra, C. Mourougane, and N. Marzari, Phys. Rev. Lett. **98**, 046402 (2007)

[156] G. Panati, Ann. Inst. Henri Poincaré **8**, 995 (2007).

[157] R. J. Duffin, Duke Math. J. **20**, 233 (1953). R. J. Duffin, and D. H. Shaffer, Duke Math J. **27**, 581 (1960).

[158] N. Marzari, and D. Vanderbilt, Phys. Rev. B **56**, 12847 (1997).

[159] B. C. Hess, G. S. Kanner, Z. V. Vardeny, and G. L. Baker, Phys. Rev. Lett. **66**, 2364 (1991).

[160] M. Trigo, J. Chen, M. P. Jiang, W. L. Mao, S. C. Riggs, M. C. Shapiro, I. R. Fisher, and D. A. Reis, Phys. Rev. B **85**, 081102(R) (2012).

[161] R. J. Hemley, R. J, and N. W. Ashcroft, Phys. Today **51**, 26 (1998).

[162] J. C. Slater, *Quantum theory of Atomic Structure* (Mc-Graw Hill, New York, 1960, Chpt. 15).

[163] E. A. Hylleraas, Z. Phys. **54**, 347 (1929); *ibid.* **60**, 624 (1930).

[164] J. E. Hirsch, Phys. Rev. Lett. **87**, 206402 (2001).

[165] T. Holstein, Ann. Phys. (N. Y.) **8**, 343 (1959).

[166] J. E. Hirsch, Phys. Rev. B **65**, 184502 (2002).

[167] J. E. Hirsch, Physica C **161**, 185 (1989).

[168] J. E. Hirsch, Phys. Rev. B **62**, 21 (2000).

[169] H. Spooner, and E. Teller, Rev. Mod. Phys. **13**, 75.

[170] I. G. Lang, and Y. A. Firsov, Zh. Eksp. Teor. Fiz. **43**, 1843 (1962).

[171] S. M. Barnett, and P. M. Radmore, *Methods in Theoretical Quantum Optics* (Oxford University Press, Oxford, 1997).

[172] R. Graham, J. Mod. Opt. **34**, 873 (1987).

[173] M. S. Kim, F. A. M de Oliveira, and P. L. Knight, Phys. Rev. A 40, 2494 (1989).

[174] G. S. Agarwal, and A. Kumar, Phys. Rev. Lett. **67**, 3665 (1991).

[175] Special issue 'Molecular Conductors', Chem. Rev. **104** (2004).

[176] M. E. Kozlov, K. I. Pokhodnia, and A. A. Yurchenko, Spectrochimica Acta Part A: Molecular Spectroscopy, **43**, 323 (1987).

[177] M. J. Rice, Solid State Comm. **31**, 93 (1979).

[178] A. Painelli, and A. Girlando, J. Chem. Phys. **84**, 5665 (1986).

[179] M. J. Rice, Phys. Rev. Lett. **37**, 36 (1976).

[180] N. Dean, J. C. Petersen, D. Fausti, R. I. Tobey, S. Kaiser, L. V. Gasparov, H. Berger, and A. Cavalleri, Phys. Rev. Lett. **106**, 016401 (2011).

[181] F. A. M. de Oliveira, M. S. Kim, and P. L. Knight, Phys. Rev. A **41**, 2645 (1990).

[182] T. Yamamoto,M. Uruichi,K. Yamamoto,K. Yakushi,A. Kawamoto, and H. Taniguchi, J. Phys. Chem. B **109**, 15226 (2005).

[183] P. Guionneau, C.J. Kepert, G. Bravic, D. Chasseau, M.R. Truter, M. Kurmoo, and P. Day, Synthetic Metals **86**, 1973 (1997).

[184] Y. Imamura, S. Ten-no, K. Yonemitsu, and Y. Tanimura, J. Chem. Phys. **111**, 5986 (1999).

[185] P. W. Anderson, Phys. Rev. **109**, 1492 (1958).

[186] C. Manzoni, M. Först, H. Ehrke, and A. Cavalleri, Opt. Lett. **35**, 757 (2010).

[187] D. Brida, G. Cirmi, C. Manzoni, S. Bonora, P. Villoresi, S. De Silvestri, and G. Cerullo, Opt. Lett. **33**, 741 (2008).

[188] J. Spałek, A. M. Olés, and K. A. Chao, Phys. Rev. B **18**, 3748 (1978); for a more complete version see: J. Spałek, A. M. Olés, and K. A. Chao, Phys. Stat. Sol. (b) **87**, 625 (1978).

[189] C. Jayaprakash, H. R. Krishnamurthy, and S. Sarker, Phys. Rev. B **40**, 2610 (1989).

[190] C. L. Kane, P. A. Lee, T. K. Ng, B. Chakraborty, and N. Read, Phys. Rev. B **41**, 2653 (1990).

[191] K. A. Chao, J. Spałek, and A. M. Olés, J. Phys. C **10**, L 271 (1977).

[192] K. A. Chao, J. Spałek, and A. M. Olés, Phys. Rev. B **18**, 3453 (1978).

[193] P. W. Anderson, Science **235**, 1196 (1987).

[194] Y. Nagaoka, Phys. Rev. **147**, 392 (1966).

[195] T. Brandes, and S. Kettemann, *The Anderson Transition and its Ramifications - Localisation, Quantum Interference, and Interactions* (Springer Verlag, Berlin, 2003).

[196] S. W. Lovesey, *Theory of neutron scattering from condensed matter*, vol. 1 (Clarendon Press, 1984).

[197] S. Blundell, *Magnetism in Condensed Matter* (Oxford University Press, USA, 2001).

[198] G. Vidal, Phys. Rev. Lett. **91**, 147902 (2003); *ibid.* **93**, 040502 (2004).

[199] N. Marzari, A. A. Mostofi, J. R. Yates, I. Souza, D. Vanderbilt, Rev. Mod. Phys. **84**, 1419 (2012).

[200] T. Ishiguro, K. Yamaji, and G. Saito, *Organic Superconductors*, 2nd ed. (Springer, 1998).

[201] A. Girlando, M. Masino, J. A. Schlueter, N. Drichko, S. Kaiser, and M. Dressel, Phys. Rev. B **89**, 174503 (2014).

[202] J. C. Cuevas, and E. Scheer, *Molecular Electronics. An Introduction to Theory and Experiment* (World Scientific Publishing Co. Pte. Ltd., 2010).

[203] J. R. Heat, and M. A. Ratner, Phys. Today **56**, 43 (2003).

[204] J. Walz, K. Ulrich, H. Port, H. C. Wolf, and F. Effenberger, Chem. Phys. Lett. **213**, 321 (1993).

[205] S. L. Gilat, St. H. Kawai, and J. M-. Lehn, Chem. Eur. J. **1**, 275 (1995).

[206] M. Irie, Th. Lifka, and K. Uchida, Mol. Cryst. Liqu. Cryst. **297**, 81 (1997); S. Kobatake, T. Yamada, and M. Irie, Mol. Cryst. Liqu. Cryst. **344**, 185 (2000); M. Irie, Chem. Rev. **100**, 1685 (2000).

Appendices

Appendix A

List of publications

- M. Mitrano, G. Cotugno, S.R. Clark, R. Singla, S. Kaiser, J. Stähler, R. Beyer, M. Dressel, L. Baldassarre, D. Nicoletti, A. Perucchi, T. Hasegawa, H. Okamoto, D. Jaksch, and A. Cavalleri, Phys. Rev. Lett. **112**, 117801 (2014).
- S. Kaiser, S. R. Clark, D. Nicoletti, G. Cotugno, R. I. Tobey, N. Dean, S. Lupi, H. Okamoto, T. Hasegawa, D. Jaksch, and A. Cavalleri, Sci. Rep. **4**, 3823 (2014).
- R. Singla, G. Cotugno, S. Kaiser, S. R. Clark, C. Manzoni, A. Cartella, H. Liu, M. Foerst, T. Hasegawa, H. Okamoto and A. Cavalleri, arXiv:1409.1088.
- R. Walters, G. Cotugno, T. H. Johnson, S. R. Clark, and D. Jaksch, Phys. Rev. A **87**, 043613 (2013).

Appendix B

Acknowledgements

First and foremost, I wish to thank S. Clark for the boundless patience and help that he's given me in these four years. It's enough to say that probably this work wouldn't have been possible without him. I am also grateful to my supervisor, A. Cavalleri, and to D. Jaksch for giving me the opportunity of working in a stimulating environment and to a variety of problems. Moreover, I thank T. Johnson for the very useful comments on my draft, and all my collaborators, especially M. Mitrano.

From a personal point of view, there are a lot of people have made these years an unforgettable experience, so I am obviously going to forget someone. Anyway, in (chronological) order, I cannot not start from my housemates in Marston, especially my persian brother Ali and my best man Alex. There has been food, chilling and endless talking. I wish there was more, but I hope that will happen soon. Since when I moved to Jericho, about three years ago now, Dave and Max have been the closest thing to siblings I have had here. I really hope I will see a lot of you guys in the future (Dave we are going to a massive festival next summer, make peace with it).

From before moving to UK, and most likely for much longer, I should thank Claudio and Giovanni for so many things I wouldn't know where to start. Trouble is, I am pretty sure you both would punch me in the face if I said something nice, so let's keep it simple: trip to Amsterdam to celebrate?

Paola, thank you so much for being so close to me when it was most needed, and Egi, a.k.a. the best dancer in town, for being always so happy and enthusiastic about anything around. Anna, my best German friend: thanks for the translation, for the trips, and the endless hours doing any sport you could imagine. I will see you in some dirty old town. Staying on the sport side of things, I cannot forget the boss-man

Richard, Ant, Sean and Oli: sorry guys for being the unhealthiest runner you've ever met, but thanks for making it so much fun.

A huge thanks goes to the best hosts I have ever met, Daniele and Lorenzo. Hamburg (and Berlin) would have never been so enjoyable without you guys. On the same note, thanks to everyone that shared trips, parties and every day life with me: Irene, Brian (I miss you man...), Erminia, Alberto, Alex, and the best party people I've come across so far, i.e., the Aussies (Luke in particular, despite his dislike of Italians, and the ultra-girls, Jess and Em). Also a heart-felt thanks to all the StX people, most notably Abi (along with Dave and Max): it's been great to have a college without having one.

In the best Italian tradition, my family (Dario, Mariangela, Peppe and my mum) has been great all along. Similarly all my friends back home that made sure that, even if I was long gone, I always had a home in my beloved country: Gaspare, Mariapina, Michela, Maria, Paola, and Federico.

Last but definitely not least, Gabby: thanks for the patience, the support and the huge amount of fun. I cannot wait for doing it again in the other hemishpere!

For all of you guys: wherever I'll be, you will always have a place to sleep, food and drinks to share, and a party to go to. Oh yes oh yes!